An experimental method to measure crystal growth rate in porous materials and quantify deformation developed during crystal growth.

Sara Mancigotti PhD Student

Department of Civil and Environmental Engineering

University of Strathclyde, Glasgow

Wednesday 27th May, 2020

This thesis is the result of the author's original research. It has been composed by the author and has not been previously submitted for examination which has led to the award of a degree.

Abstract

The aim of this thesis work is to develop a new experimental method to quantify damages produced by salt crystallisation in porous building materials, a phenomenon long considered as one of the most important cause of deterioration problems, occurring in monuments exposed to a wide range of environmental conditions [125]. Sodium sulphate in particular is widely recognised to be the most damaging salt because of the difference in solubility between phases and the very temperature-sensitive solubility of the stable phase at room temperature. It is known to have two hydrated phases at ambient conditions: the metastable heptahydrate ($Na_2SO_4 \cdot 7H_2O$) and the stable decahydrate called mirabilite ($Na_2SO_4 \cdot 10H_2O$). Damage is caused by mirabilite crystallisation from supersaturated solutions, either directly or via heptahydrate dissolution, which develops a high crystallisation pressure and relative high strain level on the porous matrix. Crystallisation of sodium sulphate hydrates is followed by ice formation when temperature drops below the solution eutectic point (c.$-3°$C). These mechanisms result in micro and macro fractures of the building materials. Damages entail costs from repair/replacement, hence a deeper quantitative understanding of strain produced from salt and ice crystallization in building materials is extremely relevant. With the new methodology presented here it can be measured how fast sodium sulphate and ice crystals grow through building stones and what strain is developed as a result. We achieved this by developing a new experimental apparatus which measures sample strain and crystal propagation rate using an LVDT and thermocouples respectively. For this thesis work we also used X-ray computed tomography (X-CT) to investigate where salts tend to distribute within stone cores. This technique enables one to image the morphology and internal structure of porous material, at very high resolution (μm), hence salt distribution within the porous matrix and at its outer surface could be detected. Understanding where different salts tend to distribute is fundamental to estimate and predict damage they can cause. Lastly, we also explored how specific stone physical and chemical parameters can affect damage caused by salts to masonry, and how damage is related to environmental parameters such as relative humidity and temperature and their cyclical changes. We did this by carrying out a field investigation at the Shetland Island Town Hall where sodium sulphate was found. For the investigation we used the apparatus developed during this work plus other diagnostic techniques.

Contents

List of Figures

List of Tables

Abbreviations

AMRL Advanced Materials Research Laboratory

DMA Differential Mechanical Analyser

DSC Differential Scanning Calorimetry

FBG Fiber Bragg Grating

FEM Finite Element Model

HES Historic Environment Scotland

ICP Inductively Coupled Plasma

LVDT Linear Variable Displacement Transducer

MIP Mercury Intrusion Porosimetry

MSMPR Mixed Suspension-Mixed Product Removal Crystallizer

NMR Nuclear Magnetic Resonance

OES Optical Emission Spectrometry

PDMS Polydimethyl siloxane

PLA Polylactic Acid

PTFE Polytetrafluoroethylene

XCT X-Ray Computed Tomography

XRD X-Ray Diffractometer

Acknowledgements

I would like to thank my supervisor, Dr. Andrea Hamilton, for her help, guidance and support throughout this PhD.

I would like to thank Derek McNee and the other technicians, Mara Knapp, Tatyana Peshkur and the AMRL staff for their assistance during my experimental work. I also want to thank Historic Environmental Scotland and the Shetland Island Council for the opportunity they gave me to carry on such interesting projects as part of my thesis work.

My gratitude also goes to my examiners, Dr. Craig Kennedy and Vernon Phoenix, for their time and their valuable and constructive feedback.

A special thanks goes to all my friends and colleagues of the Civil and Environmental Engineering Department, for all the amazing times we had together in and out of university. Thanks to Ruben for your endless love and support.

Chapter 1

Introduction

1.1 Literature review

We can define the concept of durability of material as its ability to resist the degradation over time caused by atmospheric and anthropogenic agents [106]. One of the main phenomenon affecting building materials durability is salt crystallisation. The presence of salts within building materials is directly connected to the presence of water flowing throughout the masonry. Water is a polar solvent, able to dissociate positive and negative ions that form the crystal lattice of the salt [125]. These ions are dispersed in the solvent and when this evaporates they associate themselves and crystallise. Water reaches building materials via different mechanisms (e.g. absorption and adsorption and capillary condensation) of which the main one is capillary rise. Many building materials show, in fact, an hydrophilic behave. Water in contact with rock forming mineral surfaces assumes a contact angle θ lower than 90° trying to maximise the solid-liquid interface area. Capillary rise is the main consequence of the affinity between water and building materials. If a liquid, like water, shows affinity for the walls of a capillary immersed in a container of the liquid itself, it rises spontaneously along the capillary walls under the force of a pressure P that can be calculated with Washburn Equation:

$$P = \left(\frac{2\sigma}{r_c}\right) cos\theta \tag{1.1}$$

Where σ is the surface tension of the liquid, r_c is the capillary radius and θ is the

contact angle [16]. For every hydrophilic material, if θ is lower than 90°,$cos\theta = 1$ and the value of P is higher than zero. The capillary pressure spontaneously pushes the water inside the capillary. The height of rise varies proportionally with the surface tension of the liquid rising and inversely proportional with the radius of the tube. So the same liquid will rise higher in a small diameter tube, say 5 microns, than in a large diameter tube of 50 mm. Water will continue to rise until the height h, where it reaches the equilibrium with the gravitational forces. This equilibrium can be expressed by the following equation:

$$\rho \cdot g \cdot h = \left(\frac{2\sigma}{r_c}\right) cos\theta \tag{1.2}$$

Where ρ is the density of the liquid, g is the acceleration of gravity.

Water flowing within building materials is promoted by the capillary network which functions like a collection of capillary tubes.

The porosity of a material describes the fraction of void space that it may contain, for example, air or water. It is defined by the ratio:

$$\phi = \frac{V_V}{V_T} \tag{1.3}$$

where V_V is the volume of void-space and V_T is the total or bulk volume of the material, including the solid and void components. With open porosity, we refer to the interconnected pores and the capillary network that represents the fraction of the total volume of the material in which fluids, like water, can effectively flow [16].

Although different materials will have different levels of vulnerability to salt crystallisation, depending primarily on their porosity and degree of permeability, all building materials, whether they are natural or artificial, are affected by this phenomenon.

1.1.1 Salt crystallization in pores

Salt crystallisation, as Rodriguez-Navarro and Doehne (1999) pointed out, strongly depends on the physical properties of the salt solution, in particular its interfacial tension with the stone pore system and its solubility [12], while the necessary condition for salt crystallisation is the supersaturation of the salt solution. The following equation

expresses the difference of the chemical potential between liquid and crystal phase during the process:

$$\Delta\mu = R_g \cdot T \cdot ln\left(\frac{C}{C_0}\right) \tag{1.4}$$

Where R_g is the Ideal Gas Constant, C is the solute concentration and C_0 is the solute concentration at saturation. The condition of supersaturation is reached when $C > C_0$ [108]. In this condition the hydrostatic pressure that must be applied to inhibit the crystal growing is given by the equation:

$$P_c = P_l + \frac{R_g \cdot T}{V_c} \cdot ln\left(\frac{C}{C_0}\right) \tag{1.5}$$

Where P_c is the pressure exerted in the crystal growing inside the pore and is defined by the Laplace equation:

$$P_c = P_l + \gamma_{cl} \cdot K_{cl} \tag{1.6}$$

Where P_l is the liquid pressure,K_{cl} is the curvature of the crystal/liquid interface (($K_{cl} = \frac{1}{r_1} + \frac{1}{r_2}$ with r_1 and r_2 the two principal radii of curvature) and γ_{cl} represents the surface tension between the crystal and the liquid surfaces. This tension represents the barrier of activation that must be overcome in order to start the nucleation process. Heterogeneous nucleation occurs when the pore walls act as nucleation surface and the intervention of another surface tension, γ_{sc} i.e. the solid/crystal interface tension, leads to a decrease in activation energy (in fact is demonstrated that $\gamma_{sc} < \gamma_{lc}$) [24].
Supersaturation is necessary to achieve the phenomenon of primary crystallization,which happens if no salt crystals are already present in the solution. Once crystals are present in the solution, secondary crystallization takes places. The crystal growing from a supersaturated liquid is able to push away particles suspended in the liquid. The repulsive interaction between the crystal and particle acts to reduce the total interfacial energy of the system. The contact between the crystal and the particle, in fact, leads the system to increase its total energy [124]. The interfacial energy between the crystal and the particle (γ_{cs}) becomes higher than the sum of the crystal/liquid and the particle/liquid

interfacial energies. This contact is avoided when the chemical potential is proportional to $\gamma_{cs} - (\gamma cl + \gamma_{sl})$. As the crystal can sustain a film of liquid between itself and particles, it can also sustain a liquid film between itself and the pore wall [124].

According to the theory of Correns (1949) a salt crystal can grow within a pore or a small cavity, if a thin layer of supersaturated solution is maintained at the salt-pore wall interface. Only if this layer of solution is maintained, can the crystals growing in a porous media exert pressure against the pore walls strong enough to overcome the tensile strength of the material and cause damage. Otherwise, without the liquid film, the crystals could grow until their surface comes in contact with the pore wall and then simply stop growing, without exerting any pressure. The pressure is transmitted across the solution film, which may be semi-rigid under these conditions [94]. Correns equation leads to calculate this crystallisation pressure P:

$$P = \left(\frac{RT}{V_s}\right) ln \left(\frac{C}{C_s}\right) \tag{1.7}$$

Where V_s is the molar volume of the crystal, $\left(\frac{C}{C_s}\right)$ is the supersaturation ratio, i. e. the ratio of actual to saturation concentration, R is the gas constant and T is the temperature [94].

Steiger (2008) and Flatt (2007) provided a reworked form of the Correns equation which takes into account necessary parameters related to the salt solution:

$$\Delta P = \frac{\nu RT}{V_m} \cdot \left(ln\frac{m}{m_0} + ln\frac{\gamma_{\pm}}{\gamma_{\pm,0}} + \frac{\nu_w}{\nu} ln\frac{a_w}{a_{w,0}}\right) \tag{1.8}$$

Where $\gamma_{\pm}$ is the mean ion activity, m is the concentration of the solution in moles per kg water, a_w is the activity of water (subscript zero indicates the value before crystallisation takes place), ν_w is the number of water molecules combined in the hydrate, ν is the stoichiometric number of ions, V_m is the molar volume of the salt, finally R is the gas constant and T the absolute temperature [34].

1.1.2 Sodium sulphate

Sodium sulphate has been intensively investigated due to its ability to cause great damage in building material and rocks. Sodium sulphate is known to have two hy-

drated phases at ambient conditions: the metastable heptahydrate ($Na_2SO_4 \cdot 7H_2O$) and the stable decahydrate called mirabilite ($Na_2SO_4 \cdot 10H_2O$). According with the Ostwald's rule of stages, mirabilite is more likely to crystallise from the metastable phase than directly from solution. The lower liquid-crystal interfacial energy of the heptahydrate crystal represents, in fact, a lower energetic barrier and, consequently, a lower critical supersaturation for nucleation compared to that required for the nucleation of mirabilite [98]. Damage is due to the formation of the stable mirabilite either directly, from the dissolution of the thenardite(Na_2SO_4), the anhydrous phase, or indirectly, via dissolution of the metastable phase. The transition between thenardite and mirabilite results in a large volume expansion (about 314%) [118] that causes significant crystallisation pressure. The hydration-dehydration mechanism does not proceed via absorption of moisture by a solid crystal but only by dissolution of that crystal and reprecipitation from solution [14].

In their evaporation experiments, Rodriguez-Navarro and Dohene (1999) confirmed that during rewetting/drying cycles, the rise and rapid growth of clusters of mirabilite crystals on the anhydrous phase, after its partial dissolution can generate large pressures in a porous material. The reason for this lies in the solubility of sodium sulphate (Fig. 1.1)

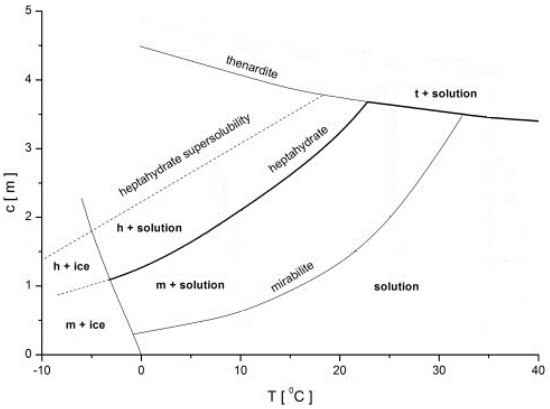

Figure 1.1: Supersolubility curve of sodium sulphate, Hartley (1908)

Thenardite is much more soluble than mirabilite so that when thenardite dissolves it produces a significantly supersaturated solution with respect to mirabilite which then crystallises rapidly. According to Correns equation(and re-worked version by Flatt et al.), the higher the supersaturation the higher the stress generated so in theory crystal-

lisation pressure can easily overcome the tensile strength of most common sedimentary building materials.

As shown in the phase diagram in Figure 1.2, thenardite is the stable phase above 32°C, while below 32°C the stable phase is mirabilite, which rapidly dehydrates at relative humidity (RH) values below 71% (20°C) to form thenardite. Thenardite will rehydrate to mirabilite if the relative humidity rises over 71% [95].

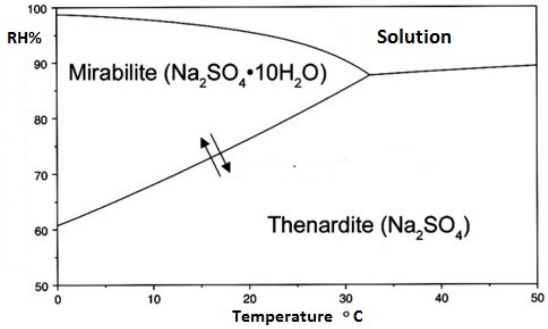

Figure 1.2: Phase diagram of Na_2SO_4 solution

However, experiments of Rodriguez-Navarro et al. (2000) pointed out that under normal (i.e. non equilibrium) conditions, thenardite can precipitate directly from solution even at temperature lower than 32°C, such as room temperature (20°C), but according to their experiments, only at low RH values ($< 40\%$) and therefore conditions of fast evaporation.

So the precipitation of thenardite is not solely a subsequence of the dehydration of mirabilite. Therefore, depending on the relative humidity the growth of both anhydrous and decahydrate crystals can be responsible for damage. At $RH < 50\%$ the anydrous salt was preferably formed, while at $RH > 50\%$ the decahydrate was preferably formed [95]. The high supersaturation degree that would be necessary for precipitation of thenardite, according to Correns equation, would result in an even larger stress on the pore wall than if one of the hydrates were to form [95].

1.1.3 Estimation of stress and strain from salt crystallisation

The Correns pressure is the maximum pressure that a crystal growing inside a pore from a supersaturated solution can exert on the pore wall [52]. According to Scherer (1999), the conditions necessary to damage building materials are that a sufficiently

large fraction of the pore wall is actually in contact with the growing crystal and that the stress generated is high enough to propagate existing flaws in the material [30].
If these conditions take place for brittle materials such as porous building materials, the stress exerted within pores can overcome the tensile strength of the material and lead to micro fractures that can easily extend [67]. The elastic energy that can be stored in a solid porous matrix is defined by Coussy (2006) in the following equation:

$$W = \frac{1}{2}\frac{\sigma^2}{K} \tag{1.9}$$

Where K is the bulk modulus of the material and σ is the tensile strength, which is roughly 3-9 MPa for a sedimentary rock. According Beltrami (1885), a brittle material cannot store elastic energy beyond some critical threshold W_{cr}. If the energy stored W equals the critical threshold, then failure occurs [17].
Brittle fracture of a porous material can be interpreted as the sudden coalescence of adjacent pores within the matrix when the pressure occurred reaches the tensile strength of the porous solid. Coussy (2006) concluded that the ultimate resistance of a stone to weathering depends strongly on the pore size distribution, and not solely on the porosity [18]. Larger pores, in fact, require larger crystals to form inside before they can exert enough stress against the pores walls to cause damage.
The work of Espinosa-Marzal et al. (2011) investigate the stress evolution inside two samples of different limestone during crystallisation of sodium sulphate. According to Coussy (2006) the local pressure induced by salt crystallisation is in fact related to the macroscopic stress $\sigma*$ by the following equation:

$$\sigma* \approx bS_c\Delta P_c = 3K\varepsilon_f \tag{1.10}$$

Where K is the bulk modulus of the drained stone, b is the Biot coefficient of the samples, S_c is the local volume fraction of salt in the pores in the crystallisation front and ε_f is the tensile strain at failure, measured during the previous phase of characterization of each sample. Equation (1.10) does not consider the different pore size distribution of the two limestone samples they used on $\sigma*$.
However, the authors point out that smaller pore size is not the only reason for enhanced

stress. In their experiment, the rate of solution transport through the pore network and the kinetics of dissolution-crystallisation reaction determined the salt distribution, pore filling and therefore evolution of stress. The system being investigated was 'rehydration' of a piece of limestone containing thenardite, where impeded solution transport and pore blocking are consequences of that experimental design that do not obviously apply to the experiments described in this thesis.

The weathering experiments of Steiger et al. (2008) pointed out that crystallysation pressure increases as temperature decreases, as a result of the strong temperature dependence of the solubility of the hydrates [88]. ΔP strongly decreases with rising temperature and vanishes at the transition temperatures of the hydrates (respectively 24°C and 32°C) as shown in Figure 1.3:

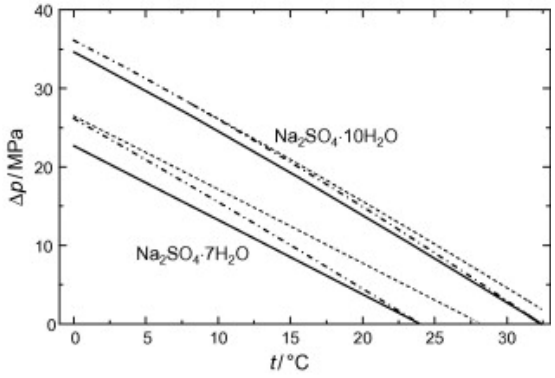

Figure 1.3: Crystallisation pressure ΔP of $Na_2SO_4 \cdot 10H_2O$ and $Na_2SO_4 \cdot 7H_2O$ as a function of temperature in crystallisation test, Steiger et al.(2008). Solid curves are calculated with a sodium sulphate solution 5 molal and dashed curves are calculated with a 3 molal solution.

The stress generated in stone or brick sample by growing salt crystals has been measured using different techniques by several investigators, often during evaporation (drying-rewetting) cycles, where RH and supersaturation degree changes play a key role.

The work of Steiger et al. (2008) cited above proposed the use of a dilatometric technique to investigate the deformation and the resulting stress within samples. In particular, during a wetting/drying cycle, digital dial indicators are used for dilatation measurement (i.e. the length change ΔL), and the strain ε is given by $\varepsilon = \frac{\Delta L}{L}$. Using the Young's modulus of the sample investigated (Ebenheide sandstone) with the measured strain is it possible to calculate the stress generated in the samples by the growth of mirabilite crystal [115]. Experiments were carried out at 27°C, when the crystallization of the heptahydrate is very unlikely hence the observed effects can be

attributed to the crystallization of mirabilite. A second experiment was carried out at 35°C and 45°C, above the thenardite-mirabilite transition temperature. Results show that damage at moderate to high RH in evaporation experiments is caused by the growth of mirabilite and, eventually at low temperatures, the heptahydrate. Maximum crystallization pressures that may be generated are of the same order of magnitude as the pressures generated in the standard crystallization test with sodium sulphate, in accordance with the graph in Figure 1.3.

Cooling experiments performed using a differential scanning calorimetry (DSC) and a dynamic mechanical analyser (DMA) by Espinosa-Marzal and Scherer (2008a, 2010a) quantified the expansion of 2 different limestones saturated with sodium sulphate 2.9 mol [29] and then cooled to form salt crystals. According to the results of this work, crystallization of heptahydrate occurred between 15 and 7°C and did not produce any real damage. Precipitation of mirabilite was often inhibited but its precipitation after heptahydrate dissolution induced a stress extremely high, above the material tensile strength. This technique, although reliable and accurate, is limited to very small sample sizes (maximum 30 mg) for the DMA analyser, therefore the rate of crystal propagation from one end of a sample to the other, and the correlation between strain produced and propagation rate could not be quantified using DMA.

1.1.4 Estimation of crystal growth rate in porous media

There is a limited literature regarding crystal propagation in porous media. This is due to the limited number of techniques available to study crystal propagation or growth in confinement (such as a porous matrix), while a large number of techniques are available to study free-surface crystal growth rates (i.e. FTIR Spectroscopy, and MSMPR crystallizer). Crystal growth rate is a very close function of the supersaturation degree of the salt solution. Supersaturation is also the driving force for crystal nucleation. At low supersaturation, crystals can grow faster than they nucleate. The results is a larger sized crystals. On the other hand, at a higher supersaturation degree, crystal nucleation is faster then crystal growth, resulting in more but smaller crystals [81], [76]. The relationship between supersaturation and nucleation and growth is defined by the

following equation.

$$G = K_g \cdot \Delta C^g \tag{1.11}$$

Where, G is growth rate, K_g is growth constant, g is growth order, ΔC is supersaturation [59]. However, when crystals grow in confinement, such as in a pore structure, their growth rate depends also, among other factors, on the reactive surface area and ion transport at the crystal-fluid interface, which in porous media depends largely on the permeability of the porous network [41] and its tortuosity. Prieto et ali. (1990) studied the nucleation of barite in a Na-rich aqueous solution, through a porous medium. The medium was a column of porous silica gel, and the crystal growth and diffusion rate was determined as a function of time by direct chemical analysis of mass transfer [90], [91]. The aim of the study is although focused on the critical supersaturation as the main factor controlling the growth kinetics. Results of their experiments shows the total number of nuclei appearing in the medium 24 hours after the first nucleation was observed. A number which decreases with the supersaturation ratio of the solution, as expected [90]. A value of speed of crystal growing through the medium is not provided. Another interesting attempt to evaluate the speed of crystal growth was carried out by Godinho et ali (2016). They studied barite growth rates in microporous silica through X-CT investigation, estimating the total number of crystals in the entire pore structure as a function of time. Results of their test show that the rate is approximately constant and similar to that observed on free surfaces. They estimated that after c.13 hours 18% of the initial pore space was filled with barite [41]. The work of Hamilton and Cimerman-Sariego (2008) proposes an experimental arrangement that uses a high speed camera and thermocouples in order to detect respectively the rate of transformation of a bed of heptahydrate crystals into mirabilite and the variation of the temperature, from the top to the bottom of the sample, to measure the velocity of the mirabilite propagation through the core. They started by nucleating heptahydrate crystals in a bottle of 3 molal solution by cooling, which formed a flat bed of crystals overnight. Then a mirabilite crystal was added to the bottle to promote rapid precipitation of the crystals. This first phase provided a reference for the results of the second phase, in

which a limestone sample is filled with sodium sulphate solution and then a mirabilite crystal is again seeded on the top of the sample to trigger mirabilite crystal growth. This is an exothermic reaction that leads to a local increase in the temperature which was detected by the thermocouples in order to determine the time it took for crystal growth to propagate through the full length of the sample [50]. The results achieved show that the propagation rate is extremely fast (c. 2 mm/s) for most of the tested samples.

Scherer et al. (2013) measured the speed of heptahydrate crystal growing along a medium of pore channels prepared in a hexagonal pattern in PDMS. Speed of crystal growth was measured using a camera mounted on the microscope. They observed that crystallisation through the channels was consistently slower than free solution since crystal growth was arrested for up to 40-60 seconds at the pore channels junctions before moving beyond the junction in a single step to the next one [102].

1.2 Scope of the thesis

The scope of PhD thesis work was to develop and test a new experimental technique to measure the speed of crystal propagation through growth a porous material and quantify the strain produced by both salt crystallisation and ice formation. The existent literature offers large number of studies on sodium sulphate, often occurring in building materials and recognized as one of the most damaging salts. Very little is known regarding the strain produced by salt crystallisation and, in particular, regarding the following ice formation under cooling, and the relationship with the kinetics of crystal propagation and the supersaturation of the salt solution. *Chapter 2* of this thesis presents the development process of a new experimental apparatus able to provide novel strain data for analysis alongside crystal growth propagation data. *Chapter 3* presents the preliminary results of experiments conducted on different sedimentary rocks and their interpretation. As part of this thesis project, an attempt to assess salt preferential distribution through the porous sample matrix was carried out by using X-Ray computed tomography. *Chapter 4* shows preliminary results of this investigation conducted with two different methodologies. Finally, an actual case of deterioration due to

salt crystallisation and, in particular, to sodium sulphate, was investigated. *Chapter 5* provides the outcome of a diagnostic survey project, which was conducted at Lerwick Town Hall, in Lerwick, Shetland Islands.

Chapter 2

A new experimental technique to measure strain from salt crystallisation and ice formation

2.1 Introduction

Starting from an experimental idea and procedure, along with a rough experimental apparatus, a prototype of a thermostated chamber was developed with the aim to be able to quantify strain exerted by salt crystallisation and ice formation, and relate these to the speed of crystal propagation. Strain developed in bulk scale (cm-m) laboratory samples is often measured using linear variable displacement transducers (LVDTs). Those are used particularly to measure elastic moduli or the co-efficient of thermal expansion, because they are highly affordable and can be used in a variety of environments. For these reasons LVDTs are one of the most common displacement sensors, used in industrial and research laboratories [112]. In the context of this work, LVDTs provide key advantages over non-contact measurement techniques. Freespace optical techniques, for example, can provide high resolution measurements of displacement ($<$ 0.01 μm), but they are expensive and are subject to errors in optical intensity that can arise due to changes in stone core target reflectivity in the presence of crystal growth. LVDTs, however, do present challenges of their own. Due to the variable sensitivities of LVDTs at low temperatures (c. -20°C), low temperature measurements can require

a complicated design of the sample cooling chamber and the use of connecting rods to transfer the movement to the LVDT mounted at environmental temperatures [77]. Furthermore, as they measure displacement via the induction currents generated by moving ferromagnets, they are extremely sensitive to electromagnetic interference, and this can discourage their use in the presence of Peltier cooling systems. This chapter describes the first experimental apparatus to use LVDTs and Peltier cells cooling system to accurately measure strain induced in porous cores during salt and ice formation from progressive cooling, while measuring crystal propagation rate through the sample at the same time. Details of the experimental technique are provided with a summary of the process leading to the development of this chamber, along with some of the issues related to its implementation.

For the purpose of this chapter the design process of the thermostated chamber is discussed in detail. The original prototype was built up by Tecnopenta s.r.l. and I carried out the implementation of the set up and the corresponding data collection. Dr. Marcus Perry carried out the verification of the design and the validation tests conducted optical fiber strain measurements and using a thermo-mechanical finite element method.

2.1.1 The experimental procedure

The experimental procedure is described as follows: Cylindrical stone samples(sandstone, limestone, etc.) of length $5cm$ and diameter $2.5cm$ are used. They are pre-drilled and dried in an oven at 100°C to constant mass. The mass of the sample is weighed before and after capillary saturation with a 3 molal sodium sulfate solution, then the sample is stored in a sealed bottle in an oven at 45° to avoid sodium sulfate formation by evaporation. A bitumen coat on the core barrel also protects against evaporation in the sealed bottle. The saturated sample is then placed within a chamber filled with mineral oil at +45°C to avoid crystallisation within the sample. The sample and the mineral oil within the chamber have to be gradually cooled, from +45°C to −7°C. Under progressive cooling and at a known temperature, the saturated sample undergoes two reactions: mirabilite crystallisation and then the ice formation. To determine the propagation rate of mirabilite the precipitation is controlled by initiating crystallization at the top of the

core when it reaches a certain temperature. By seeding a crystal of mirabilite at the top of the sample the reaction propagates along the core. Under further cooling, ice nucleates at c. $-3°C$. Both these reactions are exothermic so they lead to a temperature increase of between $+2°C$ and $+4°C$ and produce expansion and a relative strain along the core barrel of the sample. The exothermic response is measured by using a set of four thermocouples. Three of them are inserted at fixed intervals within the sample while another one monitors the temperature of the mineral oil during cooling within the chamber. The following linear expansion of the sample is measured with an LVDT located on the top of the core. Using the thermocouple data, the propagation rate of mirabilite crystal growth through the sample (mm/sec) and of ice (mm/sec) can be calculated. The temperature increase can be related to the crystal content within the sample [49]. Heat transfer rates calculations are also made in order to confirm that the temperature rises recorded by thermocouples are due to the crystals propagation and not to heat transfer within the sample, calculating the thermal diffusivity of the sample and then the time it takes for the heat to travel from the top to the bottom of the core. The LVDT is used to measure contraction and expansion during the experiment as the sample is cooled and crystal growth occurs.

2.2 Experimental design procedure

2.2.1 The perspex chamber

The original experimental set up, as it was conceived, consisted of a perspex chamber with four lateral holes for the thermocouples, connected to a Data Logger (SL7000 from Signatrol) and two holes in the lid, one to lodge the LVDT transducer (model GT1000RA RPD Electronics) and the other one for the crystal seeding tube. In order to cool down the temperature of both the mineral oil and the sample, the chamber, along with the thermocouples system and the LVDT, was placed within a fridge at $-30°C$. The reliability of the procedure is evaluated by placing the LVDT core on an Invar rod of the same size of the original samples within the chamber. Invar was chosen because it has a small coefficient of thermal expansion (1.2 x $10^{-6}K^{-1}$). The LVDT output signal is the differential a.c. voltage between the two secondary windings, which varies

according to the position of the core within the coil [85]. After the core is positioned in the centre (null position), the signal output has a linear relationship with the physical position of the core. If the core in touch with the upper surface of the sample is not moving, a flat line in the output signal is expected.

During each validation test, the LVDT output signal showed an irregular trend. Errors can indeed frequently occur when mounting the LVDT using materials with wide differences in expansion coefficients, such as plastic and metal. This can cause a false core motion resulting in a zero-shift error [85]. In particular, the thermal contraction of the perspex chamber itself introduced an error significantly higher than the expected value of the measurements, which resulted in a shift in the LVDT output level with respect to its core displacement. In particular, the unexpected non repeatability of this thermal contraction error leaded to the assumption that the LVDT itself was affected by the sudden temperature variation. LVDTs will always, in fact, exhibit greater error at both the lower and the higher values of its stated operating working range (between $+100°C$ and $-40°C$). Moreover, at very low temperatures it is likely that frost/ice builds up affecting the movement of the core. Is widely known that thermal variations can also cause changes in LVDT electrical or magnetic properties, resulting in a so called span-shift error [85].

The presence of these thermal-related errors was confirmed by tests conducted with a purpose-built structure, entirely made in Invar, and placed within the freezer chest. Figure 2.1 shows the test chamber, which was made from three small pillars connected to a circular base and a lid, all using Invar. The lid had a hole and clamp which the LVDT was inserted through.

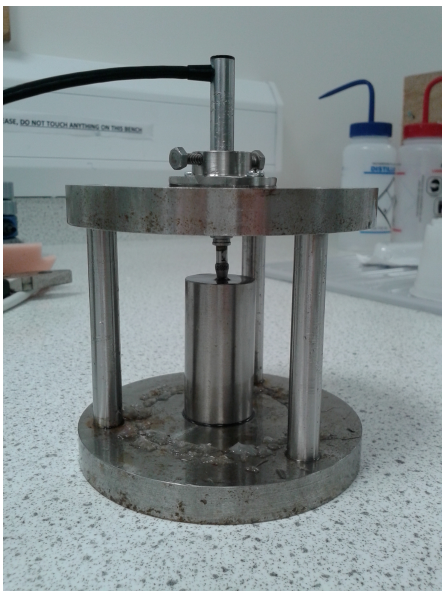

Figure 2.1: Invar structure with the LVDT core placed on an Invar rod.

The total core-shift error was quantified by testing the Invar structure with an Invar rod within the freezer chest. Temperature variation was detected by a thermocouple attached to the Invar rod.

The results of the test in figure 2.2 show that low temperatures can affect LVDT measurements, resulting in a core-shift error which is separate from movement associated with thermal contraction. By repeating the test, a total linear deformation of c. $23\,\mu m$ was recorded within the temperature range of interest (+40°C and -5°C), while the expected thermal contraction for the Invar cylinder, of diameter 2.5 cm and height $h =$ 5 cm was c. $3\,\mu m$.

During cooling ice formed on the LVDT armature, which affected the LVDT core movement and produced a small peak in the LVDT output signal, as seen in figure 2.2.

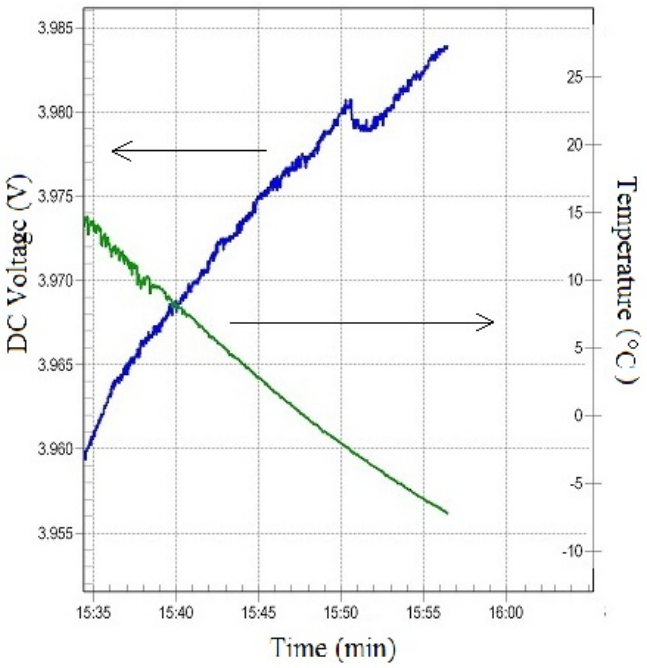

Figure 2.2: The graph shows the variation of both voltage and temperature detected by the LVDT (CH5) and thermocouple (CH6), respectively. The peak in the LVDT output signal comes from ice formation on the LVDT armature during testing.

In addition, during the tests with the persperx chamber, micro fractures were produced by the thermal shock at the chamber joints, resulting in leakage of the mineral oil from the inside of the chamber. The mineral oil surrounds the sample with the aim to avoid crystal growth by evaporation before the controlled initiation of the process and to ensure an homogeneous cooling of the sample. Therefore any mineral oil leak during the experiment should be carefully prevented.

For all those reasons, a new chamber design was adopted with the aim to avoid the use of a freezer compartment. The new chamber, made again in perspex, consisted of two concentric chambers (Fig. 2.3), the inner one hosted the sample and the mineral oil while the outer one was filled with dry ice.

Even though the LVDT was placed reasonably distant from the thermal conditioning of the sample, the output signal showed it was still affected by a consistent thermal contraction error produced by the plastic chamber (Fig. 2.4). Furthermore, the new chamber was not able to cool down the sample temperature to the mirabilite-ice eutectic point, which occurs at c. $-3°C$.

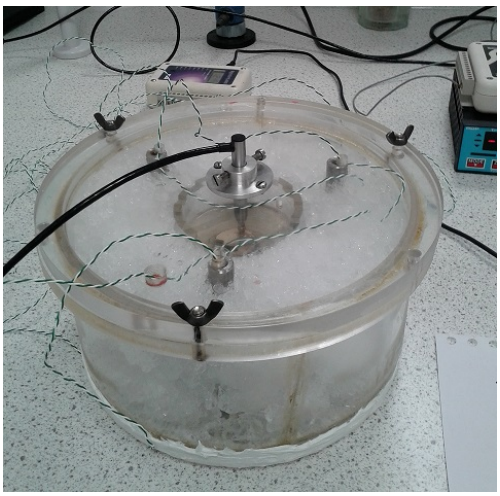

Figure 2.3: Plastic chamber for dry ice tests.

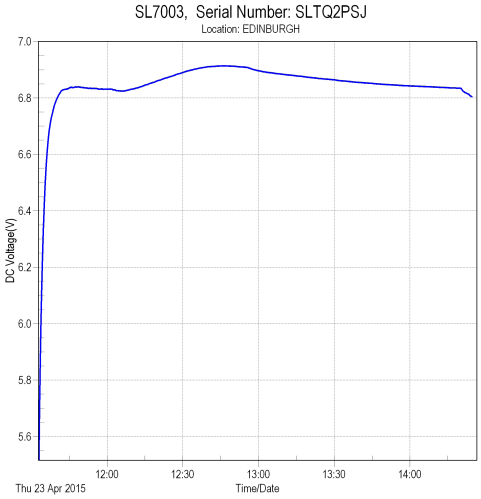

Figure 2.4: Output from the test conducted with the plastic chamber using dry ice.

2.2.2 The aluminium chamber

An aluminium chamber (Fig.2.5) was designed with the aim of using liquid nitrogen as cooling liquid which would reach a lower temperature. The chamber was made by two concentric chambers, both in aluminium. The inner one hosted the mineral oil and the sample, while in the outer one was poured the liquid nitrogen. The chamber was entirely covered by cork, with a layer of thermal insulating paste between the cork and the wall of the outer chamber. From a small hole in the cork on the upper side of the outer chamber,liquid nitrogen was poured in. On one side of the inner chamber, 5 small holes were made along the same vertical line in order to accommodate the thermocouples.

In contact with the liquid nitrogen at c.$-200°$C, which immediately evaporates, a sud-

den freezing of the aluminium is produced and the chamber temperature is rapidly lowered to c. $-100°$C. Heat transfer from the walls of the aluminium chamber to the mineral oil (plus sample) leads to a final temperature of c. $-10°$C in less than 30min. An elongation for the LVDT's head was made in bakelite to keep the head of the LVDT in touch with the upper surface of the sample while maintaining its body distant from the thermal conditioning of both the sample and the mineral oil, and from the liquid nitrogen evaporating.

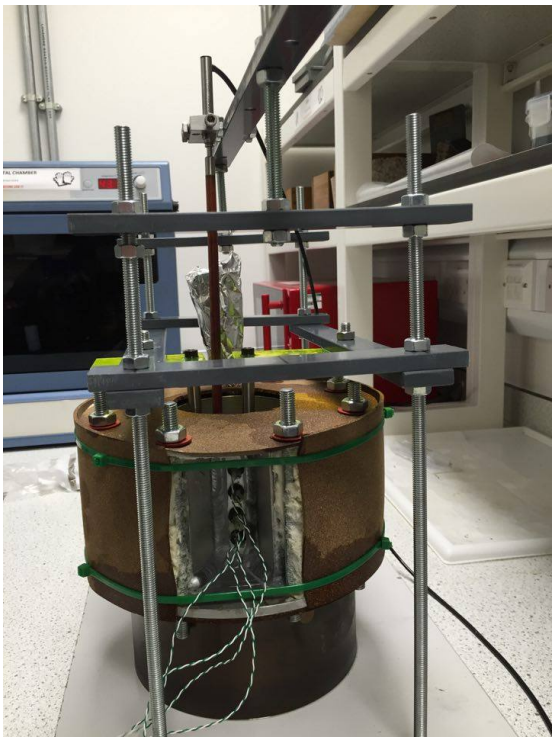

Figure 2.5: Aluminium chamber with the LVDT-holder structure and the bakelite elongation.

The significant thermal contraction of the chamber produced by c. $1L$ of liquid nitrogen considerably affected the measurements. This problem was solved by maintaining the sample detached from the bottom of the chamber using an aluminium basket-shaped sample-holder, with a base in PLA (polylactic acid), joined to a new LVDT-holder structure.

The huge thermal gradient produced from the bottom to the top of the inner chamber resulted in thermal gradient of c. $+10°$C detected between the bottom thermocouple and the upper one within the sample itself. This thermal gradient within the core was significantly reduced by covering the chamber bottom with a layer of cork $2cm$ thick

and by inserting a small fan, powered by a small rotary motor ($1.5 - 3V$), through the lowest of the lateral holes of the inner chamber. By inducing a fast circulation of the mineral oil within the inner chamber, the final thermal gradient was then of c. $+3°C$ detected between the bottom thermocouple and the upper one within the sample core. The error caused by the thermal contraction of the sample-holder was quantified for the aluminium chamber as shown in figures 2.6 and 2.7.

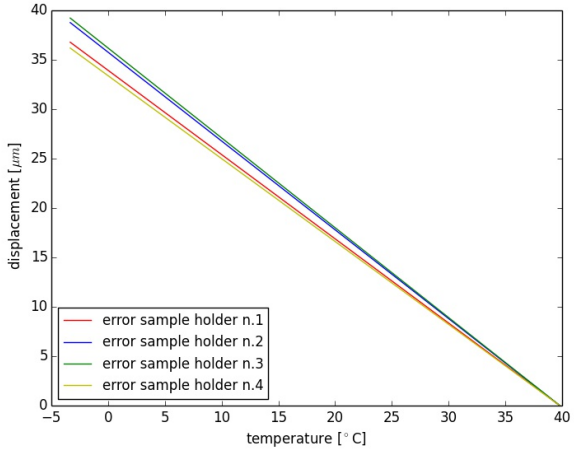

Figure 2.6: Results of several tests conducted in order to quantify the error caused by the thermal contraction of the sample-holder. The graph shows the variation of displacement value with temperature.

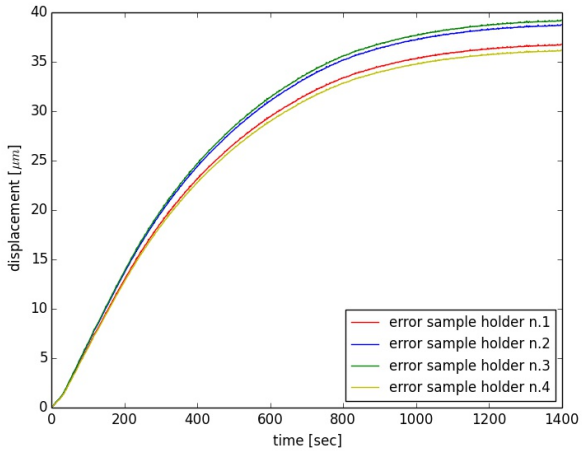

Figure 2.7: Results of several tests conducted in order to quantify the error caused by the thermal contraction of the sample holder. The graph shows the variation of displacement value with time.

The final error on the measurements was calculated to be $\pm 1\mu m$.

The aluminium chamber was also cumbersome to operate. The application process involved the use of c. $1L$ of liquid nitrogen, slowly and manually poured by the operator.

Then, only after the mineral oil is poured within the chamber the operator is able to place the sample within the same chamber, the thermocouples within the holes and the LVDT on the top of the core. This delicate operation has to be done quickly to avoid loss of important data as the mineral oil and the sample cool rapidly. Moreover, while switching on the fan particular attention must be paid to the sample holder and the sample itself as the mineral oil circulation is likely to produce micro-vibrations. It is therefore clear that the aluminium chamber operation is too prone to error.

2.3 Final design

The chambers described in the above chapters presented issues and sources of error which were eventually overcome by developing a custom-built thermostated chamber with Peltier cells which, therefore, represents the best solution for the experimental procedure. The chamber's most relevant characteristic is that it allows the LVDT to sit outside the cooling system and at environmental temperature for the whole duration of the experiment. The chambers development process, along with a detailed description of all the issues related to the use of an LVDT for specific types of measurements are presented in the following chapter.

2.3.1 The thermostated chamber

To avoid using liquid nitrogen for cooling, a purpose-built thermostated chamber (Fig. 2.8) was designed in order to provide a suitable experimental environment. A key characteristic of the chamber is that it allows the LVDT to measure core displacements from *outside* of the cooling system, therefore keeping the LVDT at ambient temperature for the duration of the experiment.

The thermostated chamber was specially designed and built in collaboration with Tecnopenta s.r.l. (Teolo, PD, Italy). This chamber is a stainless steel container of 2254 cm^3 (14 cm x 14 cm x 11.5 cm) designed to lower the sample temperature to at least -5°C with a cooling rate of c.+1°C/min. The chamber is equipped with twelve Peltier cells which control the temperature using an electronic heat pump. The twelve Peltier cells are divided into three groups of four and positioned on the bottom surface and two of the

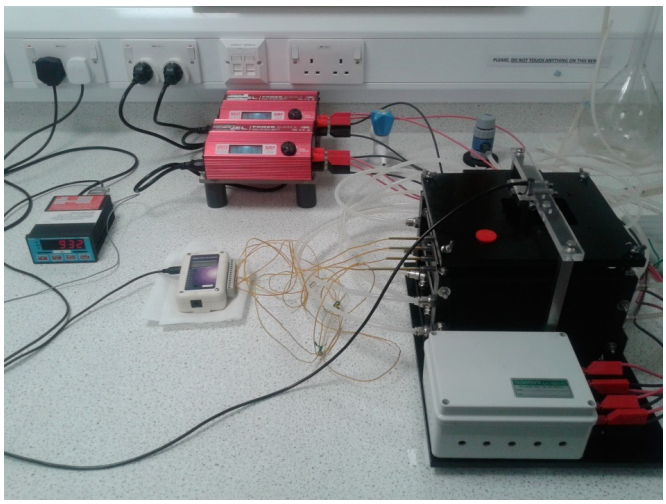

Figure 2.8: Thermostated chamber prototype.

side walls. Their cold face is in contact with the walls of the metal chamber while the hot face is in contact with an aluminum reservoir which has water circulation, for heat dissipation. The system is fed by electric current from two generic suppliers (6-15 Volts DC, up to 20 A each).

The LVDT transducer is located on the lid and distant from the thermal conditioning of the sample, as shown in figure 2.9.

Four thermocouples are located inside the chamber, at a regular distance of 8 mm from the top to the bottom of the chamber wall. Three of them are inserted within the sample and a fourth records the mineral oil temperature in the chamber. A set of four aluminum heat sinks facilitate thermal transfer from the chamber walls to the sample itself, which is located on a sample-holder on the bottom of the chamber.

2.3.2 Implementation and modification of the thermostated chamber

Chamber accuracy was tested by using an invar sample in place of a real sample, as before, over the sample temperature range of interest (+40°C to -5°C). The calculated linear thermal contraction for the Invar sample is c. 2 μm, therefore a nearly flat line in the LVDT output signal was expected. However, during each validation test, the LVDT output signal showed a drift clearly triggered by switching on the Peltier cells' current supply. The drift persisted until the two power supplies were switched off, then its trend changed drastically, as shown in figure 2.10

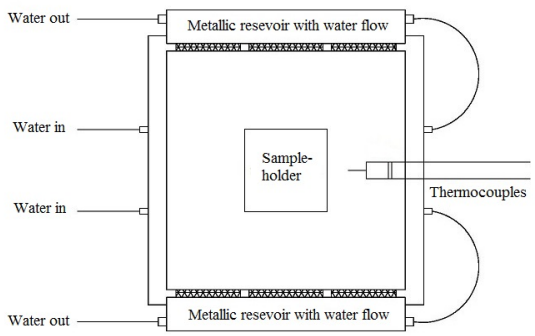

(a) Plan view of the chamber

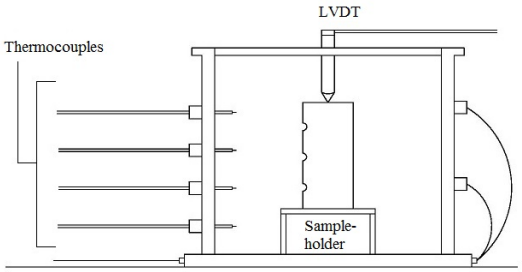

(b) Section of the chamber

Figure 2.9: Schematic of the thermostated chamber

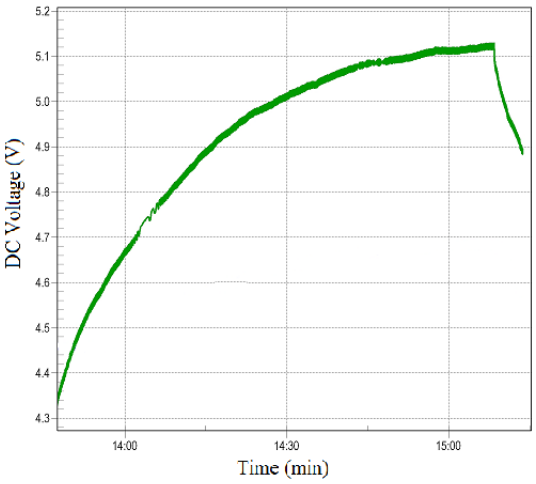

Figure 2.10: Drift in the LVDT output signal showing a significant change of the trend at the exact moment in which the Peltier cells were switched off, at 15:18 minutes.

The above drift was easily detectable from the display of the LVDT signal conditioner box which, immediately after the two power supplies were switched on, showed a sudden

and progressive increase in displacement values from the original position of the LVDT core. The presence of a magnetic field was highlighted as the cause of drift in the LVDT output signal by comparing several test results with other studies conducted on the same subject by Masi & Spiezia (2011) [75]. LVDTs are often sensitive to external magnetic fields, especially when used near current cables [75].

The influence of a magnetic field can result in a position reading error of a several hundred μm's, representing an important issue in applications where high accuracy is required [75]. Manufacturers are aware of this sensitivity, but the maximum tolerance to an external magnetic field and the consequent reduction of accuracy are not specified in device data sheets and this issue is not well addressed in the literature [112]. Therefore, the work presented here is one of the very few to explore the effect of magnetic fields generated by commonly used Peltier cells. The magnetic field was quantified using a portable GM08 Gaussmeter with a transverse probe. The intensity of the field was 0.006 mT in the centre of the chamber, above the Peltier cell system, which impacts transversally and uniformly on the LVDT, while it was c. 0.010 mT in proximity of the two power supplies, and 0.004 mT above the cable termination box.

The position reading error due to the external magnetic field showed no repeatability during each different validation test conducted with the Invar rod, resulting in a different gradient for each drift of the LVDT output signal, as shown in figure 2.11.

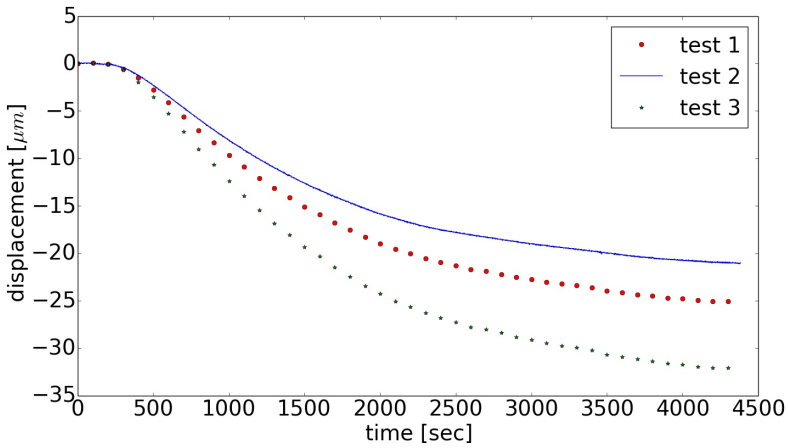

Figure 2.11: Drift in the LVDT output signal caused by external magnetic fields during three different tests.

Drift in the LVDT output signal persisted, even after an attempt at shielding the LVDT

connection cable with ferrite cores. Next, the LVDT signal condition box was replaced with a battery connected to a multimeter tester for the output signal reading, to rule out any affect of the magnetic field on the box. Again, the LVDT output signal showed a drift, suggesting that the external magnetic field was affecting the body of the LVDT. A linear potentiometric transducer was then tested, and the chamber lid was modified in order to host the new device. Even though for this kind of transducer the resolution isn't generally lower than 2 μm, they have the advantage of being more resistant to the effect of external magnetic fields. This type of transducer is affected by temperature alteration [105]. Tested using the same measurement conditions and procedure, the potentiometric transducer output signal showed an opposite trend with respect to the external magnetic field effect on the LVDT, as illustrated in figure 2.12. Moreover, the drift starting point showed a delay of several minutes after the chamber current supply was switched off, indicating there was no connection between the current flowing within the Peltier elements and the drift of the output signal.

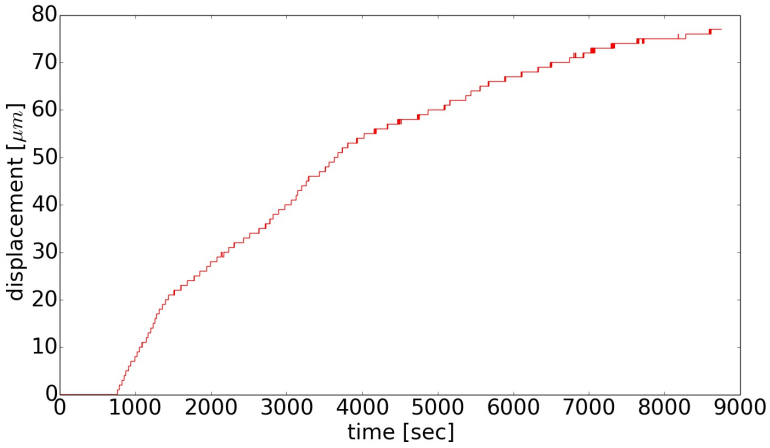

Figure 2.12: Drift in the potentiometric transducer output signal detected during the test.

The results of several tests using the potentiometric transducer showed a general instability in the output signal and confirmed the inadequacy of this type of transducer for this particular experiment, which led to the decision to keep using the LVDT. However, the results of these tests pointed to the presence of other sources of error in the experimental design, such as micro-vibrations possibly produced by cooling water flowing through the chamber.

The aim became to reduce or cancel the effect of the external magnetic field on the

LVDT transducer to allow accurate strain measurement. A differential system was then develop by placing two LVDT's within the chamber - one in contact with the sample and the other in contact with an Invar core, which was the same size as the actual stone sample. The measurement set up is shown in figure 2.13. Assuming that both LVDTs would have been affected by the same magnitude of the magnetic field, since they were both placed in the centre of the chamber and very close to each other (at a distance of c. 4.5 cm). With the differential system the output signal of the LVDT placed on the Invar rod could have been subtracted from the measurement on the stone core, thereby removing or nullifying the magnetic field effect.

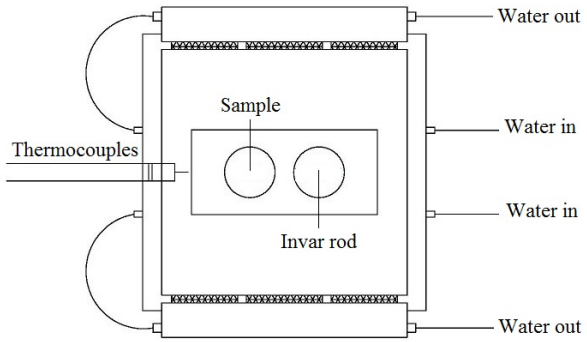

(a) Plan view of the chamber

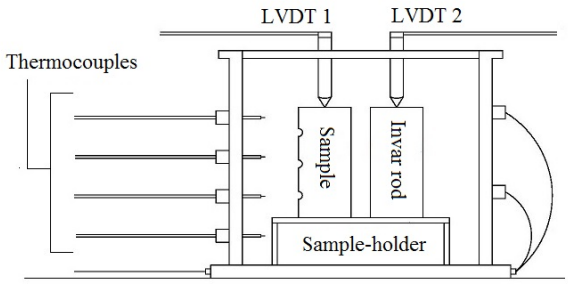

(b) Section of the chamber

Figure 2.13: Schematic of the differential system with two LVDTs. LVDT 1 in contact with the original sample (measuring sample movements plus magnetic field error), LVDT 2 in contact with an Invar rod of the same size of the original sample and is measuring only the magnetic field error.

Two LVDT's were each placed on an Invar sample of the same dimensions and tested in the same configuration to determine the reproducibility of the technique, as shown in figure 2.14.

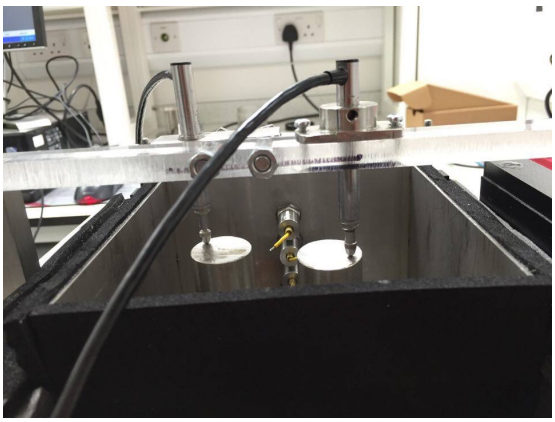

Figure 2.14: Differential system with two LVDTs mounted on the chamber lid and placed in contact with two Invar rods.

During each test the two devices, placed at a very short distance, were affected by a mutual interference resulting in a constant and severe oscillation of each LVDT output signal. Also, the output signal drifts of the two LVDTs each had a different gradient, which varied with each experiment and confirmed the two LVDTs were not affected by the same magnitude of magnetic field. The differential method was therefore inadequate. Results are shown in figures 2.15 and 2.16.

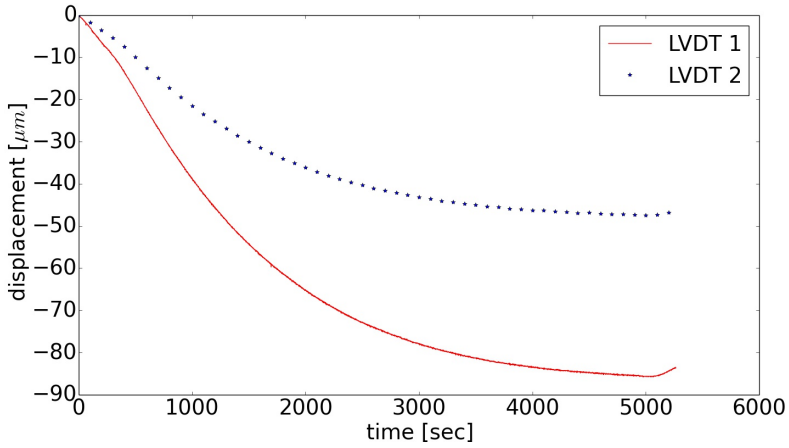

Figure 2.15: Example of a differential test conducted with two LVDTs placed within the chamber while temperature was lowered progressively from +20°C to -5°C. Each LVDT (n.1 and n.2) is affected differently by the external magnetic field, as shown by the variation in gradient between the two LVDT responses.

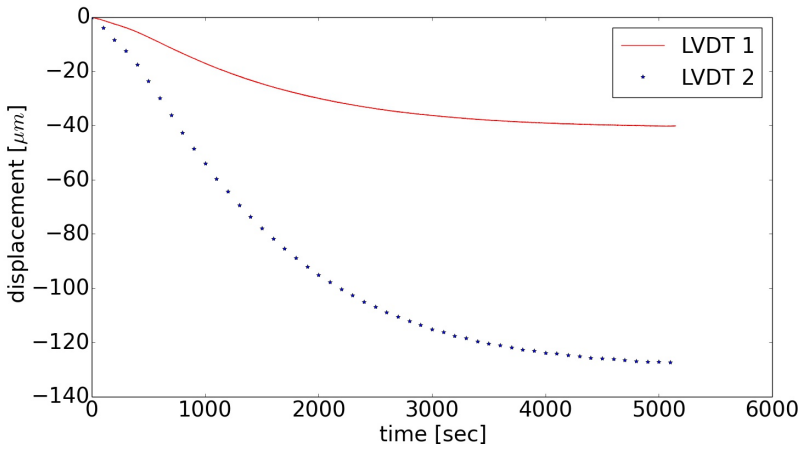

Figure 2.16: Another example of a differential test conducted with two LVDTs placed within the chamber.

A further test was carried out by shielding the LVDT body from the external magnetic field by covering it with a cylindrical sheath, 2 mm thick, of 99.95% pure iron which has magnetic permeability $\mu : 2.5 \cdot 10^{-1}[\frac{H}{h}])$. However, a simple test on an Invar sample showed the magnetic field was still affecting the data.

Finally, the magnetic field effect was cancelled out by vertically increasing the distance between the LVDT body and the source of the magnetic field, the Peltier cells system at the chamber bottom and walls.

An elongation through the head of the transducer and its main body,plus a new LVDT-holder, were made entirely in Invar. The length of the elongation, c. 8 cm, was chosen by placing the LVDT at different positions along the vertical axis at the centre of the chamber to find the closest distance at which the LVDT measurement was not affected by the magnetic field. The arrangement is shown in figure 2.17.

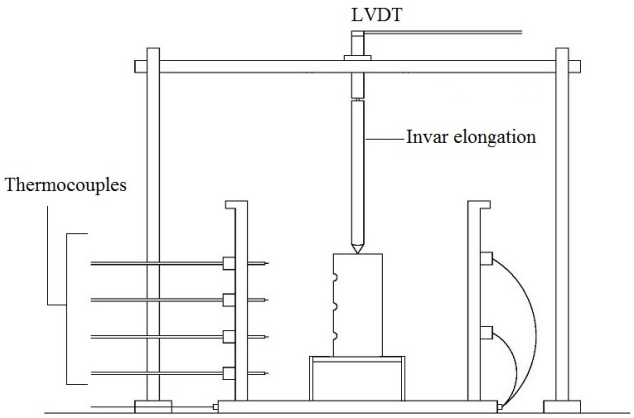

Figure 2.17: Schematic drawing of the thermostated chamber with the new LVDT elongation.

The results of the validation test showed that the slope of the output signal drift was significantly reduced, which can be seen from the displacement vs time graph in figure 2.18. In particular, the starting point of the residual drift always produced a delay with respect to switching on the current supply, suggesting this residual drift was not produced by magnetic interference. The output signal trend was comparable to the one observed by testing the potentiometric transducer, and therefore potentially related to the presence of micro-vibrations at the bottom of the chamber and thermal contraction of the sample-holder.

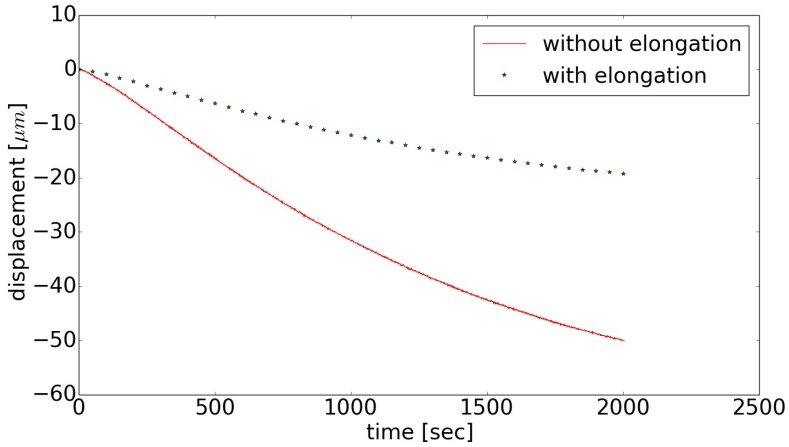

Figure 2.18: Results of the validation test conducted with and without the LVDT's elongation. The graph shows the variation of displacement with time.

The effect of micro-vibration was removed by replacing the original sample-holder with a cradle elevated from the bottom of the chamber which was joined to the new Invar

LVDT-holder to prevent artifacts from thermal contraction of the sample holder. The thermal gradient within the sample (c. +5°C) resulting from a thermal gradient within the chamber itself of c. +10°C was slightly enhanced by the metal base of the sample holder. This undesirable gradient was reduced to c. +1°C by inserting a small fan, powered by a rotary motor (1.5 - 3 V), through the chamber's lid. The final configuration of the system, as illustrated in figure 2.19 was then validated by the Invar test sample and produced a nearly flat line in the LVDT output signal for the whole duration of the experiment. This result showed only the slight thermal contraction (c. 2 μm) of the Invar itself, which was the desired result.

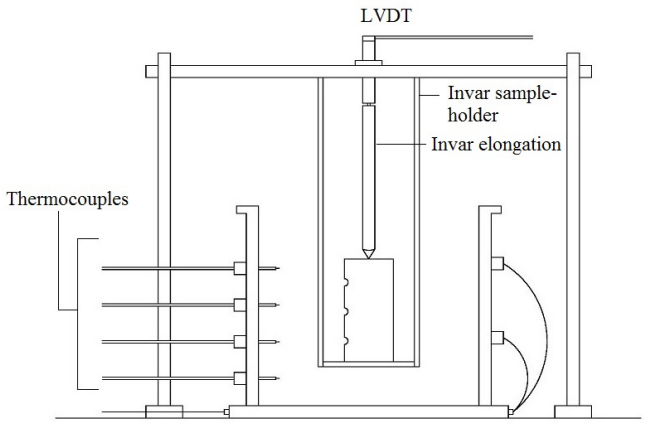

Figure 2.19: Schematic of the final configuration of the thermostated chamber.

The prototype chamber provides accurate and reliable measurements of strain developed during salt and ice crystallisation within any rock sample undergoing progressive cooling. Figure 2.20 shows the results of a test conducted on a sandstone sample. Thermocouples (TC 1,2 and 3) within the sample show its progressive cooling and the local formation of mirabilite (c. +20°C) and ice (c. -3°C). At the same time the LVDT detects a progressive contraction of the sample under cooling and expansion caused by the two reactions.

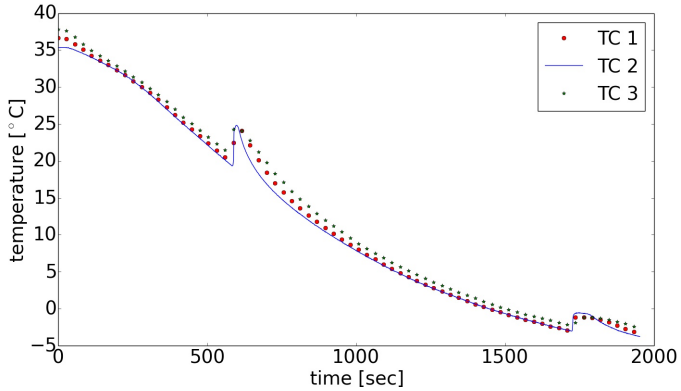

(a) Thermal response detected by thermocouples

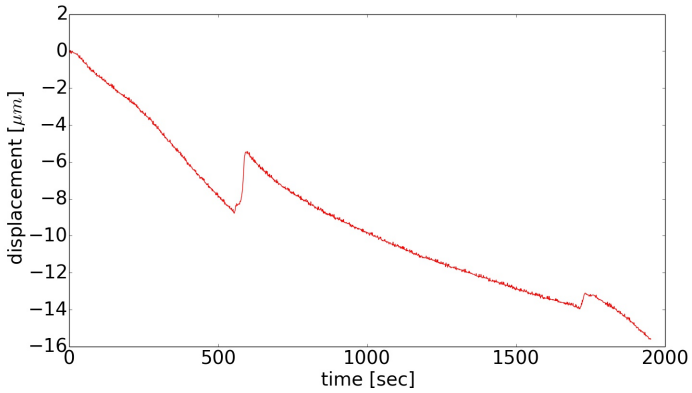

(b) Deformation detected by LVDT

Figure 2.20: Results of a test conducted on a Berea sandstone sample with the thermostated chamber.

2.4 Verification of design

A verification of the chamber design was carried out by Dr. Marcus Perry. To verify measurement accuracy, a tool steel cylinder,which has a co-efficient of thermal expansion of 11 - 12.5 x $10^{-6}K^{-1}$, was tested within the chamber. During the test the cylinder thermal contraction was monitored using both the chamber's LVDT and optical fibre sensors attached to the cylinder outer surface. Then, Dr. Perry compared LVDT displacement measurements against the thermal contraction inferred from: a) the axial strain of the steel cylinder, measured using optical fibre sensors; and b) the response of a thermo-mechanical finite element model (FEM) of the system, driven by experimental thermocouple data.

2.4.1 Optical fiber strain measurement

Optical fiber Bragg grating (FBG) sensors use the modulated properties of guided light to provide accurate, high resolution (1 $\mu\varepsilon$) measurements of substrate strain. FBGs are generally unsuitable for regular laboratory measurements of the strains induced by crystal growth in stone cores, as: a) they must be bonded to the cores and so they are single use; b) their interrogators present a high fixed cost; and c) they provide localised, rather than bulk, measurements of sample strain and this can lead to ambiguous results when crystal growth is gradual and not homogeneous. However, as they are completely immune to electromagnetic interference, they can provide reliable and accurate verification of the LVDT system used in this new experimental design, especially when used to measure the thermal expansion of steel substrates [87].

For this work, a 10 mm long FBG sensor was epoxied along the axis of a tool steel cylinder, of diameter 2.5 cm and height $h = 5$ cm. The response of the attached strain gauge was first characterised in an environmental chamber which was cycled between +15°C and -15°C in 5°C steps. At each step, the chamber was held for two hours to allow temperatures to stabilise. The attached FBG encodes its response to changes in temperature, ΔT, as a change in measured reflected wavelength, λ_B:

$$\frac{\Delta\lambda_B}{\lambda_B} = (\gamma\alpha_\Lambda + \alpha_n)\Delta T. \tag{2.1}$$

Here $\alpha_n = 7$ ppm/°C is the thermo-optic coefficient of the silica fiber and α_n is a thermal expansion term [55]. As the thermal expansion of silica glass is low, the steel substrate's response to temperature is dominant, and thus $\alpha_\Lambda \approx \alpha_{steel} = 10$ ppm/°C. Meanwhile, the strain transfer, γ, accounts for the imperfect transfer of strain from the steel cylinder to the attached FBG.

Figure 2.21 shows the fractional shift in the FBG's wavelength response as a function of environmental chamber temperature. The response is linear and reversible and comparison of the slope of the line shown in figure 2.21 with (2.1) suggests that the strain transfer is $\gamma \approx 60\,\%$.

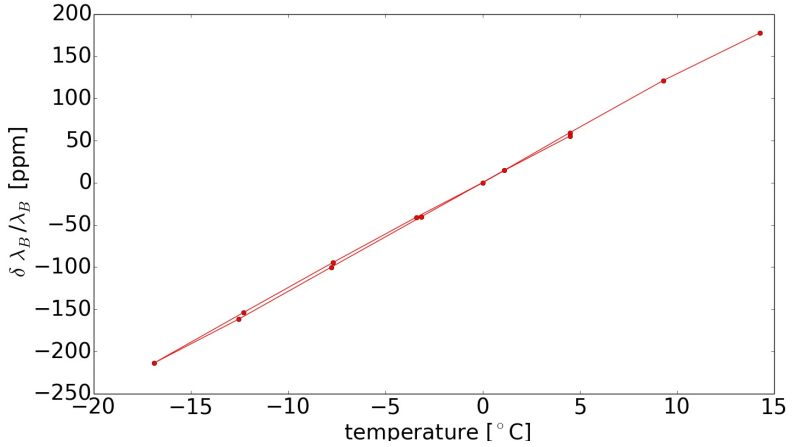

Figure 2.21: FBG response to temperature after attachment to steel cylinder.

Once characterised, the response of the FBG could be used to verify the thermal contraction of the steel cylinder during cooling in the bespoke thermostated chamber. The thermal strain measured by the FBG is converted into a bulk cylinder displacement via $\Delta h = \gamma \alpha_\Lambda h$.

2.4.2 Finite element model

The LVDT response was further verified against thermocouple data by using a thermo-mechanical FEM shown in figure 2.22. In the model, a tool steel cylinder is in contact with an Invar rod, which represents the core of the LVDT as it is exposed to the cooling mineral oil. The displacement of point A, labelled in figure 2.22b) is used to calculate a theoretical LVDT displacement. In this axisymmetric model, the boundaries of the steel cylinder, labelled *Thermocouple T* in figure 2.22a), were subjected to the temperature profile measured by a thermocouple in contact with mineral oil in the actual experimental chamber.

2.4.3 Validation results

Figure 2.23 displays the results obtained from the LVDT, FBG and the thermocouple-led FEM. There is clearly excellent agreement, particularly above temperatures of $-5°C$. Slight discrepancies between the displacements measured by the LVDT and FBG/FEM below $-5°C$ could be due to the effects of Invar's increasing coefficient of thermal expansion at these low temperatures. Nevertheless, the results confirm that the prototype

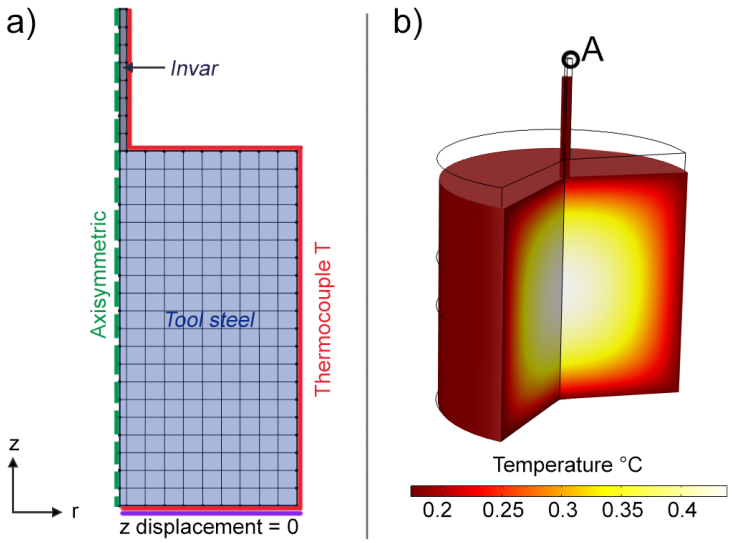

Figure 2.22: For the thermo-mechanical FEM, a) the mesh and boundary conditions, b) the temperature profile at 1000 seconds with scaled deformation, representing thermal contraction.

using the LVDT is at least as accurate as a much more costly FBG sensor. Results furthermore validate the combined use of LVDT and thermocouple measurements for use with rock core samples.

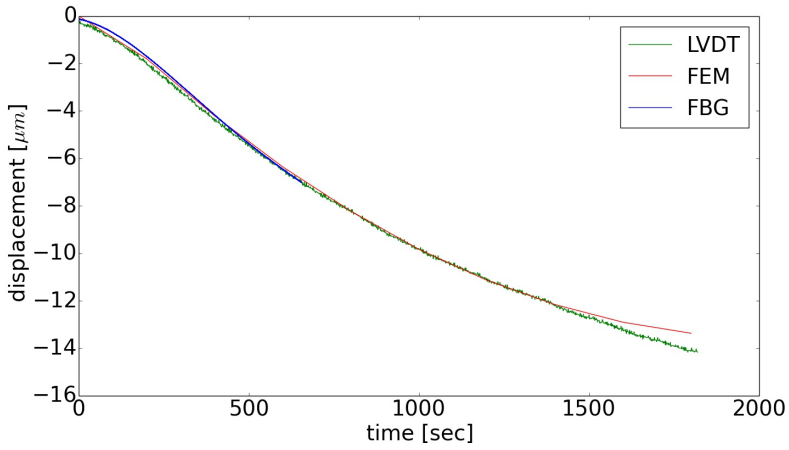

Figure 2.23: Displacements and temperatures measured via LVDT and FBG, and those inferred from thermocouple data and FEM, assuming $\alpha_{steel} = 10$ ppm/°C.

2.5 Conclusions

A detailed development procedure of a new experimental set up has been presented with accompanying evaluation and a description of the issues and the complications that arise from using an LVDT in a Peltier driven cooling system. The LVDT proved

to be extremely sensitive to external magnetic fields which produced a variable drift in the output signal that could not be reliably quantified for adjustment of real sample data. Importantly, it was proved that the LVDT output signal can be affected by thermal variations, particularly when the transducer body and head are separated, such as by an extension rod, and situated at different temperatures [77]. Although scant literature is available regarding both these sensitivities, they can considerably affect experimental measurements where high accuracy and resolution are required. These effects were eventually minimized allowing the use of the LVDT simultaneously with a thermocouple system in a new purpose-built thermostated chamber, designed with the aim to measure salt and ice crystal growth rate through building materials which have been contaminated with salt solutions. The new prototype allows to investigate the relationship between kinetics of crystal growth through porous materials and strain developed at the porous matrix, which has never been investigated before.

Chapter 3

The effect of crystal growth rate on damage: preliminary results of a new experimental technique

3.1 Introduction

The aim of this chapter was to use the thermostated chamber designed and built, as described in *Chapter 1* , to investigate a) the rate of nucleation of mirabilite ($Na_2SO_4 \cdot 10H_2O$) as crystal growth proceeds along the barrel of a core of sedimentary rock saturated with a 3 molal sodium sulphate solution and b) strain induced in the rock from crystal growth. A schematic of the experimental set up is shown below (Fig.3.1) .

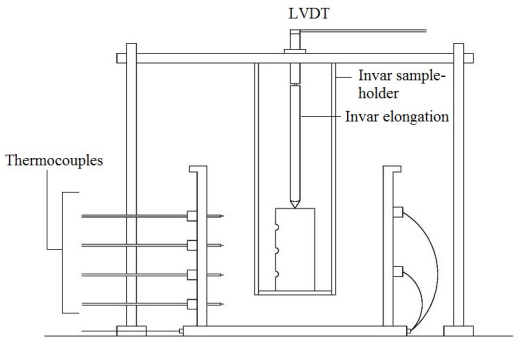

Figure 3.1: Schematic of the final configuration of the thermostated chamber.

Berea sandstone and Portland limestone were chosen because they are both sediment-

ary rocks with porosity c. 17 -22 % and will therefore hold similar amounts of solution. Berea is a silica cemented sandstone which contains no carbonate phases and only minor (c.< 10 %) kaolinite and traces of feldspar. Portland limestone has 3 main bed horizons: roach bed, whit bed and base bed. Roach bed is characterised by its high shell content and was not chosen for this work. Whit bed was chosen, which is described as an oolitic limestone with micrite matrix.

For the purpose of this chapter I carried out the laboratory experiments and data collection. Dr Andrea Hamilton carried out the thermal and mechanical data analysis. We worked together on interpretation of the results and conclusions.

3.2 Materials and method

Samples preparation

All cores (diameter 24 mm, length 48 mm) were drilled with 3 thermocouple holes of diameter c. 3 mm and placed approximately at 5, 15, 15 and 5 mm from the top of the sample as shown in figure below (Fig.3.2).

Figure 3.2: Sample with thermocouple holes.

Prior to any sample treatment, the cores were dried at 105°C in an air oven to constant mass. The barrel of the core was then sealed with bitumen paint to prevent unwanted evaporation. After 24 hours, the sealed and dry sample was capillary saturated with a 3 molal sodium sulphate solution in a screw top sample jar (Fig.3.3) and placed in a cabinet conditioned at 43°C.

Figure 3.3: Sample conditioning.

The thermocouple holes were injected with silicon grease before solution was added to the sample container. The silicon grease was used to prevent solution from entering the holes and to secure the thermocouples better during the experiment. The solution added to the sample container was stored in the same cabinet prior to use to avoid the solution crystallising, and filtered (25 mm diameter and 0.45 um pore size syringe filter, Nalgene) as it was added to the container with the sample. The volume of solution added to the container was c. 20 ml and the solution level always sat below the first thermocouple hole on the sample. Samples remained in capillary saturation for c. 2 days at which point the solution had risen to the top of the sample and it was monitored to ensure no crystallisation of thenardite, the stable phase at c. 43°C, took place in the sample container (Figure 3.4 is a phase diagram for the sodium sulphate system which shows the stable phase from 32.4°C to 43°C is thenardite). After saturation, samples were blotted (top and bottom face) on tissue paper and transferred to the chamber and placed under mineral oil which had been stored at 43°C with the saturating samples. Thermocouples were then inserted and the LVDT probe was positioned prior to chamber cooling and data collection. Samples were cooled to c. −5°C for every test. Mirabilite nucleation was initiated by gently dropping a crystal of mirabilite on the top of the core as described below and ice nucleation (not deliberately seeded) occurred at c. −3°C for every sample. The crystallisation of both mirabilite and ice is sufficiently exothermic that thermocouples can clearly see the formation of both phases.

Mirabilite crystallisation

Below 32.4°C the stable phase is mirabilite ($Na_2SO_4 \cdot 10H_2O$) and the metastable phase is $Na_2SO_4 \cdot 7H_2O$. According to Ostwald's rule of stages, the metastable phase forms first, however, the formation of heptahydrate was avoided in this experiment by inducing mirabilite crystallisation at a higher temperature than heptahydrate would spontaneously form. The lowest temperature that mirabilite crystallisation was induced at was c. 12.5°C. According to the phase diagram below (Fig.3.4), heptahydrate can precipitate from a 3 molal solution when the temperature drops below c. 18.5°C, however, it usually does not form until the temperature cools to the point that the heptahydrate supersolubility curve has been reached (Fig.3.5).

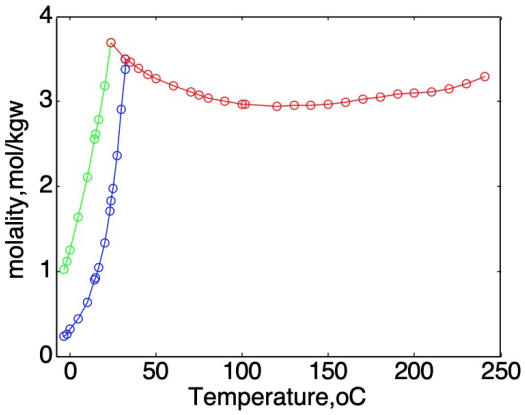

(a) a

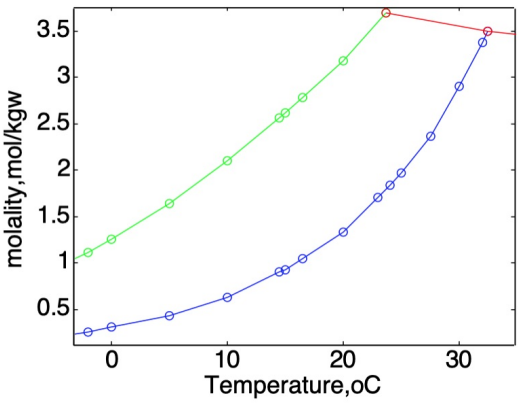

(b) b

Figure 3.4: Diagram Sodium sulphate solubility. Red is thenardite [40], blue is mirabilite and green is heptahydrate [70]. The solution concentration used was always 3 molal.

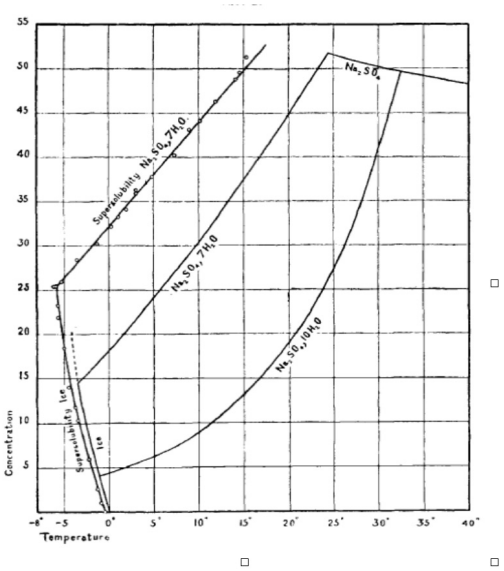

Figure 3.5: Diagram taken from Hartley et al., 1908. Solubility (y-axis) is given in g of Na_2SO_4 per 100g of water. The equivalent of a 3 molal solution is 42.613g Na_2SO_4 per 100g of water.

A 3 molal solution is 42.613 g of Na_2SO_4 per 100g of water. This means that heptahydrate should not crystallise on cooling until a temperature of c. 9°C. It is reasonable to assume that a porous material offers more nucleation sites than the glass tubes used by Hartley et al. but 23Na NMR data suggests that sodium sulphate heptahydrate formation in a porous material occurs at very similar temperatures on cooling as in a glass tube [99], which is when the supersolubility line is reached. Crystallisation of sodium sulphate heptahydrate is very difficult to detect with thermocouples, or indeed with more precise equipment such as differential scanning calorimetry [30]. Heat flow measurements from Espinosa-Marzal et al. (2008) show a very small peak when heptahydrate forms even when forming at high supersaturations (S/S_0 = c. 2.91 (mol/kg)/1.64 (mol/kg) = 1.77 when heptahydrate forms at c. 4.3°C) corresponding to c. 0.00045 W compared to the formation of mirabilite, also at a high supersaturation when precipitation occurs at c.0.33°C (S/S_0 = c. 2.91/0.32 = 9.09), produced a heat flow of 0.01W, which is 100 times higher. The crystallisation temperature of both heptahydrate and mirabilite was considerably depressed in the small samples of limestone (30 mg sample mass) used by Espinosa-Marzal et al. More standard temperatures of crystallisation for heptahydrate in larger samples, such as the cores used in the work presented here, would be c. 10°C [99]. The heptahydrate is unlikely to

have formed in the Berea cores because mirabilite precipitation was induced before the supersolublity curve would have been reached (c. 10°C) for a rock saturated with a 3 molal solution. If heptahydrate had formed, the exothermic response is not significant enough to be readily detected by thermocouples inserted in a porous material [49] so it would not have been observed. In addition, the formation of mirabilite from heptahydrate, through dissolution-precipitation is rapid [26] even though the crystallographic nature of the transformation is poorly understood. The conclusion is that without using sensitive equipment such as DSC (and therefore very small samples, c. 30 mg), the crystallisation of heptahydrate is not easily detectable inside a porous material and its formation was avoided by inducing mirabilite formation at a higher temperature than the supersolubility temperature for a 3 molal solution (c.10°C). It has also been discovered that when heptahydrate does form, as detected by synchrotron X-ray diffraction or 23Na NMR or DSC [49], [30], the potential for damage done to the porous host material is significantly less compared with the strain induced by mirabilite crystallisation. Saidov et al. [99]discovered that stress on the limestones tested, as calculated from the measured strain, was c. 20 - 100 times higher when mirabilite nucleated at c. -5°C compared with the (spontaneous) nucleation of heptahydrate at c. 10°C. The other sample they tested was a fired clay brick which had a higher porosity and lower bulk modulus than the limestones (Cordova and Indiana limestones) used but showed significantly lower increase in strain when mirabilite formed which in fact was similar to the magnitude of strain produced by heptahydrate formation (Figures 3.6 and 3.7). The distinction is interesting because the results for both limestones suggest permanent damage when mirabilite forms but not when mirabilite forms in the fired clay brick sample. All samples they use were vacuum saturated (no air trapping and therefore hydraulic pressure is possible) with the same solution and nucleated at the same temperature (therefore the same supersaturation).

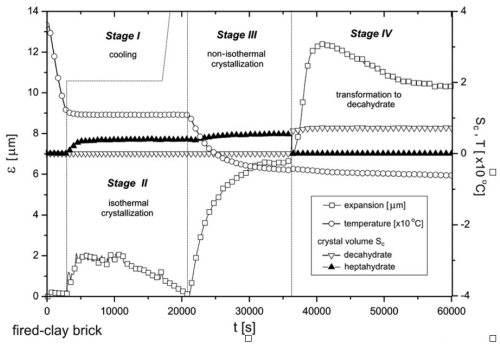

Figure 3.6: Diagram taken from Saidov et al., 2015. Expansion, temperature and volume of crystals formed of a fired clay brick sample. Sample expansion (left-hand axis) shows a length increase of 6 μm) during stage III crystallisation.

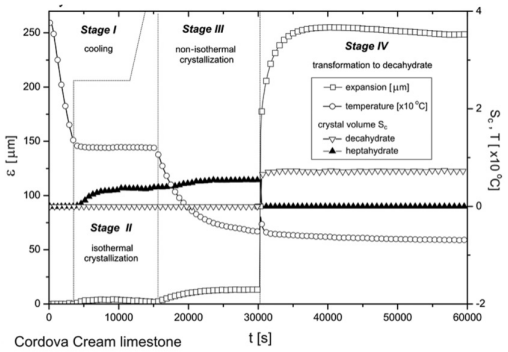

Figure 3.7: Diagram taken from Saidov et al., 2015. Expansion, temperature and volume of crystals formed of a Cordova cream limestone. Sample expansion (left-hand axis) shows a length increase of c. 220 μm) during stage III crystallisation. Expansion is compensated for thermal expansion.

Ice formation

Ice formation begins at c. $-2°$C, and as indicated by the mirabilite-ice eutectic point on figure 3.5, the solution inside the core solidifies completely, leaving solid mirabilite and ice. Nucleation of ice is not artificially seeded, although growth always occurs first at the bottom of the core, rather than the top when mirabilite is seeded.

Samples

11 samples of Berea sandstone and 7 samples of Portland limestone were tested.

Table 3.1: All Berea cores were 24 mm diameter. Seeded growth (Y) indicates the sample was successfully seeded when a crystal of mirabilite was gently dropped onto the top surface of the core. Where seeded growth did not occur (N), mirabilite nucleated before the sample could be successfully seeded (as evidenced by the thermocouple response). The difference is that growth initiates from the top of the sample when seeded from the top, but initiates from the bottom of the sample when nucleation occurs prior to seeding. BE10 was capillary saturated for longer (267 days compared with 2 days standard procedure), therefore the core is closer to full saturation and contains c. 1g more of solution than the other cores. BE10 was also cycled through 4 heating and cooling cycles.

Sample name	Core length, mm	Growth seeded [*yes*/*no*]	Temperature of mirabilite precipitation, °C	Mass of solution in the core, g	Volume fraction of pores filled with solution
BE17	48	Y	12.6	3.29	0.55
BE16	48	Y	17.6	3.27	0.67
BE15	49	N	17.6	3.35	0.70
BE14	49	Y	17.6	3.66	0.72
BE13	48	Y	18.6	3.40	0.67
BE10_cyclical	52	Y	19.9	4.64	0.79
BE19	50	Y	21.1	3.61	0.69
BE18	50	N	24.5	3.65	0.70
BE17	50	N	21.5	3.49	0.67
BE16	49	N	21.0	3.51	0.69
BE05	50	N	24.0	3.64	0.64

Table 3.2: All Portland limestone cores were 24 mm diameter. Seeded growth (Y) indicates the sample was successfully seeded when a crystal of mirabilite was gently dropped onto the top surface of the core.

Sample name	Core length, mm	Growth seeded [*yes*/*no*]	Temperature of mirabilite precipitation, °C	Mass of solution in the core, g	Volume fraction of pores filled with solution
PL07	48	Y	4.4	3.86	0.5846
PL06	49	Y	13.04	3.8	0.5856
PL05	49	Y	13.7	3.88	0.5912
PL04	48	Y	15.9	3.76	0.5733
PL03	52	Y	17.8	4.08	0.5856
PL02	50	Y	18.6	3.92	0.5769
PL01	50	Y	19.6	4.02	0.584

3.3 Data analysis

3.3.1 Strain and thermal expansion

The linear coefficient of thermal expansion is calculated, according to

$$\alpha_L = \frac{1}{L}\left(\frac{\delta L}{\delta T}\right) \tag{3.1}$$

where L is sample length and T is temperature in °C, by taking the gradient of the strain-temperature plot prior to crystallisation. The result is expressed in μm/(m $\cdot$°C). The co-efficient of thermal expansion for each sample was used to calculate thermal strain ($\varepsilon_T = \alpha_L \Delta T$) produced from the exothermic formation of mirabilite, which was subtracted from the measured strain at the point of nucleation to calculate strain from crystal growth. When ice forms and no liquid phase remains (at the bulk scale), the coefficient of thermal expansion is that of a composite material (stone+mirabilite+ice). Plotting sample temperature and sample displacement (μm) against time for sample BE13 (Berea) it is clear that there is a change in the displacement gradient after ice crystallisation which is not present after mirabilite crystallises. This change is clear in figure 5 and could be caused by either the co-efficient of thermal expansion changing or sample damage. An equation for the co-efficient of thermal expansion of the composite is taken from Wong et al. [129]. The formula was used for ceramic particle filled polymer composites and is adapted here for the matrix material (Berea) and 'particles' of ice and mirabilite.

$$\alpha_c = \frac{(1-\varphi)\, K_m \alpha_m + \varphi K_p \alpha_p}{(1-\varphi)\, K_m + \varphi K_p} \tag{3.2}$$

Where α_c is the co-efficient of thermal expansion of the composite, α_m is the co-efficient of thermal expansion of the matrix, α_p is the co-efficient of thermal expansion of the particle and φ is the volume fraction of the filler. K_m is the bulk modulus of the matrix and K_p is the bulk modulus of the particle. In this case, φ is the volume fraction porosity but the pores are not completely filled with solution, or therefore crystals. The mass of precipitating mirabilite and ice is calculated as: $M_{mir} = M_{salt} * (mm_{mir}/mm_{the})$ where M_{mir} is the maximum amount of mirabilite (g) that can form from the amount of dissolved anhydrous salt used to make the 3 molal solution (M_{salt}, g), mm_{mir} and mm_{the} are the molar masses of mirabilite (322.196 g/mol) and the anhydrous phase, thenardite (142.043 g/mol), respectively [28]. The amount of water left in the solution phase, after mirabilite precipitation that can form as ice is $M_{ice} = M_{wat}\breve{}(M_{mir} * ((mm_{mir} - mm_{the})/mm_{mir}))$ where M_{wat} is the mass of water used to make the solution. The volume of mirabilite and ice at the eutectic point is calculated

as $V_{mir} = M_{mir}/mir\_den$ and $V_{ice} = M_{ice}/ice\_den$ [49]. The density of mirabilite is 1.47 g/cm^3 [69] and the density of ice (1h) is 0.9168 g/cm^3. Dividing the total volume of precipitating phases ($V_{mir} + V_{ice}$) by the pore volume of the sample (sample volume $*\varphi$), gives the volume fraction of pores occupied by crystals, φ occupied, and values are given for each sample in tables 3.1 and 3.2. The values for φ_{ice} and φ_{mir} are calculated as $\varphi_{ice} = \varphi_{occupied} * (V_{ice}/\text{pore volume})$ and $\varphi_{mir} = \varphi_{occupied} * (V_{mir}/\text{pore volume})$. Adapting the formula to:

$$\alpha_c = \frac{(1-\varphi)\, K_{stone}\alpha_{stone} + (\varphi_{ice}K_{ice}\alpha_{ice}) + (\varphi_{mir}K_{mir}\alpha_{mir})}{(1-\varphi)\, K_{stone} + \varphi_{ice}K_{ice} + \varphi_{mir}K_{mir}} \tag{3.3}$$

Where K_{stone} is the bulk modulus in GPa of Berea and α_{stone} is the bulk modulus of the sample, measured from the linear part of the strain-temperature curve prior to any crystallisation. K_{mir} is 19.6 GPa (at -3 °C) ,α_{mir} is 95.7 (μ m/m ·°C), both taken from Fortes et al. (2013) [37], K_{ice} is 8.4 GPa [84], α_{ice} is 51.88 (μm/m ·°C) [10]. The bulk modulus of Berea is 15.8 GPa [54] and the bulk modulus of Portland limestone is 22.2 GPa. The bulk modulus of Portland limestone is calculated from:

$$E = 3K\,(1-\nu) \tag{3.4}$$

Where E is the elastic modulus (GPa), K is the bulk modulus (GPa) and ν is Poisson's ratio. The elastic modulus is calculated from measured velocities from Cole, 1976 [15] of 3896 m/s for a porosity of 0.22 (average measured porosity of 8 samples), using

$$s = \sqrt{\frac{E}{\rho_b}} \tag{3.5}$$

Where S is the velocity (m/s) and ρb is the bulk density (kg/m^3), which is 2110 kg/m^3. The calculated elastic modulus is 32.0 GPa and using a value for ν of 0.26 [64], the calculated bulk modulus is 22.2 GPa. Comparing the calculated co-efficient of thermal expansion with the measured gradient of the strain-temperature plot (Figures3.8 and 3.9), after ice formation, shows whether the strain is largely due to the increased co-efficient of thermal expansion of the composite material or the sample is damaged. The calculated co-efficient of thermal expansion is used to calculate thermal strain ($\alpha_c * \Delta T$)

for comparison with measured strain when ice forms.

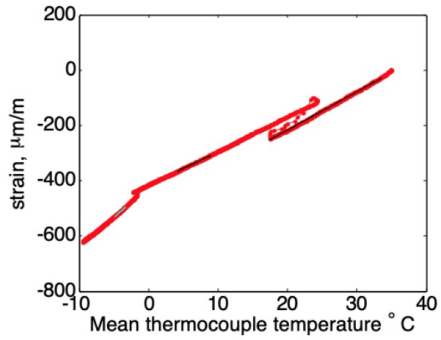

Figure 3.8: Strain plotted against sample temperature for Berea sample 13. This shows that the gradient of strain vs temperature does not significantly change after mirabilite forms (the two straight line segments in black above 0°C) are parallel until ice formation below 0°C.

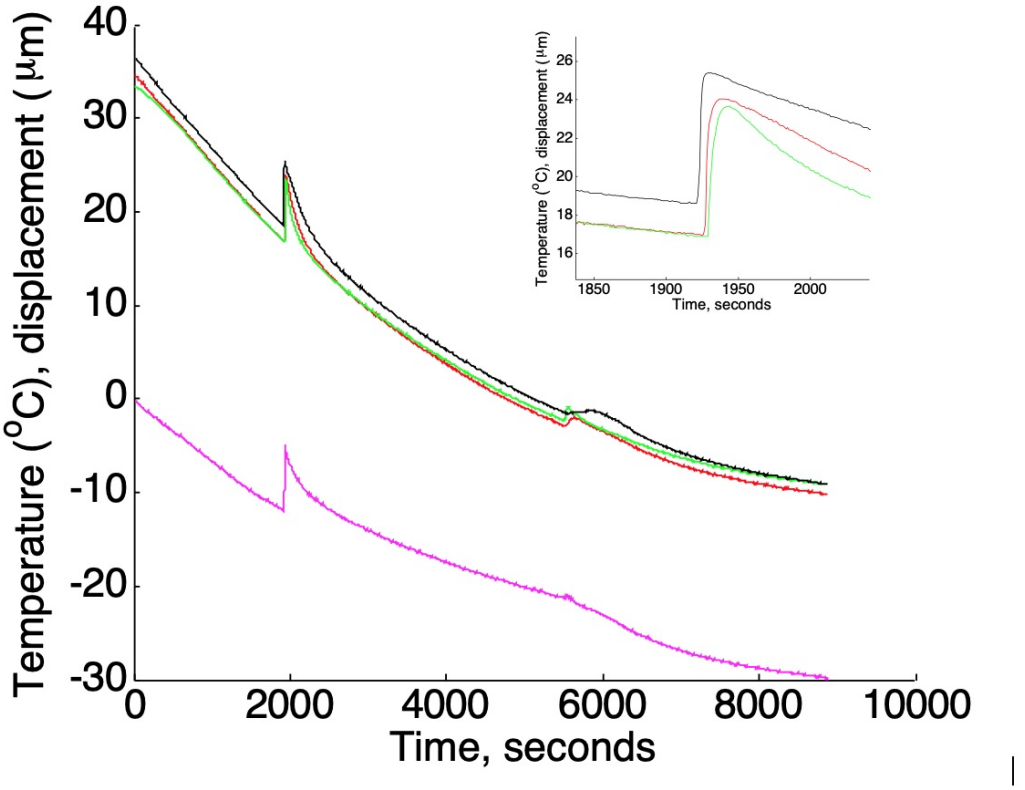

Figure 3.9: Berea sample (BE13), capillary saturated with 3 molal Na_2SO_4 solution before crystallisation of mirabilite is seeded at 18.6°C. Magenta is sample displacement (μm). Black, red and green are the top, middle and bottom thermocouple temperature readings respectively. The inset image is a magnification of mirabilite precipitation.

3.3.2 Heat of crystallisation

The aim was to calculate the expected temperature rise from the amount of mirabilite formed for comparison with the measured temperature rise. The amount of mirabilite formed when crystallisation is induced is calculated according to [29]:

$$\Delta n_c = \frac{m_w \left(C_i - C_f\right)}{1 - C_f M_w \nu} \tag{3.6}$$

Where Δn_c is the moles of salt formed, C_i is the initial concentration of the solution before crystallisation occurred (3 molal) and C_f is the concentration (molal) of the solution after crystallisation, which is calculated from the solubility curve, M_w is the molar mass of water (0.018 kg/mol) and ν is the moles of water in the hydrated salt (10) formed [29]. The heat effect accompanying the crystallisation of mirabilite (Joules) is equal to the enthalpy variation between the initial and final states of the experiment (equation 3 from Marliacy et al. (2000)):

$$\Delta H_c = H_{final} - H_{initial} \tag{3.7}$$

$$\Delta H_c = m'_w \Delta_{sol} \hat{H}(m') - m_w \Delta_{sol} \hat{H}(m) + x \Delta_{hyd} H \tag{3.8}$$

Where m_w is the final (') or initial mass of water (kg) and $\Delta_{sol}\hat{H}$ is the molal dissolution enthalpy (kJ/kg of water) and $x\Delta_{hyd}$ is the heat of hydration (kJ/mole of mirabilite formed) multiplied by the number of moles of mirabilite formed (x) as the solution crystallises [73], which is re-arranged to the following equation:

$$\Delta H_c \left(c, T\right) = \frac{\left(m'_w \Delta \hat{H}_{IS}\left(c', T\right) - m_w \Delta H_{IS}\left(c, T\right)\right)}{\Delta n_c} + \Delta H_{Hyd}\left(T\right) \tag{3.9}$$

ΔHc is the heat of crystallisation as a function of concentration and temperature, just as before but expressed as kJ/mole (of mirabilite formed) and ΔH_{IS} is the integral heat of solution (J/mol of solute) [73]. Values for the integral heat of solution were taken from Steiger and Asmussen (2008) [115] and values for the heat of hydration are taken from Marliacy et al (2000) as shown below (Fig.3.10). The heat of hydration varies

with temperature of nucleation and a linear fit is used because the heat of hydration, as calculated from the heat of formation of the components is shown to be linear [29], and agree well with experimental literature values.

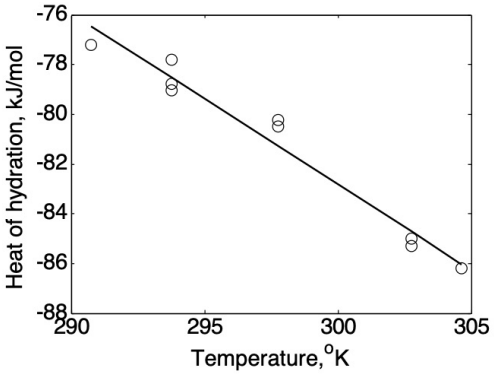

Figure 3.10: Heat of hydration (circles) from Marliacy et al. 2000. Least squares linear fit shown as a heavy black line, equation: $y = -0.6879x + 123.5546$.

In order to calculate the expected temperature rise of the core during mirabilite formation, the heat capacity of the core has to be calculated. The components of the core are a) quartz (Berea sandstone) or calcite (Portland limestone), b) aqueous solution and c) solid mirabilite and the heat capacity of the composite system is calculated using a simple rule of mixtures equation:

$$C_{p,comp} = (C_{p,mat} * mf_{mat}) + (C_{p,wat} * mf_{wat}) + (C_{p,mir} * mf_{mir}) \tag{3.10}$$

Where $C_{p,comp}$ is the composite heat capacity of the core (J/kg·K), $C_{p,mat}$ is the heat capacity of the porous matrix (quartz for Berea ([120]), calcite for limestone ([114]) and $C_{p,mir}$ is the heat capacity of mirabilite ([9]) and $C_{p,wat}$ is the heat capacity of water, used here for the solution phase (Figures 3.11, 3.12 and 3.13).

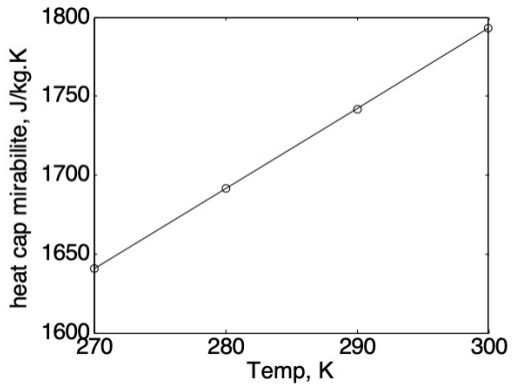

Figure 3.11: Heat capacity of mirabilite from Brodale and Giaque (1957) plotted as circles. Fitted line is a least squares straight line fit.

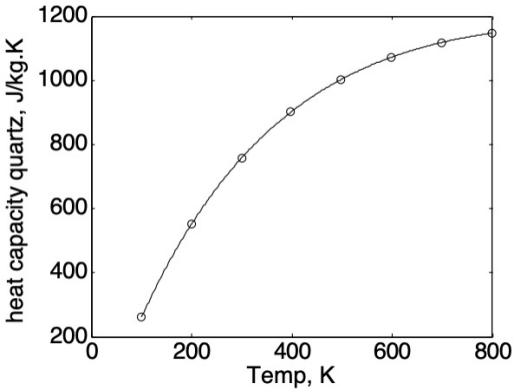

Figure 3.12: Heat capacity of quartz from deBoer et al. (1996) plotted as circles. Fitted line is a double exponential function to the data which produced the best least squares fit to the data: $y = 1388.2 * exp(-0.0001184x) + (-1536 * exp(-0.003239x))$.

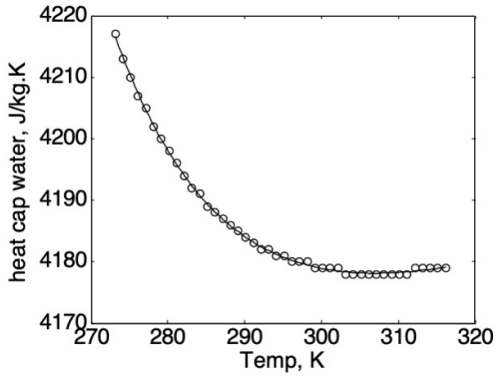

Figure 3.13: Heat capacity of (liquid) water from VAXA software plotted as circles. Fitted line is a double exponential function to the data which produced the best least squares fit to the data: $y = 3.78e^{09} * exp(-0.0658x) + (4.0439e^{03} * exp(1.0141e^{-04}x))$.

Calculating the expected heat rise from the precipitation of mirabilite:

$$\Delta T_m = \frac{abs\left(\Delta H_c \Delta n_c\right)}{totalmass * C_{p,comp}} \tag{3.11}$$

Where ΔT_m is temperature rise (°C or K), $totalmass$ is the mass of the core (kg) and $C_{p,comp}$ is the composite heat capacity of the core (kJ/kgK).

3.4 Results

3.4.1 Thermal Data

Table 3.3: Thermal data related to Berea samples. Delta T (mir) is the calculated temperature rise, Vol Frac is the volume fraction of pores filled with salt solution (sol) or with solution and crystals (mir and sol).

Sample name	Growth seeded, = yes	Temp of Precipitation (mir) °C	Speed of Growth (mir) mm/s	Coefficient of Thermal Expansion prior to any crystallisation um/(m °C)	Mass of Solution in core g	Calculated Delta T (mir) °C	Exotherm (mir) (ave of 3) °C	Thermal Strain (mir) um/m	Measured Strain (mir) um/m	Measured Strain-T Strain (mir) um/m	Core Porosity vol frac	Vol Frac Pores Filled (sol)	Vol Frac Pores Filled (mir and sol)	Vol Frac Pores Filled (mir)	Vol Frac Pores Filled Eutectic (ice)	Coefficient of Thermal Expansion Eutectic Composite um/(m °C)	Coefficient of Thermal Expansion Eutectic Composite um/(m °C)
BE13	*	18.62	2.51	14.61	3.4	8.14	6.84	100.00	146	46	0.18	0.67	0.67	0.42	0.71	23.02	20.23
BE14	*	17.59	4.00	16.16	3.66	8.99	8.24	133.27	223	90	0.18	0.72	0.7	0.34	0.76	25.29	19.67
BE09	*	21.1	0.58	13.32	3.61	7.88	3.33	44.37	20	-24	0.18	0.69	0.69	855	0.73	22.62	13.62
BE10 (1st cycle)	*	19.86	1.87	9.47	4.64	9.90	6.64	62.90	96	33	0.18	0 54	0.79	0.34	0.83	17.08	-118.12
BE10 (2nd cycle)	no mirabilite formation	N/A	N/A	2.72	4.64	N/A	N/A	N/A	N/A	N/A	0.18	N/A	0.79	N/A	0.83	14.69	12.07
BE10 (3rd cycle)	no mirabilite formation	N/A	N/A	N/A	4.64	N/A	N/A	N/A	N/A	N/A	0.18	N/A	0.79	N/A	0.83	N/A	N/A
BE10 (4th cycle)	no mirabilite formation	N/A	N/A	N/A	4.64	N/A	N/A	N/A	48	N/A	0.18	N/A	0.79	N/A	0.83	N/A	N/A
BE16	*	17.56	0.86	11.40	3.27	8.34	5.19	59.22	81	22	0.19	0.67	0.68	0.31	0.71	21.16	13.45
BE17	*	12.55	2.86	11.73	3.29	8.63	6.52	76.58	146	69	0.21	0.55	0.56	0.29	0.58	21.09	15.25
BE15	xtallised from bottom	17.6	1.68	14.69	3.35	8.18	6.03	88.55	100 77	12	0.18	0.70	0.71	0.33	0.74	23.75	24.53
BE05	xtallised from bottom	24.03	0.56	22.87	3.64	6.51	1.47	33.57	1 6	-22	0.18	0.64	0.64	0.22	0.67	30.42	19.28
BE06	xtallised from bottom	20.98	0.60	10.98	3.51	7.75	2.40	26.36	30.82	4	0.18	0.68	0.69	0.28	0.72	20.52	29.48
BE07	xtallised from bottom	21.47	1.06	10.69	3.49	7.65	4.40	47.07	6 28	17	0.18	0.67	0.67	0.27	0.70	20.04	19.33
BE08	xtallised from bottom	24.48	0.20	9.79	3.65	6.16	1.35	13.20	21.42	8	0.18	0.70	0.70	0.22	0.73	19.64	13.76

Table 3.4: Thermal data related to Portland samples. Delta T (mir) is the calculated temperature rise, Vol Frac is the volume fraction of pores filled with salt solution (sol) or with solution and crystals (mir and sol).

Sample name	Growth seeded, = yes	Temp of Precipitation (mir) °C	Speed of Growth (mir) mm/s	Coefficient of Thermal Expansion prior to any crystallisation um/(m °C)	Mass of Solution in core g	Calculated Delta T (mir) °C	Exotherm (mir) (ave of 3) °C	Thermal Strain (mir) um/m	Measured Strain (mir) um/m	Measured Strain-T Strain (mir) um/m	Core Porosity vol frac	Vol Frac Pores Filled (sol)	Vol Frac Pores Filled (mir and sol)	Vol Frac Pores Filled (mir)	Vol Frac Pores Filled Eutectic (ice)	Coefficient of Thermal Expansion Eutectic Composite um/(m °C)	Coefficient of Thermal Expansion Eutectic Composite um/(m °C)
PL01	*	19.63	1.304	4.37	4.02	8.09	5.00	21.85	25	3	0.22	0.58	0.59	0.26	0.61	12.76	7.86
PL02	*	18.69	1.24	3.91	3.92	8.30	5.56	21.77	26	4	0.22	0.58	0.58	0.26	0.61	12.78	6.74
PL03	*	17.77	1.34	4.29	4.08	8.46	5.80	24.90	31	6	0.23	0.58	0.59	0.27	0.62	12.99	5.42
PL04	*	15.89	1.99	4.50	3.76	8.44	6.34	28.52	31	2	0.22	0.57	0.58	0.28	0.60	12.42	6.82
PL05	*	13.71	3.26	4.75	3.88	8.86	7.41	35.16	33	-2	0.21	0.59	0.60	0.30	0.62	12.60	8.15
PL06	*	13.04	4.31	4.17	3.8	8.89	7.23	30.14	38	8	0.22	0.58	0.59	0.30	0.62	12.88	6.34
PL07	*	4.41	22.21	3.79	3.86	9.07	8.44	32.04	61	29	0.21	0.58	0.59	0.33	0.62	12.56	7.12

Table 3.5: Thermal and strain data related to ice formation in Berea samples.

Sample name	Growth seeded, * = yes	Exotherm (ave of 3) (ice) °C	Thermal Strain (ice) um/m	Thermal Strain (ice) um/m	Measured Strain (ice) um/m	Measured Strain-T Strain (ice) um/m	Measured Strain-T Strain (ice) um/m	Speed Ice Formation (1st to 2nd hole) seconds	Speed Ice Formation (2nd to 3rd hole) seconds
BE13	*	0.86	19.90	12.63	6.73	-5.90	-13.17	5.19	3.11
BE14	*	1.12	28.46	17.84	8.89	-8.95	-19.57	4.06	1.88
BE19	*	2.85	64.50	37.99	56.63	18.64	-7.87	25.72	9.84
BE10 (1st cycle)	*	2.94	50.29	27.89	190.99	163.10	140.69	9.02	4.9
BE10 (2nd cycle)	no mirabilite formation	2.78	40.82	7.57	226.5	218.93	185.68	N/A	N/A
BE10 (3rd cycle)	no mirabilite formation	2.45		N/A				N/A	N/A
BE10 (4th cycle)	no mirabilite formation	1.62		N/A				N/A	N/A
BE16	*	2.49	52.73	28.41	35.12	6.7179	-17.60	16.47	9.94
BE17	*	1.98	41.79	23.26	19.37	-3.88	-22.41	4.37	3.94
BE15	xtallised from bottom	2.75	65.42	40.47	31.52	-8.95	-33.91	11.44	5.84
BE05	xtallised from bottom	2.06	62.72	47.16	7	-40.16	-55.72	45.26	13.2
BE06	xtallised from bottom	1.29	26.47	14.16	10.68	-3.49	-15.79	31.4	20.6
BE07	xtallised from bottom	1.79	35.95	19.17	15.57	-3.60	-20.38	22.55	3.85
BE08	xtallised from bottom	2.10	41.20	20.55	31.17	10.62	-10.03	51	67

Table 3.6: Thermal and strain data related to ice formation in Portland samples.

Sample name	Growth seeded, * = yes	Exotherm (ave of 3) (ice) °C	Thermal Strain (ice) um/m	Thermal Strain (ice) um/m	Measured Strain (ice) um/m	Measured Strain-T Strain (ice) um/m	Measured Strain-T Strain (ice) um/m	Speed Ice Formation (1st to 2nd hole) seconds	Speed Ice Formation (2nd to 3rd hole) seconds	Gap
PL01	*	3.12	39.81	13.63	21.54	-18.27	15.61	8.63	19.63	6.98
PL02	*	3.50	44.71	13.68	25.67	-19.03	10.79	7.6	18.69	3.19
PL03	*	2.96	38.45	12.70	15.52	-22.93	10.43	7.14	17.77	3.29
PL04	*	2.92	36.21	13.11	18.08	-18.13	7	4.91	15.89	2.09
PL05	*	3.83	48.33	18.20	30.53	-17.80	3.72	3.19	13.71	0.53
PL06	*	2.64	34.03	11.02	12.65	-21.37	2.02	2.96	13.04	-0.94
PL07	*	4.08	51.22	15.48	37.40	-13.81	Simultaneous	1	4.41	

Data interpretation

All samples are capillary saturated which means they contain trapped air that is known to mitigate the worst effects of damage as opposed to fully saturated samples where there is no trapped air. This is why air entrainment is a method of avoiding freeze-thaw damage to cement [116]. The most saturated sample is BE10 which was capillary saturated for 10 days. The level of saturation is calculated based on the estimated (or measured) porosity of the sample. Plotting temperature of crystal growth against measured velocity shows a reasonably clear linear trend, albeit with some outliers (Figures 3.14 and 3.15). As the temperature of nucleation decreases, the supersaturation at nucealtion (with respect to mirabilite) is increased and the measured rate of growth increases. The data is fitted to a straight line (Berea) or exponential (Portland limestone) but the physical meaning of the fit presented has not been explored and is the subject of future work. Refining the temperature measurement, including working with longer cores with more thermocouples will be investigated in future research projects. Understanding how crystal growth proceeds within the core is important. Work on ice nucleation in along cement cores by Sun et al. 2010 indicated that ice crystals grew as dendrites along the cold long axis of the core and into the radius of the core where

the thermocouples registered the temperature rise, rather than growth proceeding uniformly through the long axis of the core [116]. How crystals actually interact with the pore structure during growth is also part of on-going research and requires access to synchrotron X-CT to obtain a high resolution image within a second or two, which is beyond the capability of most laboratory X-CT instruments.

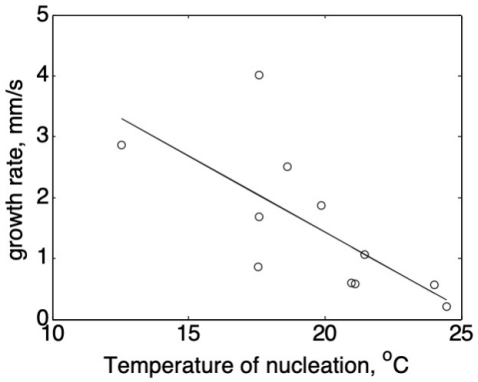

Figure 3.14: All Berea samples (circles) with straight line least squares fit to the data. $y = -0.2503x + 6.4399$.

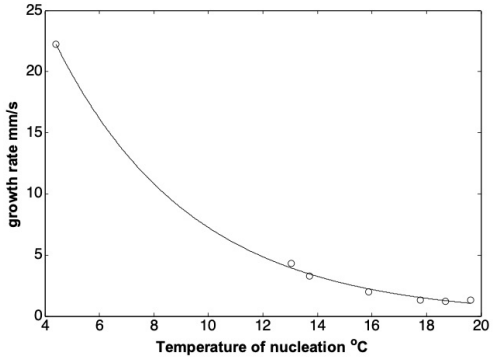

Figure 3.15: All portland limestone samples with an exponential fit to the data. $y = 53.75 * exp(-0.2003x)$.

The system described by Sun and Scherer (2010) is a 22 cm long cement block (5 x 7 cm cross section) with 7 thermocouples embedded along the long axis. The core is immersed in a kerosene bath at c. -2.5 °C to -5 °C and ice formation is initiated by touching one end of the core with ice. They explore two different boundary conditions, a cold surface and an insulated surface by either leaving the block in the cold kerosene during nucleation and growth (cold surface) or by immersing the block until sample temperature equilibrated with the bath temperature, then removing it from the bath and initiating crystallisation at room temperature (insulated surface). Their argument

is that ice forms as dendrites (the shape of the tip allows heat to disperse more quickly) and that growth occurs down the cold outside of the block and into the middle where the thermcouples are located. They discuss that this results in faster growth (c. 0.3 - 0.7 cm/s) compared to the experiments with the insulated boundary condition where growth is promoted through the long axis (c. 0.19 cm/s) because the surface is not colder than the centre and therefore does not have a higher degree of supercooling than the centre. One 'symptom' of growth along the cold surface is that the time gap between thermocouples is not even and growth appears to speed up, rather than being slowed down by heat accumulation. Figure 3.16 below shows their experimental results and thermocouple response is more evenly spaced when the insulated boundary condition is used. Comparing these results with the data presented here, in both cases the temperature of the bath is only 1-2°C different from the temperature of sample centre, which indicates the radial distribution of temperature in the core is uniform. However, a complete model should take into account two additional effects: First, the heat released at the crystallisation front diffuses a short distance ahead of the moving front, heating the solution immediately ahead of the front, into which the crystal is growing. So the local supersaturation of the front is not that of the solution at the initial uniform core temperature but at a higher temperature, close to that of the front itself. Second, the local temperature at the crystallisation front is modified near the surface of the core where heat is lost to the bath. At and behind the front, the surface region of the core is therefore somewhat cooler than the central (axial) region. This effect has been noted by Sun and Scherer (2010) but a full understanding of this effect requires extensive heat transfer modelling for the mirabilite crystallisation case. In the data presented here, the time gap between thermocouples is also not absolutely even, with the growth rate appearing to speed up as it progresses, which is counter-intuitive, as heat produced by crystal growth should slow down the growth rate. However, the effect is not as marked as witnessed by Sun and Scherer (2010). One reason could be the that a few degrees temperature difference (between the middle of the core and the outside of the core) has less effect on mirabilite crystal growth rate than on ice. We can compare the effect on growth rates of 2 degrees temperature difference using the equation for ice crystal growth rate [116] and salt crystal growth [1] where u is the

growth rate (in cm/s), Tm is the melting temperature (ice),T is the water temperature, S is the supersaturation of the solution (c/c_0) where c is the solution concentration (molal) and c_0 is the solution concentration at saturation (c_0):

$$Ice : u = constant * (T_m - T) \tag{3.12}$$

$$Salt : u = constant * (S - 1) \tag{3.13}$$

Comparing Tm=-4°C, T=-6 °C with solution concentration values for 20 °C and 18 °C (mirabilite), which are 2.206 molal and 1.949 molal, respectively we have that the effect on growth rate (u18/u20) for mirabilite is u18/u20 = 1.5, so growth would be 50% faster if the outer surface is 2 °C colder than the core interior. For ice (u-4/u-6)=3.25, so growth would be 325% faster and this may explain why the insulating effect by lifting the core out of the cold bath just prior to nucleation is so marked in Sun and Scherer experiments (Fig.3.16) and possibly why the growth rates found here are more evenly spaced between thermocouples than observed by Sun and Scherer.

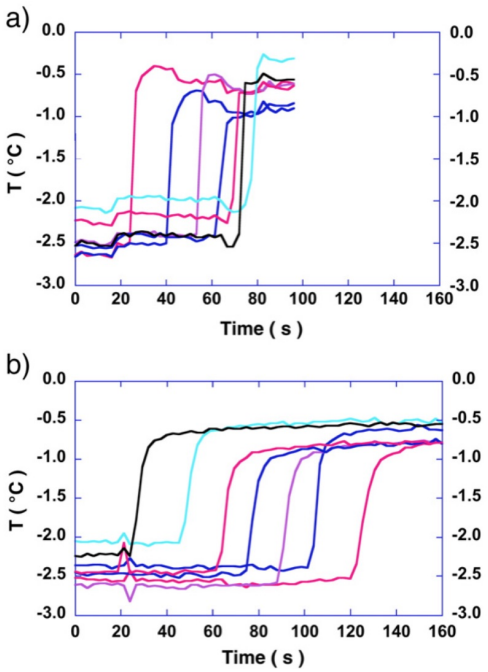

Figure 3.16: From Sun and Scherer (2010). Both plots show the thermcouple response as ice forms in the cement block when nucleation is initiated by contacting the core with a piece of ice. Plot a) is crystal growth in the bath (cold surface) and plot b) is crystal growth in the sample after it is lifted out of the bath (insulated surface). The speed of growth is slower in plot b) and the thermocouple responses are more evenly spaced, which they believe indicates growth through the core as opposed to growth down the surface (as in plot a).

Exploring heat diffusion ahead of the moving crystal growth front, equation below from Carslaw and Jaeger (1959), (p267) gives a steady state solution for the temperature at point x.

$$T_x = T_0 exp\left(\frac{-U * xx}{\kappa}\right) \tag{3.14}$$

Where κ is the thermal diffusivity of the sample. In this illustration, a value of 1.8 mm^2/s was taken for Berea from Hanley et al., 1978. U is the crystallisation front velocity as determined by the thermocouple response, in mm/s, xx is equally spaced points along the long axis of the core (mm), T_0 is the temperature rise behind the front and T_x is the temperature rise ahead of the front. The value of T_0 is taken from the temperature rise of the first thermcouple as a first approximation. The result shows the temperature distribution along the core ahead of the moving crystal growth front. The time to reach steady state is calculated as below from Hou and Komanduri (2000),

where t_{ss} is the time to reach the observed temperature rise.

$$t_{ss} = \frac{20 * \kappa}{U^2} \tag{3.15}$$

This provides a good qualitative fit to the data presented. Looking at a few examples for Berea: The measured growth rate for Berea 13 is 2.51 mm/s, the average temperature rise is 6.8 °C (Fig.3.18). Figure 3.17 shows the calculated time to reach the temperature rise based on heat diffusion of the crystal growth front as it approaches the first thermocouple, bearing in mind that growth is nucleated at the top of the core which is above the first thermocouple hole. As can be seen, the shape of the calculated temperature profile matches well with the thermocouple response. The time taken to reach the temp rise is reasonably comparable: 2s (model) versus 6s (data). Looking at example with a slower growth rate, Berea 16 has a measured growth rate of 0.86 mm/s. The model predicts 12s to reach the recorded temperature rise and the data shows 20s (Figures 3.19 and 3.20). An example of fast measured growth is Berea 14, the measured time taken to reach the temperature rise is 0.98s compared with the calculated 0.6s, which shows excellent agreement (Figures 3.21 and 3.22). The model fit could be improved by calculating a coefficient of thermal diffusion for the complete system (rock, solution, mirabilite) rather than the dry rock alone, this is planned for future work.

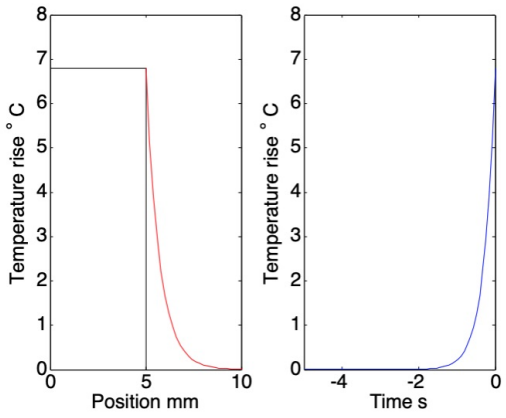

Figure 3.17: Calculated heat rise ahead of the crystallisation front as would be observed by the first thermocouple.

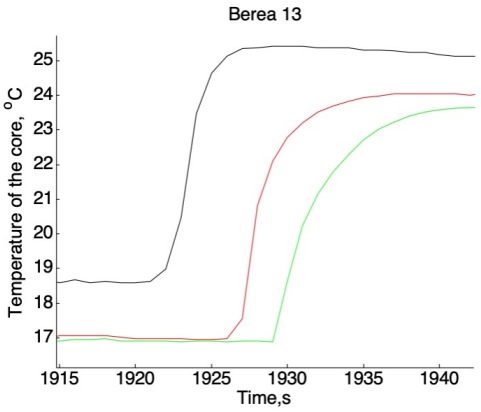

Figure 3.18: Measured thermocouple response of Berea 13.

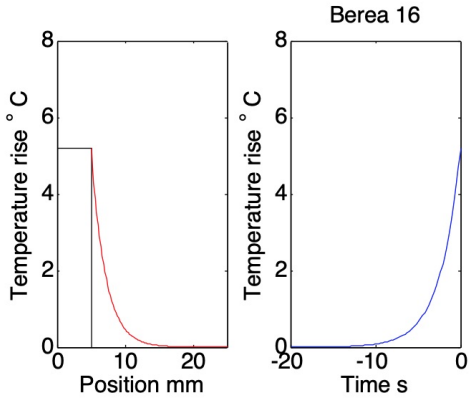

Figure 3.19: Calculated heat rise ahead of the crystallisation front as would be observed by the first thermocouple.

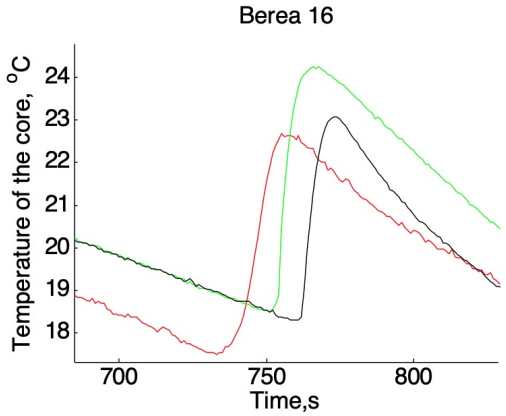

Figure 3.20: Measured thermocouple response of Berea 16.

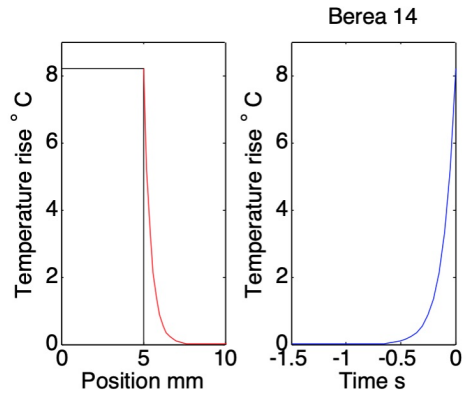

Figure 3.21: Calculated heat rise ahead of the crystallisation front as would be observed by the first thermocouple.

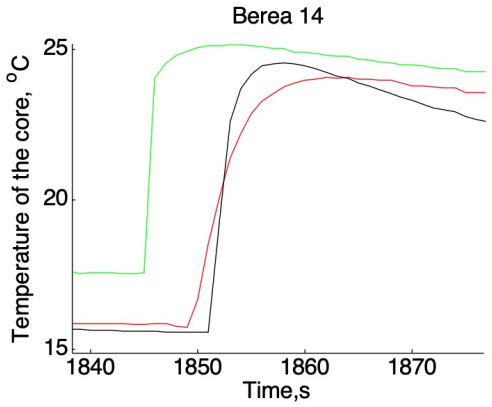

Figure 3.22: Measured thermocouple response of Berea 14.

Comparing the expected temperature rise with the measured temperature rise during mirabilite precipitation, the values are close and show relatively good agreement. The calculated value is always higher but the calculated value is not taking the dissolution of mirabilite (from the heat produced) into account, which will be included in the chemo-mechanical model being developed in future work. How mirabilite grows, whether it is through the core or down the sides of the core and into the centre (as Sun and Scherer believe they observe) is the subject of future work. However, Sun and Scherer point out that when growth is down the side of the core, a) the growth rates are comparable to free growth in solution and b) the time gap between thermocouples registering a response is erratic (Fig.3.16). To test this, crystal growth was measured in 50 ml and 15 ml universal tubes and recorded using a mobile phone camera (Fig.3.23). Growth rates are roughly 2.5 times faster than the equivalent experiment in a sedimentary rock

core, as shown in figure 3.24. This suggests that there is growth down the centre and not predominantly down the sides but this requires further work to confirm. The time gap between thermocouples shows that the growth rate speeds up regardless of whether the sample was successfully seeded (growth started from the top) or nucleated prior to seeding (growth started from the bottom of the core). This does indicate, according to Sun and Scherer model, that growth is down the side, however it is possible that growth through these cores is a mixture of both pathways, further work using fast X-CT imaging will help to answer the question.

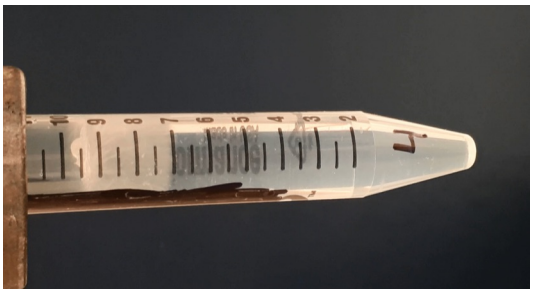

Figure 3.23: Mirabilite crystallisation in a 15 ml universal tube. The solution was nucleated from the top, at the air-solution interface.

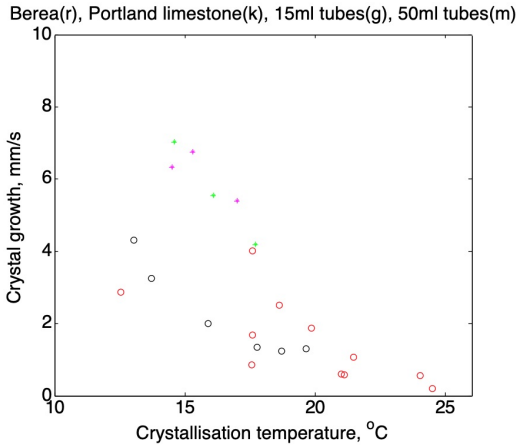

Figure 3.24: Crystal growth rates measured in tubes of solution (stars), through portland limestone (black circles) or berea sandstone (red circles). Growth rates plotted against the temperature of nucleation.

3.4.2 Mechanical response (strain)

Table 3.7: Strain data related to both mirabilite and ice formation for Berea and Portland samples.

Sample name	Growth seeded, * = yes	Thermal Strain (mir) um/m	Measured Strain (mir) um/m	Measured Strain-T Strain (mir) um/m	Thermal Strain (ice) um/m	Thermal Strain (ice) um/m	Measured Strain (ice) um/m	Measured Strain-T Strain (ice) um/m	Measured Strain-T Strain (ice) um/m
BE03	*	100.00	146	46	19.90	12.63	6.73	-5.90	-13.17
BE04	*	133.27	223	90	28.46	17.84	8.89	-8.95	-19.57
BE09	*	44.37	20	-24	64.50	37.99	56.63	18.64	-7.87
BE10 (1st cycle)	*	62.90	96	33	50.29	27.89	190.98	163.10	140.66
BE10 (2nd cycle)	no mir formation	N/A	N/A	N/A	40.82	7.57	.5	218.93	185.68
BE10 (3rd cycle)	no mir formation	N/A	N/A	N/A		N/A			
BE10 (4th cycle)	no mir formation	N/A	48	N/A		N/A			
BE16	*	59.22	81	22	52.73	28.41	35.12	6.72	-17.60
BE17	*	76.58	146	69	41.79	23.26	19.37	-3.88	-22.41
BE15	xtallised from bottom	88.5534	100.47	12	65.42	40.47	31.52	-8. 1	-33.91
BE05	xtallised from bottom	33.57	11.86	-22	62.72	47.16	7	-40.16	- 720
BE06	xtallised from bottom	26.36	30.82	4	26.47	14.17	10.68	-3.49	15.79
BE07	xtallised from bottom	47.07	64.33	17	35.95	19.17	15.57	-3.59 -	20.38
BE08	xtallised from bottom	13.20	21.42	8	41.20	20.55	31.17	10.62	10.03
PL01	*	21.85	25	3	39.81	13.63	21.54	-18.27	
PL02	*	21.77	26	4	44.70	13.68	25.67	-19.03	
PL03	*	24.90	31	6	38.45	12.70	15.52	-22.93	
PL04	*	28.52	31	2	36.21	13.11	18.08	-18.13	
PL05	*	35.16	33	-2	48.33	18.20	30.53	-17.80	
PL06	*	30.14	38	8	34.03	11.02	12.65	-21.37	
PL07	*	32.04	61	29	51.22	15.48	37.40	-13.81	

The measured strain is $\varepsilon = \frac{\Delta L}{L}$ where L is the length of the sample and ΔL is the measured dilation indicates whether damage has been caused or not. Thermal strain is calculated and subtracted from the strain value to determine mechanical effect. As described previously, thermal strain is calculated from the coefficient of thermal expansion, which is measured for each sample from the LVDT dilation, prior to mirabilite crystallisation.

Table 3.8: Mirabilite crystallisation. Where the strain is negative, the calculated thermal strain exceeds the measured strain and suggests that the sample is not damaged.

Sample	Co-efficient of thermal expansion (gradient of plot before mirabilite formation) Microns/meter. °C	Thermal strain, microns/meter	Measured strain, microns/meter	Measured strain - thermal strain	Temperature of nucleation °C
BE05	22.87	33.57	11.86	-22	24.03
BE06	10.98	26.36	30.82	4	20.9834
BE07	10.69	47.07	64.33	17	21.47
BE08	9.79	13.20	21.42	8	24.48
BE09	13.32	44.37	20	-24	"21.1
BE10 (cycle 1).	9.47	62.90	96	33	19.86
BE03	14.61	100.00	146	46	18.62
BE04	16.16	133.27	223	90	17.59
BE15	14.69	88.55	100.47	12	17.6
BE16	11.40	59.22	81	22	17.56
BE17	11.73	76.58	146	69	12.55
PL01	4.37	21.85	25	3	19.63
PL02	3.91	21.77	26	4	18.69
PL03	4.29	24.90	31	6	17.77
PL04	4.50	28.52	31	2	15.89
PL05	4.75	35.16	33	-2	13.71
PL06	4.17	30.14	38	8	13.04
PL07	3.79	32.04	61	29	4.41

In most cases, mirabilite causes damage when it forms in these capillary saturated samples and the damage is increased as the temperature of nucleation (and hence supersaturation with respect to mirabiltie) is decreased. BE10 is an interesting case because it was capillary saturated for 267 days and has the highest solution content of all samples (volume fraction of pores filled with solution is 0.785). This sample was also cycled, as the sample was allowed to warm to room temperature before being

cooled again, without being removed from the chamber. Figures showing the displacement and temperature plots are shown below for all 4 cycles (Figures 3.25,3.26,3.27 and 3.28). Mirabilite only crystallises in the first cooling when the solution is supersaturated with respect to it but during sample warming to room temperature for subsequent cycles, mirabilite is not fully dissolved, so it grows with further cooling but does not nucleate. Compared with figure 3.8, which is more standard for samples which are less fully saturated, the strain produced when ice crystallises is significantly less.

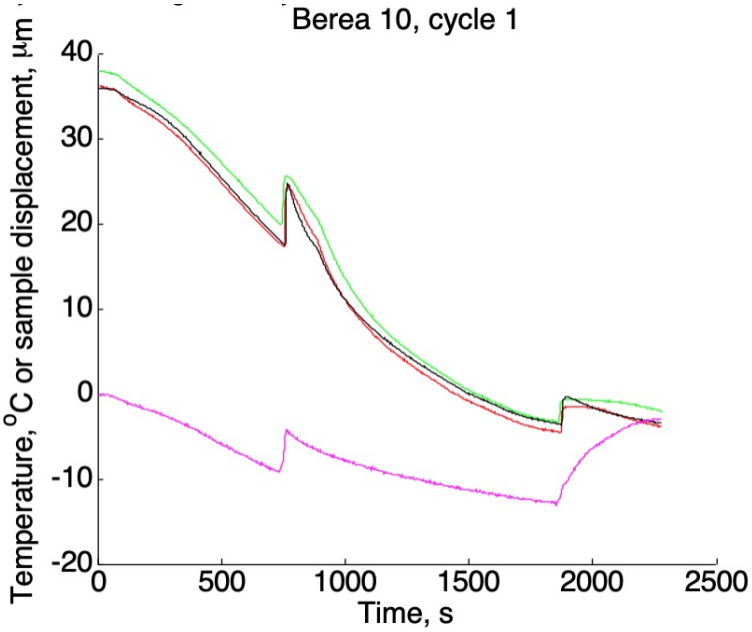

Figure 3.25: Berea 10, cycle 1. Thermcouples plotted in red, green, black. Sample displacement in magenta.

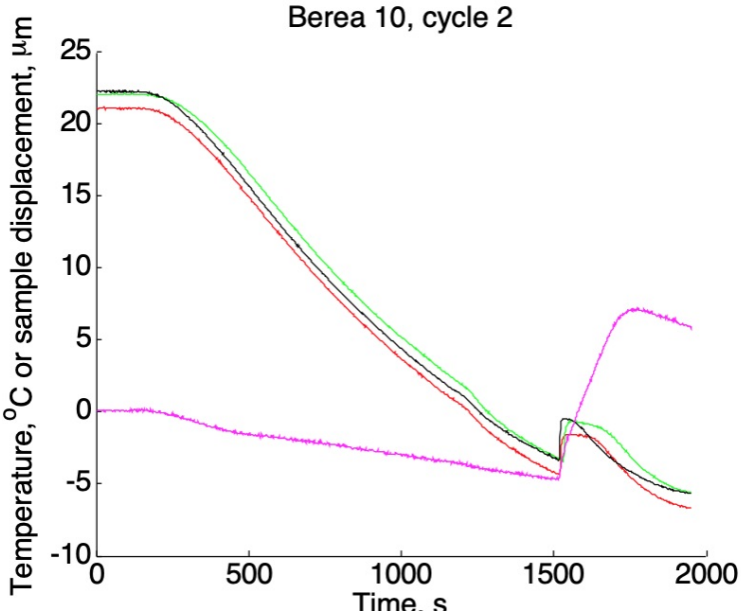

Figure 3.26: Berea 10, cycle 2. Thermcouples plotted in red, green, black. Sample displacement in magenta.

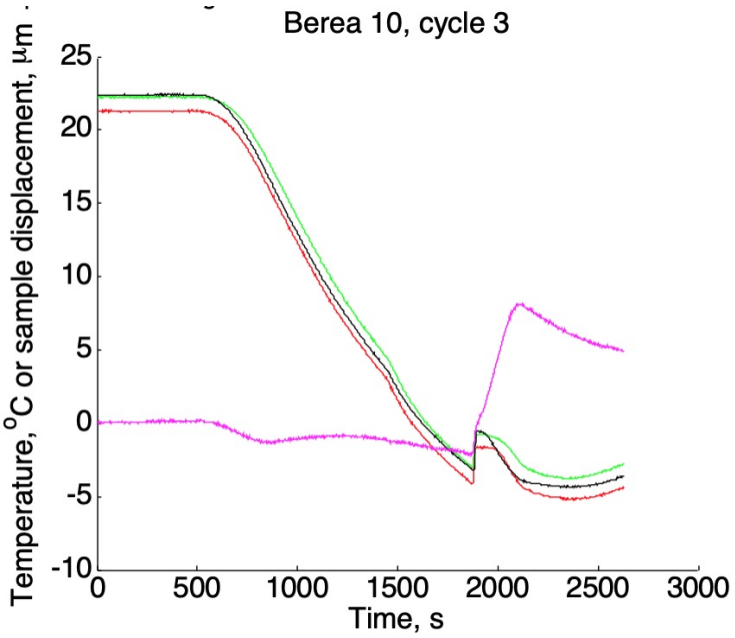

Figure 3.27: Berea 10, cycle 3. Thermcouples plotted in red, green, black. Sample displacement in magenta.

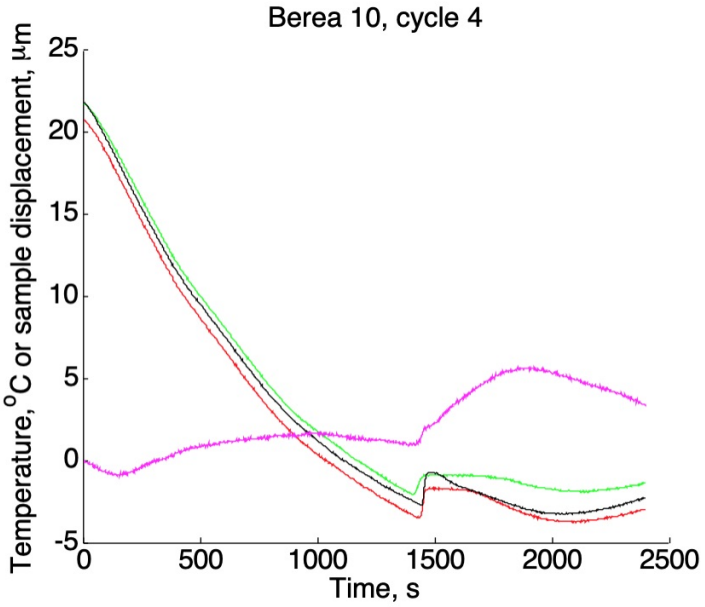

Figure 3.28: Berea 10, cycle 4. Thermcouples plotted in red, green, black. Sample displacement in magenta.

When ice forms, the coefficient of thermal expansion, α is calculated for the composite system (mirbilite, ice, limestone/sandstone), as equation 3.3.1 which is a theoretical value, and is used to calculate thermal strain. For comparison, the gradient of the strain-temperature plot is also calculated. The gradient would represent the coefficient of thermal expansion of the composite rock but at this point the sample could be damaged and therefore the strain-temperature plot is inaccurate as a value of co-efficient of thermal expansion.

3.5 Conclusions

Crystal growth experiments were carried out using a standard building limestone and sandstone - Portland limestone and Berea sandstone. Mirabilite crystal growth rate is c. 2.5 times slower through the core, as measured by thermocouples imbedded in the core, compared with free growth in solution. Crystal growth rate is correlated with the supersaturation at the point of nucleation but the physical relationship beyond basic curve fitting requires further investigation. Crystal growth through the core is probably a mix of growth down the side of the core (and into the thermocouple) and through the centre of the core based on comparison with data from Sun and Scherer (2010). Strain

Table 3.9: Coefficient of thermal expansion as calculated or as measured from the data after ice formation at the eutectic point. BE10 was saturated for 267 days and is closer to vacuum saturation than the other samples, therefore the sample showed the most obvious damage. The measured value for BE10 is meaningless because of this.

Sample name	Co-efficient of thermal expansion (calculated) after ice formation). Microns/meter. °C	Co-efficient of thermal expansion (gradient of plot after ice formation) Microns/meter. °C	Measured strain during ice formation. microns/meter
BE05	30.42	19.28	7
BE06	20.52	29.48	10.68
BE07	20.04	19.33	15.57
BE08	19.64	13.76	31.17
BE09	22.62	13.62	56.63
BE10 (cycle 1)	17.08	-118.12	190.99
BE10 (cycle 2)	N/A	N/A	226.5
BE10 (cycle 3)	N/A	N/A	193.42
BE10 (cycle 4)	N/A	N/A	88.17
BE13	23.02	20.23	6.73
BE14	25.29	19.66	8.89
BE15	23.75	24.53	31.52
BE16	21.16	13.45	35.12
BE17	21.09	15.25	19.37
PL01	12.75	7.85	21.54
PL02	12.78	6.74	25.67
PL03	12.99	5.42	15.52
PL04	12.42	6.82	18.08
PL05	12.60	8.15	30.53
PL06	12.88	6.34	12.65
PL07	12.55	7.12	37.40

data shows that the porous host is usually damaged by mirabilite precipitation, unless precipitataion occurs at higher temperatures (c. 24 °C) where the supersaturation is less. When the core is more fully saturated, such as Berea 10, the damage when ice forms at the eutectic point is more extreme. This is the first experiment to measure the rate of salt crystal growth through a porous core and assess the damage caused at the same time. As supersaturation is increased at the point of mirabilite nucleation, growth rate increases and measured strain also increases.

Chapter 4

Preliminary results on assessment of salt distribution on artificially weathered sandstone by using X-ray computed tomography.

4.1 Introduction

In January 2018 we started a collaboration with Historic Environmental Scotland (HES) aimed to further investigate damages caused by de-icing salts. Scottish sandstone buildings are particularly affected and damaged by the usage of de-icing salts during winter months. It is now known that de-icing salts effect is not limited on areas immediately in contact with spread salts, such as footpaths and roads [43]. De-icing salts spread easily on masonry and are transported by visitors within buildings, in particular on pavements [56]. Most common deicers applied often contain chlorides as freezing-point depressants because of their cost-effectiveness, including mainly sodium chloride (NaCl), magnesium chloride ($MgCl_2$), and calcium chloride ($CaCl_2$) [109]. The work of Shi et al. (2009) offers a wide review of the impacts of common de-icers on cement and asphalt pavements, respectively, detailing the various mechanisms found to cause deterioration [110]. We were asked to investigate the distribution within a sandstone of three of the most common de-icing salts used in Scotland, e.g. sodium chloride, calcium

chloride and magnesium chloride. All samples were subjected to salt crystallisation cyclical testing, during which samples are dried and then re-saturated by total immersion, as recommended by British standard BSEN12370.1999, but using 1M solutions, which is higher than the 0.46M solution of sodium sulphate indicated in the standard. This investigation was carried out by using X-ray computed tomography, a non-destructive technique, which enables the pore structure to be imaged at very high resolution (μm). When stone samples are subjected to salt weathering cycles, damage such as granular disintegration, may occur after a variable amount of cycles depending mainly on the salt distribution within the porous matrix and at it's outer surface can potentially be investigated by using X-ray computed tomography. Previous studies on salt distribution within stone samples saturated with salt solutions have used a realignment technique of the same sample before and after the treatment with salt solution. Datasets are aligned manually and then the procedure is optimized automatically with the software DataViewer (SkyScan) [22]. Where salt crystals have precipitated, it is possible to detect a change of the gray value in the X-ray images. The differential volume obtained from the two data sets of digital image subtraction represents the salt precipitation in the sample [22]. The efficacy of this procedure relies on the accuracy of the dataset alignment and it is highly sensitive to sub-voxel changes in the alignment of the sample. For instance, misalignments of < 5 degrees in the pores after salt crystallisation, may introduce significant miscalculation in the final salt volume quantification. Another method to assess salt distribution was investigated by Dewanckele et.al (2012). The XCT was used to monitor gypsum crust formation in a calcareous sandstone by measuring porosity, evolutions of micro-cracks and disintegration in the same sample after several crystallisation cycles [23]. This technique allows to detect where fractures have developed below the crust with good accuracy and relies on assignment of a specific gray value to each sample feature. The majority of the studies investigating salt distribution and precipitation patterns in porous media have mainly focused on 2-D evaporating surfaces. Three-dimensional (3-D) investigation is rare perhaps because of the difficulty and limitation of the available techniques capable of accurate visualization of the salt in the matrix. In this chapter an attempt is presented to define salt distribution by two different methodologies: 1) determine local porosity reduction and 2) assign a precise

grey value to the salt efflorescence and determine where this value redistributes within the sample. This second procedure requires the presence of a significant amount of efflorescences to assign a specific grey value to the samples. Hence, for the purpose of this second methodology, samples were treated with a 1.2M concentrated sodium sulphate solution via capillary rise. Along with the preliminary results of the XCT investigation, it is also provided a discussion on the efficacy and reliability of the widely used standard salt crystallisation procedure we were asked to carry out using de-icing salts.

For the purpose of this chapter I carried out the laboratory test and data collection. The 3D investigation was carried out with the assistance and supervision of Dr Alice Macente using the X-ray computed tomography (XCT) Nikon XT H 225 LC hosted at the Advanced Materials Research Laboratories (AMRL, Strathclyde University). Me and Alice Macente carried out the image analysis and processing using the software Avizo.

4.2 Materials and Methods

XCT working principle is based on the X-ray signal intensity attenuation of the different sample materials based on their different density [62]. The images obtained through the XCT are in 32 bit grey scale values: as a result of X-rays attenuation, denser materials will appear brighter, while pores, which contain air and/or solution, will appear darker [19] (Fig.4.1)
2D radiographs are acquired by positioning the sample in a rotary stage between the X-ray head source and a 2D pixelated detector. The acquisition of 2D projections over a full 360 degrees rotation enables the reconstruction of a 3D matrix of volume elements (3-dimensional pixels, i.e. voxels) in grey levels [123]. The Nikon XT H 225 LC XCT uses standard cone-beam geometry. In this set-up the spatial resolution depends mainly on the focal spot size of the X-ray source. The focal spot size of the head source used is 1 micron up to 3W. All sample features which are smaller than the resolution (reconstructed voxel size) cannot be distinguished on the dataset, so the voxel size reflects the resolution of the final 3D reconstruction. The smallest achievable voxel size

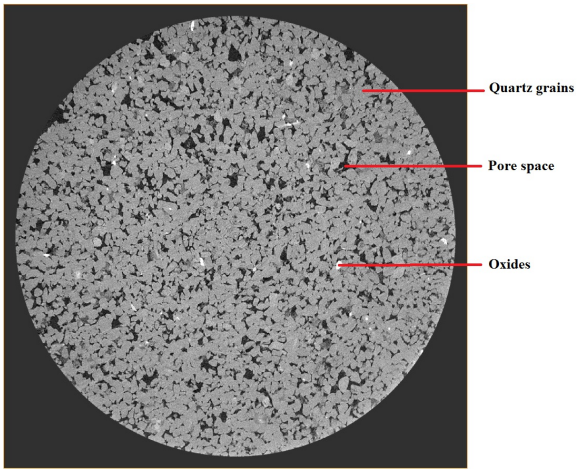

Figure 4.1: 2D projection of a Berea sandstone cylinder.

.

is a function of the sample size [63].

For this investigation we used small cylindrical samples of Berea sandstone, 2 cm high and 2.5 cm diameter. Berea sandstone is a medium to fine grained sandstone containing c. 10% of kaolinite. The open volume fraction porosity, measured using the vacuum saturation method is 0.18. The sorptivity is $0,10\ cm/mim^1/2$. Fresh samples show the scattered presence of bedding planes with a high amount of oxides which are visible on the XCT images. Fresh stone and its radiographs x-ray tomography images are shown in (Fig.4.2). The spatial resolution (voxel size) of the x-ray tomography is 13 μm.

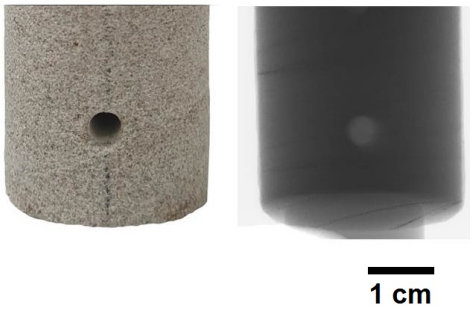

Figure 4.2: Fresh Berea sandstone core and its X-ray radiography on the right.

.

Thin section analysis (Fig.4.3) shows this is a medium sorted, fine grained sandstone, where quartz is the most common mineral, and it is mostly non-altered. Quartz and feldspar often show concave-convex contacts. Feldspar are sometimes damaged and replaced by clay minerals (pseudo-morphic replacement). The presence of kinked muscovite and directional elongation indicate the sandstone has undergone pressure solution.

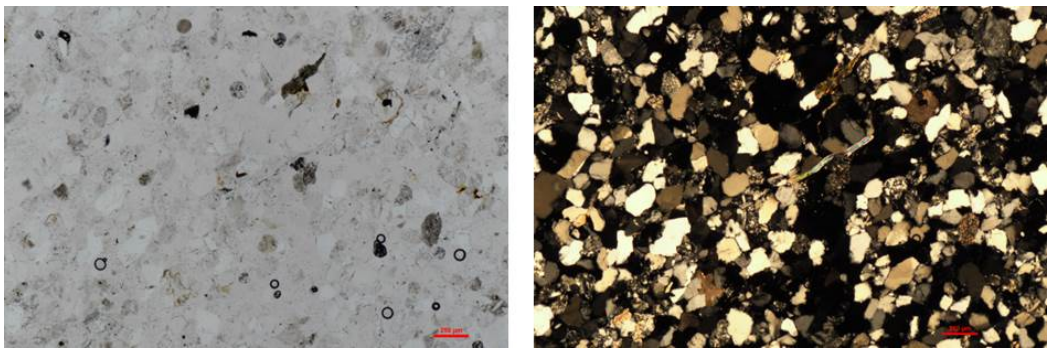

Figure 4.3: Thin section photographs of Berea sandstone , Nicols // on the left image and Nicols + on the right one. White grains are mainly quartz, with a smaller proportion of feldspar and some micas. Black patches are iron oxide and opaque minerals.

.

Samples were treated with different salt solutions made up from three of the most common de-icing salts used in Scotland, e.g. NaCl, $CaCl_2$ and $MgCl_2$. Sodium chloride (NaCl) is undoubtedly the principal deicer in use [53]. It has a eutectic point of -23°C, good ice-melting rates at low temperatures and, above all, is relatively inexpensive. $CaCl_2$ and $MgCl_2$ are secondary chloride de-icers, and are commonly used in the UK as a replacement for NaCl or are applied alongside it [43]. They exhibit a lower eutectic point than NaCl, but they also exhibit a greater depth of penetration at lower temperatures when compared to NaCl [126].

Samples of 2.5 cm diameter and 2 cm high were first dried in an oven to a constant mass at a temperature of +100°C for 48 hrs. Samples were then cooled to room temperature ($20°C \pm 1°C$) and weighed to a precision of 0.01 g. One dry sample was scanned at the XCT and used as reference sample for a qualitative assessment of porosity reduction in the treated samples. A total of 3 samples were subjected to salt crystallisation cycles accordingly with the EN 12370.1999, saturated by full immersion for 2 hrs at room temperature in salt solutions made up with de-icing salts at a concentration of 1M, as requested by Historic Environment Scotland. Molar concentrated solutions with equivalent weight % are listed in Table 4.1.

Table 4.1: Salt solutions concentration

Salt	Molar Concentration	Weight %
NaCl	1	5.66
$CaCl_2$	1	10.48
$MgCl_2$	1	18.22

Samples were then oven dried for 16 hrs at +100°C and eventually cooled at room temperature for 2 hrs to complete one cycle. Samples were dried at this high temperature, accordingly with the phase diagrams of the salts solutions (Figures 4.4,4.5 and 4.6), $CaCl_2 \cdot 2H_2O$ and $MgCl_2 \cdot 2H_2O$ are the most likely phase to form when drying at +100°C.

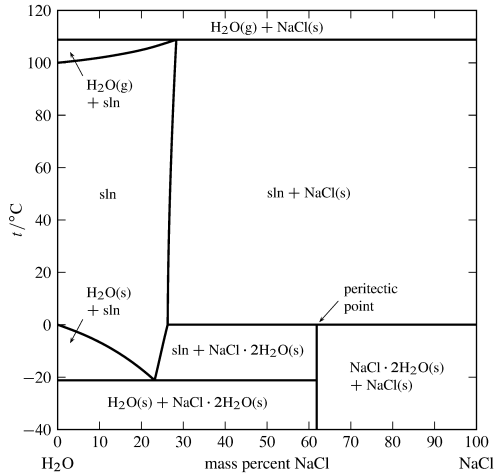

Figure 4.4: Phase diagram for the binary system of H_2O and NaCl at 1bar. [122]

.

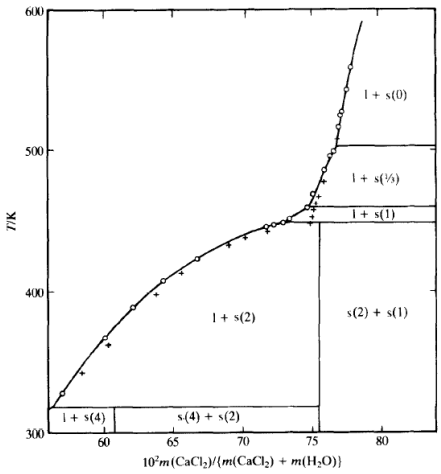

Figure 4.5: Phase diagram for the binary system of H_2O and $CaCl_2$ at 1bar. [111]

.

After a series of 5, 10 and 20 cycles samples were scanned using the XCT and their 3D reconstruction was made using the software CTPro3D (provided by Nikon). By comparing in 3D the treated samples with the fresh one, we tried to assess the salt distribution by evaluating the local porosity reduction caused by pore clogging of crystallised salts. For this thesis work we attempt a further methodology, by using efflorescence as a

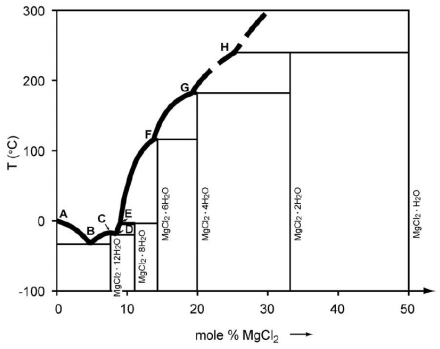

Figure 4.6: Phase diagram for the binary system of H_2O and $MgCl_2$ at 1bar. [65]

.

reference grey value for salt crystals, i.e. grey values thresholding.

In order to obtain a sensible amount of efflorescences, we scanned a sample previously saturated with a sodium sulphate solution, after it was subjected to a very slow drying at environmental temperature and 35% of RH. A sample was placed to saturate with a 1.2 M solution of sodium sulphate (Na_2SO_4) for over 20 days reaching a full saturation of the sample. The sample was saturated via capillary rise and its outer surface was sealed with silicon grease hence solution can enter the sample only from its bottom surface. By drying the sample at environmental temperature and 35% of RH, accordingly with the solution phase diagram,the formation of mirabilite and subsequent dehydration to thenardite is promoted. The relatively slow drying rate produced under these conditions was chosen to promote precipitation at the outer surface as efflorescence to aid differentiating salt from rock in the XCT images.

Each 3D reconstruction required beam hardening corrections of the sample scan. The beam hardening artifact results in a brightness at the edge of the sample, as the X-ray beam hardens differently depending on the thickness of the object as it passes through it [62]. At the object edges X-rays are proportionally more attenuated and therefore appear brighter in the resulting images. Correction of beam hardening was performed by Dr Alice Macente using the code developed by Carla Romano [27]. The reconstructed CT datasets were then visualised and processed using Avizo (www.FEI.com).

4.3 Results

4.3.1 Assessment of de-icing salts distribution by evaluating pore space reduction after crystallisation cycles.

Salt crystallisation test as proposed by EN 12370.1999 standard proved to be poorly effective in terms of stone damaging if carried on with a different salt with respect to the one suggested (e.g. sodium sulphate). Several authors [6], [12], [71] pointed out that re-saturation by full immersion proved to be time consuming and considerably less effective in terms of damage caused to stone samples when compared to the partialy immersion saturation technique. They observed significant differences in the extent and type of damage between the two test procedures [71]. During standard test via full immersion, in fact, salt content and sample mass are expected to regularly increase during repeated salt contamination while mass loss is expected to be due to damage. This is proved to not be always the case, as by full immersion in salt solutions, salts occupying the outer pores tend to dissolve during re-saturation, hence mass does not increase regularly and mass loss can increase with each cycle. Moreover, efflorescences developed only after a very high number (c.15) of re-saturation cycles and they were barely detectable by visual inspection. Results of the re-saturation cycles test conducted on a sample saturated with sodium chloride are shown in Figure **??**

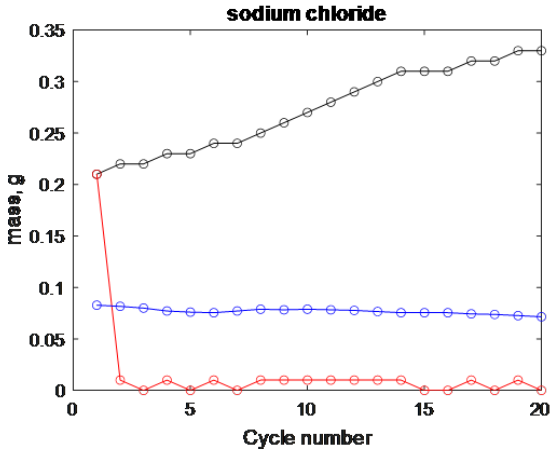

Figure 4.7: Results of the cyclical test conducted on a sample saturated with NaCl.Black is the dried mass gain of the sample relative to the initial dry mass. Blue is the mass of salt in the solution absorbed during the imbibition phase (any dissolution of dried salt deposited during the previous cycle is not taken into account because it is not measured). Red is the mass increase of the dried sample per cycle, relative to the previous cycle.

As shown in Figure ?? the black line is the mass of salt measured after drying for each cycle. This does contain water (hence the sample was not fully dried) in the case of cycle 1. After cycle 1 it is not possible to determine because solid salt from cycle 1 is getting dissolved with each re-saturation cycle. The red line is the mass gain on drying per cycle and shows that salt is being removed by dissolution each time the sample is re-saturated. The blue line shows the solid salt content that is present in the mass of solution being absorbed per cycle. This is decreasing while the solid salt mass of the sample is increasing. Either this is because the values of solid salt in the sample are inflated from trapped water or because some salt is being retained per cycle (i.e. it is not all dissolving during the re-saturation stage). If we assume that all salt is found in a $2mm$ rim of the cylinder, the volume of pores filled in that $2mm$ thick region is c. 15%. The sample porosity (calculated from solid density) is 22%. The volume fraction of pores filled with solution is 6%. This value is calculated considering the volume fraction of pores filled with solution that is absorbed at the beginning of the experiment (cycle 1) and the volume fraction of pores filled with solution at the end (cycle 20) and assuming that the difference is due to pore blocking. The volume fraction of pores filled with salt that could be deposited from each cycle of solution uptake if there was no dissolution during saturation is 25% (maximum amount), while 5% is the volume fraction of pores filled with the recorded mass of solid salt assuming no water was trapped, although we know this is not the case, and there is water trapped in the pores.

Figure 4.8 shows the solubility curve for calcium chloride hydrates. The phase diagram of Sinke et al.(1985) shows that $CaCl_2 \cdot 2H_2O$ will form during oven drying at 105°C but also, that on further removal of water $CaCl_2 \cdot H_2O$ may form. It is unclear whether both hydrates (di- and mono-) formed during drying, but assuming at least $CaCl_2 \cdot 2H_2O$ forms then the solubility chart in Figure 4.8 below shows that the dissolving $CaCl_2 \cdot 2H_2O$ will be supersaturated with respect to the stable phase at room temperature $CaCl_2 \cdot 6H_2O$.

Results of the re-saturation cycles test conducted on a sample saturated with calcium chloride are shown in Figure ??.

As shown in Figure ??, black is the mass of salt measured after drying for each cycle. The solution (1M) was made up using $CaCl_2$ anhydrous, but the stable phase at 105°C is

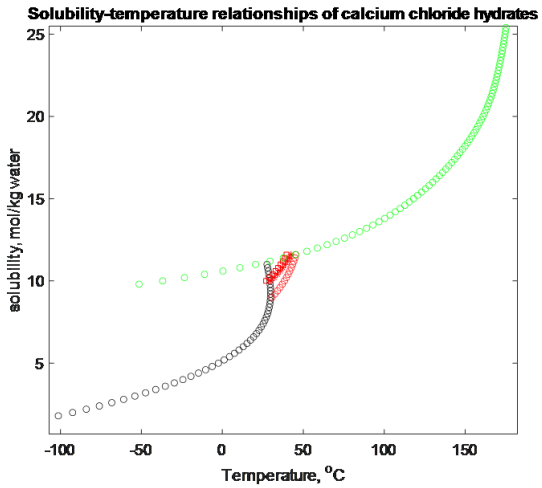

Figure 4.8: Green line is the solubility of $CaCl_2 \cdot 6H_2O$, black is the solubility of $CaCl_2 \cdot 2H_2O$, red circles show the solubility of $CaCl_2 \cdot 4H_2O$ (α), red stars show the solubility of $CaCl_2 \cdot 4H_2O$ (β) and red squares show the solubility of $CaCl_2 \cdot 4H_2O$ (γ) [130]. The solubility of $CaCl_2 \cdot 2H_2O$ is extended into the hexahydrate stability region to show the solubility difference between the phases when the oven dried sample containing $CaCl_2 \cdot 2H_2O$ is introduced to 1M $CaCl_2$ solution during the re-imbibition phase.

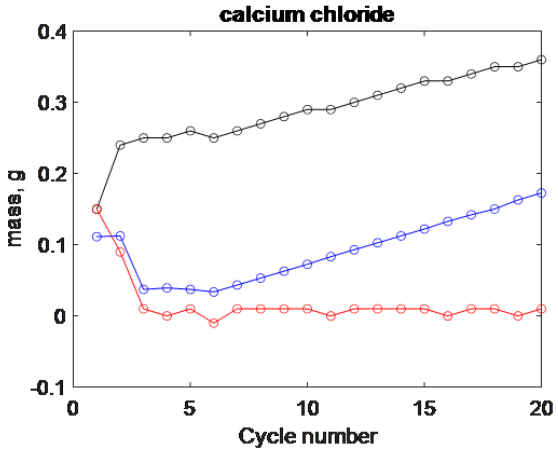

Figure 4.9: Results of the cyclical test conducted on a sample saturated with $CaCl_2$.Black is the dried mass gain of the sample relative to the initial dry mass. Blue is the mass of salt (CaCl2) in the solution absorbed during the imbibition phase (any dissolution of dried salt deposited during the previous cycle is not taken into account because it is not measured). Red is the mass increase of the dried sample per cycle, relative to the previous cycle.

sinjarite ($CaCl_2 \cdot 2H_2O$). At room temperature the stable phase is antarcticite ($CaCl_2 \cdot 6H_2O$) and calcium chloride is very hygoscopic (ERH is c. 6% for sinjarite) so we can assume that the solid $CaCl_2 \cdot 2H_2O$ will dissolve and recrystallize as $6H_2O$ in the laboratory air. This is less likely in a desiccator but not impossible. Comparing the mass of solid salt that can form (sinjarite) from solution in cycle 1 with the amount of solid salt deposited from cycle 1, then the amount deposited is slightly less than it should be rather than slightly more, so there is no trapped water during drying. Black

is the solid salt in the sample (sinjarite), red is the increase per cycle in solid salt in the sample, blue is the solid salt ($CaCl_2 \cdot 2H_2O$) in the solution and green is the solid salt in the solution expressed as a hydrate ($CaCl_2 \cdot 6H_2O$). It appears that not all solid salt is dissolved in the second re-saturation cycle,(as it is the case for the sample saturated with NaCl) because the mass of solid salt in the sample increases significantly before the increase in solid salt reduces significantly as it does in the NaCl sample. Plotted below is a figure showing the cumulative salt (sinjarite - $2H_2O$) from solution (blue stars).

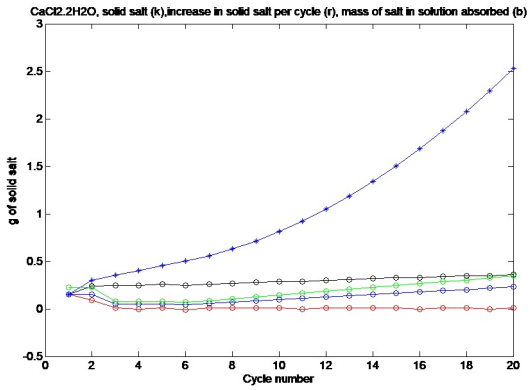

Figure 4.10: Plot showing the cumulative salt (blue stars) from solution assuming that all salt in the solution absorbed is retained and no salt is dissolved during the re-saturation that was deposited from the previous cycle. Black line is the amount of solid salt gain for all cycles.

This is assuming that all salt in the solution absorbed is retained and no salt is dissolved during the resaturation that was deposited from the previous cycle. It is clear that the amount of solid salt (black line) is less than the blue stars for cycle 2 and all other cycles, but cycle 2 could also represent no net salt gain (i.e. all solid salt deposited in cycle 1 is dissolved out and replaced in cycle 2) but the apparent mass gain comes from the formation of antarciticte ($6H_2O$) at room temperature. The evidence for this is the similarity between the green circle and black circle values for cycle 2. It is also clear that there is pore clogging between cycles 3 and cycle 6, which is probably from hydrate ($6H_2O$) formation, but from cycle 7 onwards, the solution absorbed starts to rise again. The gradient of the black line and blue line appear similar (cycle 7 onwards) which suggests that sinjarite is forming, rather than antarcticite. But perhaps it did form in cycles 2 – 6 and blocked pores. The sample porosity calculated from solid density is 25%. The maximum amount of volume fraction of pores filled with salt that could be deposited from each cycle of solution uptake if there was no dissolution during

saturation is 46%, while the volume fraction of pores filled with the recorded mass of solid salt (assuming sinjarite and no trapped water) is 6%.

Regarding the re-saturation cycles test conducted on a sample saturated with magnesium chloride, according to the phase diagram in Figure 4.6 and the solubility curve in Figure 4.11 below, at room temperature a 1M $MgCl_2$ solution will not crystallise.

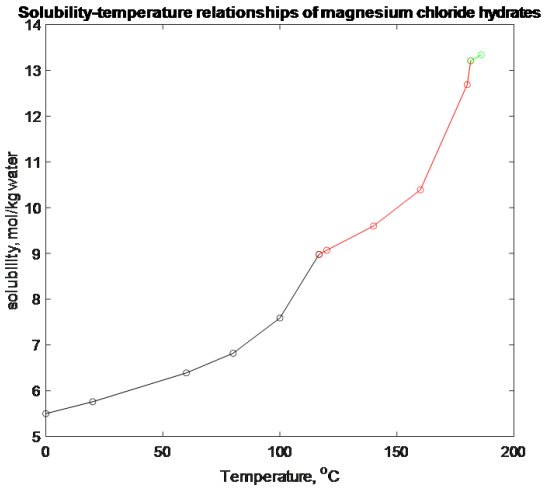

Figure 4.11: Magnesium chloride solubility, data from International Critical Tables. Black circles and line is the solubility of $MgCl_2 \cdot 6H_2O$, red circles and line is the solubility of $MgCl_2 \cdot 4H_2O$ and green circles and line is the solubility of $MgCl_2 \cdot 2H_2O$

At 105°C, $MgCl_2 \cdot 6H_2O$ (bischofite) and $MgCl_2 \cdot 4H_2O$ forms from the dehydration of $6H_2O$ at 105°C from TGA measurements [57]. The TGA measurements are not isothermal, so they do not record what phase forms when the sample is held at 105°C. Kipouros and Sadoway (2011) investigate the dehydration stages of magnesium chloride starting with the hexahydrate and progressively removing water. Removal of hydrate water to obtain $MgCl_2 \cdot 2H_2O$ is quite straightforward. They say that dehydration by heating beyond the dihydrate requires special precautions as simple heating without an HCl atmosphere will lead to hydrolysis and the formation of $MgOHCl$. We will assume that heating at 105°C for 16 hours is only enough to produce the dihydrate and not $MgOHCl$ but future work would identify the phase precipitated using XRD.

Results of the re-saturation cycles test conducted on a sample saturated with magnesium chloride are shown in Figure 4.12

It is unclear whether the hexahydrate forms or not during sample cooling or re-saturation. The amount of solution absorbed (blue line) does not drop significantly and suggests

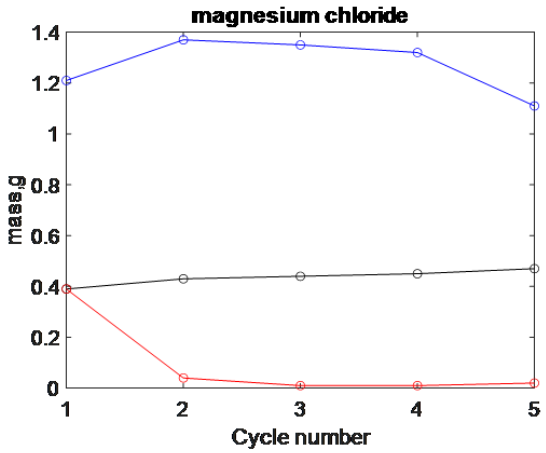

Figure 4.12: Results of the cyclical test conducted on a sample saturated with $MgCl_2$.Black is the dried mass gain of the sample relative to the initial dry mass. Blue is the mass of salt ($MgCl_2$) in the solution absorbed during the imbibition phase (any dissolution of dried salt deposited during the previous cycle is not taken into account because it is not measured). Red is the mass increase of the dried sample per cycle, relative to the previous cycle.

that there is no pore clogging from hexahydrate formation (i.e. that the hexahydrate does not form). The increase in salt content dips from cycle 2 onwards suggesting the salt is dissolved out per cycle. The difference between the measured (weighed) salt content after oven drying and the salt content in the solution (blue circles) suggests trapped water, at least after cycle 1. Behaviour is very similar to NaCl.

Although visibly obvious damage did not occur during the test described above the distribution of the studied de-icing salts within the porous matrix of the sample and at its outer surface can be qualitatively estimated. A preliminary investigation conducted on the fresh reference sample shows this stone type has a quite high porosity (16%). This was calculated in Avizo by creating a mask of the entire sample volume, using the *volume edit* operator. The pore space was selected on this mask by using gray value thresholding and the pore space volume was calculated by using the *volume fraction* operator. The final value of porosity calculated for the fresh reference sample is 16%. This compares to the porosity measured using vacuum saturation, which was 17%. Figures 4.13 and 4.14 show the 3D volume renderings of a fresh Berea sample, where blue identifies the pore space and grey the matrix.

To estimate the errors given by the segmentation/thesholding method, error bars were also included, using the same procedure as described by Fusseis (2012) and from Macente (2017). The pore space was morphologically eroded and dilated by one voxel in each

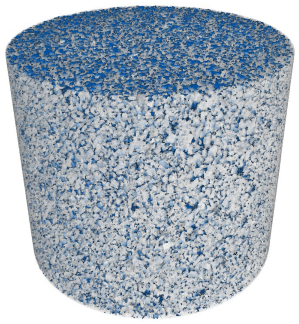

Figure 4.13: 3D volume rendering of a fresh Berea sample (2.5 cm diameter, 1.5 cm high) rotated 90° on the Y-axis. In blue is the pore space and grey is the matrix

.

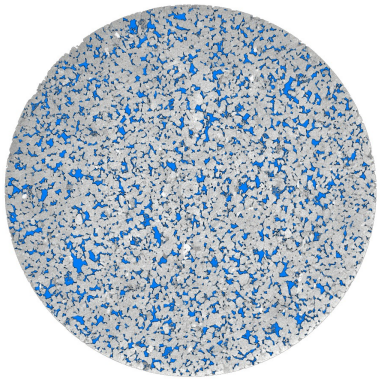

Figure 4.14: Cross section of a fresh Berea sample (2.5 cm diameter, 1.5 cm high). In blue is the pore space and grey is the matrix

.

direction and the relative volumes calculated [38]. The error on the dilated volume is 12% while the error on the eroded volume is 10%. These error bars methodology proved to overestimate the errors given by any segmentation, enabling a good validation of the porosity calculation [72].

Results of the investigation conducted on the first treated sample (BE01) saturated with sodium chloride proved that the presence of salts can be detected only after c. 20 cycles. Variations of salt content during 20 cycles are shown in APPENDIX C.

A pore clogging effect on the outer surface of the sample is visible to a depth of c. 2 mm. Figures 4.15 and 4.16 show the 3D volume renderings, where blue identifies the pore space and grey the matrix. Pore space is visibly reduced at the outer surface. We can see this from the front at the top of the sample (Fig.4.15) and from the top

to the bottom (Fig.4.16) of the sample. Figure 4.17 offers a better visualization of the pore reduction on the outer surface of figure 4.16. By comparing these images with the fresh sample, it was possible to determine where porosity reduction was localised and calculate it using Avizo. Because a preliminary assessment showed a marked effect of pore clogging in the outer surface of the sample, two separate masks were created within the sample, one at the core and one at the outer surface at a depth of c. 2 mm by using the Avizo operator *volume edit*. For each mask, the porosity was then calculated by grey value thresholding. Pore space at the outer surface resulted to be 14%, while at the core porosity value resulted to be 17%, comparable to the value of the fresh reference sample.

Figure 4.15: 3D volume rendering of BE01 (2.5 cm diameter, 1.5 cm high) re-saturated with NaCl 1 M solution after 20 cycles. Rotated 90° on the Y-axis

.

Results of the investigation conducted on the second sample (BE02) saturated with a $CaCl_2$ 1 M solution showed that the presence of salts does not considerably obstruct the sample porosity, even after c. 20 cycles. Variations of salt content during 20 cycles are shown in APPENDIX C. Figures 4.18 and 4.19 show the 3D volume renderings of the sample top and bottom respectively. Pores are shown by blue, while the matrix is in gray. It can be observed that the sample bottom exhibits more pore space reduction, mainly on the right side of the sample, where a crystallisation front seems to appear. We also observed a slight reduction of the pore space at the outer surface of the sample, which can be seen in figure 4.20. Porosity for the BE02 sample was calculated with the same procedure as the fresh sample and resulted to be 17%.

Figure 4.16: 3D volume rendering of BE01 (2.5 cm diameter, 1.5 cm high) re-saturated with NaCl 1 M solution after 20 cycles. Rotated 90° on the Y-axis,45° on the Z-axis.

.

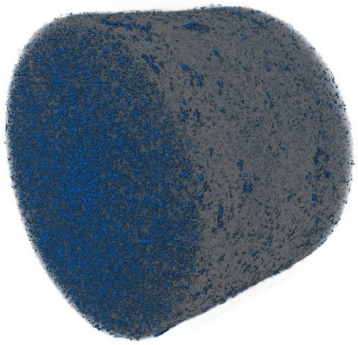

Figure 4.17: 3D volume rendering of BE01 (2.5 cm diameter, 1.5 cm high) re-saturated with NaCl 1 M solution after 20 cycles. Rotated 90° on the Y-axis,45° on the Z-axis.

.

Results of the investigation conducted on the third sample (BE03) saturated with $MgCl_2$ 1 M solution proved that the presence of salts starts to affect the sample just after only few cycles. Variations of salt content during 5 cycles are shown in APPENDIX C. Figure 4.21 shows the general porosity reduction at the outer surface of the sample BE03 and, through the vertical section (Fig.4.22), we can see the porosity reduction inside the sample as well. The black vertical plane marks the two sections of the sample. Porosity for the entire volume of the sample resulted to be 16%.

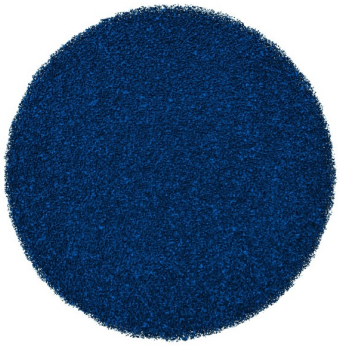

Figure 4.18: 3D volume rendering of BE02 (2.5 cm diameter, 1.5 cm high) re-saturated with $CaCl_2$ 1 M solution after 20 cycles. Rotated 90° on the Y-axis. Sample top.

.

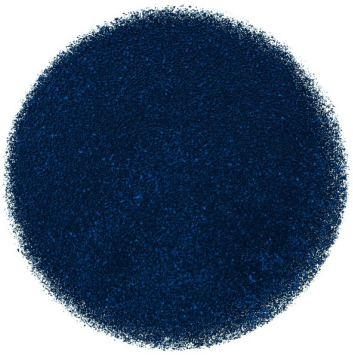

Figure 4.19: 3D volume rendering of BE02 (2.5 cm diameter, 1.5 cm high) re-saturated with $CaCl_2$ 1 M solution after 20 cycles. Rotated 90° on the Y-axis. Sample bottom.

.

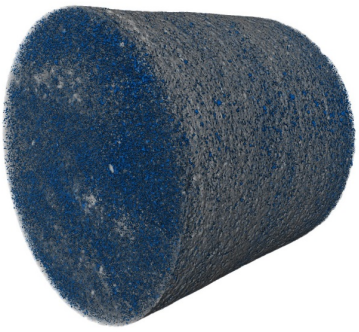

Figure 4.20: 3D volume rendering of BE02 (2.5 cm diameter, 1.5 cm high) re-saturated with $CaCl_2$ 1 M solution for 20 cycles. Rotated 90° on the Y-axis,45° on the Z-axis.

.

Discussion

Different properties of each salt solution such as the viscosity, surface tension, and density, will affect the rate of solution ingress into the core and, eventually, the depth of

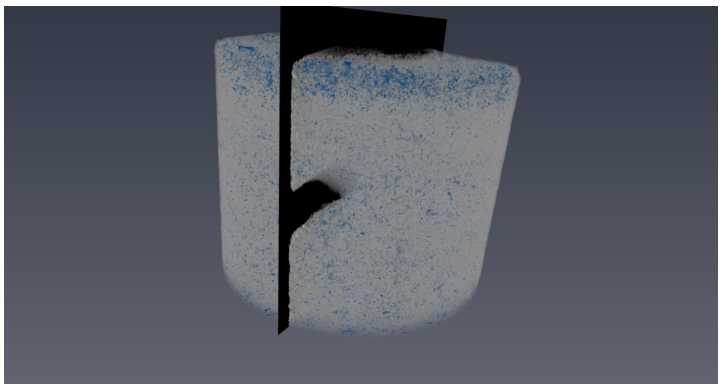

Figure 4.21: 3D volume rendering of BE03 (2.5 cm diameter, 1.5 cm high) re-saturated with $MgCl_2$ 1 M solution after 5 cycles. Sample is rotated 20° on the Y-axis.

.

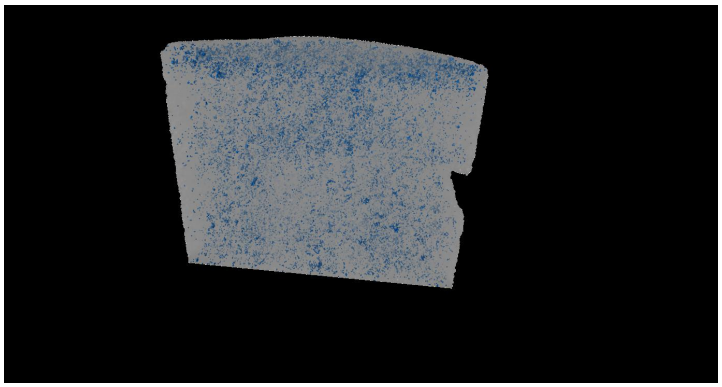

Figure 4.22: 3D volume rendering of BE03 (2.5 cm diameter, 1.5 cm high) re-saturated with $MgCl_2$ 1 M solution for 5 cycles, showed in Fig. 12. Sample is rotated 20° on the Y-axis. In blue are the open pores of the sample, while in grey is the stone matrix

.

fluid penetration. This can be calculated in order to determine whether, in two hours time of full immersion in different salt solutions, samples were actually fully saturated before being dried in the oven. Accordingly to Hall et al. the absorption and sorptivity are proportional to the square root of the ratio of surface tension and viscosity of the salt solution [32], [113]. Hence, if viscosity/density increase or surface tension decrease it can decrease solution ingress into a porous material [48]. By using equation 4.1 we can calculate the time it takes for the used solution to fully saturate the sample.

$$Saturation\,time = \frac{(L/2 \times \phi)^2}{(S_w \times \sqrt{(\frac{\sigma_s}{\eta_s}) \times (\frac{\eta_w}{\sigma_w})})^2} \tag{4.1}$$

Where L is the length of sample, ϕ is the sample porosity in volume fraction, S is the sorptivity, γ_w and γ_s are the surface tensions for water and solution in mN/m,

respectively; η_w and η_s are the viscosities for water and solution in $mPa \cdot s$, respectively. Values of viscosity and surface tension of each solutions at their specific concentration (1M) at 20°C from the International Critical Tables are listed in table below:

Table 4.2: Values of viscosity from the International Critical Tables and surface tension ([119], [20]) for the three salt solutions 1M.

Salt	Surface Tension (mN/m)	Viscosity ($mPa \cdot s$)
NaCl	72.4	1.094
$CaCl_2$	75.6	1.3
$MgCl_2$	74.7	1.468

Results of calculations proves that all samples where fully saturated after the 2 hours saturation time with the three different solutions. During the 16 hours of drying in the oven at constant temperature, salt solution in the samples undergoes two different stages of evaporation. During stage 1 there is an initial constant high evaporation rate, which exists as long as there is hydraulic connection between drying front and matrix surface by capillary flow. Stage 2 begins when the those hydraulic connections break and evaporation is driven by vapor diffusion [83]. If at any stage of the evaporation the solute concentration substantially exceeds the solubility limit (i.e. supersaturation exceeds a critical value), crystals will precipitate by first nucleating and then growing in the porous matrix [22]. The three de-icing salts studied seem to follow three different crystallisation patterns during drying, resulting in a different salt crystal distribution within the cores. The reason for this behaviour is complex, particularly as there is hydrate formation on cooling. As hydrates form they can block solution entering during the re-saturation. In this case, because there is also dissolution of crystallised salts, it is hard to determine what exactly is causing the different behaviour. Also, these solutions have different rate of transport properties of the ions in the liquid and evaporation rate [82], [6].

Whether different salts will precipitate and accumulate as a thin surface layer or within the medium, is the results of the competition between advection (capillary flow), which tends to transport the ions towards the porous medium surface, and diffusion, which tends to make the ion distribution uniform [121]. This competition can be expressed by the Peclet number which is a measure of the relative importance of advection versus diffusion. Accordingly to Pel et al. (2002) during drying of porous material the Peclet

number can be calculated using the following equation:

$$Pe = \frac{h \cdot L}{\theta_m \cdot D} \tag{4.2}$$

Where h is the drying rate, L the length of the sample, θ_m the maximum fluid content by capillary saturation, and D the effective diffusion coefficient of solute in porous media [86]. A measure of the samples drying rate (h) would be recommended for future work in order to get an estimation of the Peclet numbers and correlate it with the results of the 3D investigation. When Peclet numbers are large (Pe $>$ 1), convection is the dominant transport process and ions concentration increases at the surface of the porous medium, if the Peclet numbers are small (Pe $<$ 1), transport is controlled by diffusion, hence ions tend to distribute homogeneously through the drying porous medium and crystallisation is likely to happen inside the medium [45], [58]. The competition between advection and diffusion mechanism is also affected by salt solution properties, i.e. its viscosity, which influences the ions transport rate, and hence the ultimate location of salt deposition, as demonstrated by Kotter and Riekert (1978) and more recently by Ruiz-Agudo et al.(2007) [100]. They proved that high solution viscosity (high ionic concentration) entails slow capillary flow, which enhances the recession of the evaporation front. This ultimately results in a more homogeneous distribution of salts throughout the depth of the material [100] and this is in good accordance with the results of our investigation.

4.3.2 Assessment of sodium sulphate distribution by thresholding methodology.

We scanned a sample saturated via capillary rise with a 1.2 M sodium sulphate solution and then left to dry at environmental temperature and RH 35%. The salt content (1.02%) was measured after the sample drying stage. This treatment was aimed to a) try to induced microfractures in the sample and b) produce enough efflorescence to obtain a specific grey scale value for the salt(as shown in figure 4.23). The datasets alignment technique proposed by Desarnaud (2015) relies on the accuracy of the dataset alignment rather then on the determination of a precise grey value related to salt crystals.
The high amount of efflorescences we observed after the treatment (Fig.4.23) provided

Figure 4.23: Berea sandstone core before (right) and after (left) treatment with sodium sulphate solution

.

us a precise grey reference value for the salt at the sample outer surface, as shown in figures 4.24 and 4.25. The top and the bottom of the sample were scanned to investigate the salt distribution by looking for the distribution of that specific grey value within the core.

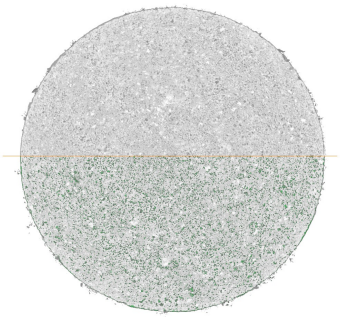

Figure 4.24: XCT image of a 2D cross-section of the sample after treatment. In green is the salt distributed through the matrix.

Results of the XCT investigation shows salt distributed more homogeneously at the top, where it occupies the 18% of the pore space. At the bottom salt occupies the 12% of the pore space. Error bars for the thresholding technique were estimated in the same way as for porosity of the fresh sample. At the top, the error bars were +1.74% and -2.1%, while at the bottom it resulted to be ±0.4%.

Figure 4.26 shows the sample top and the distribution of salt crystals, while figures 4.27 and 4.28 show the sample sections.

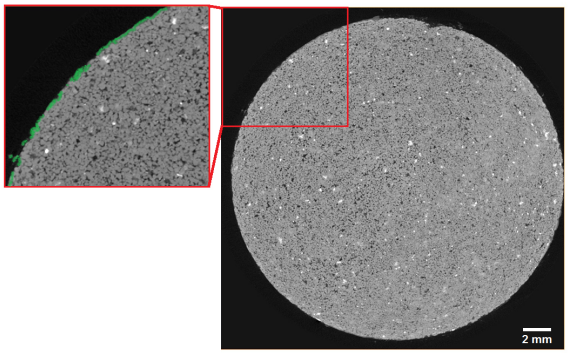

Figure 4.25: XCT image of a 2D cross-section of the sample after treatment. In green, highlighted in the squared on the left, is the salt distributed only at the outer surface.

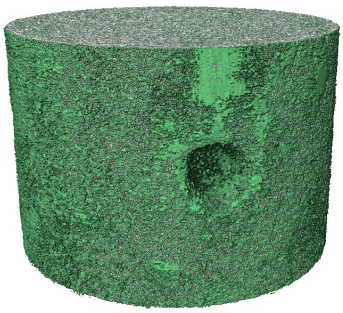

Figure 4.26: 3D volume rendering of the sample top (2.5 cm diameter, 2 cm high)

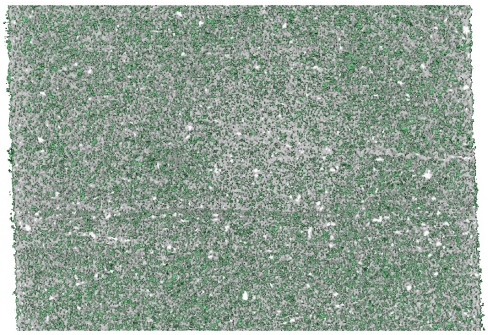

Figure 4.27: Section (XY-axes) of the sample shown in figure 12.

Figure 4.29 shows the sample bottom, visibly shows less salt is present, while figures 4.30 and 4.31 show the sample sections.

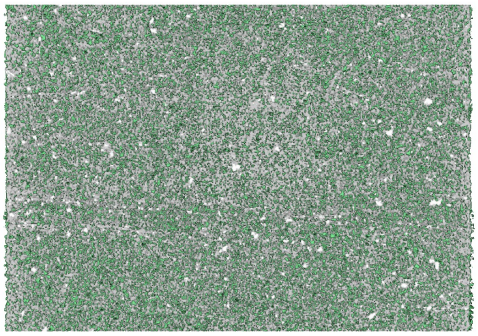

Figure 4.28: Section (XY-axes) of the sample shown in figure 12.

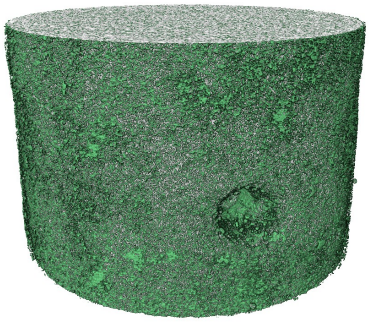

Figure 4.29: 3D volume rendering of the sample bottom (2.5 cm diameter, 2 cm high).

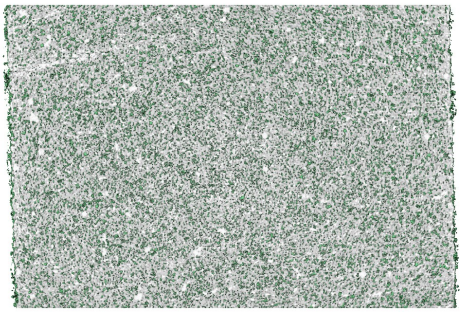

Figure 4.30: Section (XY-axes) of the sample shown in figure 15.

It was not possible to detect any micro or meso fracture in the sample.

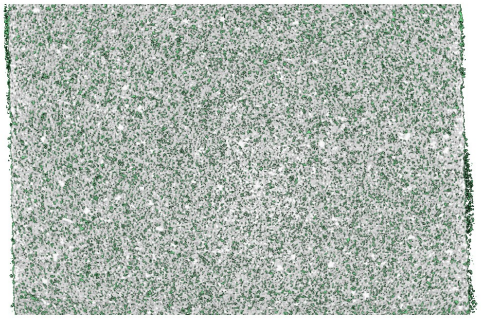

Figure 4.31: Section (XY-axes) of the sample shown in figure 15.

Discussion

By drying the sample at a very slow rate (environmental temperature) we make sure ions are advected to the surface of the sample, precipitating eventually mainly as efflorescences [58]. XCT imaging revealed a difference, however, in the salt distribution within the core, between the upper section (18% of the pore space) and the bottom section of the sample (12% of the pore space). This difference lies in a slightly different drying rate that is due to a local variation in the sample porosity and pore size distribution highlighted by the XCT imaging. Several scans in fact show the presence in this sample of specific structural features such as bedding planes of higher porosity and pore size that we did not detect in other samples previously scanned.

The presence of this bedding planes was confirmed and further investigated by observation of thin section prepared with blue resin impregnation from a fresh sample (Fig.4.32) showing the same structural features of the sample tested. In figure 4.33 it is possible to see two areas (left and right) with slightly different porosity. The left side of the image identifies a bedding plane. The right side of the image is representative of the rest of the sample. When detectable, these bands are only few mm thick (c. 2 mm) and show a slightly higher grain size distribution and higher porosity, compared to the rest of the sample (Fig.4.33).

Image analysis was conducted using imageJ to calculate the different porosity in the bedding plane identified in this thin section. A simple tresholding method of segment-

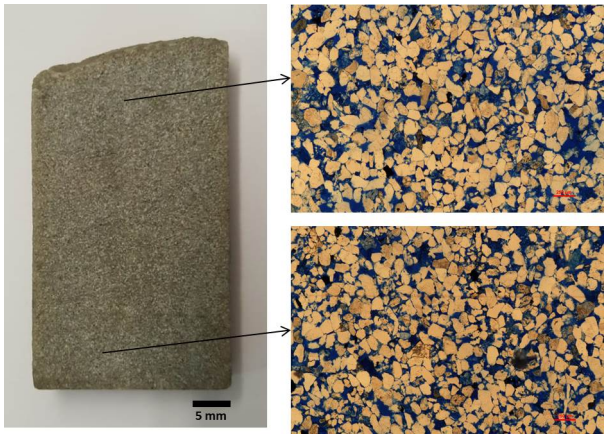

Figure 4.32: Image of the sample vertical section (left) and two photographs from its thin section, Nicols //. The images were taken in plane-polarised transmitted light. White grains are mainly quartz, with a smaller proportion of feldspar and micas. Black patches are iron oxide and opaque minerals. Pore space appears blue.

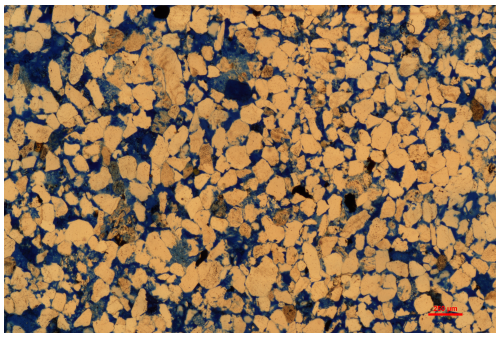

Figure 4.33: Thin section photographs of sample, Nicols //. The images were taken in plane-polarised transmitted light. White grains are mainly quartz, with a smaller proportion of feldspar and micas. Black patches are iron oxide and opaque minerals. Pore space appears blue.

ation was used to separate voids from grains (Fig.4.34b)

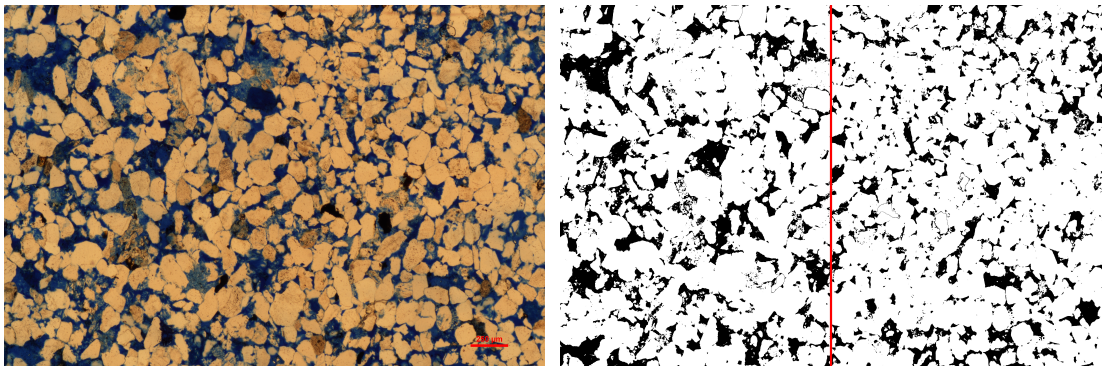

(a) (b)

Figure 4.34: Thin section photographs of sample (a), and its image acquired after tresholding (b). Grains are white, while pore space appears black.

The image was equally divided and porosity was calculated for the left (Fig.4.35) and for the right side (Fig.4.36) of the image. The bedding plane (left side of the image)

has a porosity of 22%, while the right side has a porosity of 16%, in good accordance with the average value of porosity calculated for this type of stone.

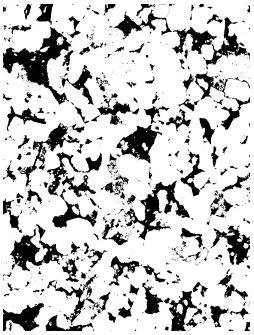

Figure 4.35: Image of the left, more porous, side of the thin section, which identifies the bedding plane. Image is acquired after tresholding. Grains are white, while pore space appears black

Figure 4.36: Images of right side of the thin section, which is representative of the average porosity of the sample. Image is acquired after tresholding. Grains are white, while pore space appears black.

Those bands plays a fundamental role during the drying process as they mark areas with different hydraulic connections between the drying front and the wet matrix within the sample.

In heterogeneous layered medium the transport of salt by advection (capillary flow) from one layer into the other is related to the pore sizes of the different materials. On drying, the layer with the smallest porosity and pore size distribution (which entail largest capillary pressure) will hold moisture the longest while the coarse porous layer will dry first. This can result in an accumulation of salts at the interface between layers and/or an accumulation of salts into the fine porous layer, where they are preferentially advected [100].

4.4 Preliminary conclusions

The growing interest in a quantification of weathering processes in 3D reflects the need to understand the relationship between the samples geological internal features and parameters (such as pore structure and bands) and the resulting damage [23]. However, little data is available on the 3D evolution and changes of those parameters caused by weathering and their quantification on the same sample. In this chapter are presented the preliminary results of a 3D investigation to assess salt distribution within samples subjected to salt weathering test as recommended by British standard BSEN12370. The investigation was carried out using the X-CT by means of two different methodologies, both leading to a qualitative evaluation of the evolution of structural 3D differences.
Using XCT by assessing changing in pore space due to crystals formation we can detect where de-icing salts tend to distribute throughout the matrix. This leads us to get valuable qualitative information on stone behavior in presence of de-icing salts. Results of previous XCT investigations on the behavior of sodium chloride contaminated sandstones, exposed to different RH conditions, proved that NaCl solution tends to clog the outer pores of the sample [22], [35]. This is in good accordance with the results of our XCT investigation. We concluded that sodium chloride tends to obstruct the immediate outer surface of the sample (c. 2 mm), without considerably affecting the inner structure. Calcium chloride, however, appears to only slightly occupy the outer surface and it seems to develop a crystallisation front in our specific case. Calcium chloride seems to only slightly affect the sample inner core porosity, showing no consistent pore space reduction anywhere after 20 cycles. XCT data suggests that salt crystallisation of magnesium chloride has the fastest effect on the samples, as the solution is more pervasive in the sample tortuosity, and it tends occupy scattered areas within the samples. The proposed methodology aims to qualitatively assess de-icing salts distribution through the sample matrix after several crystallisation cycles. Based on the encouraging preliminary results of our test further work is under-way to define an experimental procedure to reach a more accurate quantitative evaluation of porosity reduction. Porosity calculations, for instance, would benefit of a validation procedure, such as the MIP (mercury intrusion porosimetry) on each specific sample, to obtain more accurate error bars.

Results of this investigation also proved salt crystallisation tests performed in accordance with British standard BS EN12370.1999 are not really effective in terms of deterioration, if performed with a different salt with respect to the one suggested (i.e. sodium sulphate). In particular, the suggested re-saturation technique by total immersion, does not allow the salt content to progressively increase after the first cycles, as salt is still dissolving when the sample is immersed in the 1M solution.

Using the second XCT methodology, the specific grey value related to salt efflorescence was used as a reference to investigate salt distribution through the pore matrix. Results of the XCT investigation show thenardite distributed more homogeneously throughout the top of the sample, where it occupies the 18% of the pore space while at the bottom salt occupies the 12%. This is explained by the presence of structural features in the sample, such as bedding planes of different porosity that can accommodate higher percentage of salts. This was confirmed by thin section analysis of the sample. We could not see any fractures or micro-fracture development along the core. A detailed detection of micro-fractures, although possible, requires segmentation techniques using a combination of algorithms which had not been implemented in Avizo at the time of this study. Never the less, preliminary results of the investigation proved this technique can be implemented and used to investigate salt distribution throughout the porous matrix.

Further work is required to better understand the relationship between different salt distribution and solution evaporation rate, and to relate this parameters with each specific sample features and pore structure.

Chapter 5

Case study: salt crystallisation affecting building materials constituting Lerwick Town Hall in Lerwick, Shetland Islands.

5.1 Introduction

Cultural-historical building materials durability is affected by a variety of phenomenon, the most important of which is known to be salt crystallisation. Soluble salts frequently occurring include sulphates, nitrates, carbonates and chlorides of Na, K, Ca and Mg [2]. Three commonly occurring salts are thenardite (Na_2SO_4), mirabilite ($Na_2SO_4 \cdot 10H_2O$), and gypsum ($CaSO_4 \cdot 2H_2O$) [97]. Different materials will have a different level of vulnerability to this phenomenon depending on their physical properties such as porosity and pore size distribution. The mineralogical content can also affect the deterioration mechanism. In the case of sandstone, the presence of clay minerals can act as point of moisture ingress and host salts. If combined with their potential swelling properties this can significantly enhance the resulting damage [94]. Sandstones frequently contain variable amount of clays in the cement binder, which makes it highly susceptible to deterioration caused by swelling and shrinkage of clay minerals undergoing wetting and dry cycles [60]. The resistance of this type of sandstone, therefore,

highly depends from the building environment, particularly if it is exposed to rain or sea spray [60]. On the 24th October 2016 the Shetland Islands Council accepted to promote and fund our research project on Lerwick Town Hall, the most important historic building in Lerwick, built between 1881 and 1883 with Eday sandstone, entirely replaced by the Stanton Moor and Pulmers Bluff in 1977. The building is located in the center of Lerwick on raised ground, therefore exposed to high wind and sea spray. Stanton Moor sandstone is a relatively pure, quartz rich sandstone with a variable content of clay minerals. It is known to have a good work-ability and comparatively high weathering resistance. However, the observations we carried on at Lerwick Town Hall show difference in weathering processes. The building is located in the center of Lerwick on raised ground, therefore exposed to high wind and sea spray. Accordingly to a structural report on the external stonework previously submitted by David Narro Associates to the Shetland Islands Council in August 2012, the building seems to suffer from critical weathering and decay of the sandstone in several areas. The internal windows surround shows clear evidence of ongoing degradation due to salt crystallization. David Narro Associates proposed the replacement of the stone at the windows surround and the tracery. The sandstone chosen for the replacement is Clashach which, according to the BGS report (December 2010), provides the best petrographic match.

The aim of our investigation was the evaluation of the sandstone parameters (including mineral content) and how they influence the fast weathering process. The on-going replacement at Lerwick is a high cost procedure, hence a deeper understanding of the deterioration mechanism is fundamental to avoid or retard as much as possible further restoration of the building. This was achieved by applying a broad range of chemical, physical and mechanical testing, while taking into account the results of prior work. In the following chapters are provided the results of a detailed diagnostic survey on all the main materials constituting the building and affected by the on-going weathering process and a conservation strategy and recommendation for future work to be conducted on the the building, in order to prevent stone for further damage. Moreover, even though there is an extensive literature regarding durability problems for sandstones pointing at a salt weathering as main deterioration cause, we suggest clay swelling and shrinkage should be investigated, in particular in wet and cold environments such as

the one we found at Lerwick.

For the purpose of this chapter Dr Andrea Hamilton and I carried out the fieldwork. I carried out the laboratory test and data collection, the XRD Investigation (assisted by Dr. Fiona Sillars and Dr. Tiziana Marrocco (AMRL)) and the thin sections analysis. Powder samples were analysed by Dr Tanya Peshkur using ICP-OES and IC and results were elaborated using a MATLAB code written by Dr Andrea Hamilton. Dr Andrea Hamilton and I proceeded together to the final results interpretation.

5.1.1 Case study: Lerwick Town Hall

Lerwick Town Hall is the most important historic building in the town of Lerwick and a famous tourist attraction. It was built by Mr John M Aitken Lerwick between 1881 and 1883 and designed by Alexander Ross. The second son of Queen Victoria, Prince Alfred Duke of Edinburgh, laid the foundation stone in 1882. The original sandstone is Eday, from the Orkney Island. It was entirely replaced by the Stanton Moor (Yorkshire) and Pulmers Bluff (Derbyshire) in 1977. The Shetland Island Council took the building over in the 1975. It is a symmetrical Gothic and Flemish Baronial style building, with crow-stepped gables, bartizans corners and a square-plan clock tower to the east side [56]. The windows, created for the opening of the Town Hall in 1883, were made by James Ballantine and Cox & Son, Buckley, cover the history of Shetland from the 9th to the 15th century, incorporating Norse occupation and ending with the marriage of Margaret of Denmark to James III. A number of windows were donated by Amsterdam and Hamburg, to commemorate international trading connections. Over the years, the stonework around the windows has eroded. This was originally made with Eday sandstone, from the Orkney Island, which was entirely replaced by the Stanton Moor (Yorkshire) in 1977.

5.1.2 Site visit and sampling

A working visit to the Town Hall was organised in November 2016 in order to collect samples and achieve an overview of the entire building. The site sits in the centre of the town, on an exposed hillside. Samples were taken from the Stanton Moor sandstone

at the traceries and surrounds of the Lancet windows on the south side of the building (Fig. 5.1), as this exhibited the most obvious deterioration. Samples were taken from the inside and also from the outside of the building, by gently brushing the deteriorated surface or collecting pre-detached pieces for analysis.

(a) (b)

Figure 5.1: Image of the Lancet windows, Lerwick Town Hall (a) and detail of the deteriorated sandstone (b).

Other samples were taken from the green sandstone of the outer masonry, on the south side, which also showed signs of deterioration (Fig. 5.2).

(a) (b)

Figure 5.2: Image of the masonry beside the Lancet windows, Lerwick Town Hall (a) and detail of the deteriorated green sandstone (b).

Some samples were taken from the Clock Tower which includes the outer render layer, underlying brick work and mortar joints, where exposed (Fig.5.3).

A large piece of Stanton Moor sandstone (SH1) ($50 \times 10 \times 9 cm^3$) was given to us after it had been removed during the replacement of the stonework at the window surrounds of the west side of the building. The piece, which was in good condition, was used to cut some samples of fresh sandstone from its core, for reference samples of non-deteriorated

(a) (b)

Figure 5.3: Image of the clock window from inside the Clock Tower, Lerwick Town Hall (a) and detail of the deteriorated surrounding, showing the outer render and underlying brick work, Lerwick Town Hall (b).

stone for laboratory testing. A total of 19 samples were taken during the site visit. Schematic drawings of the sampling are presented below (Figures 5.4, 5.5 and 5.6). A detailed list of the samples is presented in Table 5.1.

Table 5.1: List of samples taken from Lerwick Town Hall

Sample ID	Sample description	Powder	Detachment
SH1	Fresh sandstone (reference sample)	x	x
SH2	Deteriorated sample (Lancet windows)	x	
Sh2b	Sample of the patina (Lancet windows)	x	
SH3	Deteriorated sample (Inside Lancet windows)	x	x
SH4	Deteriorated sample (Inside Lancet windows)	x	
SH5	Deteriorated sample (Inside Lancet windows)	x	
SH6	Deteriorated sample (Inside Lancet windows)	x	x
SH7	Deteriorated sample (Inside Lancet windows)	x	x
SH8	Salt scratched (Inside Lancet windows)	x	
SH9	Deteriorated sample (Inside Lancet windows)	x	x
SH10	Deteriorated sample (Inside Lancet windows)	x	
SH11	Deteriorated sample (Inside Lancet windows)	x	
SM1	Deteriorated sample (Outside Lancet windows)	x	
SM2	Deteriorated sample (Outside Lancet windows)	x	
SM3	Sample of the green sandstone (outside masonry)	x	
Brick CT	Sample from the brick masonry (Inside Clock Tower)	x	x
Mortar CT	Sample of mortar at the Clock window joint (Inside Clock Tower)	x	x
Salt CT	Sample of salt on the brick masonry (Inside Clock Tower)	x	

5.2 Methods

The composition of powder samples was determined by X-ray powder diffraction. The analysis was conducted at the Advanced Materials Research Laboratories (AMRL, Strathclyde University), using a BRUKER D8 ADVANCE with DAVINCI (2010) X-Ray Diffractometer with the assistance of Dr Fiona Sillars and Tiziana Marrocco. The software TOPAS was used to quantify the amount of each mineral phase present. Powder

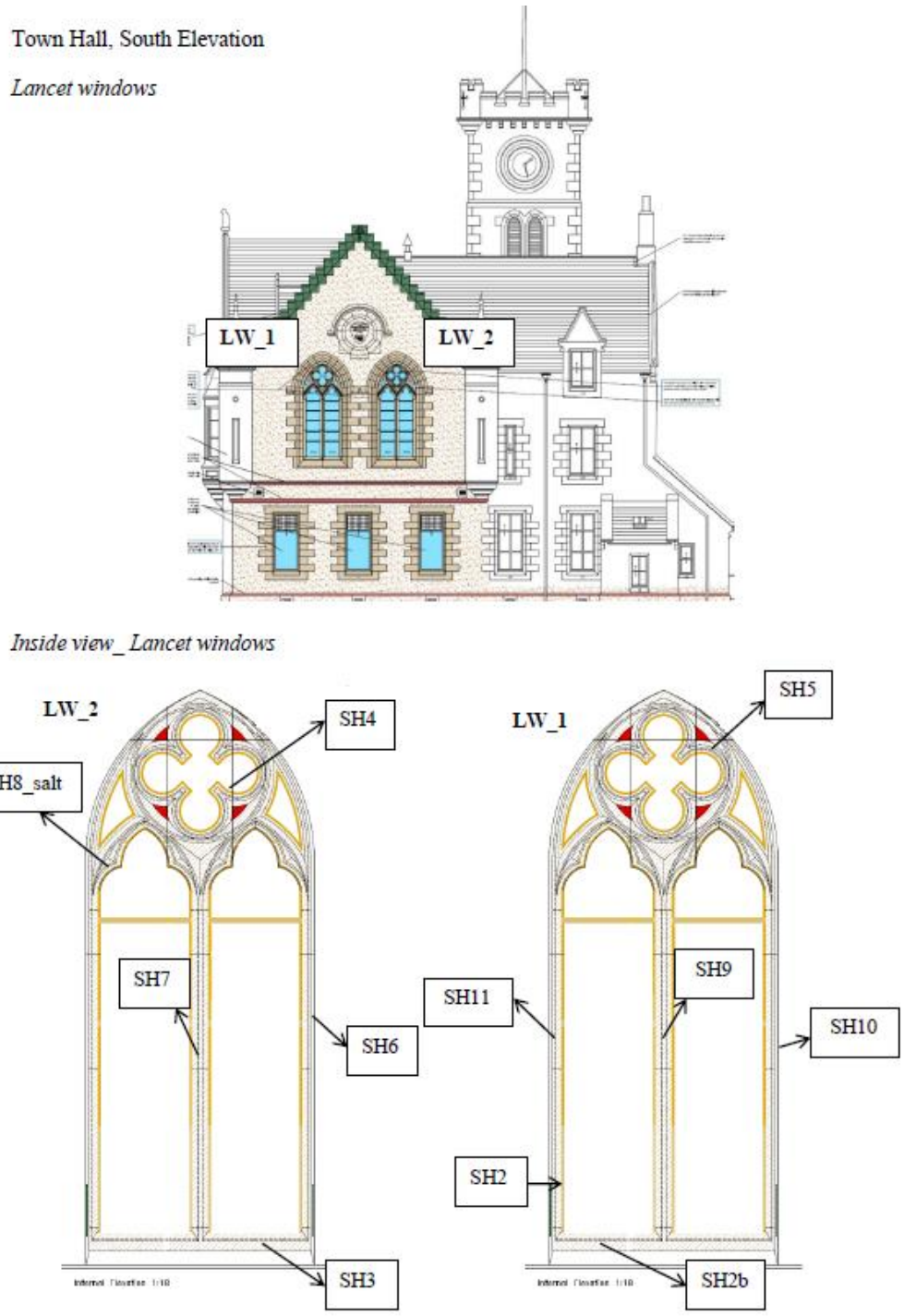

Figure 5.4: Schematic drawing of sampling from the Lancet windows, from the inside of the building (original drawings from David Narro Associates (2012) updated to show where samples were taken for the investigation presented here).

samples were then leached in de-ionised water and analysed by Dr Tanya Peshkur using ICP-OES (Thermo Scientific iCAP 6000 Series) and ion chromatography (Ionic chromatograph Compact IC Metrohm) to quantify the presence of soluble salts. All the detachments collected were used to make thin sections for the petrographic analysis

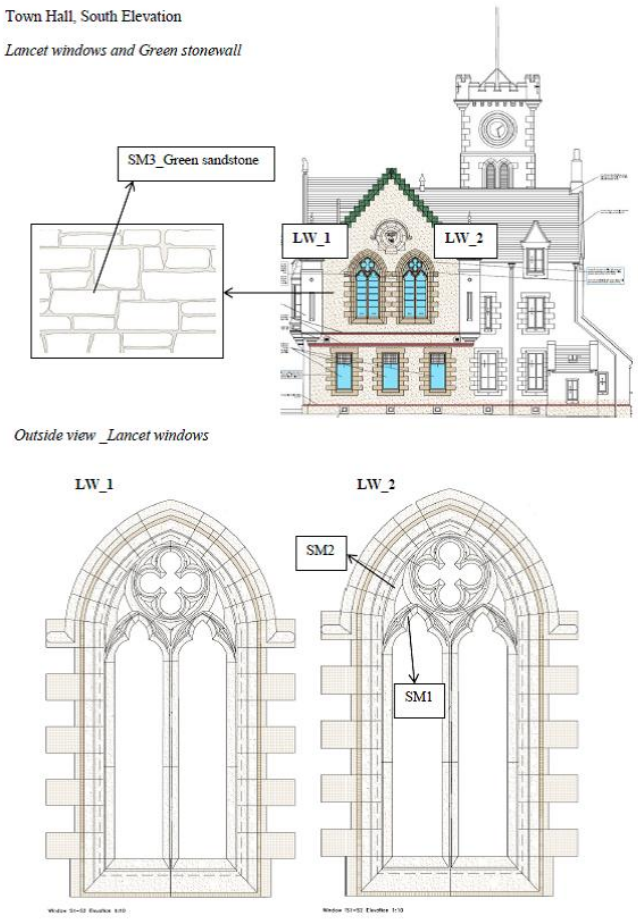

Figure 5.5: Schematic drawing of the sampling at the Lancet windows and the outer masonry, showing samples taken from the outside of the building (original drawings from David Narro Associates (2012) updated to show where samples were taken for the investigation presented here).

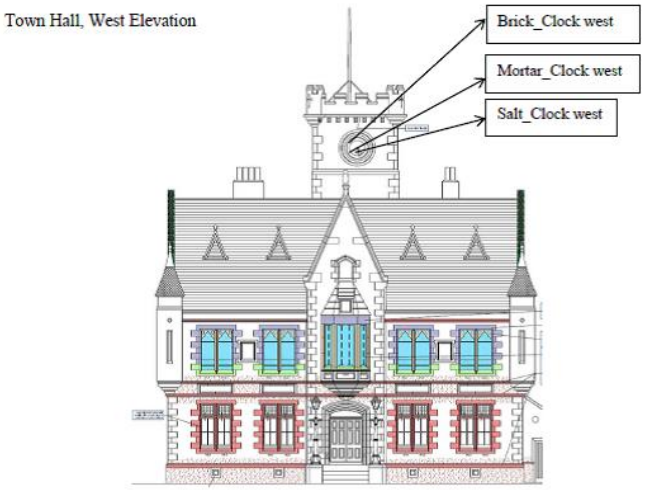

Figure 5.6: Schematic drawing of the sampling at the clock tower, from inside the tower at the clock window surrounds (original drawings from David Narro Associates (2012) updated to show where samples were taken for the investigation presented here).

carried out using a Nikon Eclipse LV100ND optical microscope, housed in the Civil and Environmental Engineering Laboratory, Strathclyde University. From the large piece of Stanton Moor was cut a small piece for thin sections analysis and few cylindrical samples (5 cm length and 2.5 cm of diameter) were drilled from the core of the stone. In order to assess the hygric behaviour of the sandstone, vacuum saturation test and sorptivity test [96] were carried out on those samples. Two of the cylinders cut from the Stanton Moor block were tested for hygric swelling using the Invar chamber (Fig.5.7), which can accurately measure swelling and strain response to water ingress. The apparatus, previously mentioned in *Chapter 1*, consists of a house-designed chamber made of Invar with an LVDT (linear variable displacement transducer GT1000RA from RDP Electronics, $\pm 1 \mu m$ resolution) located on the chamber lid, placed on the upper surface of the sample. After the core is positioned in the centre (null position) the signal output has a linear relationship with the physical position of the core, hence it can be quantified vertical deformation occurring in the sample during water ingress (Fig.5.7).

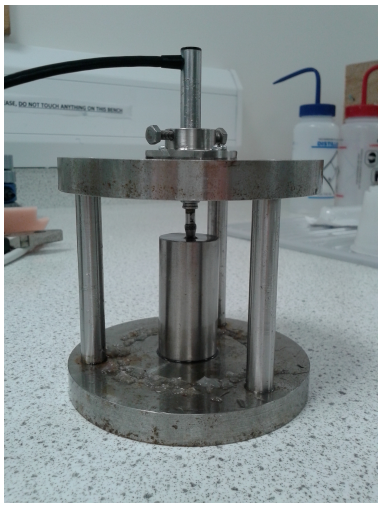

Figure 5.7: Invar structure with the LVDT core placed on an Invar rod.

5.3 Results

5.3.1 Lancet Windows

In this chapter are presented the results of the investigation on all Stanton Moor samples taken from the Lancet Windows on the inside and on the outside of the building, which exhibited an advanced state of deterioration at the time of our visit.

X-Ray powder diffraction analysis

All samples contained different amounts quartz, feldspar, micas (biotite and muscovite) and clay minerals (kaolinite and chlorite (see Table 5.2). In all the weathered samples it is possible to identify the presence of a lower amount of clay minerals (in particular kaolinite). A deeper investigation on this deterioration mechanism is presented in the water transport and hygric-swelling sections. A slightly different composition with respect to the other samples was found in sample SM1. The sample taken is powder which was scratched from a bedding plane, as shown in figure 5.8 . Bedding planes are layers occurring in sedimentary rocks that represent an event which interrupted sedimentation for a time. They are planes of deposition mineralogically distinct from normal strata of the sedimentary rock. In addition to an increased amount of calcite present, we found carbonates of magnesium and iron, which is a common component of sedimentary rock banding [104]. The presence of iron-rich carbonate could also explain the reddish colour of the bedding plane (Fig.5.8).

(a) (b)

Figure 5.8: Images of bedding planes: area of sampling of SM1, at the top of the left side of the right window (from outside) on the south side of the main hall, first floor (a) and magnification of another bedding plane on the right side of the left window.

The majority of samples also contain gypsum (calcium sulphate dihydrate). The amount of gypsum is particularly high in the sample SH2b (c. 79 wt%), which was brushed from a thin light coloured patina at the bottom of the lancet windows (Fig.5.9). The patina can be interpreted as an accumulation of percolated material (mortar debris) from the stained glass windows, the windows surrounds and the plaster joints.

Gypsum was found also in the sample SH10 (c. 43 wt%) taken from the inside surface

Figure 5.9: Light patina at the bottom of the right window (from inside) on the south side of first floor main hall.

of the Lancet Windows (Fig.5.10).

Figure 5.10: Area of sampling of SH10, on the middle of the right side of the right window (from inside) on the south side of main hall, first floor.

The presence of thenardite (Na_2SO_4) was found in a few samples. In particular, sample SH8 (c. 17 wt% thenardite) which was an efflorescence brushed from the surface of a lancet window, as shown in figure 5.11.

Soluble salts, such as sulphates (gypsum, thenardite) and chlorides (halite) are transported through the stone in solution and then crystallise at the stone surface by evaporation. As humidity rises and falls, there are cycles of dissolution and re-crystallisation which can cause damage. The key salts identified using XRD are gypsum and thenardite with traces of halite. Gypsum is the most prevalent, with 11 out of 14 samples taken containing solid (crystallised) gypsum, as determined by XRD. A small number of samples

Figure 5.11: Efflorescence on the top of the left side of the left window (from the inside) on the south side of the main all, first floor.

contained sodium sulphate (thenardite, 2 samples) and 5 samples contained solid halite. XRD can only detect salt if it is in the solid form but if it is dissolved and in the porous network of the stone, XRD cannot detect it. To get a fuller picture of the salt content, the stone fragments were leached in deionised water in order to get an analysis of the aqueous phase for metal cations (sodium, calcium, magnesium, potassium) and anions (sulphate, chloride and phosphate), as described in the next chapter. The average mineral content within all the samples calculated with TOPAS are listed in Table 5.2.

Table 5.2: Average mineral content (% wt) for all the Stanton Moor samples.

Sample ID	Quartz	Feldspars	Mica	Clay minerals	Carbonates	Gypsum	Halite	Thenardite	Mullite	Hematite
SH1	670.10	13.59	4.63	11.67	N/A	N/A	N/A	N/A	N/A	N/A
SH2	64.59	13.1	2.96	3.8	11.73	1.54	N/A	N/A	N/A	N/A
SH2b	13.84	2.89	3.93	0.37	N/A	78.97	N/A	N/A	N/A	N/A
SH3	68.29	11.2	2.32	3.82	9.95	4.43	N/A	N/A	N/A	N/A
SH4	79.65	2.07	5.34	6.8	2.92	1.01	2.22	N/A	N/A	N/A
SH5	55.56	13.24	4.08	19.2	4.73	N/A	3.20	N/A	N/A	N/A
SH6	60.55	7.36	7.73	23.56	N/A	0.09	0.71	N/A	N/A	N/A
SH7	74.30	6.65	9.29	7.23	0.77	N/A	1.76	N/A	N/A	N/A
SH8	42.69	5.28	2.88	8.16	1.06	23.25	N/A	16.67	N/A	N/A
SH9	71.59	9.56	4.10	10.39	0.50	N/A	3.86	N/A	N/A	N/A
SH10	38	2.67	0.28	15.95	N/A	43.11	N/A	N/A	N/A	N/A
SH11	50.87	1.58	4.88	5.05	N/A	13.80	N/A	23.81	N/A	N/A
SM1	42.71	20.94	6.16	N/A	30.19	N/A	N/A	N/A	N/A	N/A
SM2	54.96	16.45	19.77	7.12	1.56	N/A	0.14	N/A	N/A	N/A

All the XRD patterns of the samples from the Lancet windows are listed in APPENDIX B

Soluble salts analysis (ICP-OES and IC)

Sample powders were leached in deionised water and then filtered and analysed by Dr Tanya Peshkur using ICP-OES and ion chromatography to determine the cation and anion species present in each sample. Results of the analysis are given in ppm (mg/l) and presented to show the percentage of each ion in the total composition of each water sample. Using a MATLAB code written by Andrea Hamilton we got a correlation matrix that shows the relationship between the species in solution. Results of the analysis (Fig.5.12) from the inside of the town hall show chloride is prominent in most samples, probably from sea spray, which was detected less in the solid form (halite, sodium chloride) by XRD, indicating that this very soluble salt had not crystallised in the stone at the time of sample collection but was still present. Samples with a percentage of calcium (Ca) also have a high percentage of sulphate (SO_4), leading to the formation of gypsum ($CaSO_4 2H_2O$), the stable calcium sulphate phase at room temperature, which is in agreement with the XRD results.

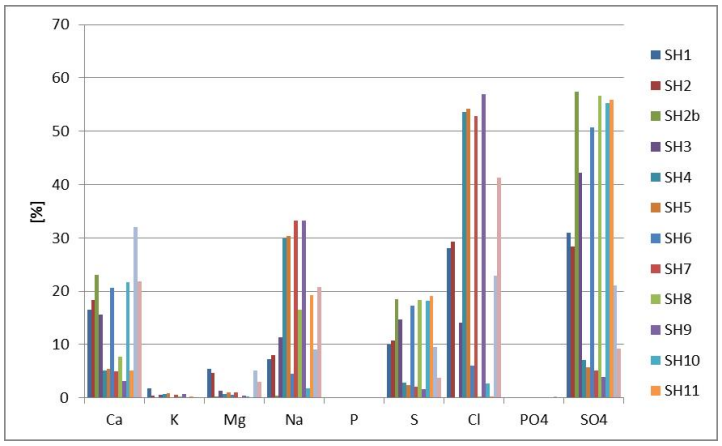

Figure 5.12: The graph shows the amount of each ion present (in ppm) as a percentage of the total composition of each leached aqueous sample (y-axis) against the ion (x-axis).

The correlation matrix shows, in numerical format, how well correlated ions are with each other (Table 5.3). Stronger correlation between ions in solution is expressed by the value closest to 1.00 and the most relevant correlations are in bold.

According to the results of the correlation matrix, both sodium (Na) and calcium (Ca)

Table 5.3: Correlation matrix for ions in the leached aqueous samples.

	Cl	SO_4	K	Mg	Ca	Na
Cl	1.00	-0.51	0.20	0.05	-0.47	0.13
SO_4	-0.51	1.00	0.61	-0.27	0.78	0.61
K	0.20	0.61	1.00	-0.17	0.15	0.95
Mg	0.05	-0.27	-0.17	1.00	-0.16	-0.29
Ca	-0.47	0.78	0.15	-0.16	1.00	0.06
Na	0.14	0.61	0.95	-0.29	0.02	1.00

correlate very well with sulphate (SO_4) confirming gypsum and thenardite are the main salts present in the inside of the building, which fits with the XRD results. Sodium (Na), however, doesn't correlate particularly well with chloride ion (Cl) because only half the samples (8 out of 15 in total) showed high levels of Cl. So sodium chloride, probably from seaspray/driving rain is present but not in all areas of the building. For sodium chloride to reach the inside wall, it would have to be transported through the wall from the outside of the building, which is exposed to sea-spray/driving rain. The source of the high levels of sulphate leading to gypsum and thenardite, however, would require further work to be found.

Thin sections analysis

The samples of Stanton Moor sandstone available for thin sections analysis were in total 5, four of which (SH3, SH6, SH7, SH9) were taken from different points at the surrounds of the Lancet Windows from the inside of the building. Reference samples were taken from SH1, which was removed from the building during renovation and was in good condition. The fresh sandstone presents a homogeneous grain size, with a well cemented fabric and a light buff background colour and pinkish buff at the bedding planes. The weathered samples show a significantly lower cohesion level with a slightly dusty white colour. The samples taken are listed below (Fig.5.13).

A summary of the conclusions drawn from the thin section analysis is presented below, while a detailed description for each thin section can be found in APPENDIX A. Based on the overall analysis it is possible to determine that Stanton Moor is a relatively pure, quartz rich sandstone ($>$ 60% quartz) with a few additional components. All samples are generally medium to fine grained. Grains are very well sorted with an angular

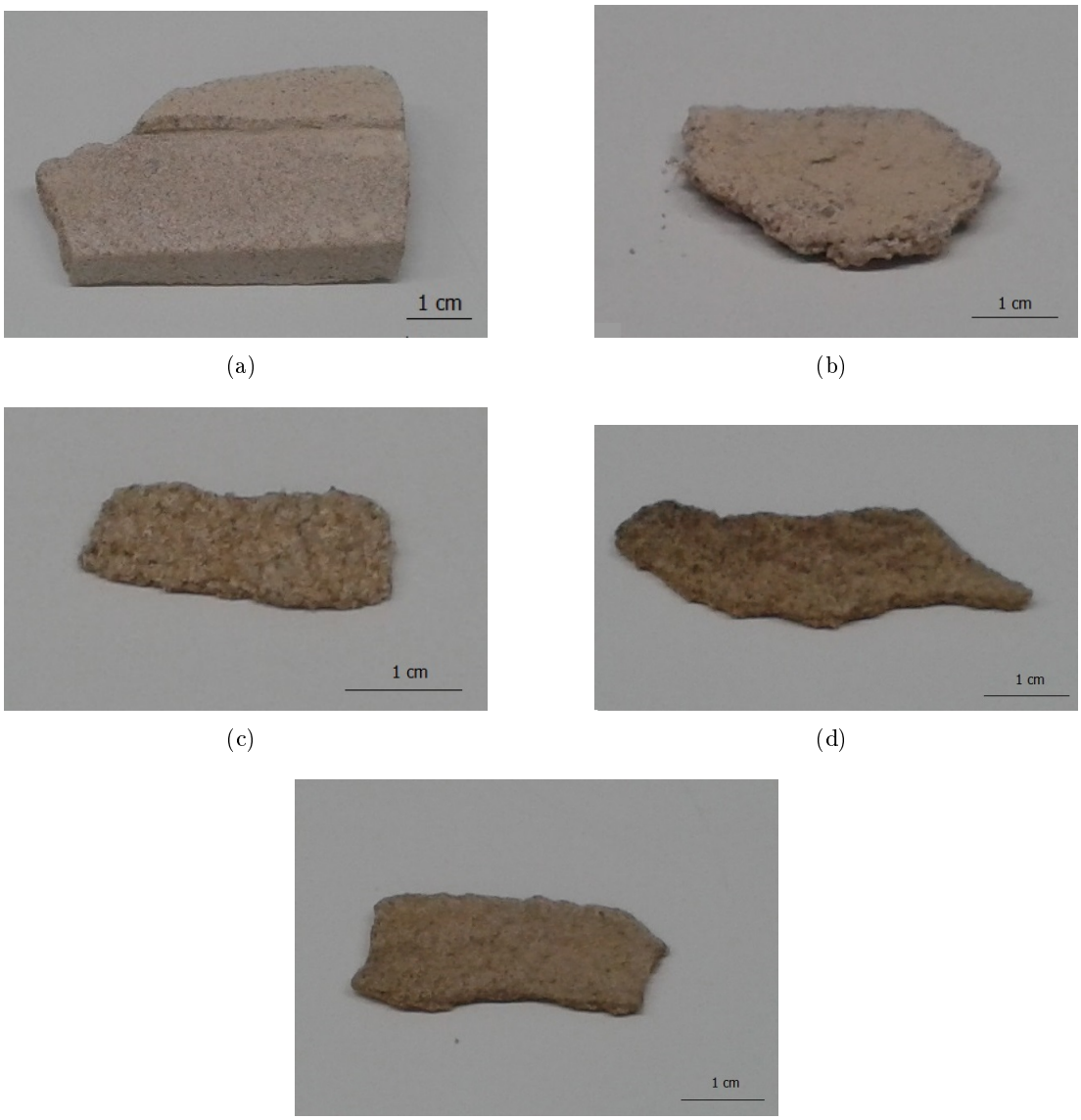

(a) (b) (c) (d) (e)

Figure 5.13: Sample SH1 (a), SH3 (b), SH6 (c), SH7 (d), SH9 (e)

to sub-angular shape. Samples show a variable proportion of iron oxide, feldspar and clay minerals. From the thin section observation it was not possible to detect the presence of any carbonate content, even though this was found in very minor quantities in the XRD analysis. The concave-convex granular contacts of quartz and feldspar plus kinked micas, reveal a high lithogenic pressure which suggests fresh samples have low permeability (SH1) (Fig.5.14).

When weathered, as particularly visible in sample SH3, the concave-convex grain contacts (quartz-quartz and quartz-feldspar) appear clearly detached, showing a significant increase in intra-granular porosity and permeability as shown by the increased blue con-

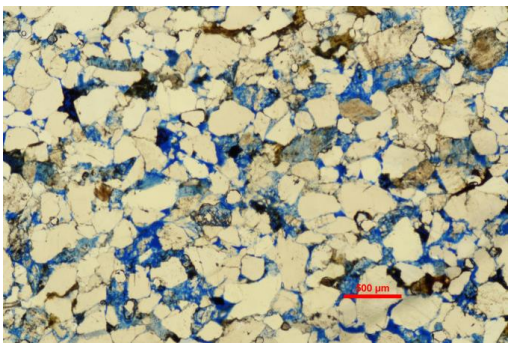

Figure 5.14: Thin section photograph of sample SH1. The image was taken in plane-polarised transmitted light. White grains are mainly quartz, with a smaller proportion of feldspar and micas. Black patches are iron oxide and opaque minerals. Pore space appears blue from resin impregnation.

tent of the image (Fig.5.15) with respect to the un-weathered sample (Fig.5.16).

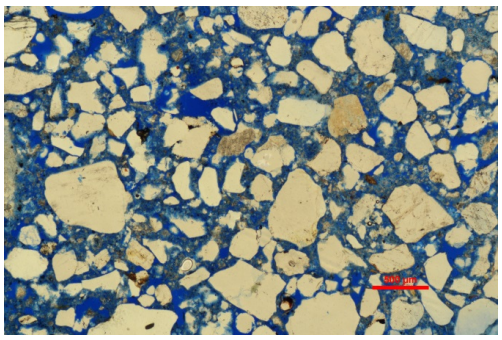

Figure 5.15: Thin section photographs of sample SH3. The images were taken in plane-polarised transmitted light. White grains are mainly quartz, with a smaller proportion of feldspar and micas. Black patches are iron oxide and opaque minerals. Pore space appears blue from resin impregnation.

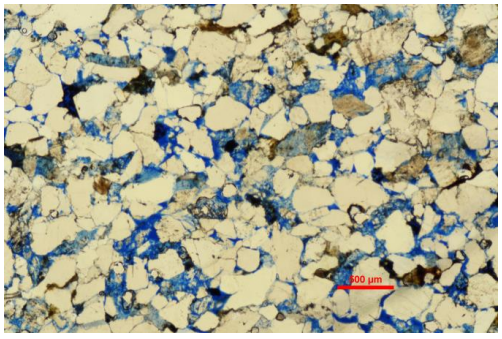

Figure 5.16: Thin section photographs of sample SH1. The images were taken in plane-polarised transmitted light. White grains are mainly quartz, with a smaller proportion of feldspar and micas. Black patches are iron oxide and opaque minerals. Pore space appears blue from resin impregnation.

In general, thin sections of weathered samples show a slight reduction in clay minerals, as confirmed by X-ray diffraction analysis and a large increase in intra-granular porosity with respect to fresh sandstone (SH1). Porosity and sorptivity are accurately measured in the following water transport study.

Water transport study

Water transport studies were carried out on unweathered samples to better understand the physical properties of the sandstone. Tests carried out were:

1) Vacuum saturation test to determine the porosity of the sandstone.

2) Sorptivity test and capillary rise test to determine how fast water can be transported through the stone.

From thin section analysis, Stanton moor sandstone is a fine-grained sublithic sandstone with a matrix of clay minerals and a low porosity and permeability. The open porosity of the unweathered sandstone was 13%. The capillary rise test is shown in figure 5.17.

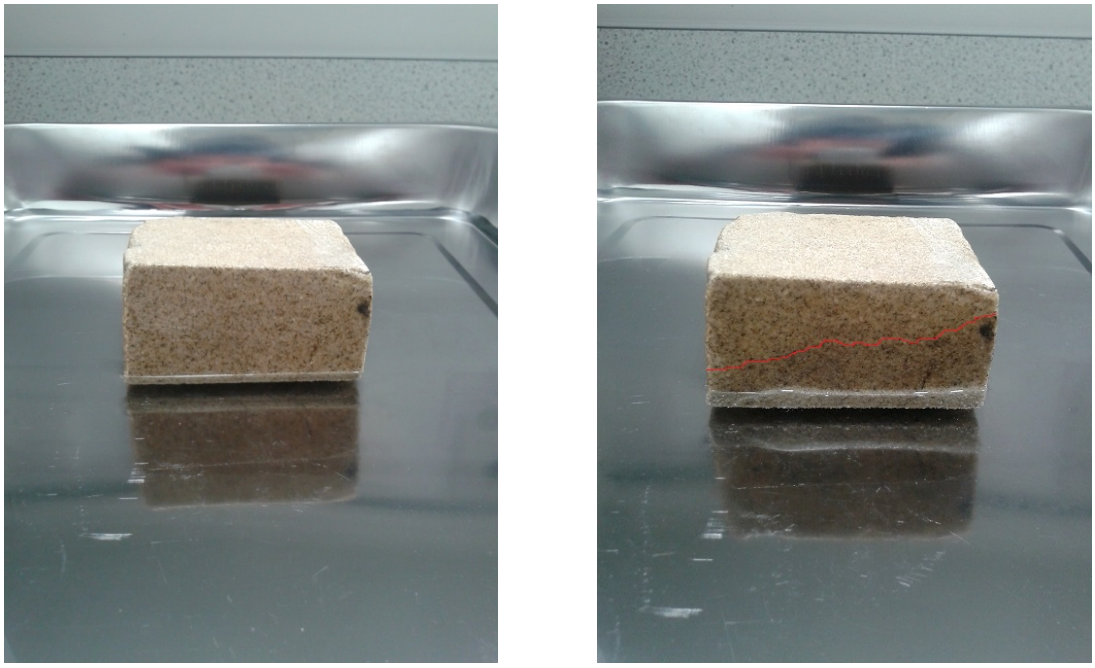

(a) (b)

Figure 5.17: Capillary rise test on a square block sample of Stanton Moor (a). The water front after 1h of testing is highlighted with a red line (b).

Results of the test show that when water is in contact with the sandstone it penetrates a few centimetres below the surface within the first few hours of the test, however, c. 16 hours are needed before capillary saturation is reached (degree of saturation = 90 %) in this block of $5.5 \times 5.5 \times 3 cm^3$. The capillary rise coefficient (European standard EN1925) represents the initial amount of water absorbed per square meter as a function of the square root of time. Results of the test show this coefficient is: 1.2 ($kg \times m^{-2} \times h^{-1/2}$).

The stone sorptivity was found to be 0.163 ($mm/min^{1/2}$). This value is low but

comparable to other sandstones, according to the table of Christopher Hall and William D Hoff (2009). For instance Baumberger sandstone shows a sorptivity of 0.32 ($mm/min^{1/2}$) while Sander sansdstone has a sorptivity of 0.16 ($mm/min^{1/2}$) [47]. However, these tests measure the properties of the stone only and not how the stone would behave under realistic conditions of driving rain and variable evaporation rate. Further work should be undertaken to determine how much water is accessing different elevations of the buildings, including how far water is absorbed into the walls. This can be done using numerical modelling coupled with environmental data analysis.

hygric-swelling test

A hygric swelling test was carried out to assess the hydro-mechanical behavior of the stone and to evaluate its swelling response to water absorption. The test was conducted on Stanton Moor sandstone and on Savonnieres limestone for comparison. Stanton Moor is a fine-grained sublithic sandstone with a matrix of clay minerals and low porosity and sorptivity. Its open porosity (measured by vacuum saturation) is 13 % and its sorptivity is 0.163 $mm/min^{1/2}$. The clay minerals contained within the matrix are kaolinite and chlorite. While neither mineral is considered a swelling clay, such as bentonite, they can react with water. Savonnieres is an oolitic limestone consisting of a calcium carbonate matrix and calcitic granules of diverse origin. Porosity is 22 % and sorptivity is higher than Stanton Moor, measuring 0.30 $mm/min^{1/2}$. This means that water travels faster through Savonnieres limestone than through Stanton Moor sandstone. Savonnieres contains no clay minerals, which is why it has been used for comparison.

The swelling test on a Stanton Moor sample was conducted by leaving a dried cylindrical sample in the chamber which was submerged in deionized water at 20°C for one week. The same test was conducted on a sample of the same size of Savonnieres limestone for comparison. Each cylinder has a diameter of 2.5 cm and is 5 cm long (Fig.5.18).

A schematic drawing of the test procedure is shown in figure 5.19. Results for Savonnieres limestone and Stanton Moor are shown respectively in figure 5.20 and 5.21.

In the 7 day test, Savonnieres limestone expands by less than 5 microns, as the mineral constituents of the limestone are not susceptible to swelling. The graph shows the sample responds to thermal oscillations as expected. However, the Stanton Moor

Figure 5.18: Cylinder of Stanton Moor tested for this work.

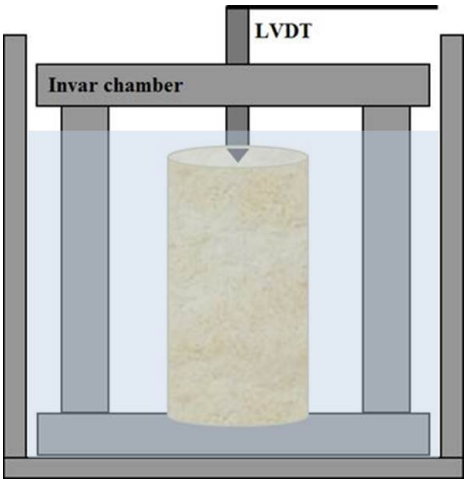

Figure 5.19: Schematic drawing of the swelling test.

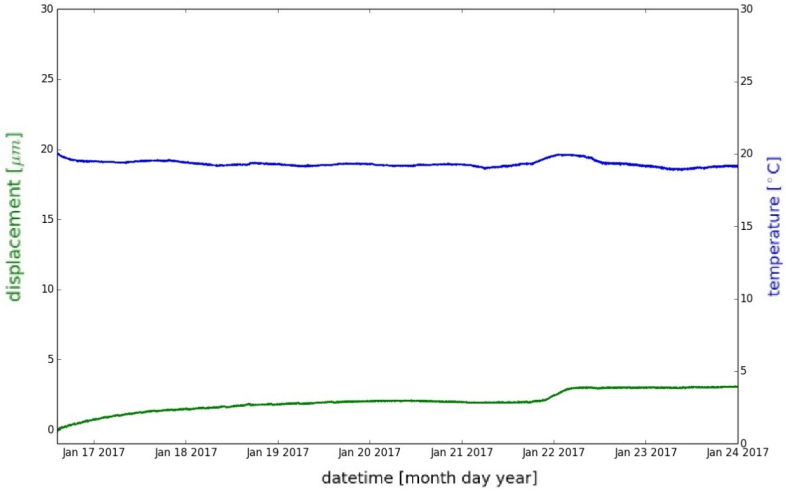

Figure 5.20: The plot shows the sample linear displacement (green) and temperature of the water (blue) during 7 days of test for Savonnieres limestone.

sample undergoes an initial contraction of c. 2 microns within the first hours of the test and then a rapid expansion of more than 8 microns in the three days of test. The

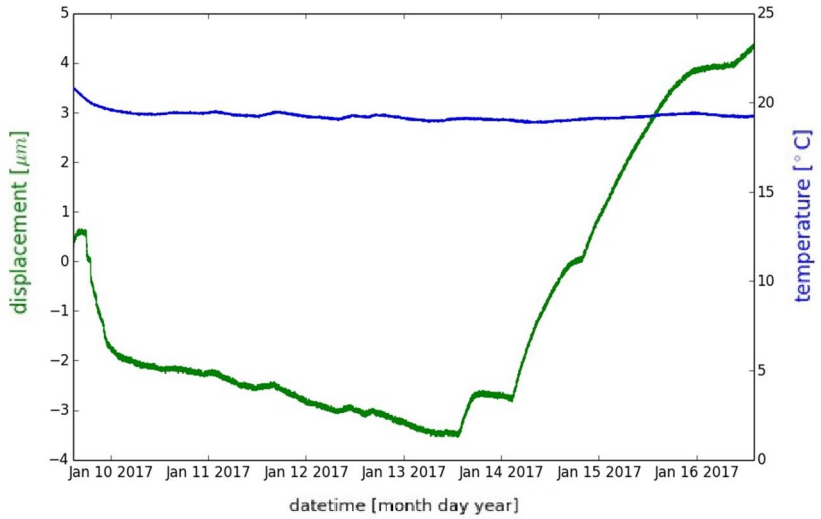

Figure 5.21: The plot shows the sample linear displacement (green) and temperature of the water (blue) during 7 days of test for Stanton Moor sandstone.

initial contraction can be explained by the sample being dried at 105°C before being placed in the chamber. High temperatures cause a slight expansion of the clay structure and, therefore, the sample undergoes a contraction when placed again at ambient temperature [8]. When the structure is back to its original dimension the sample starts expanding due to water adsorption by the clay minerals. The same test was repeated on a sample of Stanton Moor which was not previously oven dried, for comparison. Results of this second is shown in figures below (Fig.5.22).

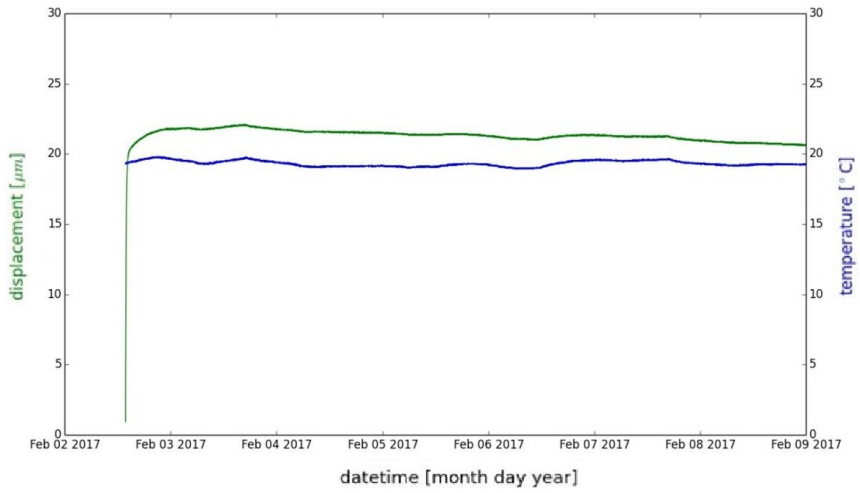

Figure 5.22: The plot shows the linear displacement of a cylindrical sample of Stanton Moor sandstone which had not been pre-heated by drying in an air oven prior to testing.

Results of this second test show that the sample starts immediately to expand, without

showing any previous contraction. The final expansion value, c. 23 microns, is reached quickly within the first 3 hours of test and it is considerably higher than that recorded for Savonnieres limestone (c. 3 microns). Displacement results for both stone types are shown together for comparison in figures 5.23 and 5.24.

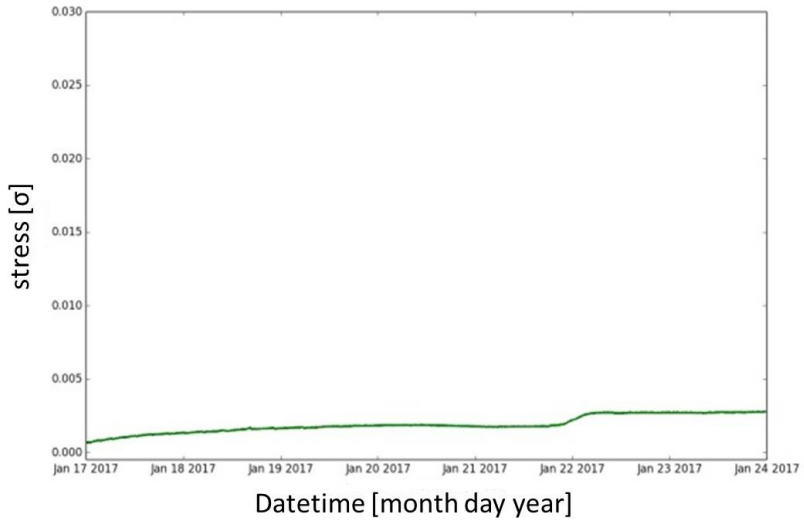

Figure 5.23: Graphs show sample displacement from wetting. Savonnieres limestone during 7 days of testing.

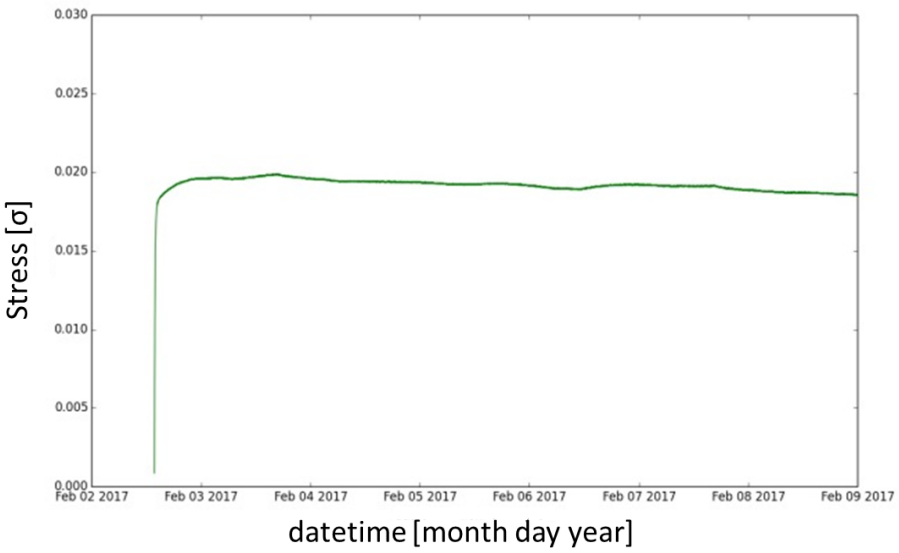

Figure 5.24: Graphs show sample displacement from wetting. Stanton Moor during 7 days of testing.

After 7 days of test an axial swelling stress of c. 2.53 MPa was calculated from the strain values for the Savonnieres limestone while an axial swelling stress of c. 17.5 MPa

was calculated for the Stanton Moor sandstone. The Stanton moor sample expanded by c. 0.046 % while the Savonnieres sample expanded by c. 0.006 %. The Stanton Moor sample started immediately to absorb water and within the end of the first day of test it had already reached its maximum linear expansion (c. 23 μm of linear displacement), then it remained stable for the remaining 6 days. The Savonnieres sample, on the contrary, gradually increases its volume for the first 5 days of test, reaching a maximum linear displacement of c. 3 μm, then remaining stable for other 2 days. Results of the hygric-swelling test show that the presence of clays, even clays regarded as non-swelling, can significantly affect the hydro-mechanical behavior of the sandstone, promoting its rapid expansion. Future work will focus on analysis of more samples for statistical analysis and clarification.

5.3.2 Outer masonry

In this section we present the results of the same investigation conducted on samples of the green sandstone constituting the entire outer masonry of the building. This kind of sandstone was suffering the effects of a clear on-going deterioration process at the time of our visit, and it has never been investigated and characterised before.

X-Ray powder diffraction analysis

The main constituents of the sample are quartz, feldspar, micas (muscovite) and clay minerals (chlorite). This sandstone is a quartz-rich sandstone with a c.10 % of chlorite content (see Table 5.4), which is responsible for the green colour of the fresh sandstone. In the tested sample only a small amount of solid salt was detected, hence salt crystallisation is unlikely to be the main cause of deterioration for this sandstone. The chlorite presence suggests damage from swelling/contraction, but further work is necessary to clarify this. This kind of mechanism is often responsible for the flaking process in sandstone facades which produces scales or flakes that are up to several centimetres long and detach from the underlying healthy stone [104]. This process is evident in the whole facade (Fig.5.25) where it is also common to find areas where an entire layer is lost.
The average mineral content within the samples calculated with TOPAS are listed in Table 5.4. The XRD pattern of sample SM3 is given in APPENDIX B.

(a) (b)

Figure 5.25: Image of the outside masonry beside the Lancet Windows (a) and detail of the advanced flaking process in the green sandstone (b).

Table 5.4: Average mineral content (% wt) for the green sandstone sample.

Sample ID	Quartz	Feldspars	Mica	Clay minerals	Carbonates	Gypsum	Halite	Thenardite	Mullite	Hematite
SM3	46.92	24.92	15.14	10.22	2.66	N/A	0.13	N/A	N/A	N/A

Soluble salt analysis (ICP-OES and IC)

Sample powder was leached in deionised water and then filtered and analysed using the ICP-OES and IC to determine the cation and anion species present in each sample. Results of the analysis (Fig.5.26) show chloride is present, probably from seaspray, but the actual ppm value is low.

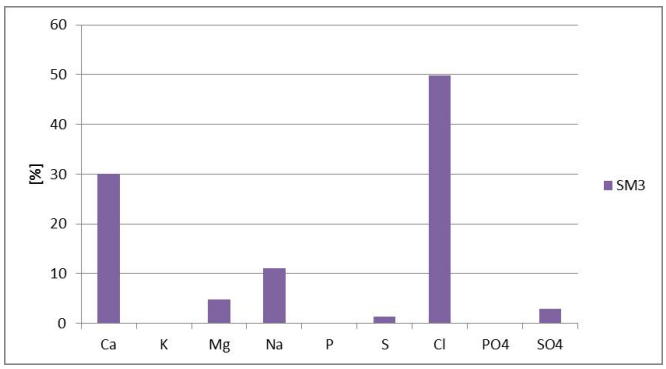

Figure 5.26: The graph shows the amount of each ion present (in ppm) as a percentage of the total composition of the leached aqueous sample (y-axis) against the ion (x-axis).

Calcium levels are elevated, most likely leached from surrounding mortar and transported to the drying front at the stone surface. However sulphate levels are low, indicating sulphate salt formation is unlikely.

Thin section analysis

Detached flakes were used to make thin sections for petrographic analysis. The fresh sandstone shows a homogeneous grain size and a well cemented fabric. The colour is variable from green to light blue. The weathered sample shows a dark grey or light brown colour, with a slightly dusty appearance (Fig.5.27).

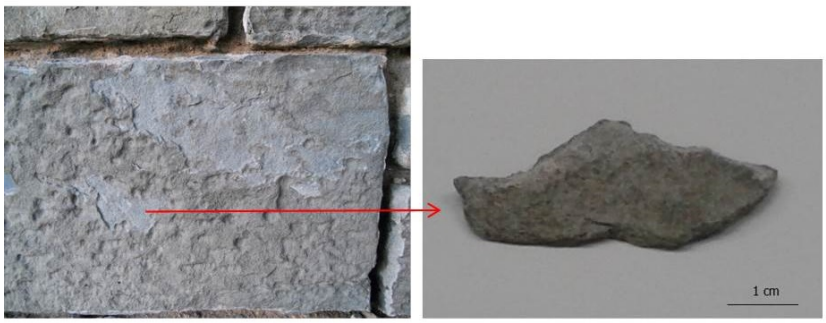

Figure 5.27: Image of the sampling area (left), and sample SM3 (right).

Overall this is a greenish-buff sandstone with a siliceous (quartz-rich) composition with a high percentage of feldspars. It is fine to very-fine grained and contains a good amount of clay minerals (e.g. chlorite c.15%) and feldspar (Figures 5.28 and 5.29).

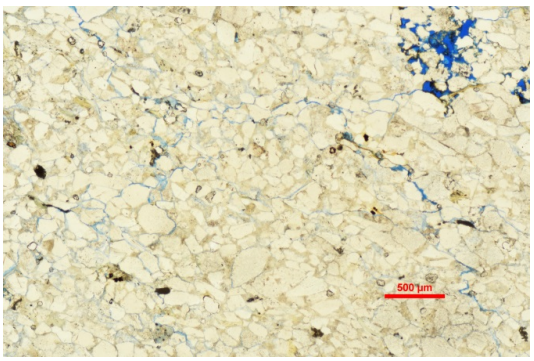

Figure 5.28: Thin section photographs of sample SM3, Nicols //. White grains are mainly quartz, with a very small proportion of feldspar and some micas. Black patches are iron oxide and opaque minerals. Pore space appears blue.

The concave-convex granular contacts and a preferential orientation of the micas reveal a high lithogenic pressure solution which entails a low permeability. However, the presence of small fractures increases the permeability and is indicative of ongoing weathering. The fractures, which appear to follow the preferential orientation of the micas in the sample (Fig.5.30), show how the material begins to fracture along these bands.

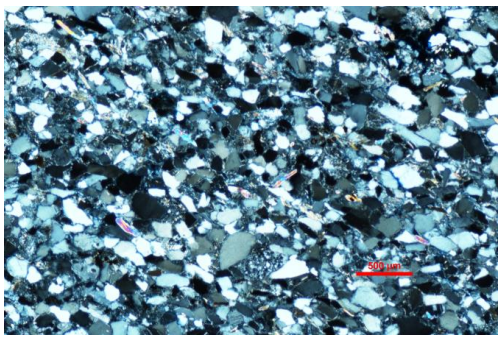

Figure 5.29: Thin section photographs of sample SM3, Nicols +. White grains are mainly quartz, with a very small proportion of feldspar and some micas. Black patches are iron oxide and opaque minerals. Pore space appears blue.

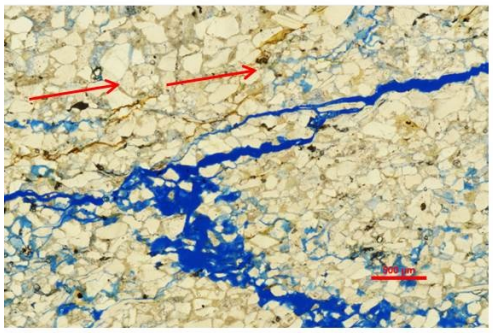

Figure 5.30: Thin section photograph of sample SM4. The image was taken in plane polarised transmitted light. Highlighted by a red arrow is the preferential orientation of micas.

When present, chlorite undergoes hygric expansion and salt water can increase the expansion and exacerbate the process [104].

5.3.3 Clock Tower

In this section we present the results of the same investigation conducted on samples of bricks and render from the inside of the clock tower. Both materials showed clear signs of weathering at the time of our visit, marked by the presence of efflorescence, crusts and detachments surrounding the windows of the clock tower.

X-Ray powder diffraction analysis

Three samples from the clock tower were analysed: A sample of the exposed brick masonry, a sample of the salt found above the brick surface and a sample of the mortar at the clock window joints, as shown in figure 5.31.

The main constituents of the brick sample: quartz, feldspar, micas (muscovite), hematite, calcite and thenardite. The main constituent of the salt sample: thenardite with

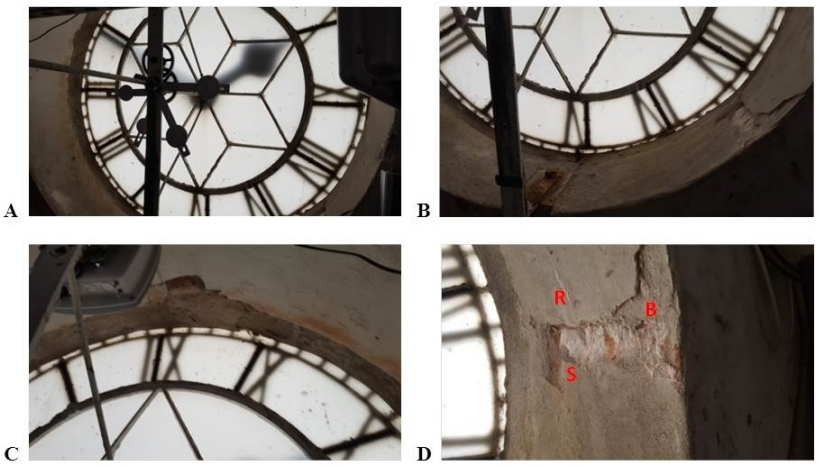

Figure 5.31: A) View of the west clock's window from inside of the tower. B) Detail of deterioration on the inner surrounds. C) Plaster detachment at the upper surrounds. D) Detail of the render (R) and salt crystallisation (S) on the bricks surface (B) below the plaster.

minor calcite and gypsum, as expected from the results of the XRD for the sample of brick. The main constituents of the mortar sample: quartz, feldspar, micas (muscovite and biotite), calcite and gypsum. The average mineral content within the sample calculated using TOPAS are listed in Table 5.5.

Table 5.5: Average mineral content (% wt) for all the Clock Tower samples.

Sample ID	Quartz	Feldspars	Mica	Clay minerals	Carbonates	Gypsum	Halite	Thenardite	Mullite	Hematite
Brick	59.51	3.66	N/A	N/A	17.30	N/A	3.68	N/A	4.96	10.89
Salt	10.59	0.04	8.08	N/A	6.48	N/A	N/A	74.82	N/A	N/A
Mortar	45.14	5.93	14.57	0.09	23.91	6.99	N/A	N/A	N/A	N/A

The high concentration of thenardite (sodium sulphate) is unusual. Clearly this is the main salt causing deterioration and is known to be one of the most aggressive salts able to damage porous materials. Traces of hydro-glauberite were also found in the sample named *Salt*. This is a sodium-calcium-sulphate-hydrate which forms from solutions of thenardite and gypsum. Calcite most likely comes from the mortar joints between the bricks or has been leached from the cement render although further analysis would be required to confirm. The presence of sulphate, which is required to form the destructive sodium sulphate salt, could come from the brick itself, calcium sulphate plaster (if used) or historic atmospheric pollution, which is less likely. Further field work and analysis would be required to determine the source and spread of sulphate within the structure. All the XRD patterns related to the samples from the Clock Tower are listed in APPENDIX B.

Soluble salts analysis (ICP-OES and IC)

Sample powder was leached in deionised water and then filtered and analysed using ICP-OES and IC to determine the cation and anion species present in each sample. Results of the analysis (Fig.5.32) show a significant percentage of sulphate (SO_4), in particular in the brick sample. Chloride, which is detected in the solid phase (halite, $NaCl$) in the brick sample, is detected by ion analysis as being present in the pore structure. Sea water is a contributing factor, but the the presence of thenardite is more likely to cause deterioration.

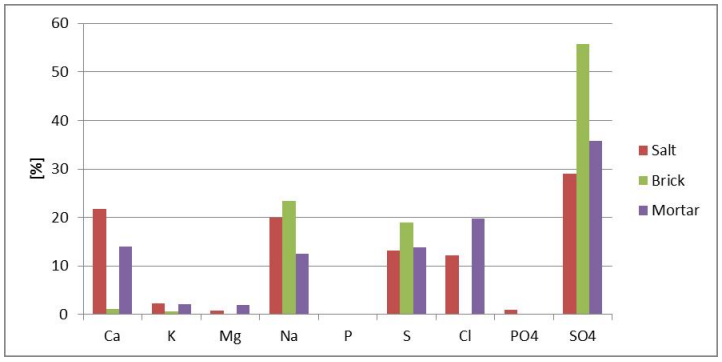

Figure 5.32: The graph shows the amount of each ion present (in ppm) as a percentage of the total composition of the leached aqueous sample (y-axis) against the ion (x-axis).

Thin section analysis

From the brick masonry and the mortar of the building clock tower small fragments were taken for the thin section analysis. They both come from the clock surround on the inside of the tower at the west elevation. Inside the tower, all the bricks at the window surrounds are covered with a plaster render. The mortar layer is at the windows joins. The mortar sample is a small fragment which spontaneously detached from the window joint while the brick sample was being gently removed from the surface and which was covered in salt. The plaster render on the top of the bricks was heavily fractured. The sample of brick appears to have an un-weathered core, while the mortar fragment is very friable. A summary of the conclusion that can be drawn from thin section analysis is presented below, while detailed analysis for each thin section can be found in APPENDIX A. Analysis shows that the main problem at the clock tower is grain de-cohesion of both the mortar at the clock window and at the plaster layer on

the brick work. Water entering from the clock windows seriously damages the mortar by leaching away the calcite-based binder producing granular de-cohesion which is particularly evident in thin section (Fig.5.33). As shown in figure 5.33, the blue pore space from resin impregnation illustrates that there is barely any cementing phase left in the material and grains are almost entirely disconnected.

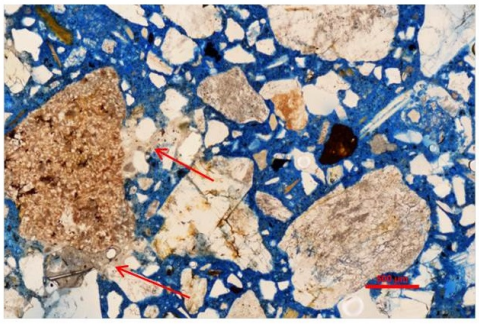

Figure 5.33: Thin section photograph of the mortar surrounding the clock. The image was taken in plane-polarised transmitted light. Grains are mainly quartz, feldspar, micas and rock fragments. Highlighted by red arrows are parts of the remaining lime binder of the mortar.

Calcite-based binder can be transported to the surface providing a source of calcium to form calcium sulphate dihydrate (gypsum). Where the sulphate comes from requires further investigation. Both the lime render above the bricks and the bricks also show a high content of calcite. Bricks in particular, present a re-precipitation of micritic calcite inside the pores at the surface. The porosity and permeability of the brick appear low, as determined from the thin section image (Fig.5.34), although not enough material was available for quantitative water transport testing.

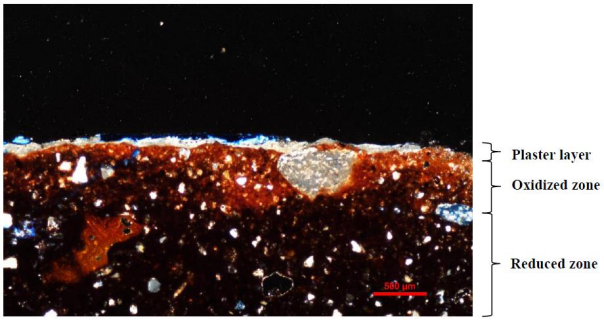

Figure 5.34: Thin section photograph of a sample of brick from the clock tower. Micritic calcite re-precipitated within the pores is highlighted with a red circle.

From observation, damage to the bricks appeared to involve only the surface which shows the presence of salt efflorescence (Fig.5.35) and has progressively promoted the

disintegration of the plaster layer above the bricks. However the mortar is almost completely disaggregated.

Figure 5.35: Efflorescence progressively fracturing the plaster render. Clock Tower window, west elevation.

5.4 Discussion

Based upon the analysis and laboratory experiments done on the different samples of Lerwick Town Hall, it can be concluded that there are 2 main deterioration mechanisms present: clay swelling and salt crystallisation damage from sodium sulphate. Swelling tests reveal that the clay content promotes expansion. Comparison is made with 1 other sedimentary rock, which is known to be devoid of clays but a fuller investigation of the quantitative effects of swelling would benefit from further work. Results of the water transport test show that moisture is retained by the sandstone at its most superficial depth, where stone is then subjected to salt crystallisation and clay swelling, and when combined, results in a progressive detachment of the grain to grain contacts. Weathering is then accelerated once the quartz-grain contact and cementing clays are dissolved as the porosity and permeability of the stone increases. The results of this mechanism are particularly evident in thin section images. Stone porosity and permeability play a fundamental role in the weathering mechanism, as they are responsible for the transport of water and salt. The low porosity and permeability of Stanton Moor sandstone can prevent initial significant uptake of salt solutions from sea-spray. However, the presence of clay minerals can facilitate the penetration of salt solutions via crack formation. The limited capillary transfer and slow water vapour transport will retard solution transport within the stone prior to weathering. Therefore, evaporation and subsequent salt crystallisation will take place at or just below the stone surface. Salt content in the stone samples taken was scattered. XRD, IC & ICP-OES analysis confirmed the

presence of gypsum and thenardite as the main salt phases present. Where the sulphate comes from requires investigation. The sandstone grain sizes and distribution also play a role in its deterioration, affecting its permeability, porosity and water transport. Stanton Moor is composed of mostly fine sand particles and silt that can become easily dislodged as a result of clay swelling behavior, and thus become transportable when in contact with water. A similar conclusion can be drawn regarding the deterioration mechanism of the green sandstone at the outer masonry of the building. The chlorite content plays a key role in the flaking mechanism of the stone. The low porosity and permeability evaluated via thin section analysis significantly reduces the salt solution transport,although solid halite was detected by XRD on SM3, it may have been at the surface of the stone. In both Stanton Moor sandstone and in the green sandstone the clay minerals swelling may be enhanced by the presence of chlorides-bearing water. Halite, in particular, plays a fundamental role when kept in solution by acting as an electrolyte in osmotic swelling processes [104]. Analysis conducted on the bricks and mortar of the clock tower revealed that the deteriorated conditions are probably mainly due to salt crystallisation. In particular, the lime mortar at the clock windows and the render layer covering the brick masonry were very friable, and the presence of sodium sulphate (thenardite) was present as both efflorescence (XRD) and subflorescence in the brick (ICP-OES, IC). The mortar around the clock tower windows was particularly friable due to the significant dissolution of the lime binder. Forster et al. pointed out that the lime binder components vulnerable to dissolution are mainly portlandite (calcium hydroxide, $\mathrm{Ca}(OH)_2$ and calcite (calcium carbonate, $CaCO_3$) [8]. It is difficult to determine the hydraulicity of the original binder without further sampling. However both portlandite and calcite dissolution will be enhanced in saturated, cold conditions because the solubility of both $\mathrm{Ca}(OH)_2$ and $CaCO_3$ increases as water temperature decreases [36].

Conservation strategy and recommendations

Currently the main form of repair at Lerwick Town Hall is the total replacement of stone. However, in order to promote the maintenance of the original stone, preventative treatments are advised to reduce the amount of replacement in the future. To

arrest or slow the sandstone deterioration mechanism, several recommendations are suggested below: those include pre-consolidation and consolidation treatments. 1. Pre-consolidation with barium hydroxide: according to the Ferroni-Dini two-step method, gypsum is first transformed with a solution of ammonium carbonate that converts the gypsum into calcium carbonate and soluble ammonium sulphate. In a subsequent treatment with a barium hydroxide solution, the ammonium sulphate is converted to barium sulphate, which is an inert and insoluble substance. In this way, existing sulfation is arrested. This method can be used to desulphate walls and surfaces affected by sodium sulphate and gypsum crystallization and to consolidate friable plasters and mortars [4].
2. Pre-consolidation with an anti-swelling agent in the clay-rich sandstones. A good anti-swelling agent can bind clays and decrease swelling without altering the materials properties, such as absorption and porosity [89].
3. Consolidation with ethyl silicates. This kind of consolidation is often used in clay-rich sandstone. Consolidating products act by depositing a silica gel as a binder into deteriorated stonework, which replaces the original binder, partially lost from weathering. By using elastified silicate-esters, which are not water repellent, it is possible to obtain an increase of the Young's Modulus of the sandstone, decreasing the impact of clay swelling [103].
4. Surface treatment with crystal growth inhibitors. Borax and ferrocyanide have been identified as possible crystal growth inhibitors for sodium sulphate and sodium chloride respectively. The presence of borax appeared to have no influence on the supersaturation ratio of the salt solution but it significantly affects the crystallization pattern of thenardite [44]. Ferrocyanide ions have proved to promote crystallization of salt near the drying surface as nondestructive efflorescence rather than destructive subflorescence [46].

Regarding protective coatings and water repellent treatment, recent work shows that sodium chloride preferentially crystallizes on hydrophobic surfaces. This suggests that water repellent treatments are not compatible where salts may accumulate (Lubelli et al. 2007) [103]. Based on climate data from the Meteorological Office related to the year 2015-2016 [79], and the preliminary results of environmental monitoring carried out by Rob Thomson it is possible to state that the diffusion of salt efflorescence is more

sensitive to fluctuations in RH than temperature as temperature variation in Lerwick is minimal.

Salts in masonry remain in solution at a characteristic deliquescence RH value (DRH). DRH value of thenardite is 84% (Tang and Munkelwitz, 1994), while gypsum has a DRH value of 99.9% (Siegesmund and Snethlage, 2014). When ambient RH values become higher than the DRH, salts particles dissolve to maintain equilibrium with the water vapour. If the RH values decreases below the DRH, the particles lose water and eventually crystallises (efflorescence) [128]. A long environmental monitoring of the RH values in the main hall and in the loft space of the building would be required to understand weather crystallisation is promoted.

5.5 Conclusions

Natural stone is widely recognised to be versatile, durable and aesthetically plausible building materials [21]. Most of the world's cultural heritage is made of natural stone, based on the local stone resources. Although highly durable no stone type can be considered immortal [101]. The recent tendency for deteriorated stones on monuments is the entire replacement by stone varieties of the same composition, preferably from the same quarries, or stone types having similar properties and appearance. However, the replacement practice involves high costs and requires an appropriate knowledge of the materials replaced and of the environmental chemical-physical parameters responsible for the deterioration of the building [7]. If not properly investigated and deeper understood, the mechanism of the deterioration of the original stone type will cause further damage to the new one, even in a shorter time, depending on the new material properties. In this specific case study all the recently replaced building materials show early signs of decay: Lerwick Town Hall, located in Lerwick (Shetlands Islands). Currently the main form of repair at Lerwick Town Hall is the total replacement of stone. The most effective conservation strategy for the building material would be a constant environmental monitoring, which data should be used to define a preventive conservation approach based on an indoor climate conditioning strategy as the internal relative humidity conditions will have a significant impact on how and where salts form. To ar-

rest or slow the sandstone deterioration mechanism we suggest some recommendations: those include pre-consolidation with barium hydroxide to desulphate walls [39] or with anti-swelling agent in the clay-rich sandstones, and consolidation treatments: by using elastified silicate-esters, which are not water repellent, it is possible to obtain an increase of the Young's Modulus of the sandstone, decreasing the impact of clay swelling [89]. Regarding protective coatings and water repellent treatment, recent work shows that sodium chloride preferentially crystallizes on hydrophobic surfaces. This suggests that water repellent treatments are not compatible where salts may accumulate [103].

Chapter 6

Conclusions

6.0.1 Summary of key findings

The PhD thesis aimed to investigate a new methodology to estimate speed of crystal growth and measure the strain produced by salt crystallisation and ice formation within stone cores.

A unique prototype of a thermostated chamber was developed and used for conducting novel experiments on crystal growth and related strain developed. During this stage I faced the issues and the complications arisen from using an LVDT in a Peltier driven cooling system. The LVDT proved to be extremely sensitive to external magnetic fields which produced a variable drift in the output signal that could not be reliably quantified for adjustment of real sample data. This work also proved that the LVDT output signal can be affected by thermal variations. Eventually, these effects were successfully minimised to use the LVDT simultaneously with a thermocouple system in a thermostated chamber custom-designed to conduct novel experiments on crystal growth.

Those experiments are the first to measure the rate of salt crystal growth through a porous core and assess the damage caused at the same time. Tests were carried out using a standard building limestone and sandstone - Portland limestone and Berea sandstone. Results show that there is a correlation between crystal growth rate and the supersaturation at the point of nucleation: When supersaturation is increased at the point of mirabilite nucleation, both the growth rate and measured strain increase. Moreover, mirabilite crystal growth rate is c. 2.5 times slower through the core, compared with

free growth in solution. Strain data shows that the porous host is usually damaged by mirabilite precipitation, unless precipitataion occurs at higher temperatures (c. 24 °C) where the supersaturation is less, while ice forming at the eutectic point creates damage only in more fully saturated cores.

Crystal growth damages were investigated on an actual case study at Lerwick Town Hall (Lerwick, Shetland Islands), where all the recently replaced building materials show early signs of decay. This is in fact mainly due to the extremely wet condition of the environment and the constant fluctuation of internal relative humidity conditions, which have a significant impact on how and where salts form. Specific characteristics of the stone-type also plays a key role when investigating the damages. We concluded that salt crystallisation and possibly clay swelling were the mechanisms most likley responsible for damage.

For the thesis work it was also carried out a 3D investigation using the X-CT to assess salt distribution within samples subjected to salt weathering test through two different methodologies. With the first methodology we assessed changing in pore space due to crystals formation hence detecting where de-icing salts tend to distribute throughout the matrix after repeated crystallisation cycles. Results suggest that different salts tend to occupy different areas of the same stone-type. Sodium chloride tends to obstruct the immediate outer surface of the sample without considerably affect the inner structure. Calcium chloride, appears to only slightly occupy the outer surface and developing crystallisation fronts. Magnesium chloride appears to be the more pervasive salt tested and tends to occupy scattered areas within the samples. None of the sample cyclically tested was considerably damaged by the test. This also proved salt crystallisation tests performed in accordance with British standard BS EN12370.1999 are not really effective in terms of deterioration when performed with a different salt with respect to the one suggested (i.e. mirabilite).

With a second methodology, the specific grey value related to salt efflorescence was used as a reference to investigate salt distribution through the pore matrix. Results of the XCT investigation show thenardite distribution varies with structural features in the sample, such as bedding planes at different porosity that can accommodate higher percentage of salts.

6.0.2 Future work

Results of the experiments conducted with the thermostated chamber proved that we can definitively correlate crystal growth rate with the supersaturation at the point of nucleation but the physical relationship between the two requires further investigation. Moreover, the effect of pore size distribution on crystal growth rate requires deeper understanding and a further investigation will be carry out by using both MIP and Nitrogen BET techniques. Preliminary results of the study conducted with the X-CT can be an encouraging base to define an experimental procedure aiming to reach a more accurate quantitative evaluation of the porosity reduction and correlate the damage caused by salt crystallisation to specific sample features. Future work will also aim to investigate crystal growth rate in real time using the synchrotron-XCT, as the laboratory X-CT cannot capture images fast enough to 'see' crystal growing. Through these real time experiment it would be possible to investigate the way and the directions taken by the liquid pushed away by growing crystals at the crystallisation front. Finally, future works will focus on determining the real concentration of the solution at the crystallisation front.

Chapter 7

Appendix A

7.1 Chapter 3: Thin sections forms

SAMPLE SH1

Hand specimen observations

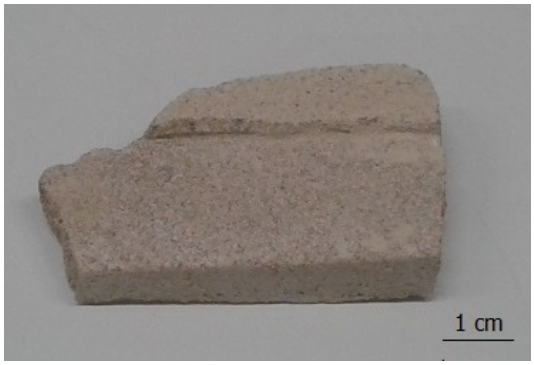

The sample is a light creamy buff colour, which presents a greyish buff on the exterior and exposed surface.The hand specimen appears strongly cohesive with a quite uniform fabric.

Thin section observations

Stone constituents:

Granular (detrital) constituents	Intergranular constituents
Quartz 40%	Silica (overgrowth) 0%
Feldspar 15%	Feldspar (overgrowth) >3%
Mica 8%	Iron/manganese oxide 4%
Opaque material 9%	Clay 10%
Other «1%	Carbonate 0%
Intragranular pores 10%	Intergranular pores 1%

Stone type (detailed classification): sublithic-arenite Grain-size: fine-sand-grade to

medium-sand-grade Grain sorting: well sorted Grain roundness: angular to subangular Stone permeability: low Cement distribution: quartz cement, iron oxides and clay minerals Supergene changes: pressure solution of feldspar and moderate dissolution of quartz and feldspar; moderate substitution of feldspars.

Comments:

1) Quartz and feldspar often show concave-convex contacts, which indicate a high pressure solution, entailing a low level of intra-granular porosity (7.1.

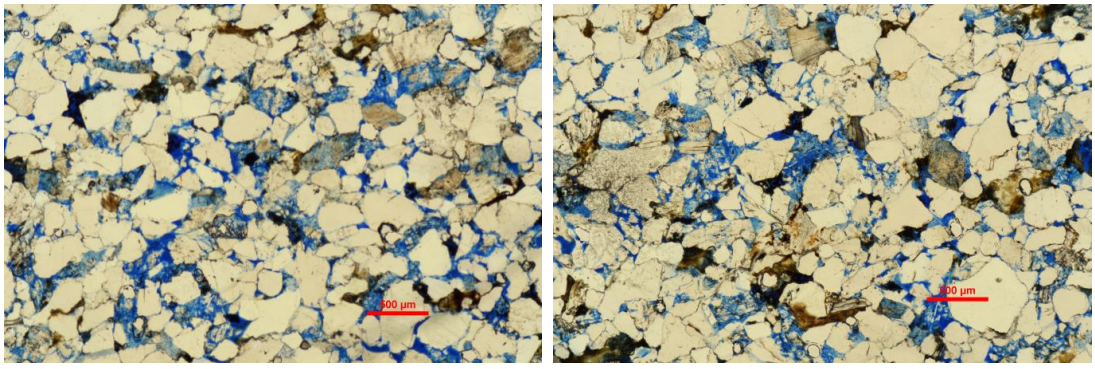

(a) (b)

Figure 7.1: Thin section photographs of sample SH1. The images were taken in plane-polarised transmitted light. White grains are mainly quartz, with a smaller proportion of feldspar and micas. Black patches are iron oxide and opaque minerals. Pore space appears blue.

2) Several feldspars have undergone pseudomorphic replacement by clay minerals. Some of them show characteristic Carlsbad twinning.

3) Micas often show a kink shape, or signs of alteration at the granular contacts. These aspects confirm the supergene changes highlighted (7.2.

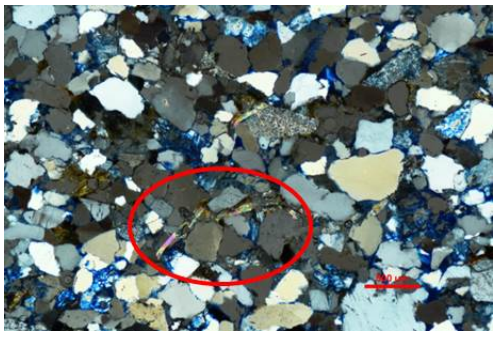

(a)

Figure 7.2: Thin section photograph of sample SH1. The image was taken in plane-polarised transmitted light. Highlighted by a red circle is a kinked muscovite mica.

SAMPLE SH3

Hand specimen observations

The sample appears very dusty and friable, and shows a white buff on the whole surface. The whole surface of the sample is significantly weathered.

Thin section observations

Stone constituents:

Granular (detrital) constituents	Intergranular constituents
Quartz 48%	Silica (overgrowth) 0%
Feldspar 7%	Feldspar (overgrowth) >3%
Mica 6%	Iron/manganese oxide 4%
Opaque material 5%	Clay 6%
Other «2%	Carbonate 0%
Intragranular pores 20%	Intergranular pores 1%

Stone type (detailed classification): sublithic-arenite Grain-size: fine-sand-grade to medium-sand-grade Grain sorting: well sorted Grain roundness: angular to subangular Stone permeability: high Cement distribution: quartz cement, Iron oxides and clay minerals Supergene changes: pressure solution of feldspar and moderate dissolution of quartz and feldspar; moderate substitution of feldspars.

Comments:

1) Quartz and feldspar, which in the un-weathered stone (SH1) often show concave-convex contact, are now clearly detached, with a significant increase in intergranular porosity and the permeability (7.3).

2) It is possible to see a general decrease in opaque material and kinked micas (Muscovite) (7.4).

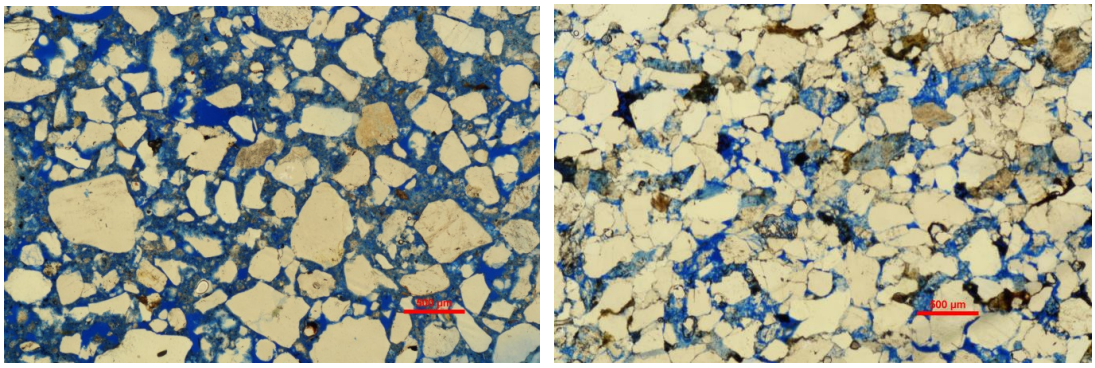

(a) (b)

Figure 7.3: Thin section photographs of sample SH3 on the left and SH1 on the right. The images were taken in plane-polarised transmitted light. White grains are mainly quartz, with a smaller proportion of feldspar and micas. Black patches are iron oxide and opaque minerals. Pore space appears blue.

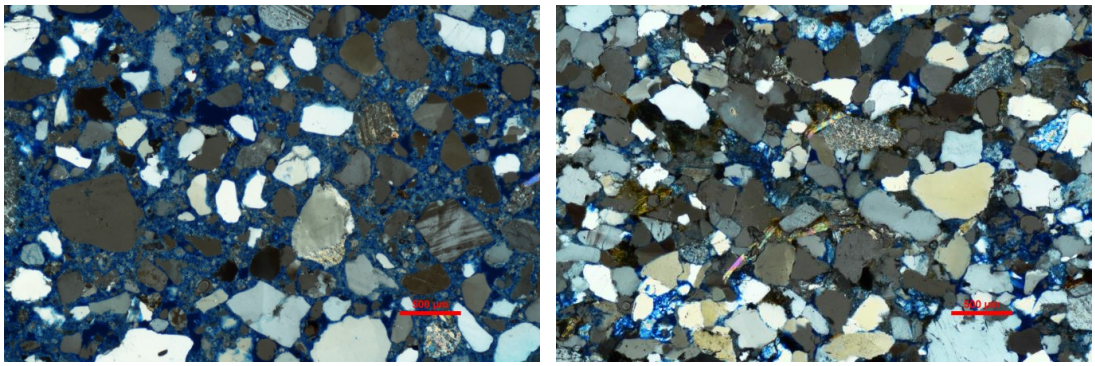

(a) (b)

Figure 7.4: Thin section photographs (crossed nicols) of sample SH3 on the left and SH1 on the right. Pore space appears blue.

3) Several feldspars have undergone a pseudomorphic replacement with clay minerals and micas (biotite and muscovite) (7.5)

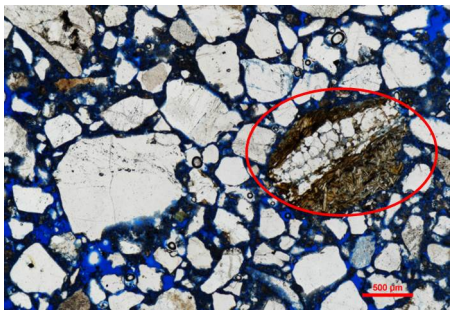

(a)

Figure 7.5: Figure 2: Thin section photograph of sample SH3. The image was taken in plane-polarised transmitted light. Highlighted by a red circle is a pseudomorphic replacement of a feldspar with a biotite.

SAMPLE SH6

Hand specimen observations

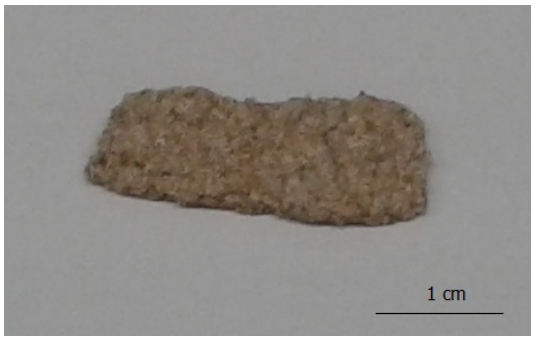

The sample is a dark creamy buff colour, different from the colour of the fresh sample (SH1). At a first look the fabric appears more strongly cohesive with respect to sample SH3.

Thin section observations

Stone constituents:

Granular (detrital) constituents	Intergranular constituents
Quartz 48%	Silica (overgrowth) 0%
Feldspar 10%	Feldspar (overgrowth) >3%
Mica 8%	Iron/manganese oxide 4%
Opaque material 9%	Clay 6%
Other «1%	Carbonate 0%
Intragranular pores 10%	Intergranular pores 1%

Stone type (detailed classification): sublithic-arenite Grain-size: fine-sand-grade to medium-sand-grade Grain sorting: well sorted Grain roundness: angular to subangular Stone permeability: medium-low Cement distribution: quartz cement, iron oxides and clay minerals Supergene changes: pressure solution of feldspar and moderate dissolution of quartz and feldspar; moderate substitution of feldspars.

Comments:

1) Quartz and feldspar show the same concave-convex contacts with respect to the fresh stone (SH1). However it is possible to see a slightly higher level of intergranular porosity, suggesting similar permeability (7.6).

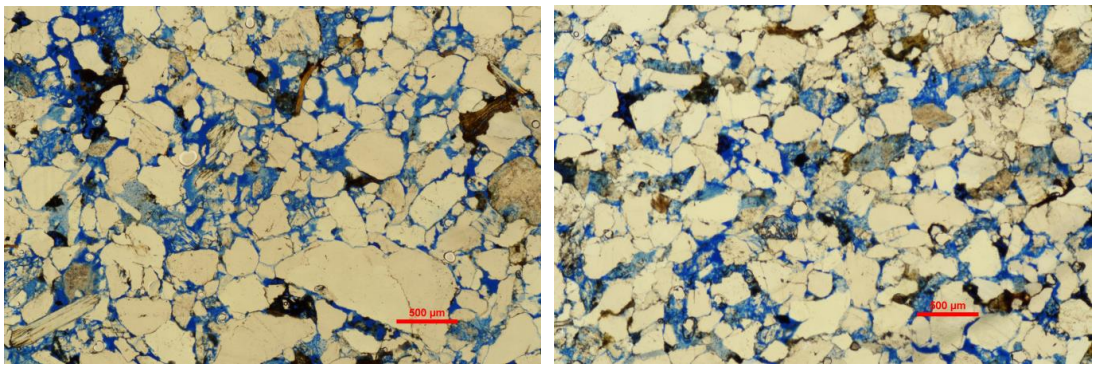

(a) (b)

Figure 7.6: Thin section photographs of sample SH6 on the left and SH1 on the right. The images were taken in plane-polarised transmitted light. White grains are mainly quartz, with a smaller proportion of feldspar and micas. Black patches are iron oxide and opaque minerals. Pore space appears blue.

SAMPLE SH7

Hand specimen observations

The sample is a dark creamy buff colour, which is different from the colour of the fresh sample (SH1) and very similar to sample SH6. At a first look the fabric appears more strongly cohesive with respect to sample SH3.

Thin section observations

Stone constituents:

Granular (detrital) constituents	Intergranular constituents
Quartz 45%	Silica (overgrowth) 0%
Feldspar 15%	Feldspar (overgrowth) >3%
Mica 8%	Iron/manganese oxide 4%
Opaque material 8%	Clay 5%
Other «1%	Carbonate 0%
Intragranular pores 10%	Intergranular pores 1%

Stone type (detailed classification): sublithic-arenite Grain-size: fine-sand-grade to medium-sand-grade Grain sorting: well sorted Grain roundness: angular to subangular Stone permeability: medium-low Cement distribution: quartz cement, iron oxides and clay minerals Supergene changes: pressure solution of feldspar and moderate dissolution of quartz and feldspar; moderate substitution of feldspars.

Comments:

1) Quartz and feldspar show the same concave-convex contacts with respect to the fresh stone (SH1). Moreover, the intergranular porosity is definitively similar with respect to sample SH1, suggesting similar permeability (7.7).

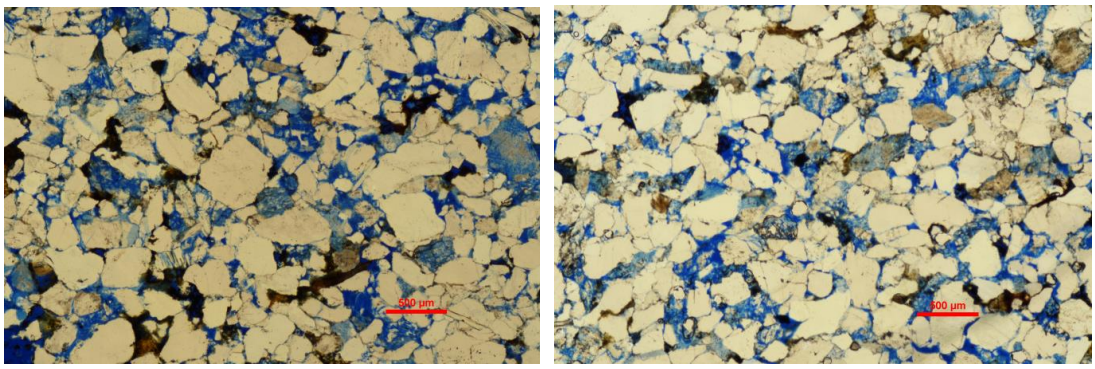

(a) (b)

Figure 7.7: Thin section photographs of sample SH7 on the left and SH1 on the right. The images were taken in plane-polarised transmitted light. White grains are mainly quartz, with a smaller proportion of feldspar and micas. Black patches are iron oxide and opaque minerals. Pore space appears blue.

SAMPLE SH9

Hand specimen observations

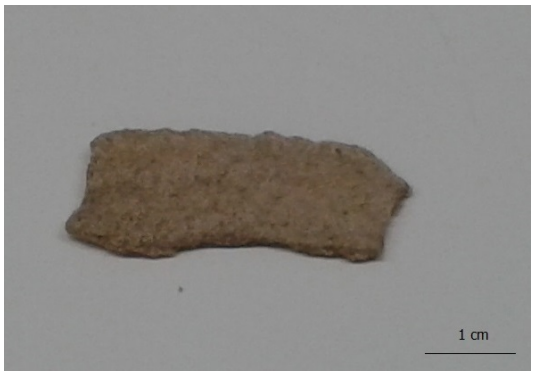

The sample is a medium dark creamy buff colour, which is different from the colour of the fresh sample (SH1) and comparable to samples SH6 and SH7. At a first look the fabric appears more strongly cohesive with respect to the sample SH3.

Thin section observations

Stone constituents:

Granular (detrital) constituents	Intergranular constituents
Quartz 50%	Silica (overgrowth) 0%
Feldspar 16%	Feldspar (overgrowth) >3%
Mica 9%	Iron/manganese oxide 6%
Opaque material 8%	Clay 8%
Other «1%	Carbonate 0%
Intragranular pores 10%	Intergranular pores 1%

Stone type (detailed classification): sublithic-arenite Grain-size: fine-sand-grade to medium-sand-grade Grain sorting: very well sorted Grain roundness: angular to subangular Stone permeability: medium-low Cement distribution: quartz cement, iron oxides and clay minerals Supergene changes: pressure solution of feldspar and moderate dissolution of quartz and feldspar; moderate substitution of feldspars.

Comments:

1) Quartz and feldspar show the same concave-convex contacts with respect to the fresh stone (SH1). At the level of intergranular porosity and permeability this sample is comparable with samples SH6 and SH7 (7.8).

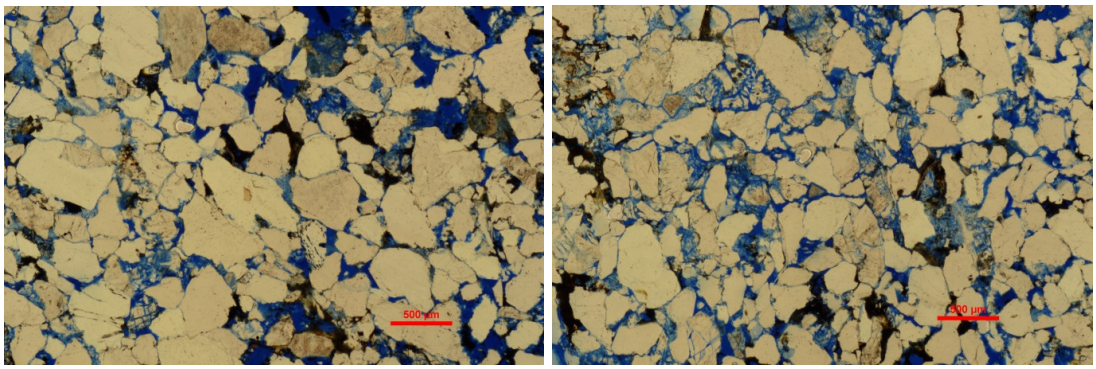

(a) (b)

Figure 7.8: Thin section photographs of sample SH9. The images were taken in plane-polarised transmitted light. White grains are mainly quartz, with a smaller proportion of feldspar and micas. Black patches are iron oxide and opaque minerals. Pore space appears blue.

SAMPLE SM3

Hand specimen observations

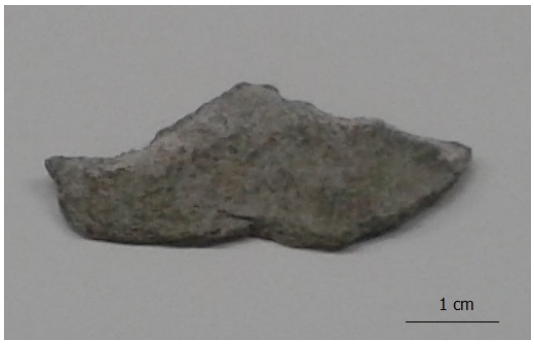

The sample is a light green buff colour, which presents a greyish buff on the exterior and exposed surface. At a first look it appears strongly cohesive with a quite uniform fabric.

Thin section observations

Stone constituents:

Granular (detrital) constituents	Intergranular constituents
Quartz 60%	Silica (overgrowth) 0%
Feldspar 10%	Feldspar (overgrowth) >2%
Mica 6%	Iron/manganese oxide 1%
Opaque material 2%	Clay 20%
Other «1%	Carbonate 0%
Intragranular pores 1%	Intergranular pores 0%

Stone type (detailed classification): sublithic-arenite Grain-size: fine-sand-grade to very fine-sand-grade Grain sorting: poorly sorted Grain roundness: angular to subangular Stone permeability: very low (presence of fractures) Cement distribution: mainly clay minerals and in smaller amount iron oxides Supergene changes: pressure solution of feldspar and pseudomorphic replacement of chlorite on micas. Moderate substitution of feldspars.

Comments:

1) Quartz and feldspar often show concave-convex contacts. The presence of kinked Muscovite and directional elongation indicate the sandstone has undergone significant pressure solution (7.9).

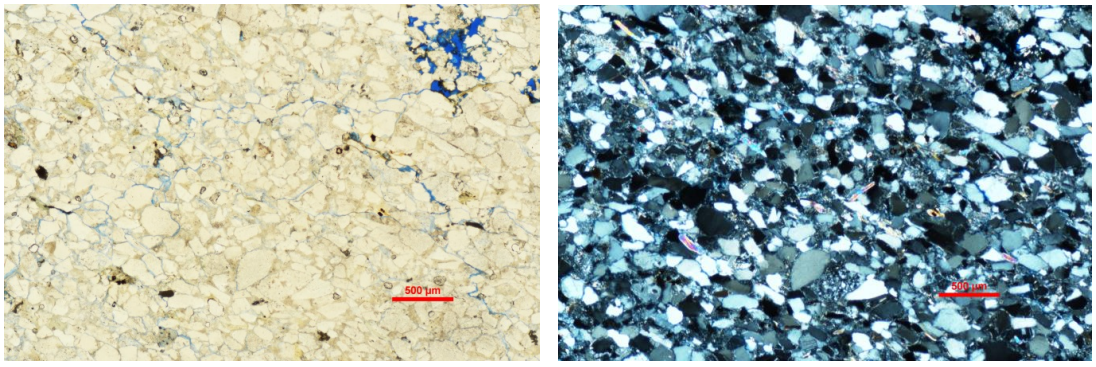

(a) (b)

Figure 7.9: Thin section photographs of sample SM3, Nicols // on the left image and Nicols + on the right one. White grains are mainly quartz. Black patches are iron oxide and opaque minerals. Pore space appears blue.

2) The porosity is extremely low and suggests low permeability. However small fractures are detected which can raise the permeability level. Fractures in a thin section can be produced during the making of the section itself. However the fractures appear to follow the preferential orientation of the micas in the sample (7.10), leading to the assumption that they are proper features of the sample.

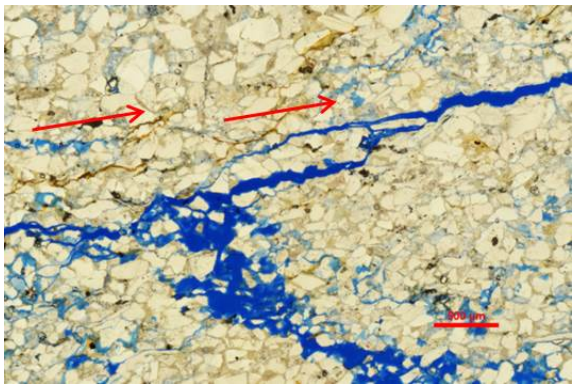

(a)

Figure 7.10: Thin section photograph of sample SM3. The image was taken in planepolarised transmitted light. Highlighted by a red arrow is the preferential orientation of micas.

3) The intergranular chlorite (7.11) appears to be pseudomorphic, produced by the supergene alteration of mafic minerals.

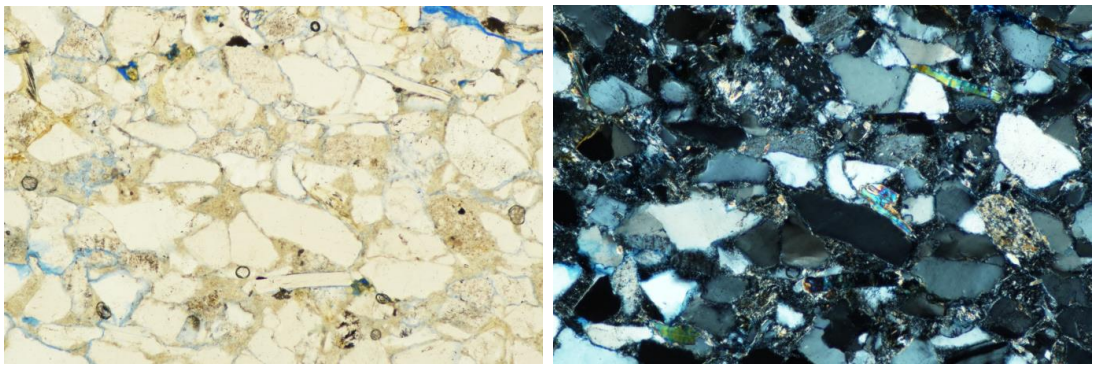

(a) (b)

Figure 7.11: Thin section photographs of sample SM3, Nicols // on the left image and Nicols + on the right one. White grains are mainly quartz, with a very small proportion of feldspar and some micas. Intragranular brownish cement is chlorite. Black patches are iron oxide and opaque minerals. Pore space appears blue.

SAMPLE Brick Clock Tower

Hand specimen observations

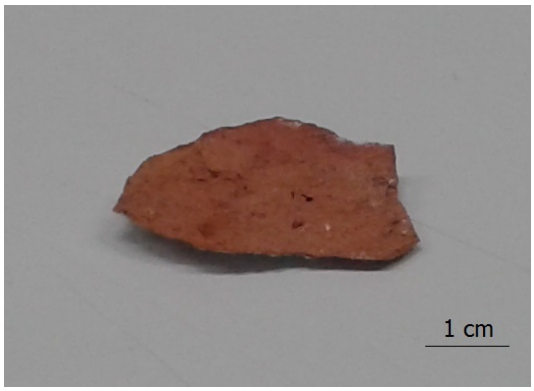

The fresh brick presents a homogeneous grain size, with a well cemented fabric and a dark red buff background color with a small amount of opaque minerals. On one side of the sample is the external layer of plaster.

Thin section descriptions

The brick paste is a dark red to tan colour. The sample shows a glassy-microcrystralline matrix. The aplastic components are mainly quartz and feldspars and a lower amount of micas (mainly muscovite). It is possible to see the presence of some sedimentary or metasedimentary rock fragments, in particular a few carbonatic wrecks can be seen in the paste. They can be interpreted as carbonatic clast transformed in their physical and optical properties during the firing process. The grain size is not well sorted and the dimension of the bigger grains is c. 300 μm. The shape of the aplastic components appears to be generally subrounded to subangular, while some rock fragments shows an elongated shape (with rounded edges). The section contains a small amount (« 8%) of iron oxides and hydroxides. The porosity and permeability appear very low. Pore size is generally lower then 200 μm, and with a rounded shape. Pores show the precipitation of micritic calcite from fluid percolation.

Comments:

1) The sample is a lighter red colour on the surface layer, in contact with the plaster layer. The outer surface can be lighter due to oxidation during firing (7.12).

2) The plaster layer has a thickness of less then 100 μm in thin section. However, the thickness of the original layer on the brick wall was c. 1 cm. The plaster has a low sand component and it is mainly lime binder (7.13).

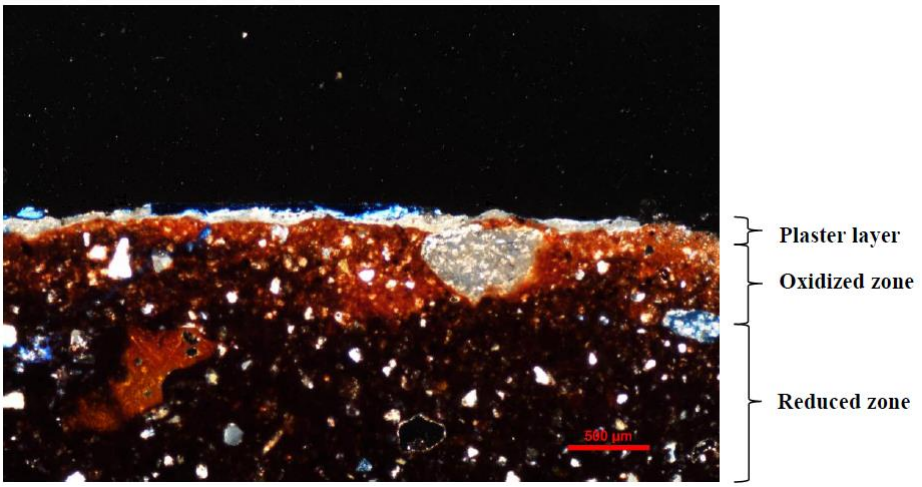

(a)

Figure 7.12: Thin section photograph of sample, Nicols +. White grains are mainly quartz and feldspar. Pore space appears blue.

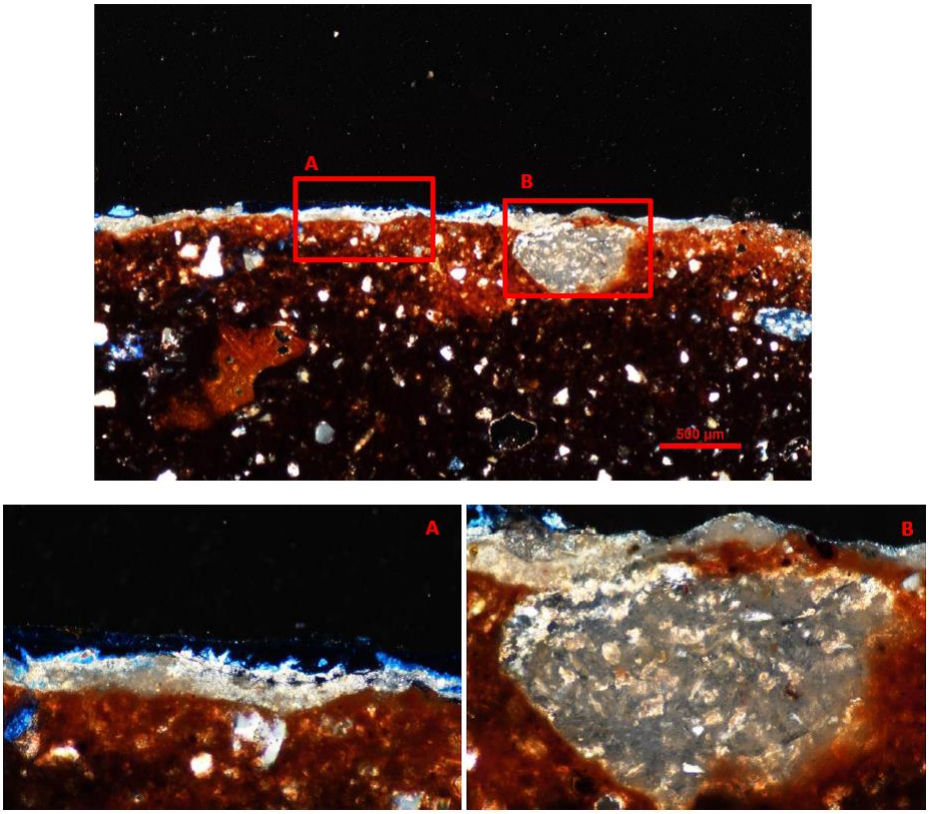

(a)

Figure 7.13: Thin section photographs of sample, Nicols +. A) Magnification (10x) of the plaster layer, showing calcite birefringence. B) Magnification (10x) of the plaster block clogging a pore on the surface of the brick.

3) The presence of micritic calcite inside the pores borders (7.14) is due to a reprecipitation from the water flowing from the outside surface (i.e. the plaster layer).

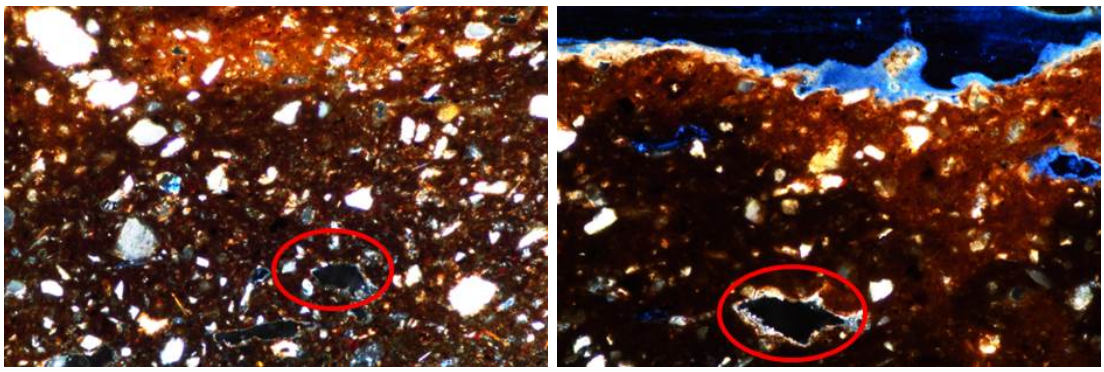

(a) (b)

Figure 7.14: Thin section photographs, magnification 10x, of sample, Nicols +. Pores with micritic calcite are circled in red.

4) The micritic calcite is present only in the primary porosity, while is totally absent in the cracks and the secondary pores (7.15). This could mean that cracks are relatively new and not yet filled with calcite.

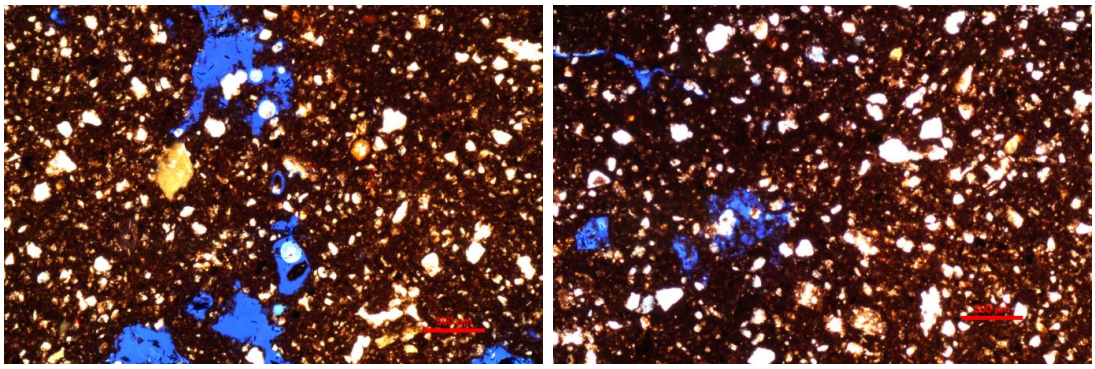

(a) (b)

Figure 7.15: Thin section photographs of sample. The images were taken in plane-polarised transmitted light. White grains are mainly quartz and feldspar, with a smaller portion of micas. Black patches are iron oxide and opaque minerals. Pore space appears blue.

SAMPLE Mortar Clock Tower

Hand specimen observations

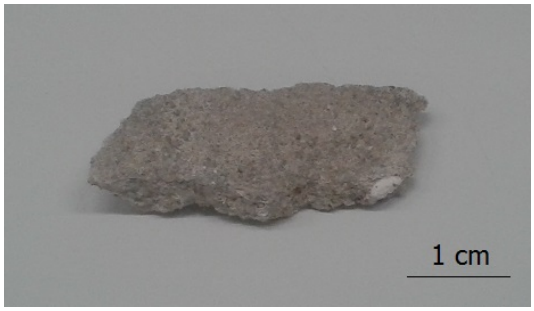

The sample of deteriorated mortar shows a very well sorted grain size, a general light grey buff and a low level of fabric cohesion, visibly dusty and friable. It is possible to see a small amount of opaque minerals in the hand specimen.

Thin section descriptions

The mortar sample in thin section appears to be a hydraulic lime mortar, which shows a high level of intergranular porosity and permeability. Rock fragments, mainly sedimentary and metasedimentary, are c. 30% of the sample and contribute to the maximum grain size of the sand aggregate, which is 5mm. The binder shows a light grey color and its amount is considerably lower than expected for a natural hydraulic lime mortar (1:3 ratio by volume).

Comments:

1) Quartz and feldspar are the main mineral components of the mortar. Quartz is either mono or polycrystalline and shows concave-convex contact (7.16).

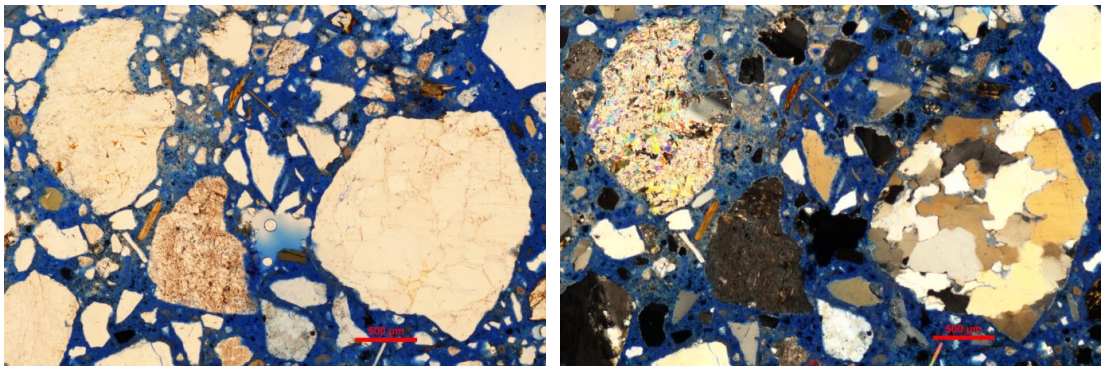

(a) (b)

Figure 7.16: Thin section photographs of sample, Nicols // on the left image and Nicols + on the right one. White grains are mainly quartz. There is a smaller proportion of feldspar, micas and opaque minerals. Pore space appears blue. On the right of the image is clearly visible a large polycrystalline quartz particle.

2) The aggregate is predominant while the binder appears to be almost absent. This

is a typical characteristic of deteriorated hydraulic lime mortars. Very high moisture content and water flowing have the potential to leach binder from the mortar. In this process soluble components within the mortar dissolve and migrate to be re-deposited within the porosity or on the external surface of masonry. This loss of binder is associated with progressive fracturing of the mortar (7.17).

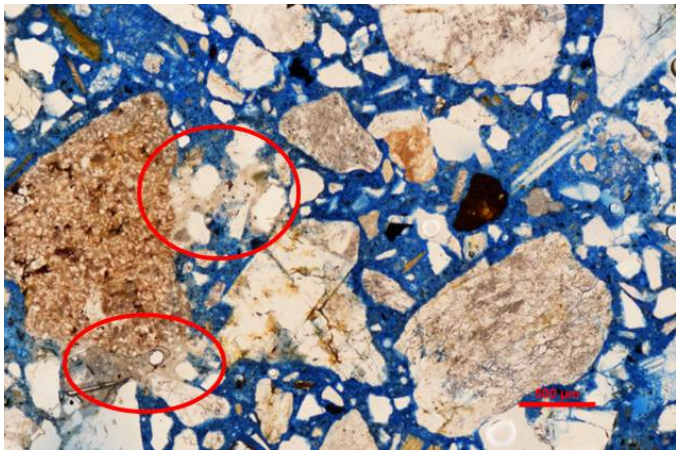

(a)

Figure 7.17: Thin section photograph of sample, Nicols // . The image was taken in planepolarised transmitted light. Grains are mainly quartz, feldspar, micas and rock fragments. Highlighted by a red circle is a part of the remaining lime binder of the mortar.

3) The sample shows locally an even higher level of permeability and porosity (7.18), which is definitively enhanced by the progressive deterioration phenomenon.

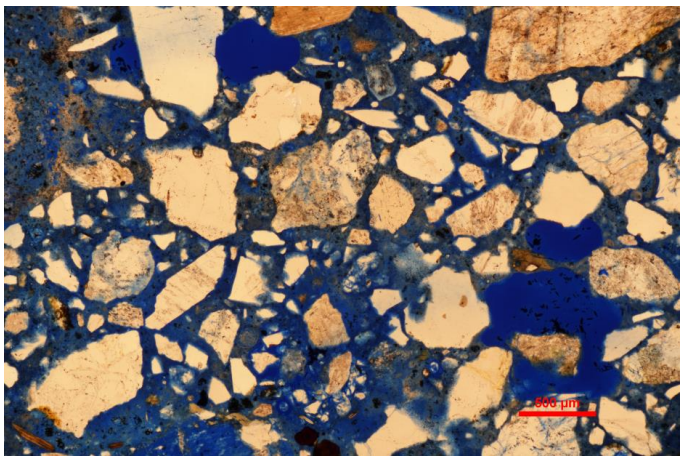

(a)

Figure 7.18: Thin section photograph of sample. This image was taken in planepolarised transmitted light. Grains are mainly quartz, feldspar, micas and rock fragments.

Chapter 8

Appendix B

8.1 Chapter 3: X-Ray diffraction patterns

XRD patterns for each sample are presented below. Major components are identified by different peak positions and each of them is marked with a label.

SAMPLE SH1

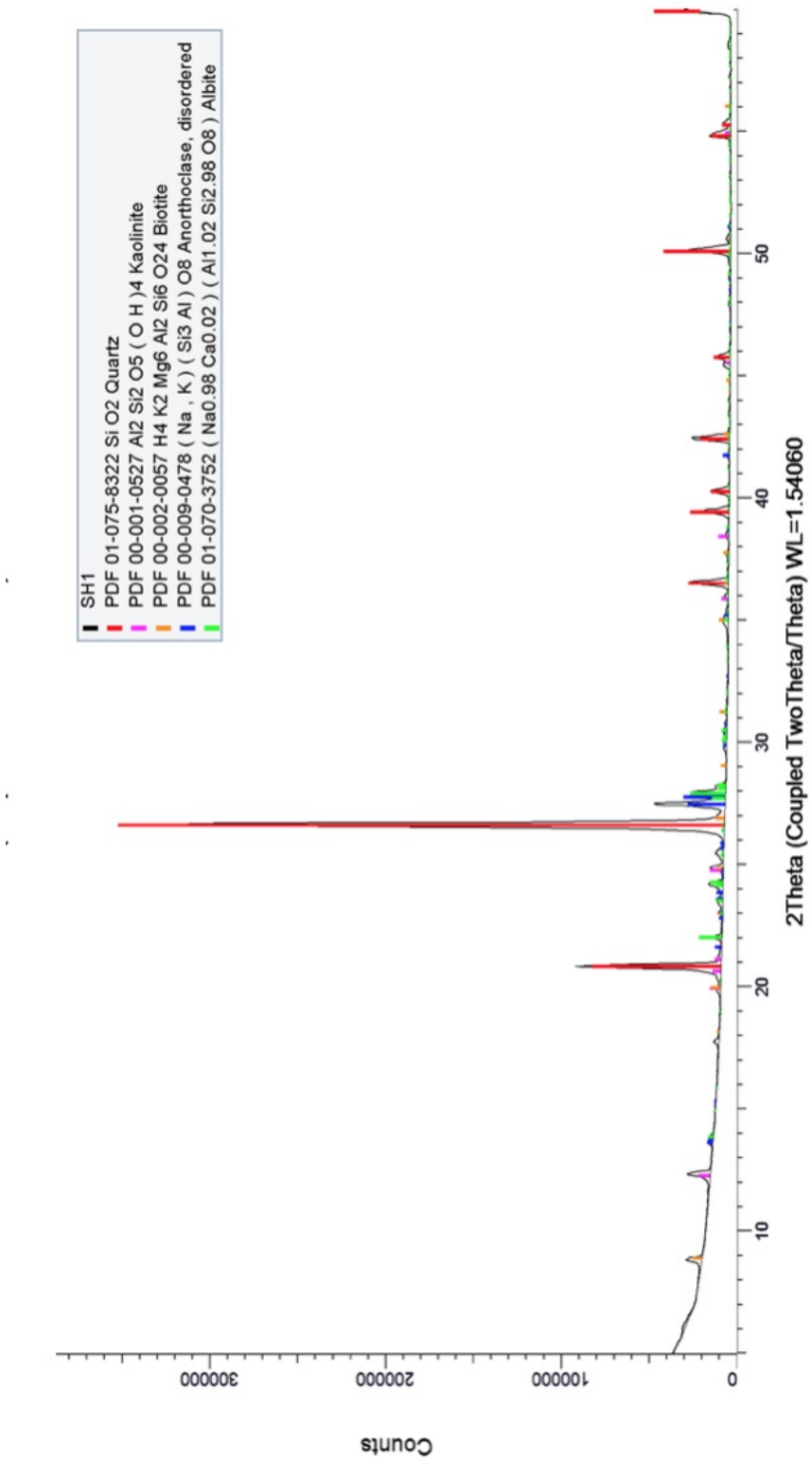
SH1
PDF 01-075-8322 Si O2 Quartz
PDF 00-001-0527 Al2 Si2 O5 (O H)4 Kaolinite
PDF 00-002-0057 H4 K2 Mg6 Al2 Si6 O24 Biotite
PDF 00-009-0478 (Na , K) (Si3 Al) O8 Anorthoclase, disordered
PDF 01-070-3752 (Na0.98 Ca0.02) (Al1.02 Si2.98 O8) Albite
Counts
0
100000
200000
300000
10
20
30
40
50
2Theta (Coupled TwoTheta/Theta) WL=1.54060

SAMPLE SH2

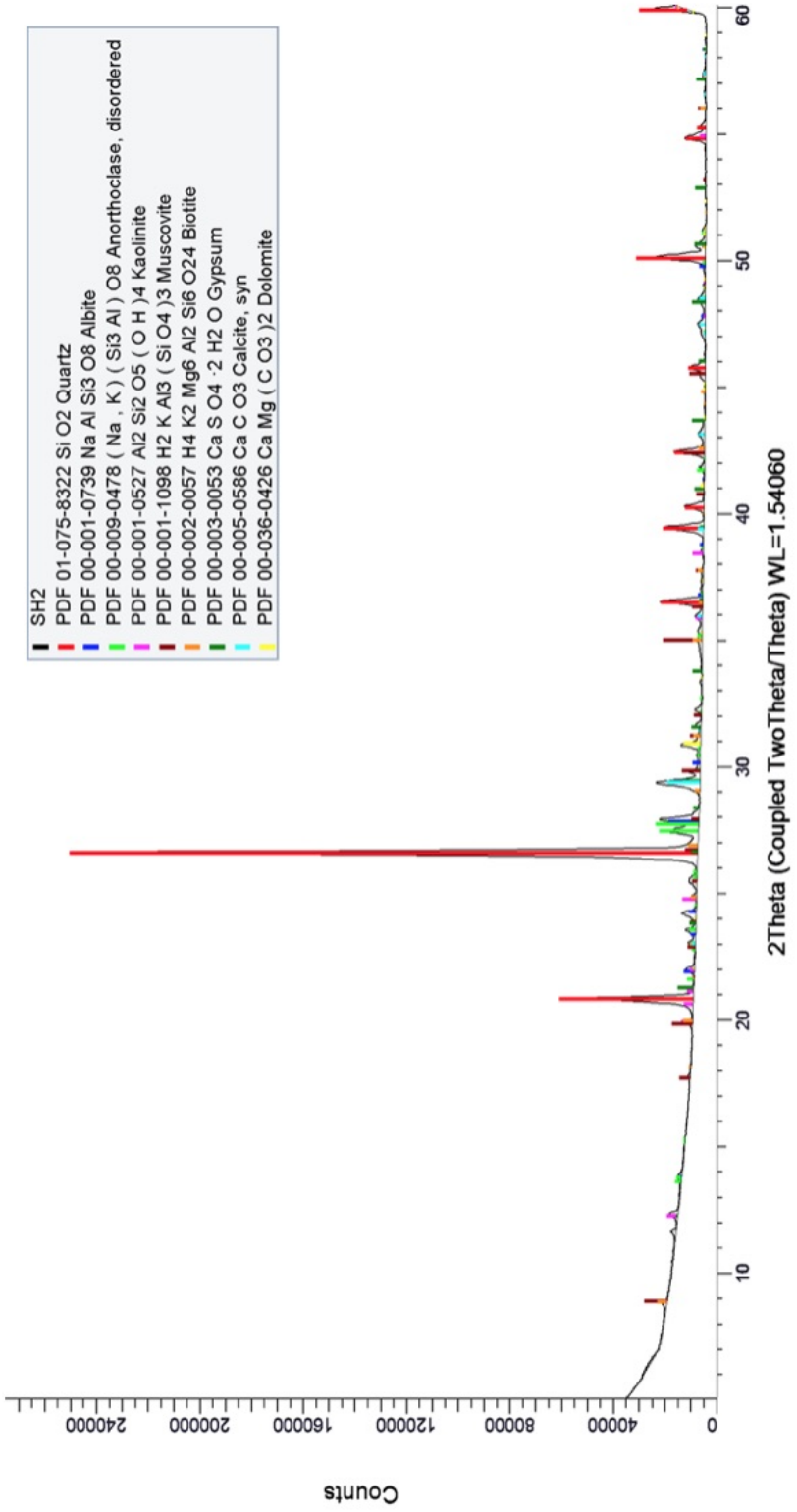
SH2
PDF 01-075-8322 Si O2 Quartz
PDF 00-001-0739 Na Al Si3 O8 Albite
PDF 00-009-0478 (Na , K) (Si3 Al) O8 Anorthoclase, disordered
PDF 00-001-0527 Al2 Si2 O5 (O H)4 Kaolinite
PDF 00-001-1098 H2 K Al3 (Si O4)3 Muscovite
PDF 00-002-0057 H4 K2 Mg6 Al2 Si6 O24 Biotite
PDF 00-003-0053 Ca S O4 · 2 H2 O Gypsum
PDF 00-005-0586 Ca C O3 Calcite, syn
PDF 00-036-0426 Ca Mg (C O3)2 Dolomite
Counts
0
4000
8000
12000
16000
20000
24000
10
20
30
40
50
60
2Theta (Coupled TwoTheta/Theta) WL=1.54060

SAMPLE SH2b

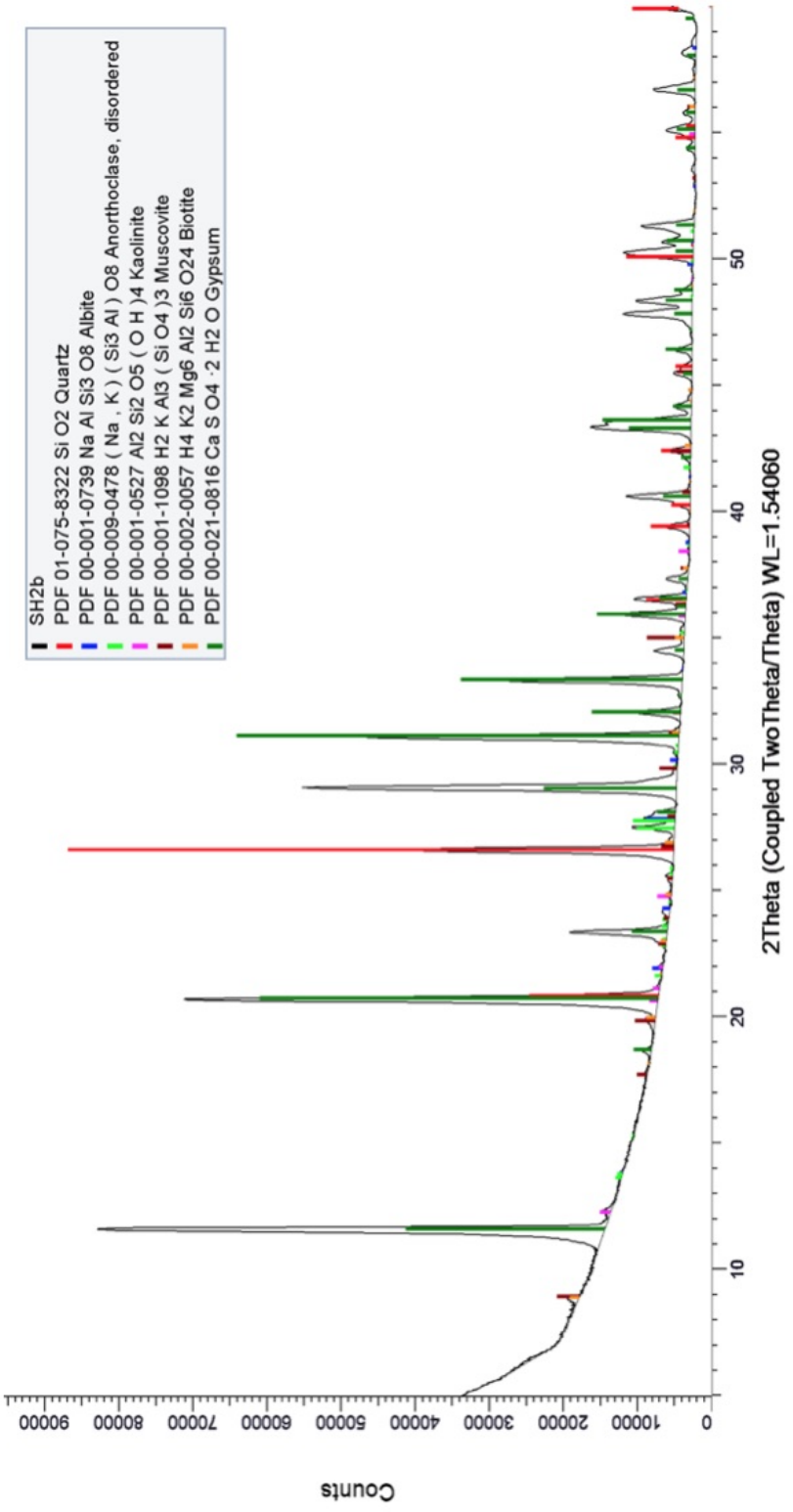
SH2b
PDF 01-075-8322 Si O2 Quartz
PDF 00-001-0739 Na Al Si3 O8 Albite
PDF 00-009-0478 (Na , K) (Si3 Al) O8 Anorthoclase, disordered
PDF 00-001-0527 Al2 Si2 O5 (O H)4 Kaolinite
PDF 00-001-1098 H2 K Al3 (Si O4)3 Muscovite
PDF 00-002-0057 H4 K2 Mg6 Al2 Si6 O24 Biotite
PDF 00-021-0816 Ca S O4 · 2 H2 O Gypsum
Counts
0
10000
20000
30000
40000
50000
60000
70000
80000
90000
10
20
30
40
50
2Theta (Coupled TwoTheta/Theta) WL=1.54060

SAMPLE SH3

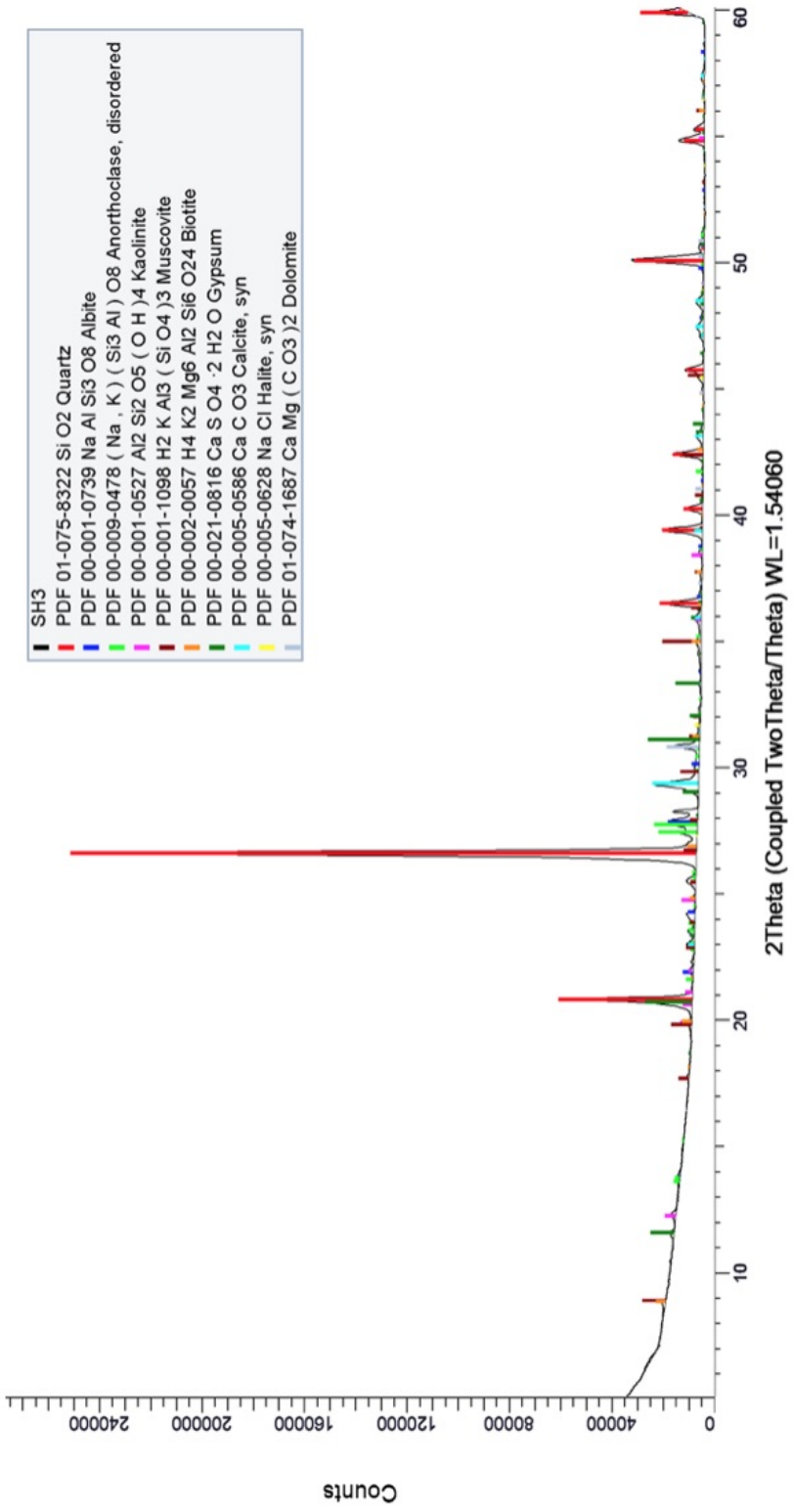
SH3
PDF 01-075-8322 Si O2 Quartz
PDF 00-001-0739 Na Al Si3 O8 Albite
PDF 00-009-0478 (Na , K) (Si3 Al) O8 Anorthoclase, disordered
PDF 00-001-0527 Al2 Si2 O5 (O H)4 Kaolinite
PDF 00-001-1098 H2 K Al3 (Si O4)3 Muscovite
PDF 00-002-0057 H4 K2 Mg6 Al2 Si6 O24 Biotite
PDF 00-021-0816 Ca S O4 · 2 H2 O Gypsum
PDF 00-005-0586 Ca C O3 Calcite, syn
PDF 00-005-0628 Na Cl Halite, syn
PDF 01-074-1687 Ca Mg (C O3)2 Dolomite
Counts
0
4000
8000
12000
16000
20000
24000
10
20
30
40
50
60
2Theta (Coupled TwoTheta/Theta) WL=1.54060

SAMPLE SH4

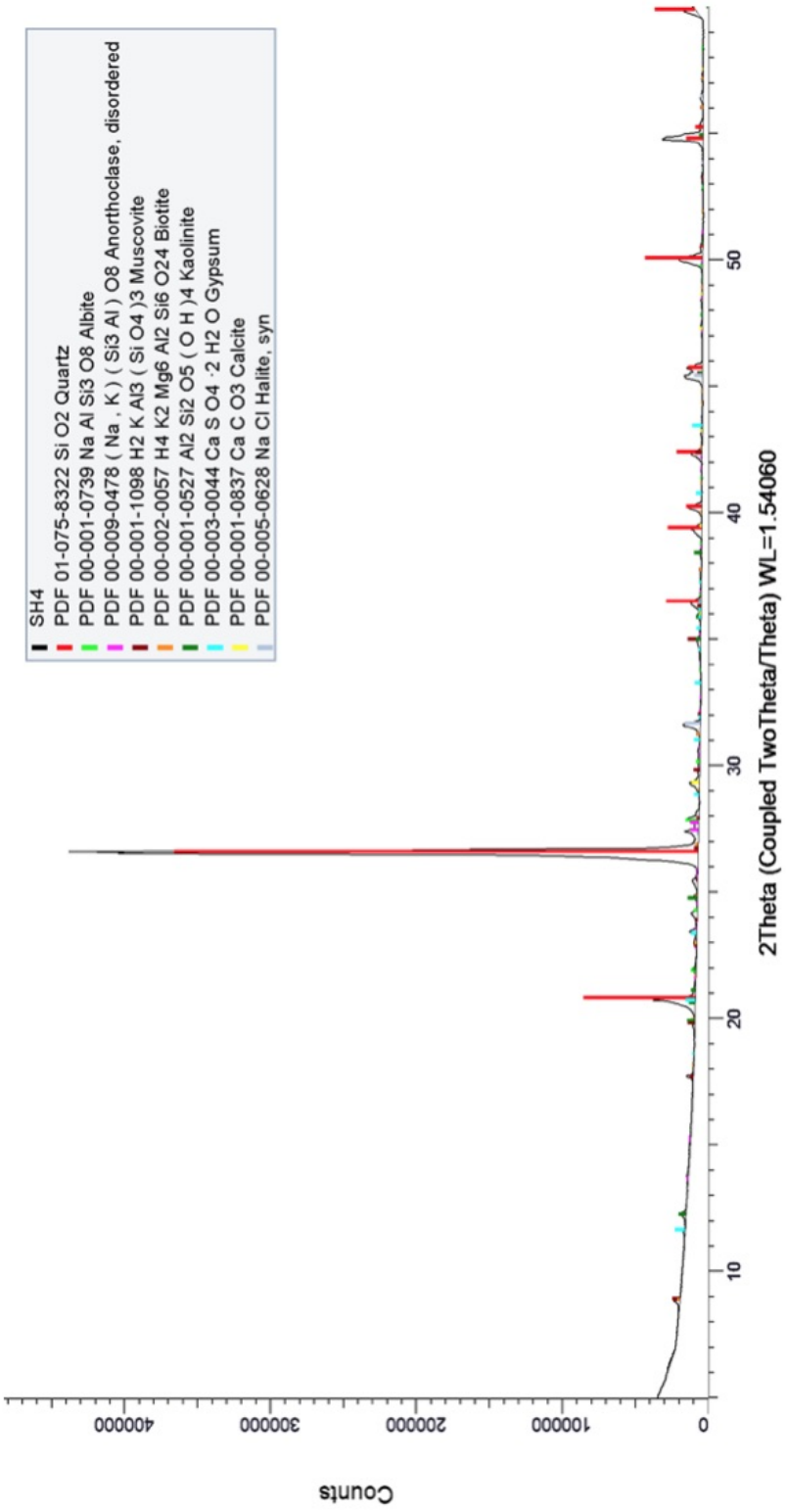
SH4
PDF 01-075-8322 Si O2 Quartz
PDF 00-001-0739 Na Al Si3 O8 Albite
PDF 00-009-0478 (Na , K) (Si3 Al) O8 Anorthoclase, disordered
PDF 00-001-1098 H2 K Al3 (Si O4)3 Muscovite
PDF 00-002-0057 H4 K2 Mg6 Al2 Si6 O24 Biotite
PDF 00-001-0527 Al2 Si2 O5 (O H)4 Kaolinite
PDF 00-003-0044 Ca S O4 ·2 H2 O Gypsum
PDF 00-001-0837 Ca C O3 Calcite
PDF 00-005-0628 Na Cl Halite, syn
Counts
0
100000
200000
300000
400000
10
20
30
40
50
2Theta (Coupled TwoTheta/Theta) WL=1.54060

SAMPLE SH5

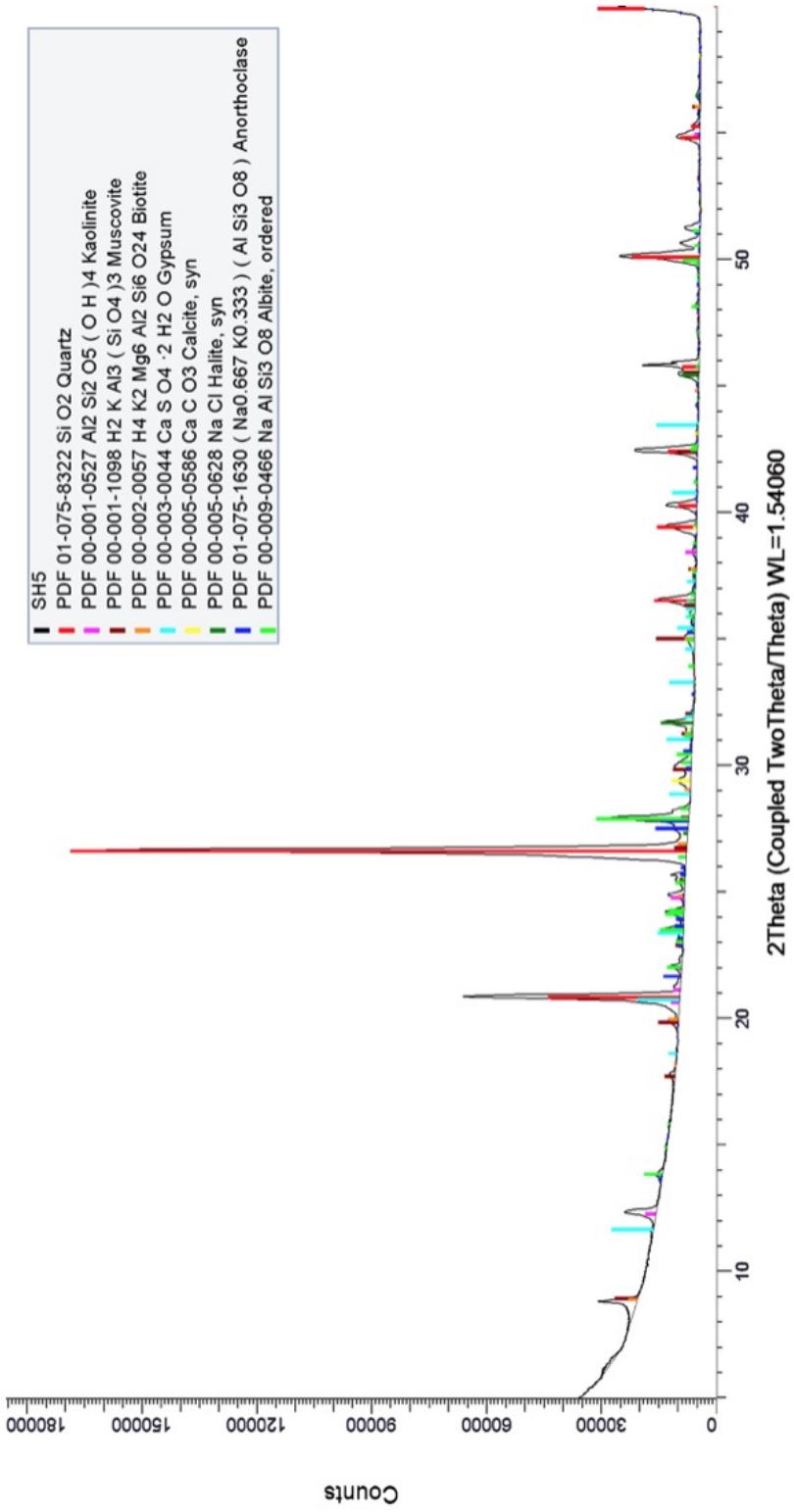
SH5
PDF 01-075-8322 Si O2 Quartz
PDF 00-001-0527 Al2 Si2 O5 (O H)4 Kaolinite
PDF 00-001-1098 H2 K Al3 (Si O4)3 Muscovite
PDF 00-002-0057 H4 K2 Mg6 Al2 Si6 O24 Biotite
PDF 00-003-0044 Ca S O4 · 2 H2 O Gypsum
PDF 00-005-0586 Ca C O3 Calcite, syn
PDF 00-005-0628 Na Cl Halite, syn
PDF 01-075-1630 (Na0.667 K0.333) (Al Si3 O8) Anorthoclase
PDF 00-009-0466 Na Al Si3 O8 Albite, ordered
Counts
0
3000
6000
9000
12000
15000
18000
10
20
30
40
50
2Theta (Coupled TwoTheta/Theta) WL=1.54060

SAMPLE SH6

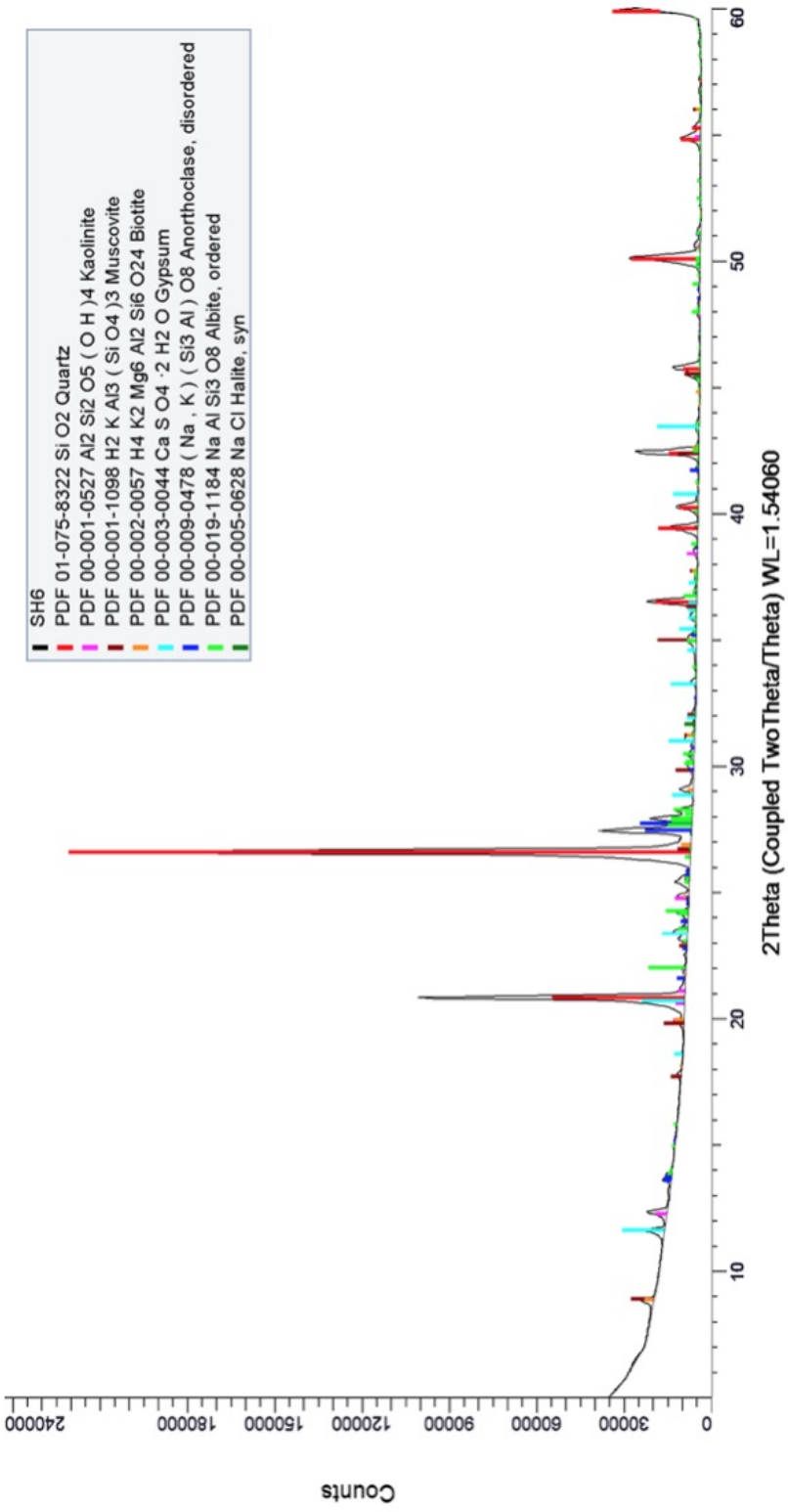
SH6
PDF 01-075-8322 Si O2 Quartz
PDF 00-001-0527 Al2 Si2 O5 (O H)4 Kaolinite
PDF 00-001-1098 H2 K Al3 (Si O4)3 Muscovite
PDF 00-002-0057 H4 K2 Mg6 Al2 Si6 O24 Biotite
PDF 00-003-0044 Ca S O4 ·2 H2 O Gypsum
PDF 00-009-0478 (Na , K) (Si3 Al) O8 Anorthoclase, disordered
PDF 00-019-1184 Na Al Si3 O8 Albite, ordered
PDF 00-005-0628 Na Cl Halite, syn
Counts
0
3000
6000
9000
12000
15000
18000
24000
10
20
30
40
50
60
2Theta (Coupled TwoTheta/Theta) WL=1.54060

SAMPLE SH7

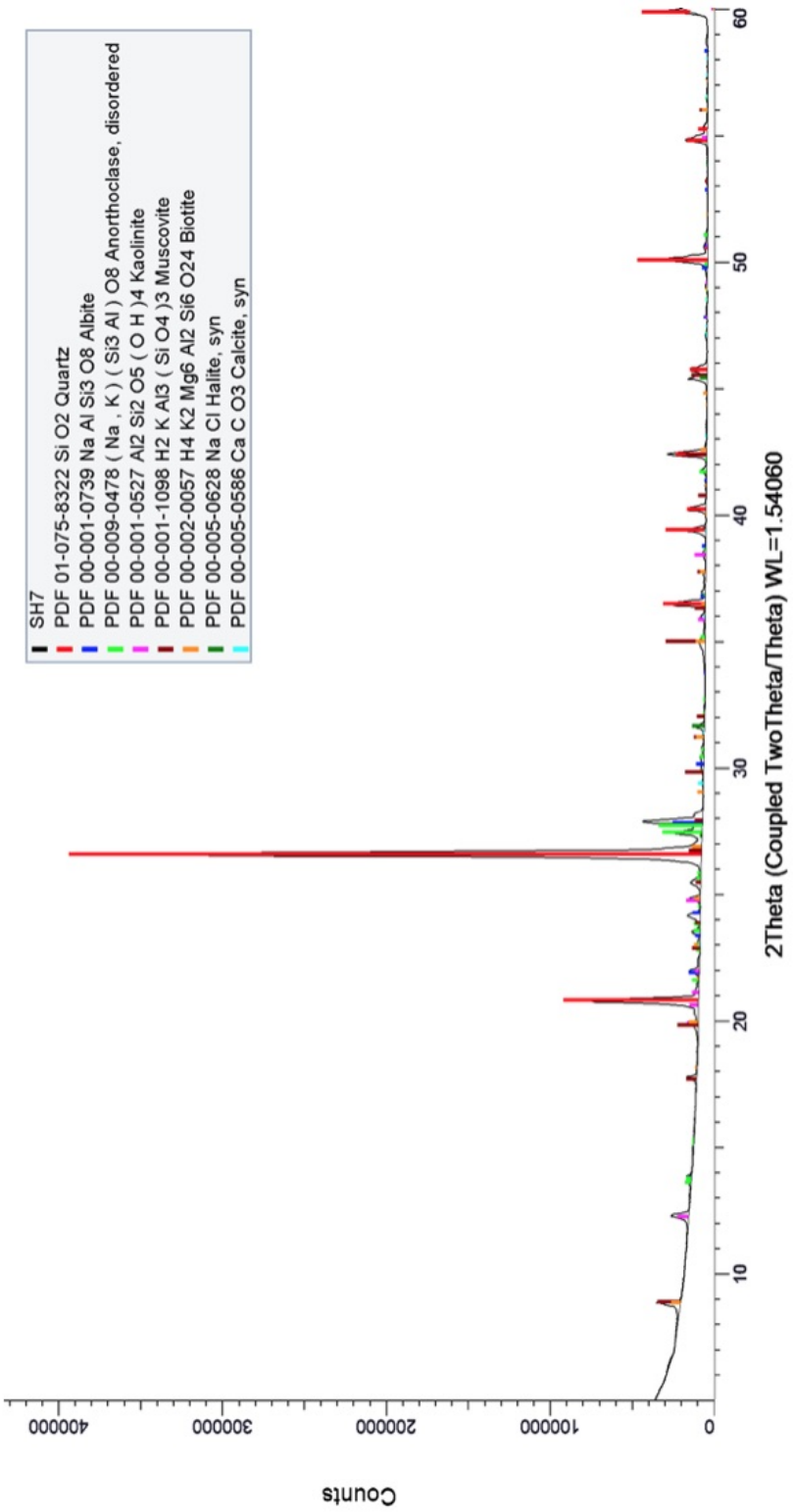
SH7
PDF 01-075-8322 Si O2 Quartz
PDF 00-001-0739 Na Al Si3 O8 Albite
PDF 00-009-0478 (Na , K) (Si3 Al) O8 Anorthoclase, disordered
PDF 00-001-0527 Al2 Si2 O5 (O H)4 Kaolinite
PDF 00-001-1098 H2 K Al3 (Si O4)3 Muscovite
PDF 00-002-0057 H4 K2 Mg6 Al2 Si6 O24 Biotite
PDF 00-005-0628 Na Cl Halite, syn
PDF 00-005-0586 Ca C O3 Calcite, syn
Counts
0
100000
200000
300000
400000
2Theta (Coupled TwoTheta/Theta) WL=1.54060
10
20
30
40
50
60

SAMPLE SH8

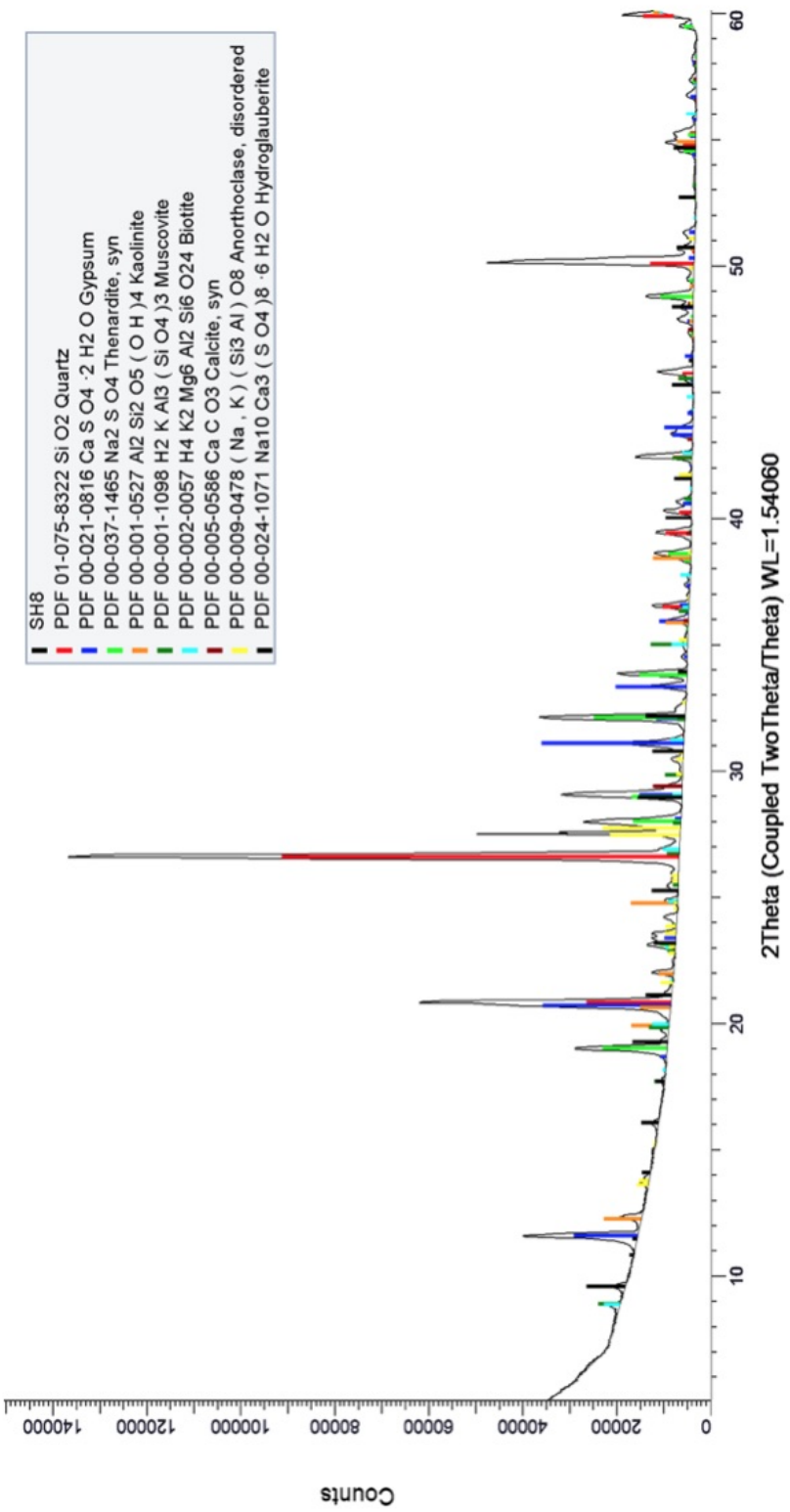
SH8
PDF 01-075-8322 Si O2 Quartz
PDF 00-021-0816 Ca S O4 ·2 H2 O Gypsum
PDF 00-037-1465 Na2 S O4 Thenardite, syn
PDF 00-001-0527 Al2 Si2 O5 (O H)4 Kaolinite
PDF 00-001-1098 H2 K Al3 (Si O4)3 Muscovite
PDF 00-002-0057 H4 K2 Mg6 Al2 Si6 O24 Biotite
PDF 00-005-0586 Ca C O3 Calcite, syn
PDF 00-009-0478 (Na , K) (Si3 Al) O8 Anorthoclase, disordered
PDF 00-024-1071 Na10 Ca3 (S O4)8 ·6 H2 O Hydroglauberite
Counts
0
20000
40000
60000
80000
100000
120000
140000
2Theta (Coupled TwoTheta/Theta) WL=1.54060
10
20
30
40
50
60

SAMPLE SH9

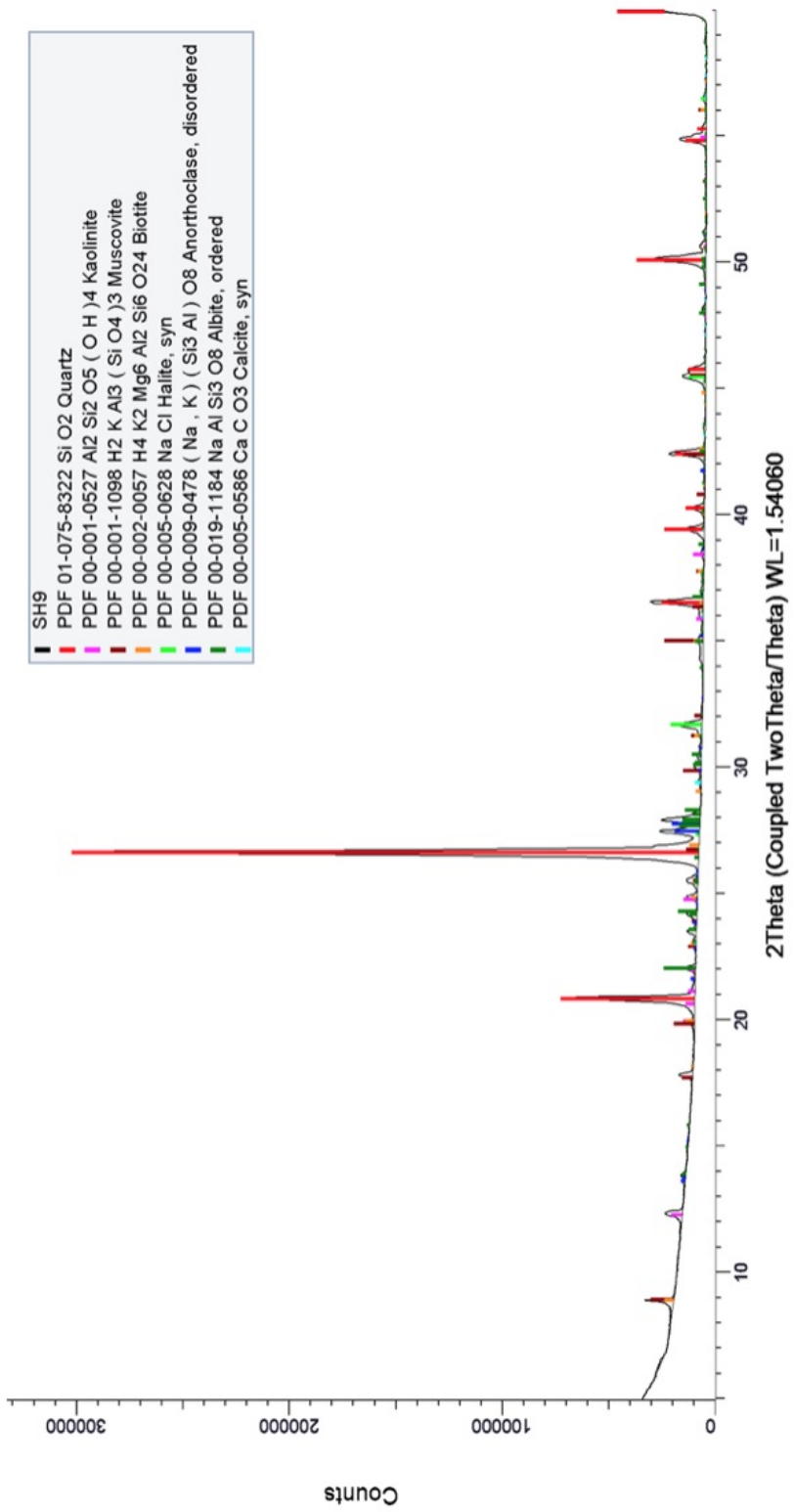
SH9
PDF 01-075-8322 Si O2 Quartz
PDF 00-001-0527 Al2 Si2 O5 (O H)4 Kaolinite
PDF 00-001-1098 H2 K Al3 (Si O4)3 Muscovite
PDF 00-002-0057 H4 K2 Mg6 Al2 Si6 O24 Biotite
PDF 00-005-0628 Na Cl Halite, syn
PDF 00-009-0478 (Na , K) (Si3 Al) O8 Anorthoclase, disordered
PDF 00-019-1184 Na Al Si3 O8 Albite, ordered
PDF 00-005-0586 Ca C O3 Calcite, syn
Counts
0
100000
200000
300000
10
20
30
40
50
2Theta (Coupled TwoTheta/Theta) WL=1.54060

SAMPLE SH10

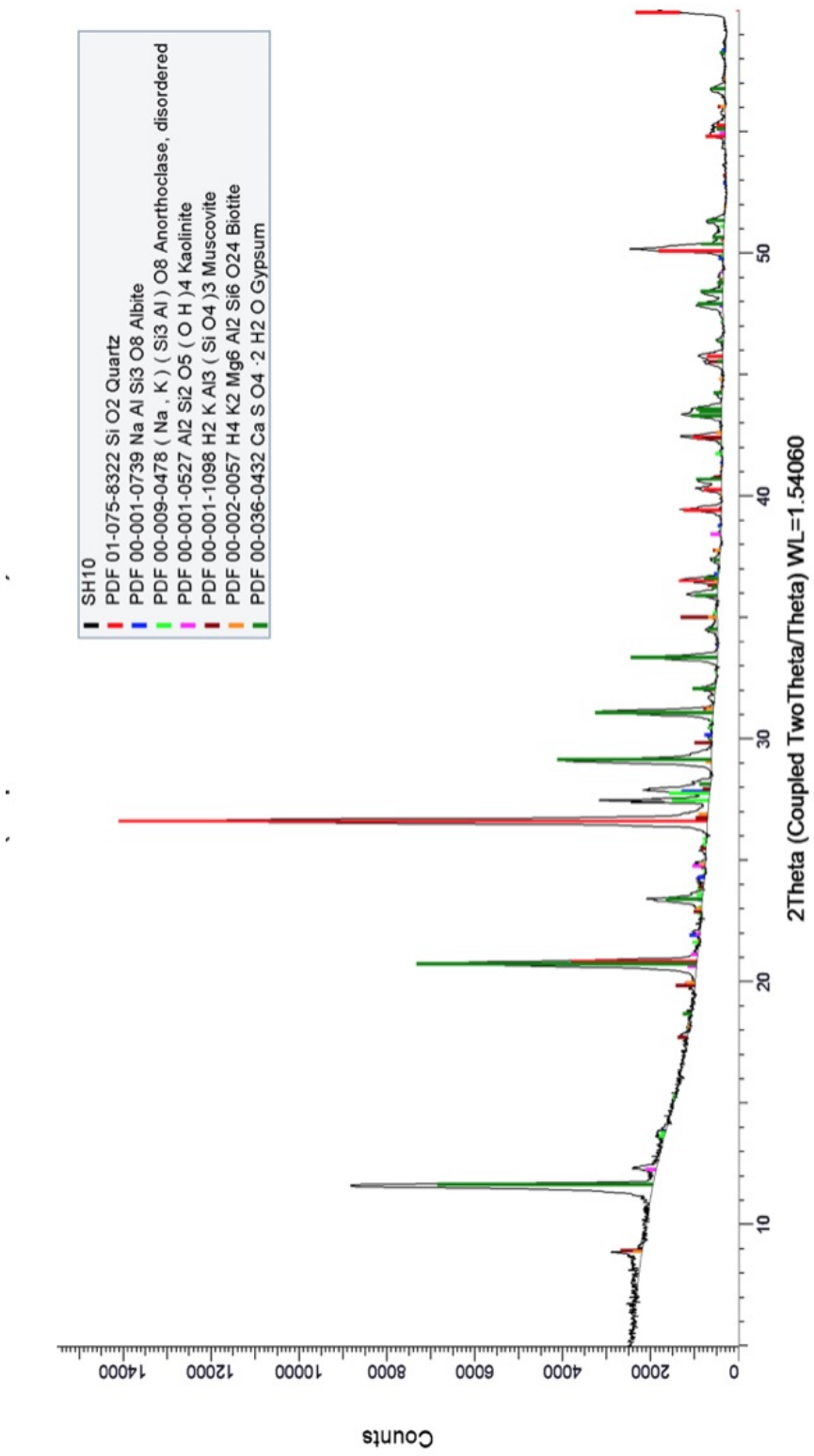
SH10
PDF 01-075-8322 Si O2 Quartz
PDF 00-001-0739 Na Al Si3 O8 Albite
PDF 00-009-0478 (Na , K) (Si3 Al) O8 Anorthoclase, disordered
PDF 00-001-0527 Al2 Si2 O5 (O H)4 Kaolinite
PDF 00-001-1098 H2 K Al3 (Si O4)3 Muscovite
PDF 00-002-0057 H4 K2 Mg6 Al2 Si6 O24 Biotite
PDF 00-036-0432 Ca S O4 · 2 H2 O Gypsum
Counts
0
2000
4000
6000
8000
10000
12000
14000
10
20
30
40
50
2Theta (Coupled TwoTheta/Theta) WL=1.54060

SAMPLE SH11

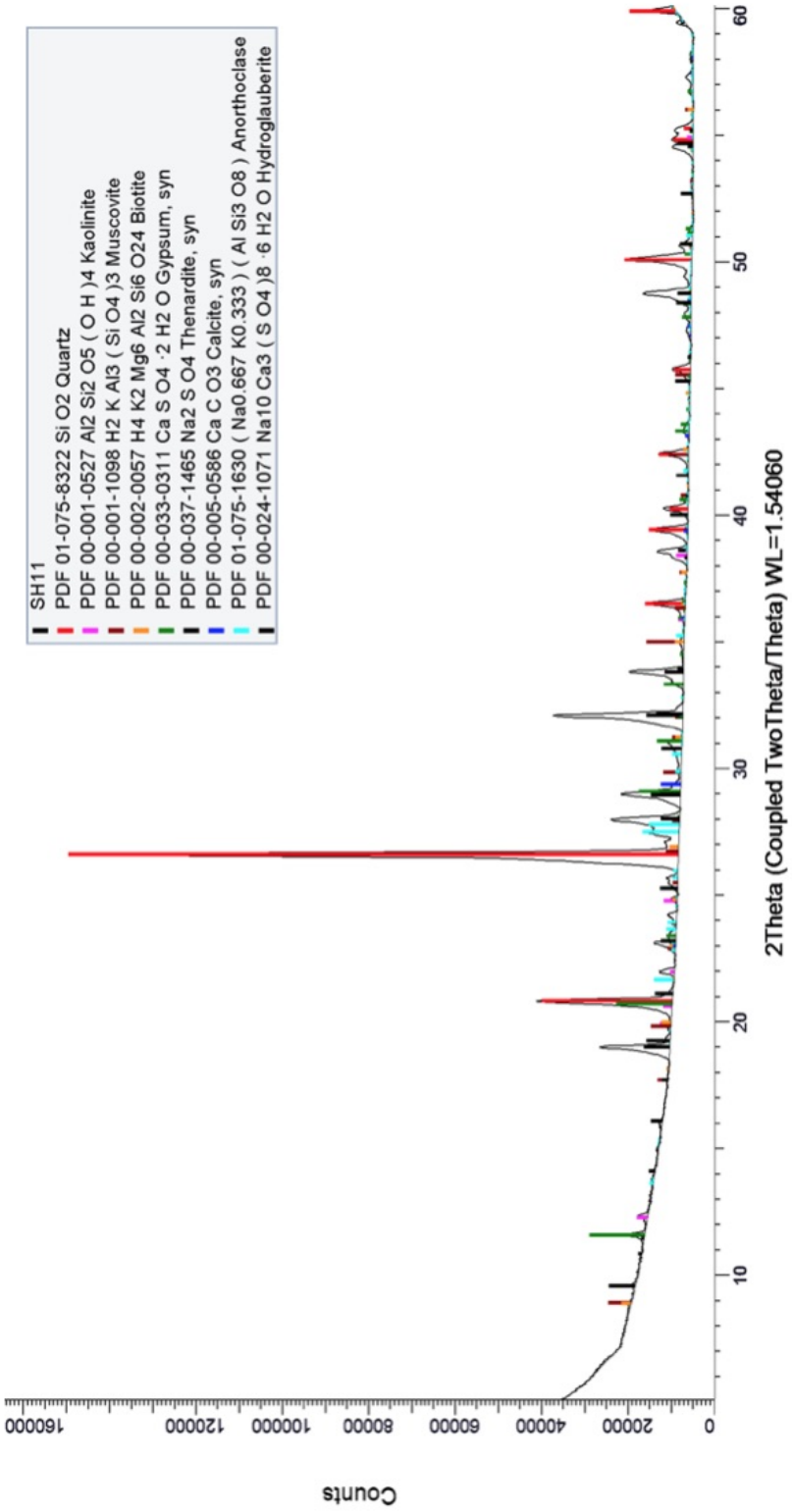
SH11
PDF 01-075-8322 Si O2 Quartz
PDF 00-001-0527 Al2 Si2 O5 (O H)4 Kaolinite
PDF 00-001-1098 H2 K Al3 (Si O4)3 Muscovite
PDF 00-002-0057 H4 K2 Mg6 Al2 Si6 O24 Biotite
PDF 00-033-0311 Ca S O4 ·2 H2 O Gypsum, syn
PDF 00-037-1465 Na2 S O4 Thenardite, syn
PDF 00-005-0586 Ca C O3 Calcite, syn
PDF 01-075-1630 (Na0.667 K0.333) (Al Si3 O8) Anorthoclase
PDF 00-024-1071 Na10 Ca3 (S O4)8 ·6 H2 O Hydroglauberite
Counts
0
20000
40000
60000
80000
100000
120000
140000
10
20
30
40
50
60
2Theta (Coupled TwoTheta/Theta) WL=1.54060

SAMPLE SM1

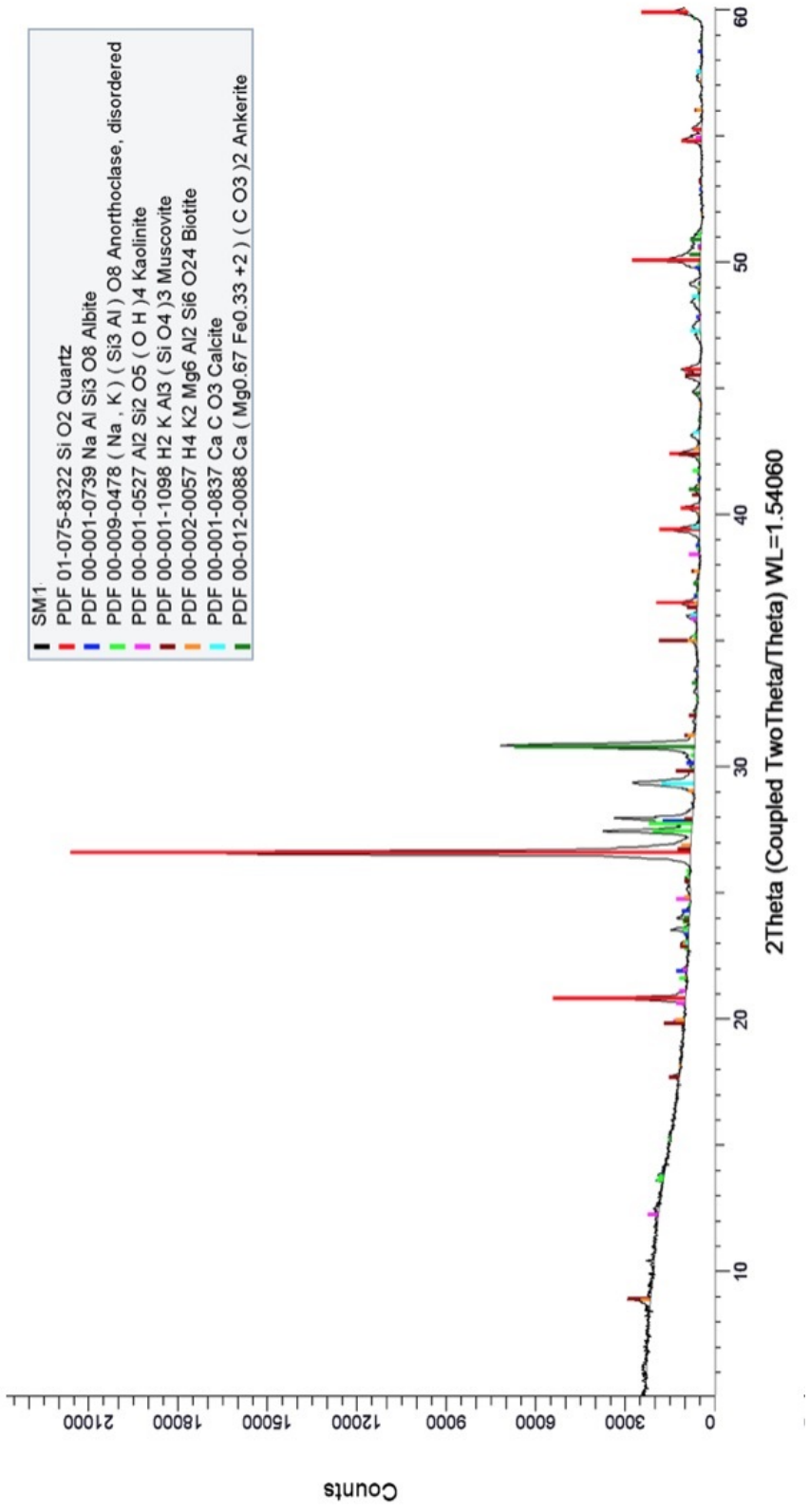
SM1
PDF 01-075-8322 Si O2 Quartz
PDF 00-001-0739 Na Al Si3 O8 Albite
PDF 00-009-0478 (Na , K) (Si3 Al) O8 Anorthoclase, disordered
PDF 00-001-0527 Al2 Si2 O5 (O H)4 Kaolinite
PDF 00-001-1098 H2 K Al3 (Si O4)3 Muscovite
PDF 00-002-0057 H4 K2 Mg6 Al2 Si6 O24 Biotite
PDF 00-001-0837 Ca C O3 Calcite
PDF 00-012-0088 Ca (Mg0.67 Fe0.33 +2) (C O3)2 Ankerite
Counts
0
3000
6000
9000
12000
15000
18000
21000
10
20
30
40
50
60
2Theta (Coupled TwoTheta/Theta) WL=1.54060

SAMPLE SM2

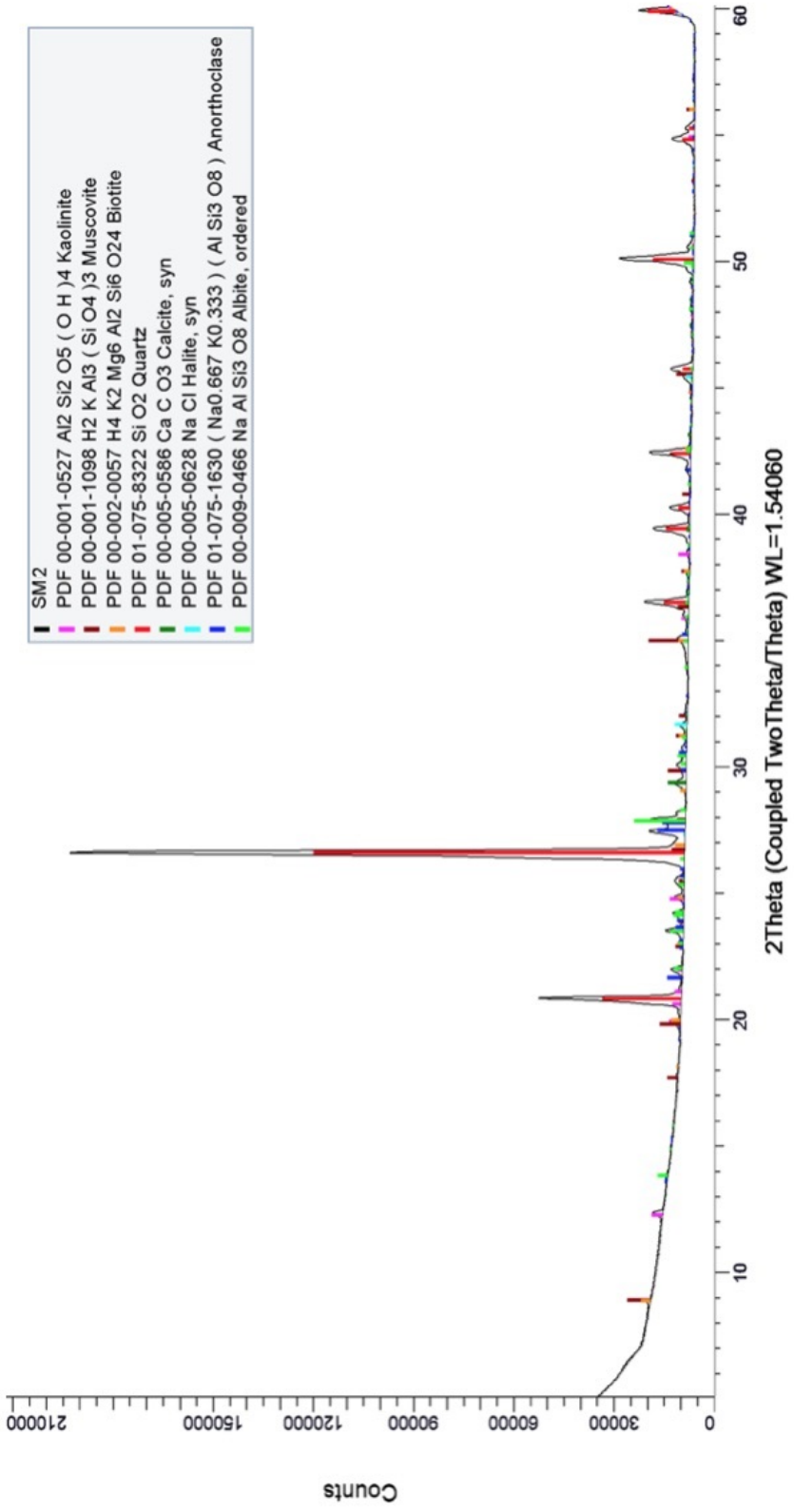
SM2
PDF 00-001-0527 Al2 Si2 O5 (O H)4 Kaolinite
PDF 00-001-1098 H2 K Al3 (Si O4)3 Muscovite
PDF 00-002-0057 H4 K2 Mg6 Al2 Si6 O24 Biotite
PDF 01-075-8322 Si O2 Quartz
PDF 00-005-0586 Ca C O3 Calcite, syn
PDF 00-005-0628 Na Cl Halite, syn
PDF 01-075-1630 (Na0.667 K0.333) (Al Si3 O8) Anorthoclase
PDF 00-009-0466 Na Al Si3 O8 Albite, ordered
Counts
0
30000
60000
90000
120000
150000
210000
10
20
30
40
50
60
2Theta (Coupled TwoTheta/Theta) WL=1.54060

SAMPLE SM3

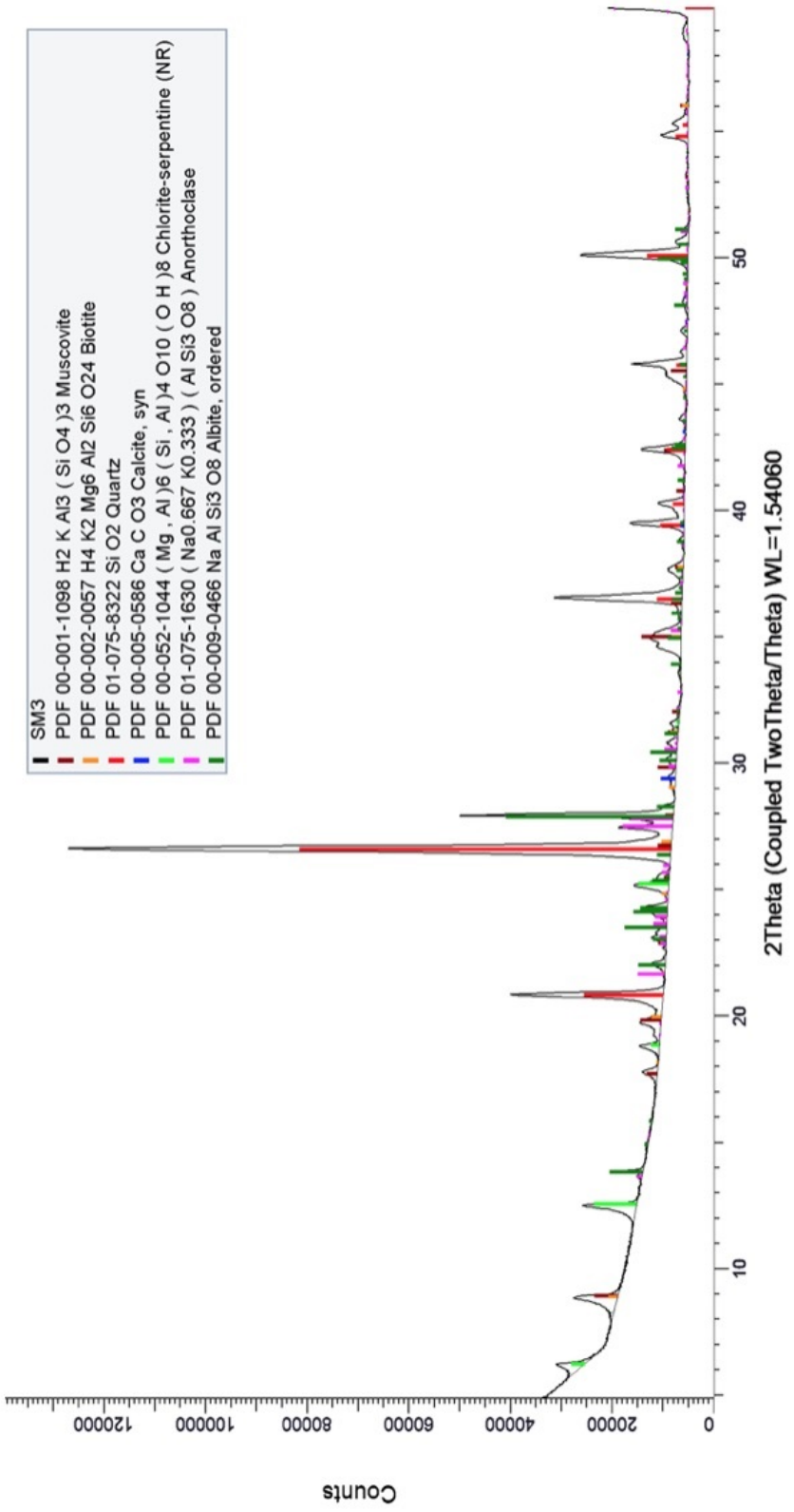
SM3
PDF 00-001-1098 H2 K Al3 (Si O4)3 Muscovite
PDF 00-002-0057 H4 K2 Mg6 Al2 Si6 O24 Biotite
PDF 01-075-8322 Si O2 Quartz
PDF 00-005-0586 Ca C O3 Calcite, syn
PDF 00-052-1044 (Mg , Al)6 (Si , Al)4 O10 (O H)8 Chlorite-serpentine (NR)
PDF 01-075-1630 (Na0.667 K0.333) (Al Si3 O8) Anorthoclase
PDF 00-009-0466 Na Al Si3 O8 Albite, ordered
Counts
0
20000
40000
60000
80000
100000
120000
10
20
30
40
50
2Theta (Coupled TwoTheta/Theta) WL=1.54060

SAMPLE Brick Clock Tower

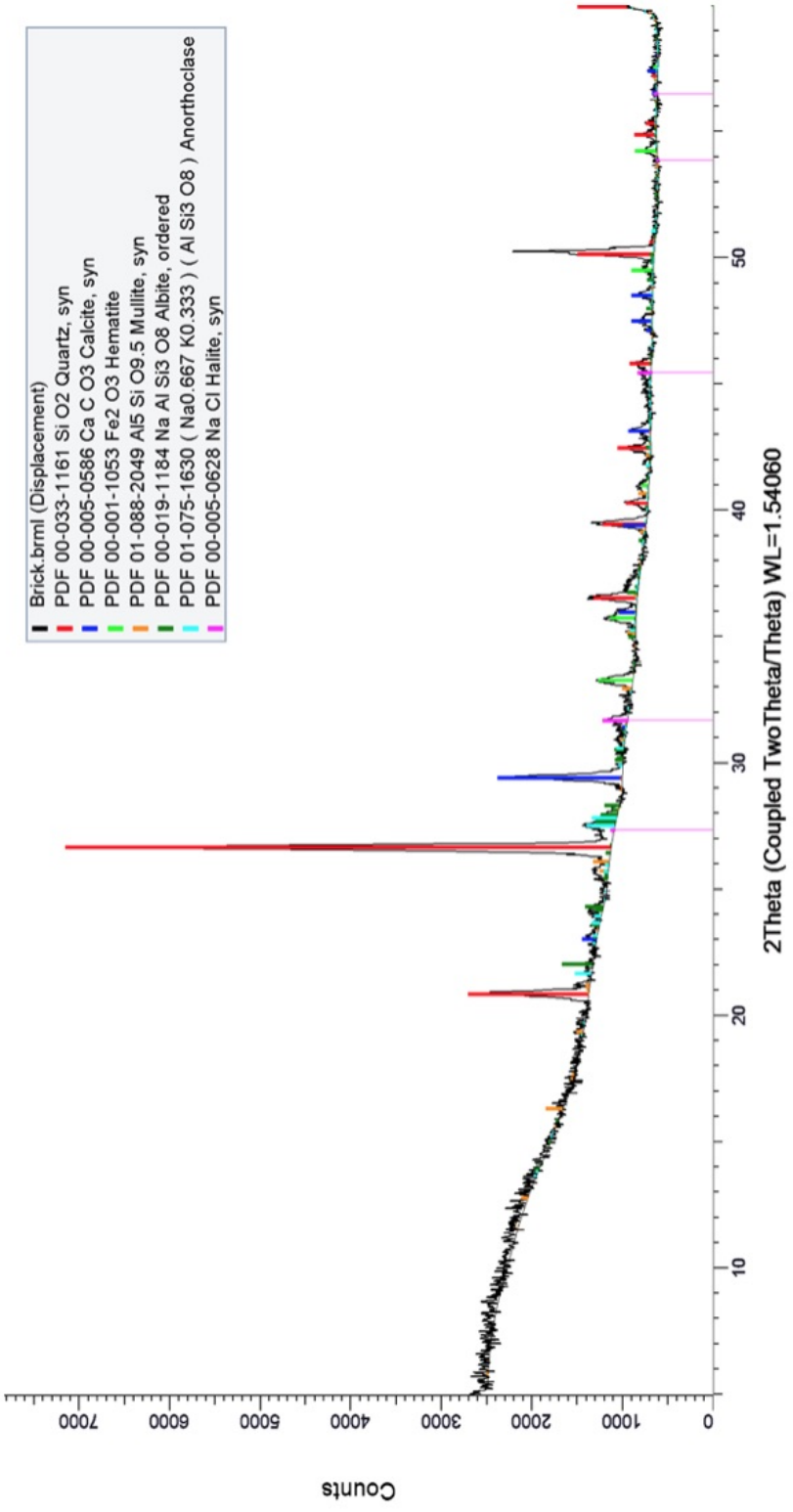

SAMPLE Mortar Clock Tower

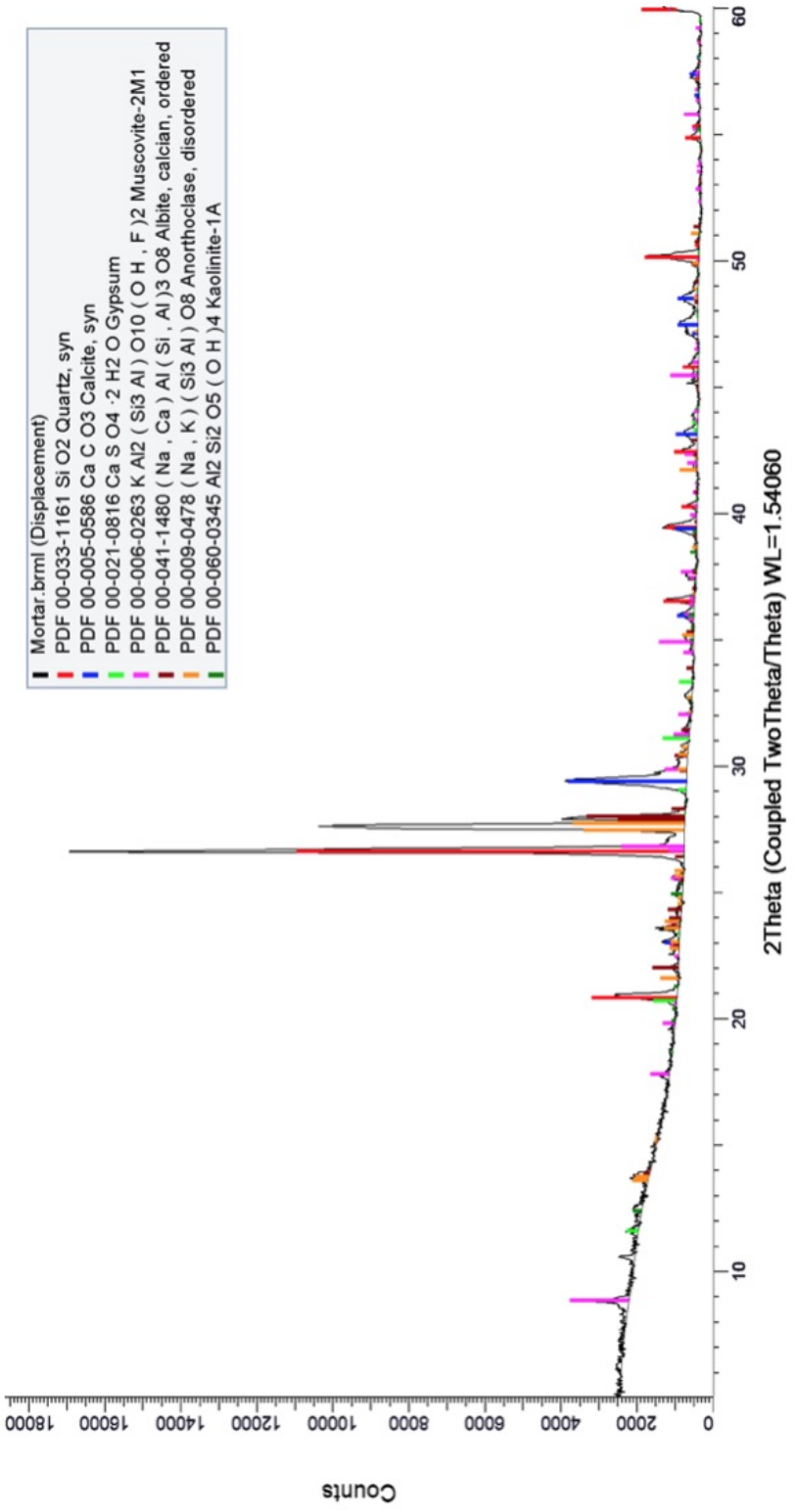

SAMPLE Salt Clock Tower

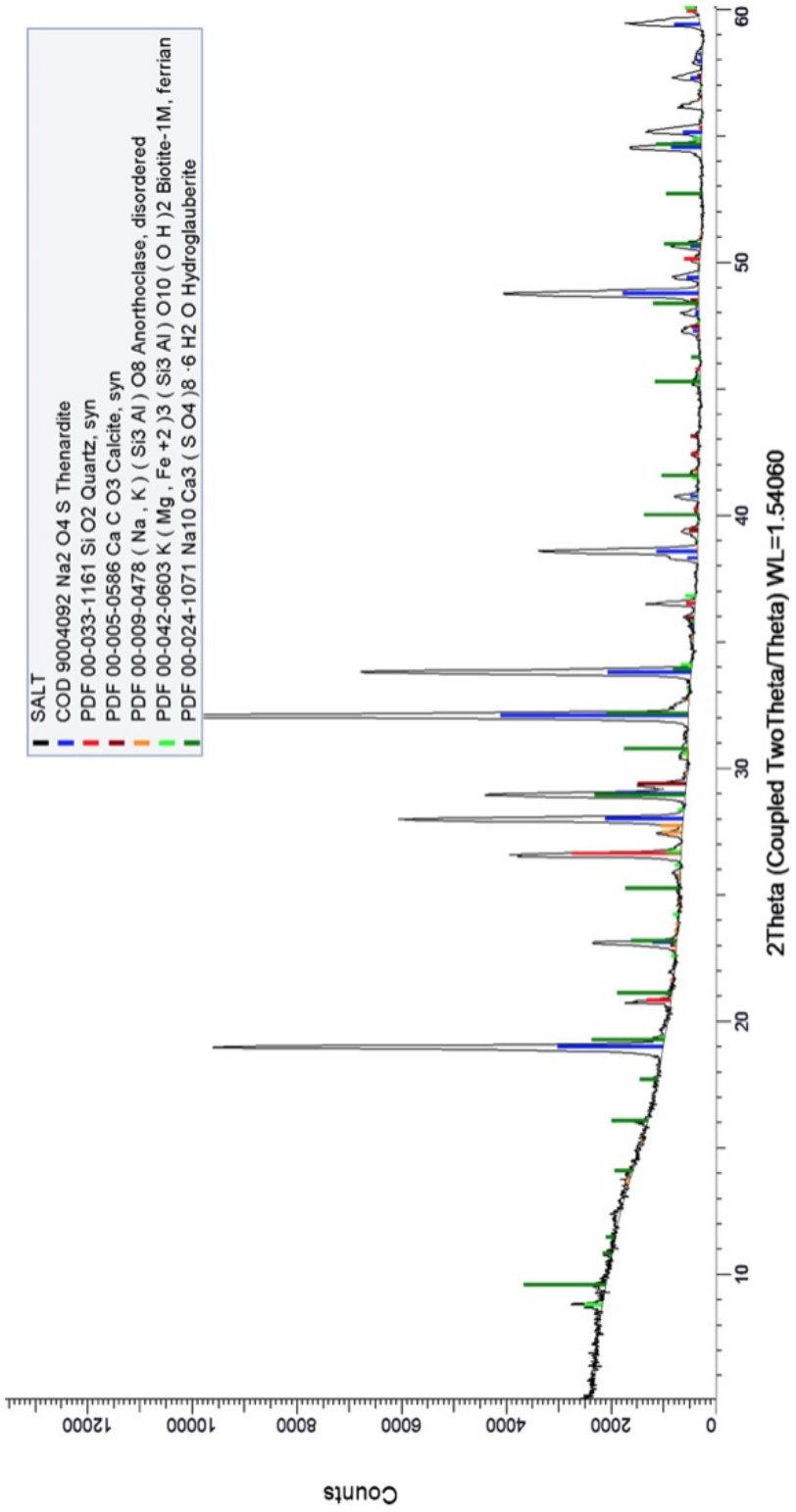

Chapter 9

Appendix C

9.1 Chapter 4: Salt content tables

Table 9.1: BE01 salt content variation

Cycle number	Dry W	Sat W	Mass increase relative to the dry mass (g)	Dry mass gain per cycle (g)	Solution content	Actual salt from solution content (g)	Water residue (g)
dry	26.13	27.77	0	0	1.64	0.092	N/A
1	26.34	27.81	0.21	0.21	1.47	0.083	0.12
2	26.35	27.8	0.22	0.01	1.45	0.08	0.14
3	26.35	27.77	0.22	0	1.42	0.08	0.14
4	26.36	27.73	0.23	0.01	1.37	0.08	0.15
5	26.36	27.71	0.23	0	1.35	0.08	0.15
6	26.37	27.71	0.24	0.01	1.34	0.07	0.16
7	26.37	27.74	0.24	0	1.37	0.08	0.16
8	26.38	27.78	0.25	0.01	1.4	0.08	0.17
9	26.39	27.78	0.26	0.01	1.39	0.08	0.18
10	26.4	27.8	0.27	0.01	1.4	0.08	0.19
11	26.41	27.8	0.28	0.01	1.39	0.08	0.20
12	26.42	27.8	0.29	0.01	1.38	0.08	0.21
13	26.43	27.79	0.3	0.01	1.36	0.08	0.22
14	26.44	27.78	0.31	0.01	1.34	0.07	0.23
15	26.44	27.78	0.31	0	1.34	0.07	0.23
16	26.44	27.78	0.31	0	1.34	0.07	0.23
17	26.45	27.77	0.32	0.01	1.32	0.07	0.24
18	26.45	27.76	0.32	0	1.31	0.07	0.24
19	26.46	27.75	0.33	0.01	1.29	0.07	0.26
20	26.46	27.73	0.33	0	1.27	0.07	0.26

Table 9.2: BE02 salt content variation

Cycle number	Dry W	Sat W	Mass increase relative to the dry mass (g)	Dry mass gain per cycle (g)	Solution content	Actual salt ($CaCl_2 \cdot 2H_2O$) from solution content (g)
dry	23.41	24.63	0	0	1.22	0.16
1	23.56	24.65	0.15	0.15	1.09	0.15
2	23.65	24.75	0.24	0.09	1.1	0.15
3	23.66	24.025	0.25	0.01	0.36	0.05
4	23.66	24.045	0.25	0	0.38	0.05
5	23.67	24.035	0.26	0.01	0.36	0.05
6	23.66	23.99	0.25	-0.01	0.33	0.04
7	23.67	24.095	0.26	0.01	0.42	0.06
8	23.68	24.2	0.27	0.01	0.52	0.07
9	23.69	24.305	0.28	0.01	0.61	0.08
10	23.7	24.41	0.29	0.01	0.71	0.096
11	23.7	24.515	0.29	0	0.81	0.11
12	23.71	24.62	0.3	0.01	0.91	0.12
13	23.72	24.725	0.31	0.01	1.00	0.14
14	23.73	24.83	0.32	0.01	1.1	0.15
15	23.74	24.935	0.33	0.01	1.19	0.16
16	23.74	25.04	0.33	0	1.3	0.17
17	23.75	25.14	0.34	0.01	1.39	0.19
18	23.76	25.23	0.35	0.01	1.47	0.198
19	23.76	25.355	0.35	0	1.59	0.21
20	23.77	25.46	0.36	0.01	1.69	0.23

Table 9.3: BE03 salt content variation

Cycle number	Dry W	Sat W	Mass increase relative to the dry mass (g)	Dry mass gain per cycle (g)	Solution content	Actual salt from solution content (g)	Water residue (g)
dry	36.9	38.54	0	0	1.64	0.20	N/A
1	27.29	38.5	0.39	0.39	1.21	0.15	0.19
2	27.33	38.7	0.43	0.04	1.37	0.17	0.28
3	27.34	38.69	0.44	0.01	1.35	0.16	0.27
4	27.35	38.67	0.45	0.01	1.32	0.16	0.28
5	37.37	38.48	0.47	0.02	1.11	0.13	0.31

Bibliography

[1] Andreassen, J. P., Lewis, A. E. 2017 - *Classical and Nonclassical Theories of Crystal Growth* - A.E.S. Van Driessche et al. (eds.), New Perspectives on Mineral Nucleation and Growth. Springer International Publishing Switzerland.

[2] Arnold, A., Zehnder, K., 1991 - *Monitoring wall paintings affected by soluble salts. In: Cather S (ed) The Conservation of Wall Paintings.* - Proceedings of the symposium organized by the Courtauld Institute of Art and the Getty Conservation Institute, London, July 13-16. Los Angeles, pp. 103-135

[3] ASTM, 1992 - *Standard Guide for Computed Tomography (CT) Imaging* - ASTM Designation E 1441 - 92a. In: 1992 Annual Book of ASTM Standards, Section 3 Metals Test Methods and Analytical Procedures. ASTM, Philadelphia, pp. 690-713.

[4] Baglioni, P., Chelazzi, D., Giorgi, R., 2014 - *Nano-technologies in the Conservation of Cultural Heritage: A compendium of materials and techniques* - Springer - pp. 144

[5] Benavente, D., 2004 - *Role of pore structure in salt crystallisation in unsaturated porous stone* - J. Cryst. Growth. 260,532–544

[6] Benavente, D., Garcia del Cura, M., Bernabeu, A., Ordonez, S., 2001 - *Quantification of salt weathering in porous stones using an experimental continuous partial immersion method.* - Eng Geol 59(3-4):313-325.

[7] Bianchin, S., Favaro, M., Vigato, P.A., Botticelli, G., Germani, G., Botticelli, S., 2009 - *The scientific approach to the restoration and monitoring of mural paintings*

at S. Girolamo Chapel - SS. Annunziata Church in Florence - J Cult Herit., 10 (3): 379-387.

[8] Boynton, R., S., 1980 - *Chemistry and Technology of Lime and Limestone* - Wiley, New York

[9] Brodale, G., W.F. Giauque, 1958 - *The Heat of Hydration of Sodium Sulfate. Low Temperature Heat Capacity and Entropy of Sodium Sulfate Decahydrate* Journal of the American Chemical Society. 80 (9): 2042 - 2044.

[10] Butkovich, T. R., 2004 - *Thermal Expansion of Ice.* - Journal of Applied Physics 30, 350 (1959)

[11] CEN, 1999, EN 12370 Natural stone test methods. Determination of resistance to salt crystallization

[12] Charola, E., 2000 - *Salts in the deterioration of porous materials: an overview* - JAIC, Volume 39, Number 3, Article 2.

[13] Charola, E., Rousset, B., Blauer, C., 2017 - *Deicing Salts: An Overview* - SWBSS 2017. 20-22 September 4th International Conference on Salt Weathering of Buildings and Stone Sculptures

[14] Charola, A. E., Weber, J., 1992 - *The hydration-dehydration mechanism of sodium sulphate* - In Seventh International Congress on the Deterioration and Conservation of Stone, ed. J.Delgado Rodrigues et al.Lisbon: Laboratorio Nacional de Engenharia Civil. 581-590.

[15] Cole, D. I., 1976 - *Velocity/Porosity relationship in limestones from the Portland group of southern England.* - Geoexploration, 14: 37-50.

[16] Collepardi, M., 1991 -*Scienza e tecnologia del calcestruzzo* - HOEPLI EDITORE, Italy.

[17] Collins, J.A., 1993 - *Failure of Materials in Mechanical Design: Analysis, Prediction, Prevention* - John Wiley & Sons, p. 654.

[18] Coussy, O., 2006 - *Deformation and stress from in-pore drying-induced crystallization of salt* - Journal of the Mechanics and Physics of Solids, Volume 54, Issue 8, pp. 1517-1547.

[19] Cuddle,V., Boone, M.N., 2013 - *High-resolution X-ray computed tomography in geosciences: A review of the current technology and applications* - Earth-Science Reviews Volume 123. pp. 1-17.

[20] Cupples, H.L., 1945 - *The surface tensions of calcium chloride solutions at* $25°C$ *measured by their maximum bubble pressures.* - J. Am. Chem. Soc., 67, 6, 987-990.

[21] Currier, L.W., 1960 - *Geological appraisal of dimension-stone deposits.* - Geological Survey Bulletin 1109:1-78.

[22] Desarnaud, J., Derluyn, H., Molari, S., De Miranda, S., Cnudde, V., Shahidzadeh N., 2015 - *Drying of salt contaminated porous media: Effect of primary and secondary nucleation* - Journal of Applied Physics 118, 114901

[23] Dewanckele, J., De Kock, T., Boone, M.A., Cnudde, V., Brabant, L., Boone, M.N., Fronteau, G., Van Hoorebeke, L., Jacobs, P., 2012 - *4D imaging and quantification of pore structure modifications inside natural building stones by means of high resolution X-ray CT* - Science of The Total Environment - Volume 416, pp. 436-448.

[24] De yoreo, J.J., Vekilov, P.J., 2003 - *principles of crystal nucleation and growth* - Rev. Mineral. Geochem. 54, 57-94.

[25] Doehne, E., Price, C., 2010 - *Stone Conservation: An Overview of Current Research* - The Getty Conservation Institute Los Angeles.

[26] Doehne, E., Selwitz, C., Carson, D., 2002 - *The Damage Mechanism of Sodium Sulfate in Porous Stone* - Proceedings of the SALTeXPERT Meeting, Prague, ARCCHIP and GCI.

[27] http://dx.doi.org/10.15129/2fb54088-1187-48f2-832b-ef76cf5e7bc1

[28] Espinosa-Marzal, R.M., Hamilton, A., McNall, M., Whitaker, K., Scherer, G.W., 2011 - *The chemomechanics of crystallization during rewetting of limestone impregnated with sodium sulfate* - Journal Of Materials Research - Pittsburgh then Warrendale, 26, 12. pp. 1472-1481.

[29] Espinosa Marzal, R., Scherer, G. W., 2008 - *Crystallization of sodium sulfate salts in limestone* - Environmental Geology, 56(3-4), pp. 605-621.

[30] Espinosa-Marzal, R., Scherer, G. W., 2009 -*Crystallization Pressure Exerted by in-Pore Confined Crystals* - Poro-Mechanics Iv. 1013-1018.

[31] Espinosa-Marzal, R., Scherer, G. W., 2010 - *Mechanisms of damage by salt* - Geological Society, London, Special Publications, 331(1), pp.61-77.

[32] Farnam, Y., Washington, T., Weiss, J., 2015 - *The Influence of Calcium Chloride Salt Solution on the Transport Properties of Cementitious Materials* - Advances in Civil Engineering, Volume 2015, Article ID 929864

[33] Farnam, Y., Wiese, A., Bentz, D., Davis, J.,Weiss, J. 2015 - *Damage development in cementitious materials exposed to magnesium chloride deicing salt* - Construction and Building Materials 93, pp. 384–392

[34] Flatt, R.J., Caruso, F., Aguilar Sanchez, A.M., Scherer, G.W., 2014 - *Chemomechanics of salt damage in stone* - Nature Communications volume 5, Article number: 4823.

[35] Flatt R.J., Mohameda, N., Caruso, F., Derluyn, H., Desarnaud, J., Lubelli, B., Espinosa-Marzal, R.M., Pel, L., Rodriguez-Navarro, C., Scherer, G.W., Shahidzadeh, N., Steiger, M., 2017 - *Predicting salt damage in practice: a theoretical insight intolaboratory tests* - RILEM Technical Letters 2: 108-118

[36] Forster,A.M., Szadurski, E.M. , Banfill, P.F.G., 2014 - *Deterioration of natural hydraulic lime mortars, I: effects of chemically accelerated leaching on physical and mechanical properties of uncarbonated materials* - Constr. Build. Mater, 72, pp. 199-207

[37] Fortes, A. D., Brand, H. E. A., Vocadlo, L., Scott L. A.-Fernandez-Alonso, F., Wooda, I. G., 2013 - *P–V–T equation of state of synthetic mirabilite ($Na_2SO_4 \cdot 10D_2O$) determined by powder neutron diffraction.* - Journal of Applied Crystallography. ISSN 0021-8898

[38] Fusseis, F., Schrank, C., Liu, J., Karrech, A., Llana-Funez, S., Xiao, X., Regenauer-Lieb, K., 2012 - *Pore formation during dehydration of a polycrystalline gypsum sample observed and quantified in a time-series synchrotron X-ray micro-tomography experiment* - Solid Earth, 3, 71-86.

[39] Giorgi, R., Ambrosi, M., Toccafondi, N., Baglioni, P., 2010 -*Nanoparticles for Cultural Heritage Conservation: Calcium and Barium Hydroxide Nanoparticles for Wall Painting Consolidation* - Chemistry - A European Journal, 16,pp. 9374 - 9382.

[40] Gmelin, L. 1981 - *Gmelin Handbook of Inorganic and Organometallic Chemistry - 8th edition* - GMELIN Institute for Inorganic Chemistry of theMax-Planck-Society for the Advancement of Science

[41] Godinho J., Gerke K.M., Stack A., Lee P., 2016 - *The dynamic nature of crystal growth in pores.* - Scientific Reports,2016, 6: 33086

[42] Goudie, A.S., Viles, H.A., 1997 - *Salt Weathering Hazards, Cataclasis and Deformation Band Formation in Unconsolidated Marine Terrace Sand* - John Wiley & Sons: UK.

[43] Graham, C.J., 2016 - *A petrographic investigation into the durability of common replacement sandstones to the crystallisation of de-icing salts.* - PhD thesis, University of Glasgow.

[44] Granneman, S.J.C., Shahidzadeh, N., Lubelli, B., Van Hees, R.P.J., 2017 - *Effect of borax on the wetting properties and crystallization behaviour of sodium sulphate* - CrystEngComm, 19.

[45] Guglielmini, L., Gontcharov, A., Aldykiewicz, A. J., Stone, H. A., 2009 - *Drying of salt solutions in porous materials: intermediate-time dynamics and efflorescence* - Phys. Fluids 20, 077101.

[46] Gupta, S., Terheiden, K., Pel, L., Sawdy, A., 2012 - *Influence of ferrocyanide inhibitors on the transport and crystallization processes of sodium chloride in porous building materials* - Crystal Growth & Design.

[47] Hall, C., Hoff, W. D., 2012 - *Water Transport in Brick, Stone and Concrete* - Spon Press, New York, NY, USA, 2nd edition.

[48] Hall, C., Marchand J., Gerard, G., Sosoro, M., 1997 - *Transport of fluids in homogenous isotropic cementitous composites* - Penetration and Permeability of Concrete, H. W. Reinhardt, Ed., RILEM Report 16, pp. 5–79, 1997.

[49] Hamilton, A., Cimerman-Sariego, A., 2011 - *Measuring crystal growth propagation through porous materials: transformation of sodium sulphate heptahydrate to mirabilite* - Second international conference on Salt Weathering on Building Stones and Sculptures, Limassol, pp. 15-22.

[50] Hamilton, A., Hall, C., Pel, L., 2008 - *Sodium sulfate heptahydrate: direct observation of crystallization in a porous material* - Journal of Physics D: Applied Physics, 41(21), p.212002.

[51] Hamilton, A., Hall, C., Pel, L., 2008 - *Salt damage and forgotten metastable sodium sulphate heptahydrate: Direct observation of crystallisation in a porous material* - Journal of Physics D: Applied Physics 41.

[52] Hamilton, A., Hall, C. and Pel, L., 2008 - *Sodium sulfate heptahydrate: direct observation of crystallization in a porous material*- Journal of Physics D: Applied Physics, 41.

[53] Harnick, A.B., Meier, V., Rosli, A., 1980 - *Combined influence of freezing and deicing salt on concrete: physical aspects* - In: Sereda PJ, Litvan GG, editors. Durability of building materials and components. ASTM STP 691. pp. 474-84.

[54] Hart, D. J., Wang, H. F., 1995 - *Laboratory measurements of a complete set of poroelastic moduli for Berea sandstone and Indiana limestone.* - Journal of Geophysical Research, Vol.100, No. B9, pp. 17,741-17,751

[55] Hill, K. O., Meltz, G. 1997 - *Fiber Bragg Grating Technology Fundamentals and Overview* - Journal of Lightwave Technology, Vol. 15, No. 8.

[56] http://portal.historicenvironment.scot/LB37256

[57] Huang, Q., Lu, G., Wang, J., Yu, J. 2011 - *decomposition mechanisms of MgCl2·6H2O and MgCl2·H2O* - Journal of Analytical and Applied Pyrolysis. Vol 91.

Huinink, H. P., Pel, L., Michels, M. A. J., 2002 - *How ions distribute in a drying porous medium: a simple model* - Phys. Fluids 14 (4), 1389–1395

[58] Huinink, H. P., Pel, L., Michels, M. A. J., 2002 - *How ions distribute in a drying porous medium: a simple model* - Phys. Fluids 14 (4), 1389–1395

[59] Jackson, K.A., 2004 - *Kinetic Processes: Crystal Growth, Diffusion, and Phase Transitions in Materials* - Wiley-VCH, ISBN-10: 3527306943, Weinheim

[60] Jimenez-Gonzalez, I., Rodriguez-Navarro, C., Scherer, G. W., 2008 - *Role of clay minerals in the physicomechanical deterioration of sandstone* - Journal of Geophysical Research, 113(F2).

[61] Karha, P. and Jaakkola, T., 2008 - *Simple active method for reducing magnetic interference in a thermoelectrically cooled photomultiplier tube* - Review of Scientific Instruments, 79(4), p.043102.

[62] Ketcham, R.A., Carlson, W.D., 2001 - *Acquisition, optimization and interpretation of X-ray computed tomographic imagery: Applications to the geosciences.* - Computers and Geosciences, 27, 381-400.

[63] Ketcham, R.A., 2005 - *Three-dimensional grain fabric measurements using high-resolution X-ray computed tomography* - Journal of Structural Geology 27. pp.1217-1228.

[64] Kimber,O. G., Allison, R. J., Cox, N. J., 1998 - *Mechanisms of failure and slope development in rock masses.* - Trans Inst Br Geogr NS 23 353–370. ISSN 0020–2754

[65] Kipouros, G.,Sadoway, D., 1987 - *The chemistry and electrochemistry of magnesium production.* Advances in Molten Salt Chemistry. 6. 127-209.

[66] Kruth, J.P., Bartscher, M., Carmignato, S., Schmitt, R., De Chiffre, L., Weckenmann, A., 2011 - *Computed tomography for dimensional metrology* - CIRP Ann. Manuf. Technol. 60. pp. 821-42.

[67] La Iglesia, A., Gonzalez, V., Lopez-Acevedo, V., Viedma, C., 1997 - *Salt crystallization in porous construction materials: I. Estimation of crystal-lization pressure* - J Cryst Growth 177.

[68] Lawrence, M., Jiang, Y., 2017 - *Porosity, Pore Size Distribution, Micro-structure* - RILEM State-of-the-Art Reports 23

[69] Levy, H. A., Lisensky, G. C., 1978 - *Crystal Structures of Sodium Sulfate Decahydrate (Glauber's Salt) and Sodium Tetraborate Decahydrate (Borax). Redetermination by Neutron Diffraction** - Acta Cryst. B34, 3502-3510

[70] Linke,W., F., Seidel, A., 1958 - *of Inorganic and Metal Organic Compounds* - Vol. 2, 3th edn., (Am. Chem. Soc., Washington)

[71] Lubelli, B., Cnudde, V., Diaz-Goncalves T., Franzoni, E., van Hees, P.J.R., Ioannou, I., Menendez, B., Nunes, C., Siedel, H., Stefanidou, M., Verges-Belmin, V., Viles, H., 2018 - *Towards a more effective and reliable salt crystallization test for porous building materials: state of the art* - Materials and Structures 51:55

[72] Macente, A., Fusseis, F., Menegon, L., Xianghui, X., John, T., 2017 - *The strain-dependent spatial evolution of garnet in a high-P ductile shear zone from the Western Gneiss Region (Norway): a synchrotron X-ray microtomography study.* - J. metamorphic Geol., 35, 565-583

[73] Marliacy, P., Solimando, R., Bouroukba, M., Schuffenecker, L., 2000 - *Thermodynamics of crystallization of sodium sulfate decahydrate in $H2O{\pm}NaCl{\pm}Na2SO4$:*

application to $Na_2SO_410H_2O$-based latent heat storage materials. - Thermochimica Acta 344, 85-94

[74] Martino, M., Danisi, A., Losito, R., Masi, A., Spiezia, G., 2010 - *Design of a Linear Variable Differential Transformer With High Rejection to External Interfering Magnetic Field* - IEEE Transactions on Magnetics, 46(2), pp.674-677.

[75] Masi, A., Danisi, A., Losito, R., Martino, M., Spiezia, G., 2010 - *Study of magnetic interference on a LVDT prototype* - IEEE Transactions on Instrumentation and Measurements, 60, pp. 219-223.

[76] Matusita, K., Komatsu, T., Yokota, R., 1984 - *Kinetics of non-isothermal crystallization process and activation energy for crystal growth in amorphous materials.* - Journal of Materials Science, 19, pp. 291-296, 0022-2461

[77] McDonald, P., Iosifescu, C., 1998 - *Use of a LVDT displacement transducer in measurements at low temperatures* - Measurement Science and Technology, 9(4), pp.563-569.

[78] McLaren, S., Goudie, A., Viles, H., 1999 - *Salt Weathering Hazards* - The Geographical Journal, 165(2), p.234.

[79] https://www.metoffice.gov.uk/pub/data/weather/uk/climate/stationdata/lerwickdata.txt

[80] Moncmanova, A., 2007 - *Environmental factors that influence the deterioration of materials* - In: Escrig, F. (Ed.), Environmental Deterioration of Materials. Athenaeum Press Ltd, Great Britain, pp. 4-21

[81] Mullin, J.W., (2001) - *Crystallization* - Butterworth- Heinemann, ISBN-10: 0750648333, London

[82] Nachshon, U., Weisbrod, N., 2015 - *Beyond the salt crust: On combined evaporation and subflorescent salt precipitation in porous media* - Transport in Porous Media, ISSN 0169-3913

[83] Nachshon, U., Weisbrod, N., Dragila, M. I., Grader, A., 2011 - *Combined evaporation and salt precipitation in homogeneous and heterogeneous porous media* - Water Resour. Res., 47, W03513

[84] Neumeier, J. J., 2018 - *Elastic Constants, Bulk Modulus, and Compressibility of H_2O Ice Ih for the Temperature Range 50 K-273 K* - J. Phys. Chem. Ref. Data 47, 033101

[85] Nyce, S. D., 2004 - *Linear Position Sensors: Theory and Application* - John Wiley & Sons, pp. 184.

[86] Pel, L., Huinink, H.P., Kopinga, K., 2002 - *Ion transport and crystallization in inorganic building materials as studied by nuclear magnetic resonance* - Applied Physics Letters, 81(15) 2893-2895.

[87] Perry, M., Yan, Z., Sun, Z., Zhang, L., Niewczas, P., and Johnston, M., 2014 - *High stress monitoring of prestressing tendons in nuclear concrete vessels using fibre-optic sensors* - Nuclear Engineering and Design, 268, pp.35-40.

[88] Price, C. A., 1978 - *The use of the sodium sulphate crystallisation test for determining the weathering resistance of untreated stone* - In UNESCO/RILEM International Symposium, Paris, vol. 3.6, pp. 1 - 23.

[89] Price, C.A., Doehne, E., 2010. - *Stone Conservation: An Overview of Current Research* - 2nd Ed. Getty publications.

[90] Prieto, M., Putnis, A., Fernandez-Diaz, L., 1990 - *Factors controlling the kinetics of crystallization: supersaturation evolution in a porous medium. Application to barite crystallization.* - Geological Magazine 127, 485-95.

[91] Putnis, A., Prieto, M., Fernandez-Diaz, L., 1995 - *Fluid supersaturation and crystallization in porous media.* - Geological Magazine 132, 1-13.

[92] Rad, M. N., Shokr, N., 2012 - *Nonlinear effects of salt concentrations on evaporation from porous media* - GEOPHYSICAL RESEARCH LETTERS, VOL. 39, L04403

[93] Robertson, E. C., 1998 - *Thermal properties of rocks* - U.S. Dept. of the Interior, Geological Survey, Books and Open-file Reports Section.

[94] Rodriguez-Navarro, C., Doehne, E., 1999 - *Salt weathering: influence of evaporation rate, supersaturation and crystallization pattern* - Earth Surface and Landforms, Earth Surf. Process. Landforms 24(3), pp. 191-209.

[95] Rodriguez-Navarro, C., Doehne, E., Sebastian, E., 2000 - *How does sodium sulphate crystallize? Implications for the decay and testing of building materials* - Cement and Concrete Research 30.

[96] Roels,S., Carmeliet, J., Hens, H., Adan, O., Brocken, H., Cerny, R., Pavlik, Z., Hall, C., Kumaran, K., Pel, L., Plagge, R., 2004 - *Interlaboratory Comparison of Hygric Properties of Porous Building Materials* - Journal of Thermal Envelope and Building Science, 27: 307-325.

[97] Ruiz-Agudo, E., Mees, F., Jacobs, P., Rodriguez-Navarro, C., 2007 - *The role of saline solution properties on porous limestone salt weathering by magnesium and sodium sulfates.* - Environ Geol 52(2):269-281

[98] Saidov, T., Pel, L., Espinosa-Marzal, R.M., Scherer, G.W., 2012 - *Nucleation of sodium sulfate heptahydrate on mineral substrates studied by nuclear magnetic resonance* - Journal of Crystal Growth, 338(1), pp. 166-169.

[99] Saidov, T. A., Pel, L., Kopinga, K. 2019 - *Crystallization Pressure of Sodium Sulfate Heptahydrate* - Cryst. Growth Des. 2015, 15, 2087-2093

[100] Sawdy, A., Heritage, A., Pel, L. 2008 - *A review of salt transport in porous media : assessment methods and salt reduction treatments.* - Salt weathering on buildings and stone sculptures (SWBSS), 10-08, Copenhagen, Denmark

[101] Schaffer, R.J., 2004 - *The Weathering of Natural Building Stones.*

[102] Scherer, G.W., Gupta, S., 2013 - *Pressure from Crystallization in Pore Channels* - Poromechanics V: Proceedings of the Fifth Biot Conference on Poromechan-ics (Am. Soc. Civil Eng., Reston, VA) pp. 766-771

[103] Scherer, G. W., Wheeler, G.S., 2009 - *Silicate Consolidants for Stone* - Key Engineering Materials (Volume 391) p. 5.

[104] Sebastian, E., Cultrone, G., Benavente, D., Linares-Fernandez, L., Elert, K., Rodriguez-Navarro, C., 2008 - *Swelling damage in clay-rich sandstones used in the church of San Mateo in Tarifa (Spain)* - Journal of Cultural Heritage, Vol. 9.

[105] Seippel, R., 1988 - *Transducer interfacing* - Englewood Cliffs, New Jersey: Prentice Hall.

[106] Sereda, P.J., 1978 - *Durability of Building Materials and Components* - Proceedings of the First International Conference: a Symposium Presented at Ottawa, Canada, 21-23 Aug, Ed. 691

[107] Shahidzadeh-Bonn, N., Desarnaud, J., Bertrand, F., Chateau, X., Bonn, D., 2010 - *Damages in porous media due to salt crystallization* - Physical Review E81.

[108] Sherer, G.W., 1999 - *Crystallization in pores* - Cement and Concrete Research, Volume 29, Issue 8, 1347-1358.

[109] Shi, X., Liu, Y., Mooney, M., Berry, M., Hubbard, B., Fay, L., Leonard, A., 2010 - *Effect of chloride-based deicers on reinforced concrete structures.* - WSDOT Research Report.

[110] Shi, X., Akin, M., Pan, T., Fay, L., Liu, Y., Yang, Z., 2009 - *Deicer Impacts on Pavement Materials: Introduction and Recent Developments* - The Open Civil Engineering Journal, 2009, 3, pp.16-27

[111] Sinke, G.C.,Mossner, E.H.,Curnutt, J.L., 1985 - *Enthalpies of solution and solubilities of calcium chloride and its lower hydrates* - The Journal of Chemical Thermodynamics, Volume 17, Issue 9,Pp. 893-899

[112] Spiezia, G., Losito, R., Martino, M., Masi, A., Pierno, A., 2011 - *Automatic Test Bench for Measurement of Magnetic Interference on LVDTs* - IEEE Transactions on Instrumentation and Measurement, 60(5), pp.1802-1810.

[113] Spragg, R. P., Castro, J., Li, W., Pour-Ghaz, M., Huang, P.-T., Weiss, J., 2011 - *Wetting and drying of concrete using aqueous solutions containing deicing salts* - Cement and Concrete Composites, vol. 33, no. 5, pp. 535–542.

[114] Staveley, L. A. K., Linford, L. G., 1969 - *The heat capacity and entropy of calcite and aragonite, and their interpretation.* - J. Chem. Thermodynamics 1,1, l-11

[115] Steiger, M., Asmussen, S., 2008 - *Crystallization of sodium sulfate phases in porous materials: The phase diagram Na2SO4-H2O and the generation of stress* - Geochimica et Cosmochimica Acta, Volume 72, Issue 17, pp. 4291-4306.

[116] Sun, Z., Scherer, G. W. 2010 - *Measurement and simulation of dendritic growth of ice in cement paste* - Civil & Env. Eng., Princeton University, Princeton, NJ 08544 USA

[117] Tamerlan, A.S., Pel, L., Kopinga, K., 2017 - *Sodium sulfate salt weathering of porous building materials studied by NMR.* - Materials and Structures, 50:145.

[118] Tsui, N., Flatt, R.J., Sherer, G.W., 2003 - *Crystallization damage by sodium sulphate* - Journal of Cultural Heritage 4.

[119] Tuckermann, R., 2007 - *Surface tension of aqueous solutions of water-soluble organic and inorganic compounds* - Atmospheric Environment 41 (2007) 6265–6275.

[120] Van Santen, R., Parker, S. C., Watson, G. W., 1996 *Free-energy calculations of thermodynamic, vibrational, elastic, and structural properties of quartz at variable pressures and temperatures* - Physical review. B, Condensed matter.

[121] Veran-Tissoires S., Prat., M., 2014 - *Evaporation of a sodium chloride solution from a saturated porous medium with efflorescence formation* - J. Fluid Mech., vol. 749, pp. 701–749., Cambridge University Press

[122] Washburn, E. W. 1928 - *International Critical Tables of Numerical Data, Physics, Chemistry and Technology* - Vol. III, McGraw-Hill, New York

[123] Wenjuan S., Brown, S., Leach, R., 2011 - *An overview of industrial X-ray computed tomography* - NPL REPORT ENG 32

[124] Uhlmann, D.R., Chalmers, B., Jackson, K.A., 1964 -*Interractions between particles and a solid-liquid interface* - Journal of Allied Physics 35.

[125] Viles, H., - *Salt Crystallisation in Masonry* - http://www.buildingconservation.com/articles/salt-crystallisation/salt-crystallisation.htm

[126] Wang, K., Nelsen, D.E., Nixon, W.A., 2006 - *Damaging effects of deicing chemicals on concrete materials* - Cement Concr Comp. vol. 28, no. 2, pp.173-188.

[127] Weinberger, R., Reches, Z., Eidelman, A., Scott, E. T., 1994 - *Tensile properties of rocks in four-point beam tests under confining pressure* - Rock mechanics, Nelson & Laubach (eds), Balkema, Rotterdam.

[128] Wise, M.E., Semeniuk,T.A., Bruintjes, R., Martin, S.T., Russell, L.M., Buseck, P.R., 2007 - *Hygroscopic behaviour of NaCl-bearing natural aerosol particles using environmental transmission electron microscopy* - J. Geophys. Res., 112, D10224.

[129] Wong, C. P., Raja, S., Bollanpally, L., 1999 - *Thermal Conductivity, Elastic Modulus, and Coefficient of Thermal Expansion of Polymer Composites Filled with Ceramic Particles for Electronic Packaging* - Journal of Applied Polymer Science, Vol. 74, 3396–3403

[130] Zeng, D., Zhou, Voigt, W., 2007 - *Thermodynamic consistency of solubility and vapor pressure of a binary saturated salt + water system. II. CaCl2 + H2O. Fluid Phase Equilibria* - 253. 1-11. 10.1016/j.fluid.2006.12.017.